Seeing the First Light

A Study of the Dark and Dim Ages

Emma Olivia Chapman

Submitted for the degree of Doctor of Philosophy

Department of Physics and Astronomy

University College London

November 2013

I, *Emma Chapman*, confirm that the work presented in this thesis is my own.

Where information has been derived from other sources, I confirm that this has been indicated in the thesis.

Abstract

The Epoch of Reionization (EoR) represents a major phase shift in the history of our Universe. After a long, dark, period of expansion and cooling, the first ionizing sources began to ionize the surrounding hydrogen atoms. These bubbles of ionized hydrogen grew and overlapped until eventually the Universe was mostly ionized. Though there are some constraints on the duration and end of reionization from CMB experiments such as WMAP, the EoR remains a largely mysterious and unconstrained era.

The hyperfine transition of the hydrogen atom produces a photon of wavelength 21-cm. This 21-cm radiation can be measured by current generation radio telescopes such as the Low Frequency Array (LOFAR) to provide statistical information, and future radio telescopes such as the Square Kilometre Array (SKA) to produce tomographic maps. A statistical detection of the EoR is a key priority of the LOFAR-EoR project but is not a straight-forward task due to the considerable contribution of 21-cm radiation from non-EoR sources. Galactic synchrotron, Galactic free-free emission and extragalactic foregrounds dominate the cosmological EoR signal by up to 3 magnitudes and require accurate and precise cleaning in order to make trustworthy constraints on the EoR. In this thesis I introduce two statistical methods for EoR foreground removal: one based on statistical independence and one based on sparsity. Both have had success in CMB foreground removal and I show that they also produce impressive EoR power spectrum reconstructions.

I also consider the effect of the movement of the EoR hydrogen atoms on the observations made by a telescope such as LOFAR. The peculiar velocity of a hydrogen atom upon emission of a 21-cm photon has a marked effect on the 21-cm intensity and the frequency at which we observe the photon. This observed 'redshift-space' is noticeably different from the 'real-space' simulations output by many EoR simulation codes. In this thesis I take the semi-analytic reionization code SIMFAST21 and adapt it to output a multi-frequency observation in redshift space, a 'light cone', fully incorporating the peculiar velocities of the atoms. These light cones are essential for accurate comparison with forthcoming observations and I detail the numerous theoretical steps taken to create this code. I show that the result of including these peculiar velocities is non-negligible and in fact very large on small scales.

I then go on to tackle the idea that foreground avoidance is a viable alternative to foreground subtraction. Recent publications suggest that there is an area of k-space where the EoR signal is the dominant contribution when compared to the foregrounds - the 'EoR window'. This would suggest that statistical analysis could be carried out within that region only, relieving the need for foreground subtraction methods. Unlike the other publications on this topic, I consider a physically-motivated foreground model and show that the supposed EoR window is completely compromised as a result of the varying spectral index in the Galactic synchrotron model. I conclude that, though the EoR window is a useful tool for estimating where statistics will be most accurate, foreground removal is still essential to recover the EoR signal.

Finally, I apply my foreground subtraction methods to the first LOFAR-EoR data. Though not quite 'science ready', the 54 hours of data provide an exciting glimpse of how the foreground subtraction techniques introduced in this thesis work on real data. I find that GMCA not only removes the foregrounds impressively well for such raw data but actually acts as a powerful tool for the identification of systematics within the data. I identify these systematics and in several cases attempt modification and optimisations of the code in order to mitigate them. I find the results extremely promising and discuss how GMCA can be further optimised for future data and act as a feedback step for the calibration method.

Acknowledgements

To those I have worked with: I have never met a more friendly group to work with than the LOFAR-EoR team and I am so pleased to have been a part of it. A special thanks to Ger, Saleem, Vibor, Panos and Geraint who answered countless ignorant questions and were so welcoming right from day one. Mario - Thank you for letting me butcher your code and especially for ganging up on Fil with me. Jean-Luc and Jérome - GMCA is awesome, thank you for letting me use it and for explaining every part of it repeatedly to me!

To my supervisor: Fil, what can I say? It has been a rollercoaster! You are without a doubt one of the most difficult and frustrating and inspiring people I have encountered. You have put me through the wringer both intellectually and emotionally and I wouldn't take a second of it back. You have led me faultlessly through my PhD - being exceptionally accommodating towards my idiosyncrasies and providing me with a confidence in myself and what I do that I never knew I had. You've made me laugh and you've made me cry, you've sent me to sandy beaches and to A&E but at the end of it all I have been left not only with a PhD but with a good friend. Thank you.

To my husband: Steve. I have written this paragraph dozens of times because I just can't find the words! I don't have enough space to write about the countless times you did more than your share at home or made me cups of tea to fuel my writing. I said 'just half an hour more' way too many times and I thank you for never making me feel bad about it. Your unfaltering calm attitude made me think about the world in a different way from the moment I met you and helped me enjoy my work so much more once you taught me to relax! You are my best friend and the best father Lyra could wish for - I love you.

To my family: Mum and Dad - When I was considering my career options at school, not once did it occur to me that there were limits on what I could aim for and this is thanks to you. You gave me the most loving and wonderful childhood possible and you continue to be the most fantastic support now I have a family of my own. Mum, those early worksheets you created gave me a love of maths which finally led me to physics but your unconditional support for anything I put my mind to gave me the confidence to get there. Dad - growing up you seemed to know everything in the world. It was wanting to be like you that caused me to enjoy studying so much and your praise when I got my SATS, GCSEs and beyond meant more than the actual grade. I love you both so much.

To my oldest and best friends. Christine: You have been unconditionally there for me for as long as I can remember. You have never asked for anything and never complained when I wanted to play sylvanian families for the umpteenth time, moaned incessantly about boys or gave you a hug with my baby instead of a birthday present. Thank you, you are a constant and wonderful presence in my life and you never fail to cheer me up. Rachael: We've been through pretty much everything you can go through together and I wouldn't have got through a hell of a lot of it without you. Your limitless passion and fearlessness inspired me to get over my own fears and attack anything that scares me with a roar. You are the most awesome person I know and who the term 'kick-ass' surely was invented for.

To my little girl: Lyra, you will be too young to read this for quite some time but know that your giggles and smiles picked me up every time I thought I couldn't code another line. I hope that you find something in life which makes you as excited as cosmology makes me - if you do, grab it and don't let go!

To Steve ...

... who lights up my Universe

Contents

List of Figures

List of Tables

Chapter 1

Introduction

> Our whole universe was in a hot dense state, then nearly fourteen billion years ago expansion started. Wait...
>
> **Big Bang Theory Theme - Barenaked Ladies (2007)**

Our model of the past, present and future Universe has constantly evolved with more observations and greater understanding of those observations over time. The Universe has a way of tricking cosmologists into a false sense of security ... how many times has it been said that we had figured out the 'standard model' of the Universe, only for an observation such as a flat galactic rotation curve to be announced to incredulity, disbelief, amazement and then acceptance. As a graduate of the mid 2000s, being taught about dark matter had little more exotic flavour than the baryonic make-up of our Universe. The speed with which our community changes, accepts and evolves never ceases to amaze me and gives me the drive to do my research knowing that the next moment of disbelief and frantic re-thinking of theories could be just around the corner.

1.1 Timeline of the Universe

To provide context for this project, this section provides a brief outline of the current standard model for the evolution of the Universe up until the Epoch of Reionization. A graphical representation of the different epochs can be seen in Fig. 1.1. Edwin Hubble's discovery that galaxies were receding from us at velocities proportional to their distance (Hubble, 1929) provided cosmologists with the first hint that the deep in the past, a cataclysmic event had caused a Universal expansion - the Big Bang theory. The predictions for light element abundances (Alpher et al., 1948) and the intensity of the cosmic microwave background (CMB) radiation (Wilson & Penzias, 1965) left over from the Big Bang have been stunningly matched with observational evidence (e.g. Stompor et al., 2001; Page et al., 2007; Spergel et al., 2007; Komatsu et al., 2011; Ade et al., 2013a). The physics of the singularity remains the domain of theorists, however one is hard pressed to find modern papers which do not simply assume the Big Bang model as fact.

Despite the success of the Big Bang theory in explaining a lot of the observational evidence, there are three attributes of the Universe which the Big Bang theory fails to explain. Firstly, without calling upon the anthropic principle, the seemingly flat Universe in which we live requires a very specific set of initial conditions. Secondly, regions in the Universe which are not in causal contact yield the same values for physical properties such as temperature. Thirdly, Big Bang theory predicts the creation of a large number of magnetic monopoles which, despite being stable enough that we should still observe them today, have remained elusive. The solution to all of these problems lies in the theory of inflation (Guth, 1981). Inflation is the rapid expansion of the Universe in the first fraction of a second after the Big Bang, such that the scale factor grows by a factor of 10^{30} or more. Consideration of the densities in the Universe show that no matter what initial conditions are chosen, the critical density is always driven to unity during expansion resulting in a flat Universe. The huge increase in the scale factor results in a region which was in causal contact before inflation being blown up to a size larger than the observable Universe resulting in the isotropy and homogeneity we observe today. Lastly, no matter how great the number of magnetic monopoles produced in the early Universe, the exponential expansion ensures that the observed density now would be small enough such that it would be highly unusual if we were to observe one. There are many ongoing theoretical arguments over the form of the scalar field which could cause this expansion or indeed talk of more exotic theories (e.g. Linde, 2008) however inflation provides a cosmologically sound extension to Big Bang theory accepted by the majority of cosmologists.

One of the first eras after inflation which we can describe confidently is the Quark Era. Just 10^{-35} s after the Big Bang, there was constant particle pair production in a background of highly

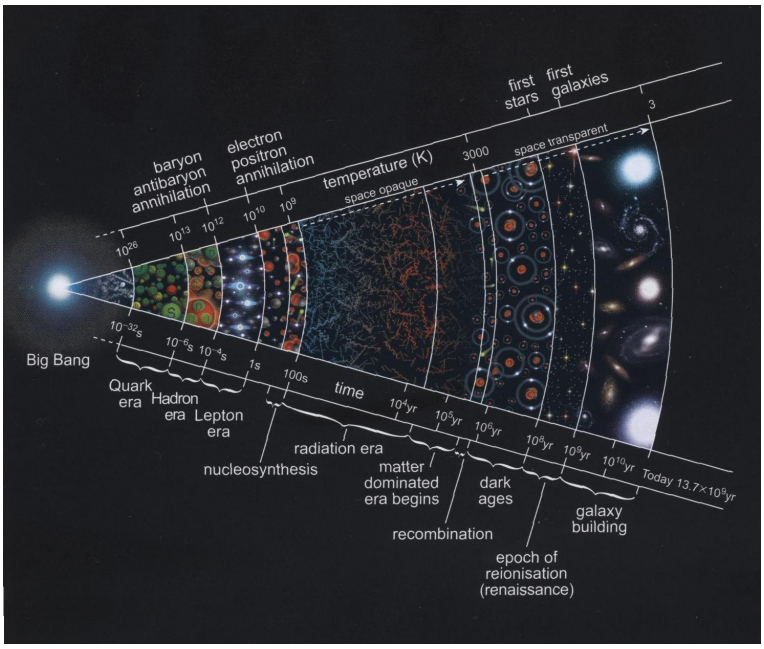

Figure 1.1: A graphical representation of the evolution of the Universe. Taken from Nicolson (2007).

energetic radiation. These particle-antiparticle pairs regularly annihilated, resulting in energetic photons. This reversible process maintained matter-radiation temperature equilibrium as the expansion of the Universe rapidly cooled the Universe from roughly 10^{27} K at the beginning of the quark era.

At 10^{-6} s, the Universe had cooled to a level at which baryon and quark pair production could no longer occur. This 'hadron era' saw trios of quarks binding to form the first stable protons, neutrons and their antiparticle equivalents. The particle and antiparticle pairs quickly annihilated (at 10^{-4} s) but, for unknown reasons, there was a small excess of particles over antiparticles (Sakharov, 1967). For every billion baryon antiparticles, it is thought there were one billion and one particles. This small excess remained, providing the building blocks of everything we see today.

1 s after the Big Bang, the temperature of 10^{10} K was cool enough to allow the electrons to follow the baryons in annihilating with their antiparticles, again leaving a small excess. During this time collisions meant that protons were converting into neutrons and vice versa regularly. However, since the energy required to create a neutron is slightly higher, the neutron to proton reaction was favoured resulting in roughly 7 protons to every neutron (e.g. see Pg. 292 of Peacock (1999)).

The photons were still of high enough energy to split apart any higher atomic nuclei which might form but once the temperature dropped to 10^{9} K nucleosynthesis could occur, as protons

and neutrons came together to form deuterium, He-4, He-3 and lithium. The neutrons were swept up into atomic nuclei in this way, resulting in a Universe with a total baryonic mass consisting of roughly 75% hydrogen and 25% helium (e.g. Burles & Tytler, 1998; Burles et al., 2001).

After nucleosynthesis was complete 100 s after the Big Bang, the Universe continued to steadily expand and cool. The mixture of atomic nuclei, electrons and other particles was still highly energetic and a photon could not travel far before a collision. In this way, atomic nuclei were instantly ionized upon formation and the Universe was opaque to electromagnetic radiation and, up until recently, it was thought that the galaxies simply formed from accretion of this cooled matter over time. In the 1970s, however, the discovery of flat galactic rotation curves indicated there was more than meets the eye to the matter in our Universe.

Spiral galaxies were known to rotate as far back as 1914, when the first inclined absorption lines in a galaxy spectrum were detected in M31 and the Sombrero galaxy (Slipher, 1914; Wolf, 1914). For several decades observations covered only the most inner parts of the galaxies and the first hint of missing matter came from studies of the spectra of M31 and NGC3115 which did not seem to bear any relation to the visible matter distributions (Babcock, 1939; Oort, 1940). Previously, Zwicky (1933) had noted that the large relative motions of cluster galaxies would result in the dissolution of the cluster unless each galaxy was one hundred times more massive than their luminosities suggested. This was the first direct reference to dark matter, however was doomed to lay in obscurity in relation to rotation curve work for decades.

By the 1950s technical advances meant that many rotation curves managed to reach the turnover point of the velocity, but not much further. A very slowly falling rotation curve for M31 (van de Hulst et al., 1957) and a flat rotation curve for M33 (Volders, 1959) were revealed at the end of the decade, but with no connection to dark matter both results were quietly put down to a variable mass-to-light ratio or dust absorption. Such explanations continued until Freeman (1970) remarked that if the velocity maps of M33 and NGC300 were to be trusted, there must be 'additional matter that is not detected'. The floodgates opened, with the publication of an M31 rotation curve that was flat over the last 30% of the optical disk (Rubin & Ford, 1970) and Einasto et al. (1974) and Ostriker et al. (1974) commenting that the flat rotation curves evidenced a serious mass underestimation of galaxies. Roberts & Whitehurst (1975) declared the rotation curve for M31 mathematically flat and when Bosma (1978) released 25 rotation curves with all but a few exhibiting flat rotation curves, it was clear that they were no longer the exception, but the rule, Fig. 1.2. The comprehensive review of the field by Faber & Gallagher (1979) cemented acceptance in the majority and was the first time a reference to Zwicky's dark

matter in reference to flat rotation curves appeared in print.

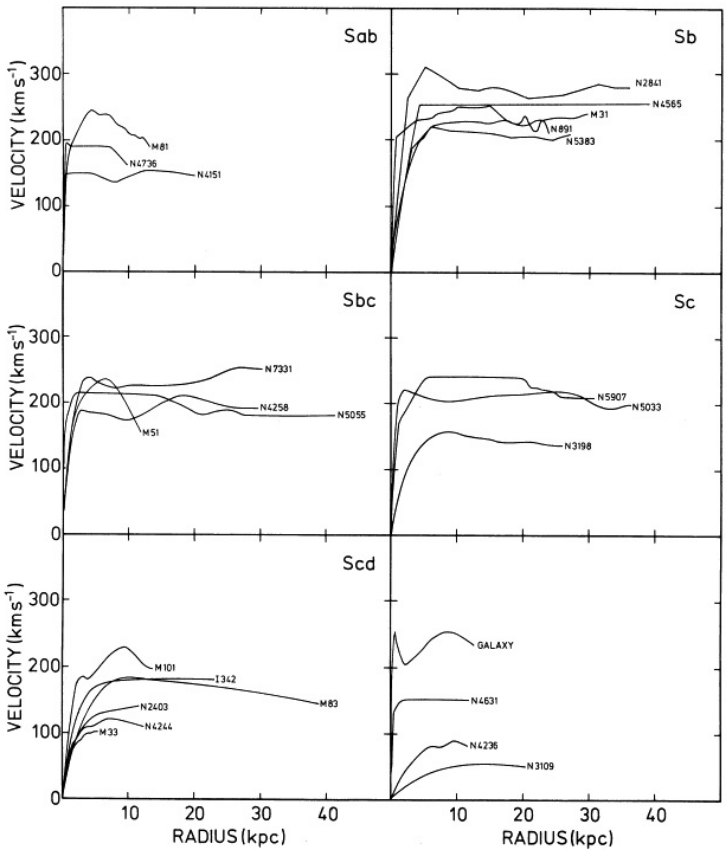

Figure 1.2: Rotation curves of 25 galaxies taken from Bosma (1978). This plot was fundamental in the realisation that flat rotation curves were the rule, not the exception.

Though it had been accepted by many that dark matter existed, it was still to be established how much of it existed and what it was. Big Bang Nucleosynthesis (BBN) arguments suggested that the density parameter for baryons, Ω_b, was over an order smaller than the unity that a flat Universe would require. Also, investigation into galaxy formation in a flat Universe composed entirely of baryons gave CMB anisotropies above the constraints at the time (Wilson & Silk, 1981; Uson & Wilkinson, 1984). It was assumed that the dark matter particles dominated the Universe (and, to fit with the BBN data, were necessarily non-baryonic) and the cosmological matter density parameter, Ω_m, was split into baryonic and dark matter constituents, $\Omega_m = \Omega_{dm} + \Omega_b$.

Over the ensuing decades, public opinion has favoured a cold dark matter (CDM) model, first suggested by Peebles (1982). The basic CDM model assumes a flat Universe dominated by weakly interacting massive particles (WIMPs). It must be weakly interacting so as to survive in the large densities we surmise and cold because the weakly interacting particles dominating the universe were non-relativistic even at early epochs. Other forms of dark matter have been mooted, for example hot dark matter which is relativistic right up until recombination, wiping out a lot of

density perturbations. Extensive N-Body and analytic experiments (White et al., 1984, 1983) have shown that in a Universe of hot dark matter, it is not possible to match the small-scale galaxy clustering structure we observe without an unrealistically late epoch of galaxy formation. In contrast, CDM models have shown much more success in replicating galactic structure (e.g. Blumenthal et al., 1984), since the particles are too slow to travel all but a negligible distance out of a perturbation, keeping galactic scale density perturbations intact. Candidates for the dark matter particle include axions and most promisingly the neutralino. The latter is the lightest particle in the supersymmetry (SUSY) framework connecting fermions and bosons, whereby each boson has a corresponding fermion and vice versa. By definition of being the lightest particle, it cannot break down into any other particle which makes it an ideal candidate for the weakly interacting dark matter. Though there is more than enough indirect evidence for the existence of dark matter through the galactic rotation curves and galaxy cluster arguments, evidence for what the dark matter actually is remains a lot more elusive. Indirect methods include looking for the gamma rays and neutrinos supposedly produced as a result of WIMP annihilation in the galactic halo while more direct methods hope to record the actual passage of a WIMP through a cryogenic detector (for a review of methods see Bertone et al. (2005)).

The CDM model of the 1980s was one of a flat Universe dominated by dark matter, with a zero cosmological constant, i.e. $\Omega = \Omega_m = 1$ where Ω is the total density parameter of the Universe. Peebles (1984) suggested that actually a non-zero cosmological constant, Λ, was compatible with inflation and could result in a flat Universe. Early indications that $\Omega_m << 1$ came from the galaxy clustering power spectrum when it was noticed that there was more structure in the Universe at large scales than CDM models predicted (Efstathiou et al., 1990). This discrepancy could be solved if a new component, Λ, contributed up to 80% of Ω, defining a best fit matter model of $\Omega_m = 0.2$ where $\Omega = \Omega_m + \Omega_\Lambda = 1$. This was uncomfortable reading, but fit with the later evidence of an accelerating Universe from supernovae published by (Riess et al., 1998; Perlmutter et al., 1999). Measurements of the flux from Type Ia supernovae were fainter than the characteristic light curves implied, suggesting an accelerating Universe, Fig. 1.3. It was stated that for a low mass density Universe, the probability of a non-zero and positive cosmological constant was above 99% (Perlmutter et al., 1999). The cosmological constant is the limiting case of a more general 'dark energy'. The more general theory considers that Λ may be time dependent - quintessence (Wetterich, 1988; Ratra & Peebles, 1988; Peebles & Ratra, 1988) where just as with inflation, a rolling scalar field produces the energy for the acceleration of the Universe.

The significance of the supernovae data is still debated, with the idea that gravity could

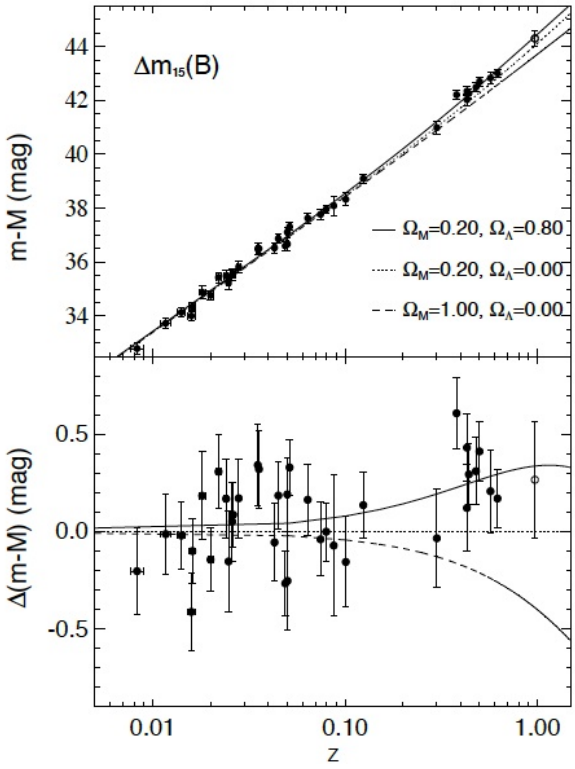

Figure 1.3: The Hubble diagram for the Riess et al. (1998) supernovae data. Together with Perlmutter et al. (1999), this plot revolutionised the way we think about the expansion of the Universe.

act differently on different scales (modified gravity theories (e.g. Nojiri & Odintsov, 2007)) still holding fort against a blind acceptance of dark energy as a form of Einstein's cosmological constant.

The investigation of the CMB radiation in the 1990s tied all the ΛCDM theories together and helped constrain cosmological parameters to new levels of accuracy. The CMB is the redshifted remnants of the radiation from the Big Bang and contains a wealth of information about the early Universe and the cosmological parameters. Before recombination, the photon and baryon fluids were free to interact, and gravitational potential fluctuations were closely matched by temperature fluctuations. When the fluids stopped interacting at recombination, these temperature anisotropies were frozen into the CMB - giving us the opportunity to probe the epoch before recombination.

The CMB was first detected by Penzias & Wilson (1965) and the first comprehensive maps of the CMB and its anisotropies were produced by the COBE experiment (Mather & et al.,, 1990). The CMB maps showed a characteristic temperature anisotropy (e.g. Smoot & et al.,, 1992; Bennett & et al.,, 1992; Kogut & et al.,, 1992; Wright & et al.,, 1992) in agreement with the predictions of inflation.

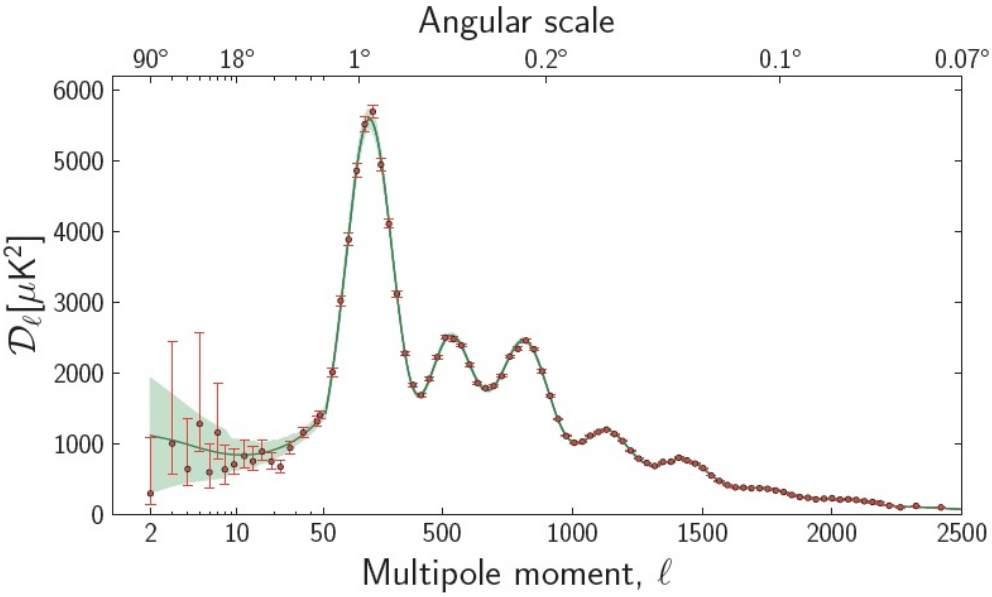

Figure 1.4: The temperature angular power spectrum of the CMB as observed by Planck (Ade et al., 2013a) (points) and the ΛCDM model (solid line). The green shading represents cosmic variance.

Launched in 2001, the Wilkinson Microwave Anisotropy Probe (WMAP) endeavoured to investigate the anisotropies on much finer scales. One of the most obvious features of a CMB power spectrum are the acoustic peaks (e.g. Miller & et al.,, 1999; Knox & Page, 2000; Mauskopf & et al.,, 2000). These peaks are as a result of oscillations in the photon-baryon fluid before recombination and dependent on the cosmological parameters at the time. For example, in simulations, the amplitude of the first acoustic peak varies with the matter density parameter. The astounding agreement of the temperature power spectrum measured by WMAP to the predictions of the ΛCDM model are heralded as one of the most exciting cosmological results of all time.

By 2000, massive galaxy surveys had provided further evidence, independent of the supernovae measurements, for the domination of a dark energy component. The Two-Degree-Field Galaxy Redshift Survey (2dFGRS) and Sloan Digital Sky Survey (SDSS) provided comprehensive galaxy clustering power spectra for which galaxy models could be easily compared (Percival et al., 2001; Tegmark et al., 2006). It was found that the best fit model was a Universe dominated by dark energy and a matter component dominated by dark matter.

We have now entered a new era of cosmology with the launch of the Planck space mission in May 2009 to measure the CMB power spectrum to a new realm of accuracy, Fig. 1.4 (Ade et al., 2013a). A few of the cosmological parameters constrained by Planck are summarised in Table 1.1 (Ade et al., 2013b).

	Planck	Planck + Lensing	Planck + WP
$\Omega_b h^2$	0.0207 ± 0.00033	0.02217 ± 0.00033	0.02205 ± 0.00028
$\Omega_{dm} h^2$	0.1196 ± 0.0031	0.1186 ± 0.0031	0.1199 ± 0.0027
τ	0.097 ± 0.038	0.089 ± 0.032	$0.089^{+0.012}_{-0.014}$
$\Omega_m h^2$	0.314 ± 0.020	0.307 ± 0.019	$0.315^{+0.016}_{-0.018}$
$\Omega_\Lambda h^2$	0.686 ± 0.020	0.693 ± 0.019	$0.685^{+0.018}_{-0.016}$
z_{re}	$11.4^{+4.0}_{-2.0}$	$10.8^{+3.1}_{-2.5}$	11.1 ± 1.1
H_0	67.4 ± 1.4	67.9 ± 1.5	67.3 ± 1.2

Table 1.1: A few of the cosmological parameters constrained by Planck, Planck + Planck lensing and Planck + WMAP polarization data. From top to bottom these are the baryonic and dark matter density parameters, optical depth, matter and dark energy density parameters, reionization redshift (for sudden reionization) and the Hubble parameter.

1.2 Epoch of Reionization

At about 380,000 years old, the Universe had finally cooled to a level where photons were unable to instantly ionize atoms. The electrons were quickly taken in by all the atomic nuclei to form the first stable atoms and provide the photons with a clearer path, allowing the Universe to become transparent. This era of recombination left a sea of photons of visible and infrared wavelengths able to traverse the length of the Universe. As the Universe continued its expansion this wavelength was stretched into the microwave and left what we see now as the CMB, with a temperature of 2.725 K. Immediately after recombination the Universe would have looked like a glowing red mass but, as this radiation cooled out of visible wavelengths, this would have faded until it entered what we have termed the Dark Ages. For hundreds of millions of years the Universe would remain exactly that, dark and steadily expanding and cooling. But, though not visible, the seeds of the first sources had been sown. At recombination there would have been regions of higher mass density which over time could gravitationally attract more and more mass until, over hundreds of millions of years, a structure was formed through gravitational collapse. These first structures emitted high energy UV photons which quickly ionized the surrounding regions and began the Epoch of Reionization.

The Epoch of Reionization (EoR) is the era of the Universe where the intergalactic medium (IGM) made a phase transition from being completely neutral to being almost entirely ionized. It occurred roughly 400 million years after the Big Bang, bringing an end to the Dark Ages which had set in after recombination. The EoR has been the domain of theoretical astrophysicists up until the present day, but with the first data expected imminently from the new generation of radio telescopes, the EoR is for the first time becoming accessible to observations.

1.2.1 Reionization Models

In recent years, considerable effort has been placed in testing models of reionization which are compatible with the few constraints so far deduced from observation. This includes investigation of the different possible sources of reionizing photons, how the patches of ionized universe evolve and overlap, and how the IGM is heated according to density.

The physics of reionization is very complex, with simulations requiring the modelling of radiative equations, making detailed analytic models difficult. Similarly, the computational power required for numerical simulations to model all the elements involved in detail is far out of our reach (Choudhury & Ferrara, 2006). As a result, most models tend to focus on no more than a few elements affecting reionization at a time.

The effect of reionization on an inhomogeneous IGM is fairly undefined. Furlanetto et al. (2006) cites examples of analytic models which have concluded that, since recombination rates are higher in high density regions, it is these regions which are ionized last. Conversely, also cited are models which conclude inside out reionization is more likely - with high density regions ionized first as most ionizing sources reside in high density haloes.

The IGM can be ionized by any number of processes, including even dark matter annihilation (this process is thought to be insignificant in reionizing the Universe as a whole (Mapelli et al., 2006)). The sources thought most likely to be responsible for reionization are stars and mini-quasars. How much each of these contributes and when is key to the individual model histories.

Stellar Sources

The stars which populate our Universe in the present day are either Population I or Population II (Baade, 1944). Population II stars have low metallicity and reside mainly in the bulge and halo of a galaxy. Once there have been several generations of Population II supernovae in a region, the newly forming stars have high enough metallicity to be categorised as Population I - young, high metallicity stars found mainly in the disk of a galaxy. While Population I stars are too young to have contributed to reionization, it is possible that Population II could have helped along reionization. However, the constraints set out in Section 1.2.2 suggest that if reionization was indeed due to stellar sources, these sources would need to provide a least an order of magnitude more ionizing photons per baryon than the Population II stars we observe today (Wyithe & Loeb, 2003; Schaerer, 2002; Bromm et al., 2001; Sokasian et al., 2003). In order to reconcile this, it has been mooted that the first metal-free stars, so-called Population III stars, were responsible for the bulk of any stellar reionization.

Population III stars are thought to form inside dark matter mini-haloes of mass $\approx 10^6 M_\odot$

which should have been in existence since around $z \approx 20 - 40$. The inability of the gas to cool through heavy metal cooling leads to very high stellar masses (on the order of 100 $M_{\odot}$) when the gas does fragment through H_2 cooling (Abel et al., 2000, 2002; Bromm & Larson, 2004; Glover, 2005). As the UV radiation from one of these first stars can easily ionize the surrounding H_2, it was generally thought to be unlikely that more than one PopIII star would form in any one mini-halo (Omukai & Nishi, 1999; Kitayama et al., 2004) since this route of cooling would quickly be impossible, though consideration was put to the idea that binary systems could possibly form in a small fraction of mini-haloes (Turk et al., 2009). There are recent simulations however, which suggest that not only might PopIII stars be a small as 10s of solar masses, but that they may form as binaries quite regularly, if not in groups of up to a dozen in any one halo (Stacy et al., 2010; Clark et al., 2011; Smith et al., 2011; Greif et al., 2011, 2012; Stacy & Bromm, 2013), though such large groups have been not reproduced when dark matter annihilation is taken into account (Smith et al., 2012).

At the end of their lives (thought to be on the order of 3 Myr), PopIII stars within the mass ranges $25M_{\odot} \leq M_{*} \leq 140M_{\odot}$ or $M_{\odot} \geq 260M_{\odot}$ collapse into black holes without a great deal metal enrichment of the surrounding environment as a result. Stars with masses $140M_{\odot} < M_{*} < 260M_{\odot}$ have a rather more violent ending as pair instability supernovae, PISNe, enriching the surrounding environment with heavy elements. These supernovae explosions are much more energetic than Type Ia supernovae and leave no compact remnant. Once the shocked environment has suitably cooled, Population II stars can form. PISNe are about 100,000 brighter than their host galaxies and so, despite the large amount of photon scattering due to intermediate neutral hydrogen, we can hopefully expect to see several in the future James Webb Space Telescope survey (Hummel et al., 2012).

As the UV photons from stars belonging to either Population II or III ionize the surrounding IGM, compact bubbles of high temperature ionized hydrogen form around the sources as a result of the photons not being energetic enough to ionize atoms at large distances (Thomas & Zaroubi, 2011). It is thought that these bubbles grow and eventually overlap until the Universe is mainly ionized. The UV radiation emitted by stars sets the spin temperature through Lyman-α pumping (see Section 1.2.3), but also heats the IGM through atomic recoil (Furlanetto et al., 2006). As the IGM becomes gradually more enriched with metals through supernovae, the Population III star population will have declined as the Population II population increased.

Quasars

Constraints from observation, in particular the Thomson optical depth (see Section 1.2.2), has led to theories of non-stellar sources for reionization. Currently favoured are mini-quasars - AGN powered by accretion onto intermediate mass black holes. While there has been evidence of a quasar population decline after $z \approx 2$ (Nusser & Silk, 1993), observations of high redshift quasars ($z \approx 6$) has suggested that the super massive black hole (SMBH) seeds must have been in place before $z \approx 10$ and have masses of above 1000 $M_{\odot}$ (Fan et al., 2006). In order to satisfy observational constraints, Madau et al. (2004) has suggested two periods of quasar activity. The first consists of a mini-quasar population. They are thought to result from either the death of PopIII star resulting in a black hole mass, M_{BH}, of $30 - 1000 M_{\odot}$ or the collapse of rare, very low angular momentum halos with virial temperature $> 10^4 K$ (Shapiro, 2004; Zaroubi et al., 2007). After the reionization epoch, these mini-quasars could largely photo-disassociate due to the large UV background unbinding the gas from shallow mini haloes before a second quasar era began at $z \leq 10$, as accretion onto black holes began again. It is these AGN that keep the Universe ionized at $z \leq 4$.

The mean free path of an X-ray photon emitted by a mini-quasar is larger than the typical separation of sources in some simulations (Madau et al., 2004). Thus, since one of these photons is not associated with any particular source when it ionizes a H atom, the pattern of reionization is much more diffuse and homogeneous than for stellar sources. The bubbles around sources are of higher temperature than stellar sources (Thomas & Zaroubi, 2011) and of radius of several comoving Mpc. Recombination timescales for neutral hydrogen are smaller by an order of magnitude than ionization timescales, allowing ionized bubbles to remain ionized for some time after the source, whether stellar or AGN, has died. Thomas & Zaroubi (2008) found that bubbles surrounding mini-quasars remained ionized for longer periods of time than stellar bubbles.

The difference in evolution of reionization and the IGM temperature depending on the sources provides a possible way of distinguishing between models. The X-rays emitted by mini-quasars heat the IGM out to greater distances from the ionization front (Thomas & Zaroubi, 2008). For quasars, the hydrogen ionization front is thought to propagate much faster than for reionization powered just by stars and possess a sudden step increase in the neutral hydrogen fraction (Zaroubi & Silk, 2005). Figure 1.5, taken from Thomas & Zaroubi (2011), demonstrates the results of three simulations with different source types: stars, mini-quasars and a mixture of both. The more diffuse and faster reionization due to quasars is clearly evident, whereas a more 'swiss cheese' model is apparent for stellar sources alone. If the next generation of telescopes such as the SKA achieve the spatial resolution required for meaningful tomography, we may be

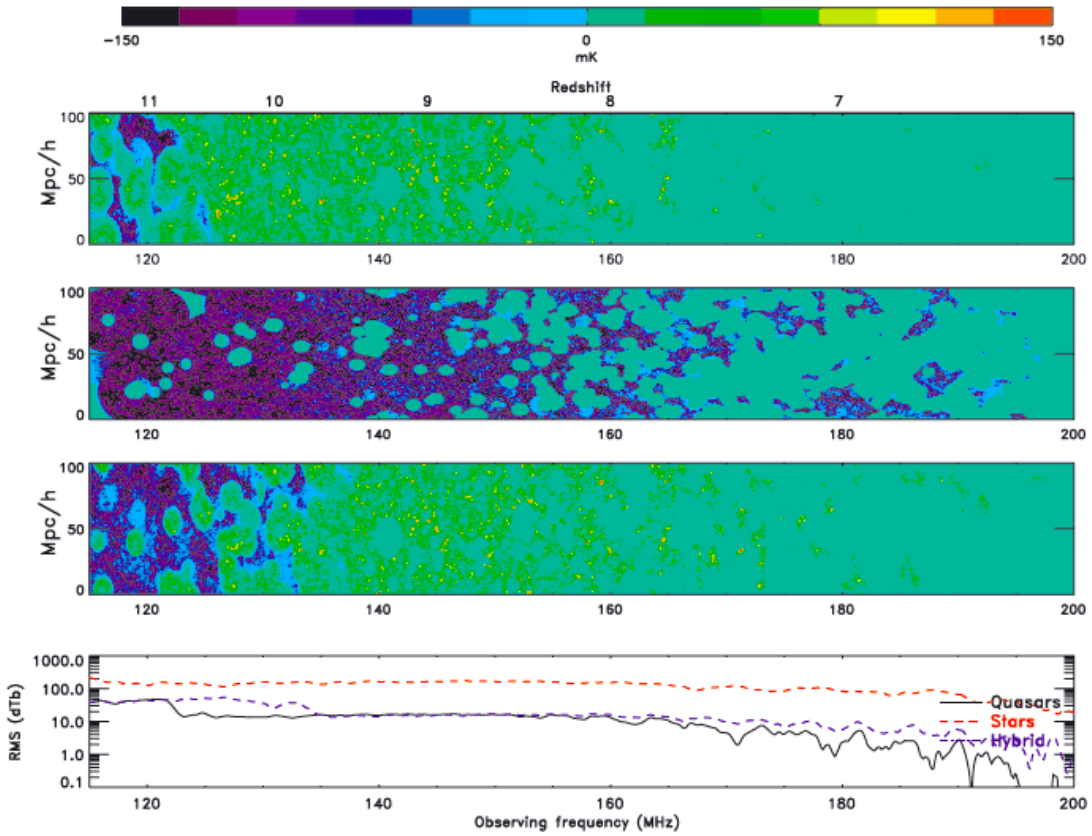

Figure 1.5: N-Body reionization histories for mini-quasar sources, stellar sources and a mixture of both (top to bottom). The very bottom panel plots the rms of δT_b for the three scenarios. This figure is taken from Thomas & Zaroubi (2011).

able to clearly determine the sources involved.

Other sources

At the end of the first stars' life, there was a production of ionizing photons in the resulting supernovae shocks. Despite the rate of production being significantly smaller in the shocks as opposed to the original stellar processes, the photons emitted have a harder spectra and as such there is a greater escape fraction of ionizing photons. Supernovae as source of reionization could have enhanced the fraction of hydrogen ionized by stellar sources by up to 10% (Johnson & Khochfar, 2011).

Theoretical Modelling

Shapiro & Giroux (1987) (and, later, Fan et al. (2003)) showed that the number density of quasars implied by observations at high redshift was not high enough to be solely responsible for the ionization of the neutral hydrogen at high redshift, and that stellar sources are likely

to have dominated at $z > 6$. However, research has also implied that star forming galaxies are also of insufficient number density to completely reionize the Universe, unless some extreme assumptions are made about their escape fractions, metallicity, or number density below the detection limit (Bunker et al., 2010).

The apparent inability of any one source to completely reionize the Universe (e.g. Wyithe & Loeb (2003); Ricotti & Ostriker (2004a); Zaroubi et al. (2007)) suggests that reionization was a multi-step process, incorporating the different possible sources in a source evolution model. For example, Cen (2003) suggests the early stages of reionization were carried out by Population III stars before a partial recombination as Pop III formation came to a halt. The Universe would then have been fully reionized by Pop II stars. Zaroubi & Silk (2005) suggests that ionization may have begun due to Pop III stars before, upon their death, their conversion into a population of mini-quasars maintained the IGM at a partial state of ionization due to the high energy X-ray emission. Complete reionization at later times is then due to lower energy photons from the same mini-quasars. Similar models by Ricotti & Ostriker (2004a,b); Madau et al. (2004) has the mini-quasars quickly creating an X-ray background preventing mass recombination before stellar sources, i.e. Pop II complete reionization at $z \approx 7$.

Traditionally the role of mini-haloes in reionization has been assessed to be very small (Haiman et al., 2000) due to the strong suppression of star formation in mini-haloes in ionized regions. Instead, it was thought that the majority of stellar-led reionization was caused by atomic cooling haloes, or ACHs. These higher mass halos (M $\geq 10^8 M_\odot$) can cool by atomic hydrogen line cooling and, if massive enough, can maintain star formation even in ionized regions. However, a recent radiative transfer simulation by Ahn et al. (2012) found that the reionization histories of ACHs alone compared to ACHs+mini-haloes were markedly different at high redshifts ($z \geq 8$). They found the first stars, which began forming in mini-haloes at a redshift of roughly 40, dominated reionization right up until a redshift of 10 when the star formation was suppressed by the increasingly ionized environment. In comparison, ACHs were rare up until redshift 10, resulting in a boost in the Thomson scattering τ of as much as 40% when mini-haloes are considered. The ACHS themselves can be split into lower mass galaxies ($10^8 M_\odot \leq$ M $\leq 10^9 M_\odot$), LMACHs, and higher mass galaxies (M $\geq 10^9 M_\odot$), HMACHs, with a reionization scenario dominated by LMACHs+HMACHs being distinguishable from reionization dominated by HMACHS alone via statistical measures such as the power spectrum (Iliev et al., 2012).

There are three categories of computer model for reionization. Numerical simulations use N-body dark matter simulations combined with prescriptions for galaxy formation and radiative transfer to create high resolution, but small volume, realizations which can explore a small section

of parameter space. For example Mellema et al. (2006) simulated a $(100h^{-1}\text{Mpc})^3$ volume and looked at the different reionization histories produced by simulations with different values of gas clumping on small scales and ionizing source photon production efficiencies, while Baek, S. et al. (2010) looked at the effect on the same volume of different IMFs, chemistry, the fraction of total luminosity due to X-rays and the X-ray spectral index. However, the parameter space needed to analyse reionization experiments is very large, due to the lack of understanding of the Universe at high redshift, and numerical methods cannot hope to explore more than a small fraction of the parameter space. Just as troublesome is the large dynamic range needed to model both the large scale ionization regions and the small scale reionization sources.

In direct contrast, analytic models can explore a larger parameter space and draw conclusions on the dependence of statistical functions such as the power spectrum in computationally cheap way. Furlanetto et al. (2004) developed an analytical model for the growth of ionized regions and considered how the power spectrum constructed from this model evolves with redshift for different ionization histories. Pritchard & Loeb (2008) analytically calculated the 3D power spectrum as a function of redshift for different astrophysical parameters such as luminosity and spectra for ionizing sources, Lyman-series photons and X-rays, and analyzed the different mean reionization and fluctuation histories.

Semi-numerical models such as the two used in this thesis (21CMFAST (Mesinger et al., 2011) and SIMFAST (Santos et al., 2010)) bridge the gap, providing large volume realizations with fairly good resolution. Until computing power comes at a smaller cost, there is no one category which provides the answer to all the questions we have regarding the evolution of reionization and they can be used in tandem - with semi-analytic results being checked against numerical models and analyzed with reference to analytic models.

1.2.2 Observational Constraints

Despite no direct observations of the EoR, there are currently three main constraints on the EoR from indirect observations. These constraints can be seen in Fig. 1.12.

CMB Data

Reionization has an effect on the photons from the surface of last scattering, one which we can use to constrain reionization itself. Though models have shown that different reionization histories produce different effects on the CMB, Fig. 1.6, the parameter degeneracies and limiting sensitivity of the instruments used to detect it mean only integral constraints (i.e. parameters which tells us about reionization as a whole) have so far been formulated.

Along a line of sight, observed CMB photons have been scattered by intervening free electrons produced by the EoR, setting the Thomson optical length (τ). Measuring τ indicates how much scattering has occurred and, by extension, how long the Universe has been reionized. A larger τ indicates more electron scattering occurring since recombination and thus a more extended reionization epoch. The optical depth is degenerate with the primordial matter power spectrum, A_s, such that it is τA_s which is directly measured by most CMB experiments and for precise estimates this degeneracy must be broken. CMB temperature anisotropies and the angular polarization power spectrum are both suppressed on small scales by $e^{-2\tau}$ but while the former remain largely unaffected by different reionization models on large scales, the polarization power spectrum also has a large peak in power at large scales mainly due to Thompson scattering (Furlanetto et al., 2006). This provides a way to break the degeneracy and is the method utilised by WMAP.

Early CMB anisotropy experiment MAXIMA-I [1] was able to set a limit of $\tau \leq 0.5$ through measurement of temperature anisotropies, implying a rather loose constraint on the redshift of reionization of $z_{reio} \leq 40$ (Stompor et al., 2001).

WMAP (e.g. Page et al. 2007; Spergel et al. 2007; Komatsu et al. 2011) measured both the polarization and temperature power spectra to provide more robust estimates, setting $\tau = 0.088 \pm 0.015$ or, for instantaneous reionization, $z_{reio} \approx 10.6 \pm 1.2$. As the Planck polarization observations are still undergoing post-processing, Planck uses the fact that lensing depends on the size of A_s and so the Planck lensing potential reconstruction provides a way to loosen the degeneracy. Planck constrains $\tau = 0.089 \pm 0.032$ and $z_{reio} \approx 10.8^{+3.1}_{-2.5}$ though this is expected to improve once the polarization power spectrum is considered.

Despite the increasingly tight constraints, τ is an integral constraint giving us little information on the source, duration or evolution of reionization.

The movement of the free electrons producing the photon scattering also imparts a signal onto the CMB which can give us information about the duration of reionization. The Doppler shift of scattered photons due to the movement of the free electrons and the resulting temperature anisotropy is called the kinetic Sunyaev-Zel'dovich (kSZ) effect (Sunyaev & Zel'dovich, 1980; Sunyaev & Zeldovich, 1970). On scales where the ionized bubbles are larger than velocity perturbations this effect cancels out on linear order as the Doppler shift imparted by the peaks of the perturbation is equal and opposite to the Doppler shift imparted by the troughs of that perturbation. Instead, a measurable temperature anisotropy is only created when the ionized region covers only part of the velocity perturbation. The scale at which this signal peaks will be

[1] http://cosmology.berkeley.edu/group/cmb/

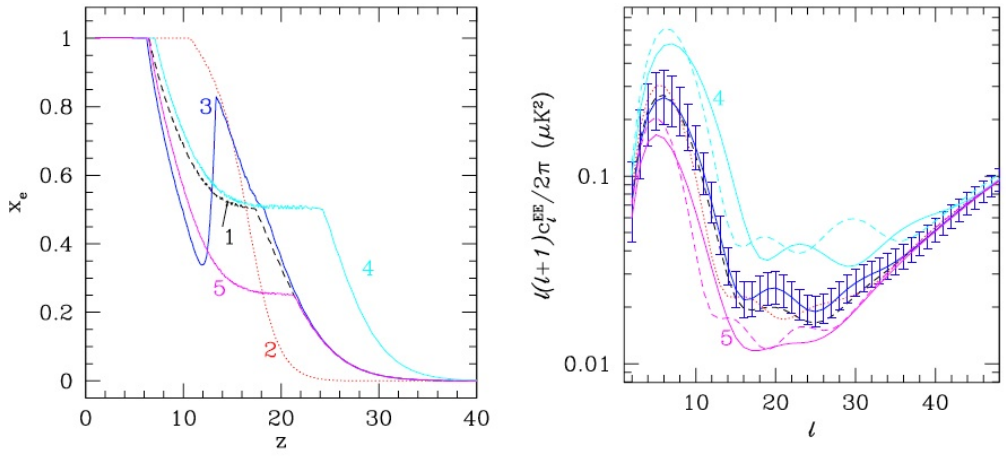

Figure 1.6: The effect of 5 different reionization histories (left panel) on the CMB polarization power spectrum (right panel), where all power spectra have been normalized to have the same power at l=50 and the error bars show cosmic variance. Taken from (Haiman & Holder, 2003).

characteristic of the bubble size at the redshift of observation. The longer the bubble remains smaller than the velocity perturbation, the greater the temperature anisotropy and so this kSZ effect becomes a measure of the duration of reionization.

The South Pole Telescope (SPT) has recently measured the kinetic Sunyaev-Zel'dovich effect, constraining the duration of reionization to $\Delta z \equiv z_{\bar{x}_e=0.20} - z_{\bar{x}_e=0.99} \leq 4.4$ with 95% confidence, or, allowing for correlations between the cosmic infrared background (CIB) and the thermal SZ power (tSZ), $\Delta z \leq 7.9$ (Zahn et al., 2012). The kSZ measurements can break the degeneracy between the duration and end of reionization experienced by WMAP, Fig. 1.7, constraining the end of reionization to $z > 5.8$ with the CIB-tSV correlations as part of the model or $z > 7.2$ when they are assumed to be zero.

Quasar Spectra

Quasars are extremely luminous and distant active galactic nuclei (AGN) whose spectra exhibit discrete absorption lines known as the Lyman-α forest (Lynds, 1971; Sargent et al., 1980), where the Ly-α line is the energy difference when an electron moves between the n=1 and n=2 quantum levels in a hydrogen atom. Quasars release high energy photons which are gradually redshifted as they travel towards us. At any one point between the observer and the quasar there will be clouds of neutral hydrogen, the extent of which will depend on the stage of Universal reionization. When a cloud is encountered, those quasar photons which have been redshifted precisely to the Ly-α transition energy in the frame of the cloud will be absorbed, resulting in a spectral absorption line. Photons emitted at higher energies will travel further before they are

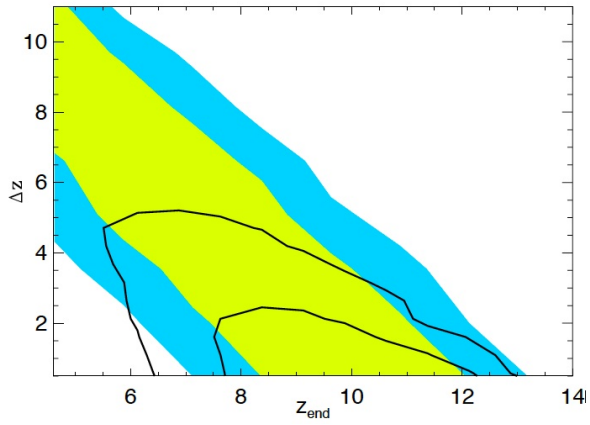

Figure 1.7: A contour plot showing the kSZ data breaking the WMAP degeneracy between the redshift of the end of reionization and the duration of reionization. The shaded contours are WMAP data while the lined contours are for WMAP + SPT data. The limits are 68% and 95%. Taken from (Zahn et al., 2012).

redshifted into Ly-α resonance, allowing us to map where a neutral cloud exists along the line of sight.

The most distant quasars will have emitted photons at a time when the Universe was largely neutral. All photons emitted blue-wards of the Ly-α energy will be absorbed creating so many absorption lines that a trough appears - the Gunn-Peterson trough. The length and completeness of this trough is a measure of how much neutral hydrogen is present at the redshift in which the quasar is observed. The fact that we see singular absorption lines at all in some quasar spectra allowed Gunn & Peterson (1965) to calculate that the Universe must be highly ionized by $z \approx 2$. The Gunn-Peterson (G-P) trough is not observed in quasars of $z < 6$, suggesting the Universe was highly ionized by $z \approx 6$ (Choudhury & Ferrara, 2006). The Sloan Digital Sky Survey[2] (SDSS) has now identified quite a few quasars at $z > 6$. These exhibit very long or complete absorption troughs compared to the incomplete troughs at redshifts below 6, implying a very rapid increase in x_{HI}, Fig. 1.8. This suggests that reionization is in the very last stages around $z \approx 6$ (e.g. Fan et al. (2006, 2003); White et al. (2003); McGreer et al. (2011)).

One can construct transmission profiles of quasars by dividing the observed spectrum by a composite spectrum composed of hundreds of catalogued quasars with their absorption lines masked. This transmission profile can then be compared to the Ly-α damping profiles for different neutral fractions. For example, Mesinger & Haiman (2007) compared model spectra with three $z > 6.2$ quasar spectra, claiming a lower limit of $x_{HI} > 0.033$ while the ULAS J1120+0641 quasar at $z = 7.085$ has a transmission profile consistent with $0.1 < x_{HI} < 1$, Fig. 1.9 (Mortlock et al., 2011).

[2]http://www.sdss.org/

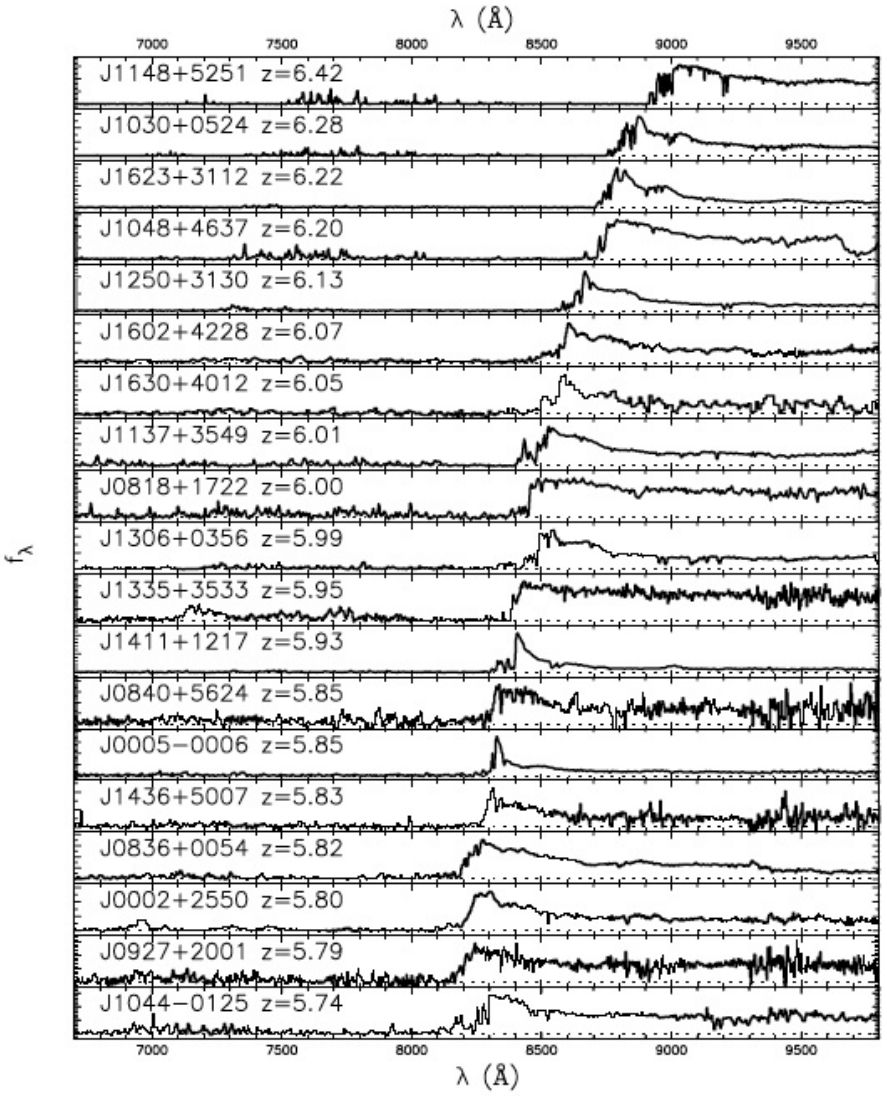

Figure 1.8: 19 SDSS quasar spectra demonstrating the change in depth and completeness of the Gunn-Peterson trough with increasing redshift. Taken from Fan et al. (2006).

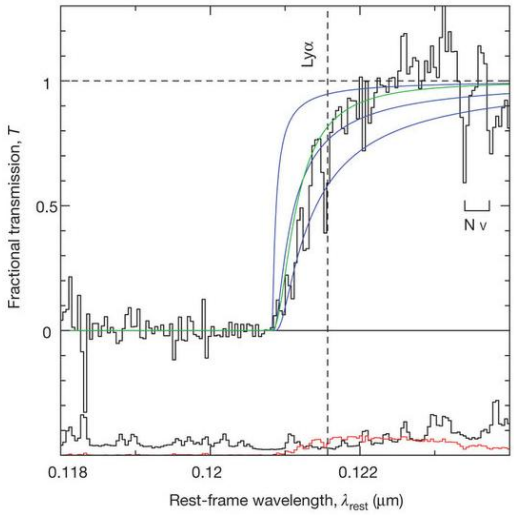

Figure 1.9: The transmission profile of ULAS J1120+0641 (black; upper) compared with Ly α profiles of an IGM with $x_{HI} = [0.1, 0.5, 1.0]$ (blue; from top to bottom). The transmission profile could also be as result of a rare high strength Ly α damped system (green). The random error spectrum (black; lower) and systematic uncertainty in transmission profile (red) are also plotted. Taken from (Mortlock et al., 2011).

The way in which the Gunn-Peterson trough ends is known as the Lyman-α damping profile and gamma ray bursts (GRB) have spectra from which these profiles can be extracted (Barkana & Loeb, 2004). Totani et al. (2006) used a gamma ray burst at z=6.3 to constrain $x_{HI} < 0.17$ and $x_{HI} < 0.60$ at 68% and 95% confidence limits respectively. It is however thought that Gamma ray burst constraints are somewhat compromised by damped Ly-α absorbers (Furlanetto et al., 2006).

Because the Lyman series saturates so quickly, quasar spectra are most useful for the investigation of the very end of reionization. The swift saturation means that the mean G-P optical depth measurements can only constrain the neutral fraction to roughly $x_{HI} > 10^{-3}$ (Furlanetto et al., 2006) and we must look to what else quasar spectra can tell us. The distribution of gaps in the Ly-α forest have the potential to be a useful statistic (e.g. Croft, 1998; Songaila & Cowie, 2002; Nusser et al., 2002). A 'dark gap' is defined as any part of the spectra with optical depth greater than 2.5 over regions greater than $1\mathring{A}$. Because of the large Ly-α damping profile, observations will show small ionized regions as optically thick (Miralda-Escud, 1998) and therefore if we do observe a transmission spike in the G-P trough this must indicate a large ionized region with a strong ionizing source. Together with a model for these ionizing sources, observations of transmission spikes/dark gaps can be used to put an upper limit on the neutral fraction (Fan et al., 2006). Gallerani et al. (2006) used semi-analytic simulations to measure simulated dark gap distributions along 300 lines of sight. By measuring the largest gap in each line-of-sight they showed that the distribution of these gaps was starkly different according to whether the

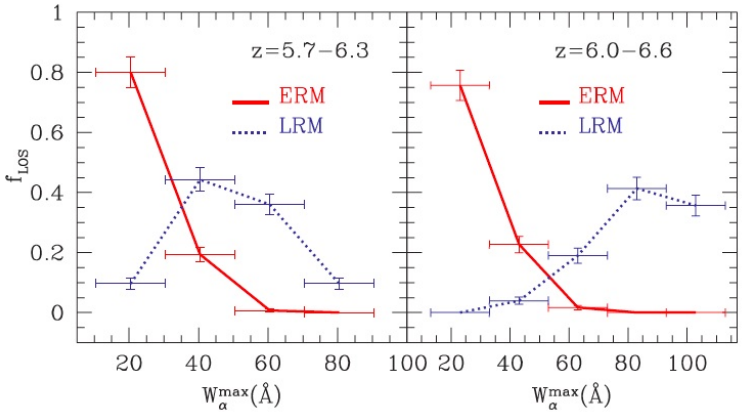

Figure 1.10: The fraction of LOS (f_{LOS}) of dark gaps with a maximum dark gap width (W_α^{max}) larger than a particular value. The distributions differ significantly according to whether the simulation was for early or late reionization. Taken from Gallerani et al. (2006).

simulation was early or late reionization (ERM/LRM), Fig. 1.10. Though the high redshift quasar sample is currently small, in the future we could possibly use them to constrain the type of reionization.

The size of the ionized region around a quasar is also an indication of the state of the IGM as a whole (e.g. Wyithe et al., 2005; Fan et al., 2006). The size of the ionized region (or "Strömgren sphere") is related to the neutral fraction at the time allowing us to theoretically constrain the neutral fraction, Fig. 1.11. However, the sample of high redshift quasars remains so small that they are likely to inhabit highly biased regions of our Universe and thus absolute measurements for the neutral fraction are fraught with uncertainty (Fan et al., 2006). However the rate of change in the ionized regions (also called proximity zones) can give us a much more model-independent measure of how the IGM is changing. For example a decrease in the region sizes by a factor of 2.4 indicated an increase by a factor of 14 in the neutral fraction for redshifts 5.7-6.4 (Fan et al., 2006).

Though quasar spectra have the potential to tell us much about reionization, the small numbers at redshifts relevant for reionization limit the constraints available. In time we will see this data set grow and the constraints improve considerably.

Temperature of the IGM

The temperature of the IGM, T_{IGM}, can be measured from the width of Ly-α absorption lines. Since thermal timescales are long, T_{IGM} at $4 < z < 6$ depends on the reionization history. Measurements of T_{IGM} at $z \approx 4$ and $z \approx 6$ (Schaye et al., 2000; Theuns et al., 2002; Bolton et al., 2010) have been extrapolated back leading to the conclusion that reionization must have

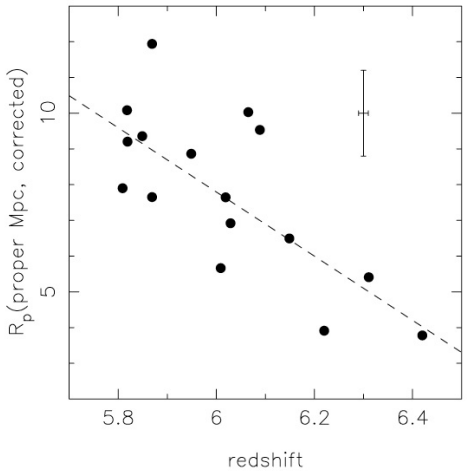

Figure 1.11: The size of the ionized region (R_p) around a quasar is related to the redshift of emission. Taken from (Fan et al., 2006).

occurred at $z_{reio} < 9$. This constraint is rather weaker than the previous two due to inherent assumptions about IGM heating and cooling rates.

The quasar and Thomson optical length constraints are both consistent with reionization occurring in one step at $z_{reio} \geq 15$ and the Universe remaining highly ionized afterwards. However Hui & Haiman (2003) notes that taking into account T_{IGM} constraints along with the large value of τ, this model of single step reionization is unworkable as T_{IGM} would be much lower than that measured from Ly-α forests. Instead they suggest a more complex reionization history where reionization could have started early, say at $z \approx 15$ but with the significant changes in the neutral hydrogen fraction, x_{HI}, occurring between $6 < z < 10$. This conclusion was however based on the first-year WMAP estimated of $\tau \approx 0.17$ (Kogut et al., 2003).

Other Constraints

Galaxy surveys have also been used to constrain x_{HI}. There are large observed populations of Ly-α emitting galaxies at $z \approx 5.7$ and $z \approx 6.5$ - close enough in cosmological timescale to not be subject to any intrinsic evolution (Furlanetto et al., 2006). As a result any evolution in Ly-α luminosity function can be associated with x_{HI} (with a certain level of assumption) with estimates varying (at $z \approx 6.5$) between $x_{HI} \leq 0.2$ for isolated galaxies to $x_{HI} \leq 0.5$ if clustering is included (Ouchi et al., 2010; Malhotra & Rhoads, 2004).

A summary of many of the constraints discussed in this section can be seen in Fig. 1.12.

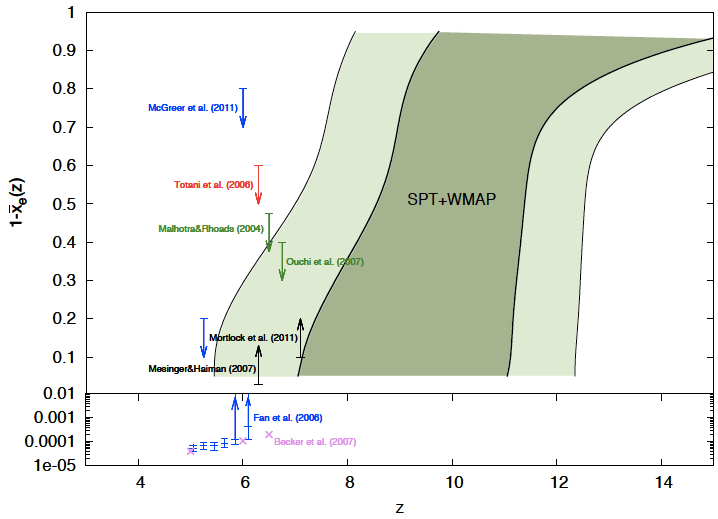

Figure 1.12: The constraints provided by SPT and CMB data, taken from Zahn et al. (2012). The thick/thin and dark/light shading represent the 68/95% confidence limits. The other constraints shown are based on quasar spectra (Fan et al., 2006; Rauch & Sargent, 2007; Mesinger & Haiman, 2007; Mortlock et al., 2011; McGreer et al., 2011) (blue,violet and black points), a gamma ray burst damping profile (Totani et al., 2006) (red) and Ly-α emitter (Malhotra & Rhoads, 2004; Ouchi et al., 2010) (green points).

1.2.3 The 21-cm Cosmological Signal

The 21-cm line is currently the most promising astrophysical probe of the Epoch of Reionization. The emission of a photon of wavelength 21-cm originates from the interactions between the proton and electron in a ground state hydrogen atom. The ground state of a neutral hydrogen atom has two hyperfine levels: an excited triplet state where the proton and electron spins are parallel, and a singlet state where the spin are anti-parallel. When a hydrogen atom undergoes a transition from the excited triplet state to the singlet state, a photon is emitted of wavelength 21-cm (frequency ν_{10}=1420 MHz).

The 21-cm spectral line is forbidden - the probability of a 21-cm transition is $2.9 \times 10^{-15} s^{-15}$ (Wild, 1952), equivalent to triplet state lifetime of 10^7 years. Even so, the vast amounts of hydrogen in the Universe lead to a rare event being observable through quantity (van de Hulst, 1945). The first observations of the 21-cm spectral line occurred in March and May of 1951 (Ewen & Purcell, 1951; Muller & Oort, 1951). The 21-cm line was observed in emission allowing astronomers to immediately conclude that the temperature of the 21-cm emission was higher than that of the CMB.

1.2.4 Spin Temperature

The intensity of 21-cm radiation is determined by the spin temperature, T_{spin} defined through (Field, 1958):

$$\frac{n_1}{n_0} = \frac{g_1}{g_0} \exp\left(\frac{-T_*}{T_{spin}}\right) = 3 \exp\left(\frac{-T_*}{T_{spin}}\right), \tag{1.1}$$

where g_i is the statistical weight of the atom energy state, where for the 21-cm event $g_0 = 1$ and $g_1 = 3$.

The spin temperature is a fundamental measure of the number densities of the triplet and singlet states (n_1, n_0) where $T_* = \frac{h\nu_{10}}{k_b} = 0.0681K$.

If the neutral hydrogen atoms were in the presence of the CMB background alone, thermal equilibrium would be reached on a time scale of $3 \times 10^5 (1+z)^{-1}$ yr and the 21-cm signal would be unobservable, either in emission or absorption (Ciardi & Madau, 2003). Since observations have been made, there must exist mechanisms to decouple the CMB temperature, T_{CMB}, and T_{spin}.

Field (1958, 1959) calculated T_{spin} as a weighted average of T_{CMB}, the gas kinetic temperature T_k and ambient Lyman-α temperature, T_α :

$$T_{spin} = \frac{T_{CMB} + \gamma_k T_k + \gamma_\alpha T_\alpha}{1 + \gamma_\alpha + \gamma_k}. \tag{1.2}$$

The two couplings, γ_α and γ_k have the form:

$$\gamma_{k,\alpha} = \frac{T_*}{T_{k,\alpha}} \frac{P_{10}^{k,\alpha}}{A_{10}}, \tag{1.3}$$

where A_{10} is the Einstein A coefficient (the probability of the spontaneous n=1 to n=0 emission) and $P_{10}^{k,\alpha}$ is the rate of transitions caused by collisions or Lyman-α photons. Each of these coupling terms will be discussed in turn. The couplings themselves will help to constrain the form of reionization sources. For example, stars tend to decouple T_{spin} through radiative Lyman-α pumping whereas mini-quasars decouple through collisional Lyman-α pumping (Chuzhoy et al., 2006; Zaroubi et al., 2007).

Decoupling via Lyman-α Photons

The Lyman-α background is the dominant decoupling mechanism in the diffuse IGM, allowing mixing of the hyperfine populations.

The Lyman series corresponds to electron transitions between energy levels of quantum num-

ber n $\geq$ 2 and n=1 resulting in the emission of a UV photon. Due to the sheer volume of hydrogen in the Universe, any photon redshifted into a Lyman series resonance will be absorbed promptly allowing the possibility of a later 21-cm radiation emission through de-excitation. Due to the increased number of scatterings a higher Lyman series photon (for example Lyman-β) undergoes, the probability of a direct coupling from a Lyman series photon above α is strongly suppressed (Furlanetto et al., 2006). It is therefore usual to only consider the overwhelming contribution of Lyman-α photons.

A Lyman-α photon has the characteristic wavelength (1216×10^{-10}m) corresponding to a transition between hydrogen atom energy levels of quantum numbers n=2 and n=1. The Wouthuysen-Field effect (Wouthuysen, 1952; Field, 1958) is the dominant decoupling mechanism between the CMB and spin temperature and mixes the populations in the hyperfine states, Fig. 1.13. It allows the indirect excitation of the 21-cm line via these Lyman-α photons, coupling the spin and kinetic temperatures.

The populations can be mixed either via a Lyman-α photon exciting an electron from the singlet state up to the n=2 state followed by a de-excitation to the triplet state or the Lyman-α photon can excite an electron in the triplet state up to the n=2 level before a de-excitation brings it directly down to the singlet state. In the former case the atom can then undergo spontaneous or collisional de-excitation back to the singlet state, emitting 21-cm radiation as indirect effect of the Lyman-α photon.

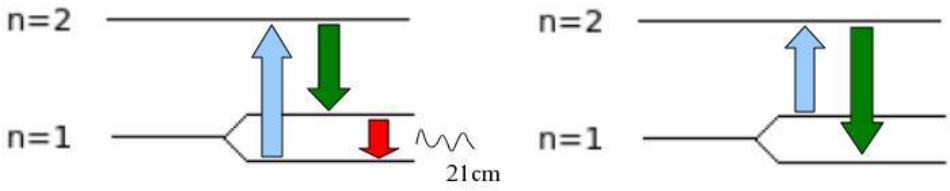

Figure 1.13: The hyperfine ground state population mixing of the 21-cm line via Lyman-α photons. The arrows from left to right represent successive electron transitions between energy levels. The blue arrow represents excitation by an Lyman-α photon, the green and red arrows either spontaneous or collisional de-excitations.

Through these methods, the populations of the two hyperfine states are mixed and the thermal equilibrium which would occur in the presence of only CMB photons is disrupted. The Lyman-α photons undergo a large number of scattering events in a static gas, causing their temperature distribution to redden due to recoil events. This allows, in the vast majority of situations, the assumption that $T_\alpha \approx T_k$ (Wouthuysen, 1952).

Collisional Decoupling

In high density regions or at very high redshift, collisions are also effective in decoupling T_{spin} from T_{CMB} (Madau et al., 1997). Collisional excitation of 21-cm radiation occurs mainly through spin exchange whereby a H atom collides with another H atom with an electron of opposite spin. In rarer events, where the electron density is larger than a few per cent of the H density, spin exchange can occur between a H atom and a free electron with opposite spin to the bound electron. While collisions can occur with other species, the events are much rarer. For example, spin exchange with protons is possible but sub-dominant due to the large masses involved (Field, 1958).

Spin Temperature Evolution

The evolution of the gas, CMB and spin temperatures tell us much about the state of the Universe, however models are not precise and can differ greatly, Figs. 1.14 and 1.15.

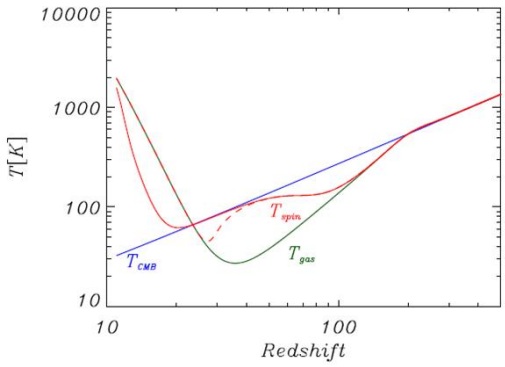

Figure 1.14: A possible evolution history of the kinetic (gas;green), spin (red) and CMB temperatures (blue) with redshift. The dashed line shows another possible history for the spin temperature, where coupling to the gas occurs earlier, allowing the spin temperature to be seen in absorption for a short time. Taken from Zaroubi (2010).

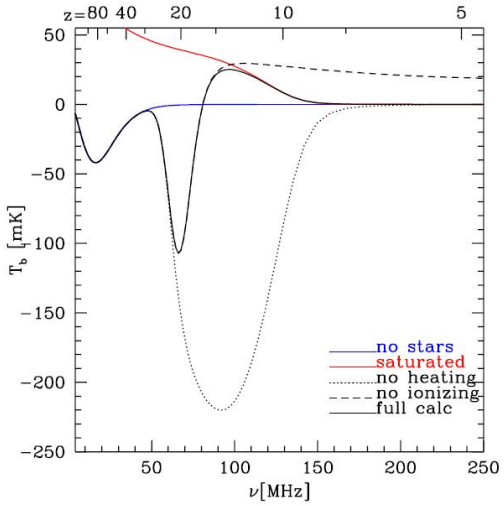

Figure 1.15: A possible evolution history of the spin temperature (black;solid) with redshift, along with how the evolution changes if key parts of the model are left out. Taken from Pritchard & Loeb (2010).

The evolution can be divided into stages:

$\mathbf{T_k = T_{CMB} = T_s}$ At high redshift, both T_{spin} and T_k are coupled to the CMB due to scattering of residual recombination era electrons.

$\mathbf{T_k = T_s > T_{CMB}}$ This coupling due to Compton scattering becomes inefficient at $z \approx 300 -$

1000 due to the low densities of electrons (Zaroubi, 2010; Pritchard & Loeb, 2010) and is negligible by $z \approx 150$ (Furlanetto et al., 2006). At some point before this the gas decouples from the CMB and is left to adiabatically cool as $(1+z)^2$. The temperature of the CMB meanwhile evolves steadily as $(1+z)$ rapidly leading to an absorption feature in the temperature spectrum.

$\mathbf{T_k < T_s \leq T_{CMB}}$ Between redshifts of $z \approx 80 - 100$ the collisions coupling the gas and spin temperatures become inefficient due to low densities, allowing the CMB photon collisions to couple the spin temperature to the CMB. As a result the spin temperature increases until the two are equal and no signal would be visible to us.

$\mathbf{T_k < T_s < T_{CMB}}$ As the first sources start ionizing the Universe, Lyman-α photon scattering couples the spin and gas temperatures via the Wouthuysen-Field effect, resulting in an absorption feature. Note though that, as seen in Figure 1.14, it is possible that this gas coupling was too weak to pull the spin temperature away from the CMB until a later time, resulting in a lack of absorption feature here.

$\mathbf{T_k \geq T_s > T_{CMB}}$ As reionization continues and ends, the X-ray heating of the gas and the Lyman-α coupling cause the 21-cm line to be seen in emission.

When one assumes that $T_{spin} \gg T_{CMB}$ we find that the differential brightness temperature allows us to probe the primordial density field. If observations push back to a time when this assumption no longer holds, we find instead that the differential brightness temperature can be used to probe the neutral hydrogen density fraction (Zaroubi, 2010).

1.2.5 The 21-cm Observable

The fundamental quantity of radiative transfer is the specific intensity or brightness, $I(\nu)$ which is expressed in terms of brightness temperature, T_b, in the Rayleigh-Jeans Law (Rybicki & Lightman, 1979):

$$I(\nu) = 2\frac{\nu^2}{c^2}k_B T_b. \tag{1.4}$$

As LOFAR is a radio interferometer T_b is detected as a deviation from T_{CMB} - the differential brightness temperature δT_b (Field, 1958, 1959):

$$\delta T_b = 28mK(1+\delta)x_{HI}\left(1 - \frac{T_{CMB}}{T_{spin}}\right)\left(\frac{\Omega_b h^2}{0.0223}\right)\sqrt{\left(\frac{1+z}{10}\right)\left(\frac{0.24}{\Omega_m}\right)}, \tag{1.5}$$

where δ is the mass density contrast, h is the Hubble constant in units of 100 km s^{-1} Mpc^{-1}, x_{HI} is the fraction of neutral hydrogen and Ω_b and Ω_m are the baryon and matter densities in critical density units. The derivation of this quantity is outlined in Section 4.4.2.

1.2.6 21-cm Measurements

We can use the brightness temperature observable to learn about different aspects of reionization depending on how we choose to make our observations.

Power Spectra and Other Statistical Measures

The current generation of radio telescopes such as LOFAR will concentrate mainly on statistical measures of reionization - namely the power spectrum of 21-cm fluctuations. Even the next generation of telescopes will need such statistical measures at large redshift as at small scales imaging is too difficult, even with the expected signal-to-noise of SKA (Mellema et al., 2012).

The power spectrum is defined as the Fourier transform of the spatial 2-point correlation function such that:

$$< T_b(\mathbf{k}, z) T_b(\mathbf{k}', z) >= (2\pi)^3 \delta^{(3)}(\mathbf{k} - \mathbf{k}') P(\mathbf{k}, z), \tag{1.6}$$

where $\delta^{(3)}(\mathbf{k} - \mathbf{k}')$ is the 3D Kronecker delta-function. The 3D power spectrum is found by computing the average power over spherical k-bands and should in principle allow the tightest constraints on reionization models due to the large number of modes taken into account, however there are advantages to considering different power spectrum statistics. The 2D power spectrum is calculated for every frequency over interest, with power being averaged over annuli constant in frequency. The 1D, or line of sight, power spectrum is calculated along each line of sight and then averaged over the total number of lines of sight.

The power spectrum tells us how the variance of the data changes with scale and its shape tells us much about the structure of reionization and different reionization histories (Zaldarriaga et al., 2004; Furlanetto et al., 2004). When the neutral fraction is large, the 21-cm power spectrum traces the matter density power spectrum, with a small bump/turnover at the scales characteristic of the ionized regions at that redshift. This feature will move to smaller k scales as redshift decreases since the ionized bubbles grow with time (Zahn et al., 2007). When the ionized regions begin to overlap the ionization field takes over as the dominant contribution to the 21-cm power spectrum, with the characteristic bubble size (which provides the turnover feature) trending towards infinity, thus power on and above the characteristic bubble size is increased by up to a factor of 10 (Furlanetto et al., 2004).

The power spectrum can also distinguish between different source histories, though not with universal ease. For example Iliev et al. (2012) used the 21-cm power spectrum to distinguish between source histories with LMACHs+HMACHS and HMACHs alone, however Furlanetto et al. (2004) found that single-source models of PopII and Pop III stars produced power spectra with very little difference.

Furlanetto et al. (2004) showed explicitly that as ionization progresses, the hydrogen density distribution has non-Gaussianities introduced into it due to non-Gaussian processes such as ionization and heating and so power spectrum analysis can be complemented by the use of higher order statistics such as kurtosis and skew, as defined in Equations 1.7 and 1.8 respectively,

$$\gamma_1 = \frac{\frac{1}{N}\sum_i (T_i - \bar{T})^3}{(\frac{1}{N}\sum_i (T_i - \bar{T})^2)^{\frac{3}{2}}} \tag{1.7}$$

$$\gamma_2 = \frac{\frac{1}{N}\sum_i (T_i - \bar{T})^4}{(\frac{1}{N}\sum_i (T_i - \bar{T})^2)^2} - 3, \tag{1.8}$$

where N is the number of lines of sight/pixels, T_i is the brightness temperature of pixel i and $\bar{T}$ is the average brightness temperature across a map. Qualitatively, skewness is a measure of how tailed a distribution is such that if a distribution is concentrated mainly at low values on the x-axis and has a high-x tail, skew is positive. Kurtosis is a measure of how peaked a distribution is. Gaussian distributions have a kurtosis and skew of zero.

The evolution over redshift of skewness is also a point of interest and can be understood by following the evolution of the δT_b distribution, Fig. 1.16. At high redshifts, the neutral hydrogen distribution has a positive skew due to gravitational instabilities in the density field. Considering a reionization scenario where ionized bubbles form around sources, the skew becomes less positive over redshift. During the late stages of reionization, the few neutral regions remaining form a high differential brightness temperature distribution tail, increasing skewness once again, Fig. 1.17.

The kurtosis of δT_b undergoes a clear evolution with redshift also. At high redshift, when the 21-cm distribution is still tracing the density field, the distribution is fairly Gaussian leading to a near zero kurtosis. As redshift decreases, the bi-peak distribution developed by bubble formation leads to kurtosis decreasing further before the large distribution peak at late times causes a rise in kurtosis. (Harker et al., 2009) found that while kurtosis showed a clear evolution, Fig. 1.18, it was more difficult to recover than skewness.

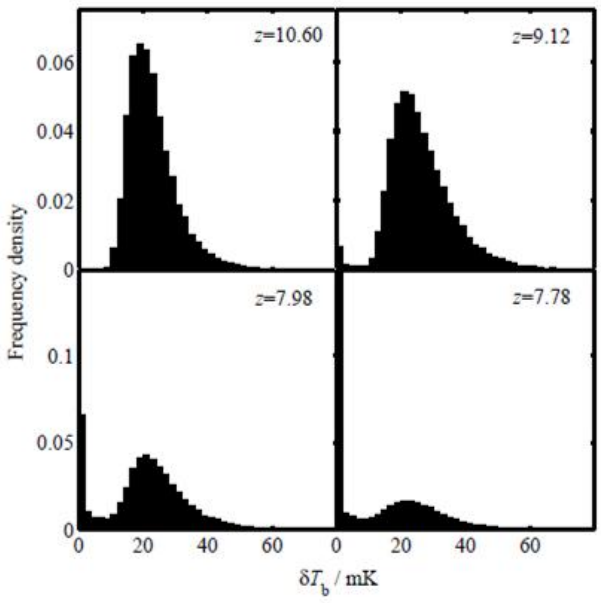

Figure 1.16: The δT_b distribution at four different redshifts for a simulation. Figure taken from Harker et al. (2009).

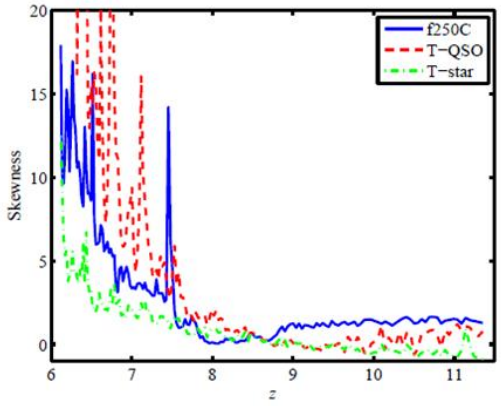

Figure 1.17: Skewness evolution with redshift, for three different reionization models: f250c and T-star where reionization is carried out by stars and T-QSO where reionization is by quasars. The first is based on simulations by Iliev et al. (2008), and the T-simulations are detailed in Thomas et al. (2008). Figure taken from Harker et al. (2009).

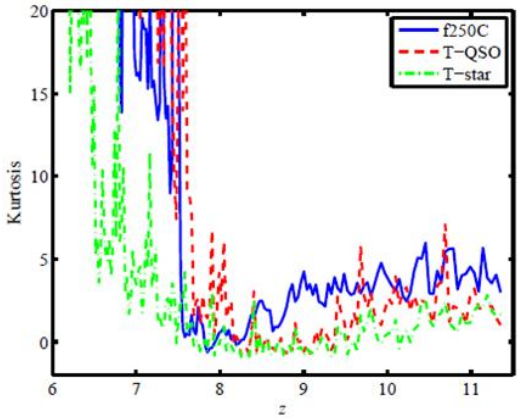

Figure 1.18: Kurtosis evolution with redshift, for three different reionization models: f250c and T-star where reionization is carried out by stars and T-QSO where reionization is by quasars. The first is based on simulations by Iliev et al. (2008), and the T-simulations are detailed in Thomas et al. (2008). Figure taken from Harker et al. (2009).

21-cm Forest

The 21-cm forest is the set of absorption lines which appear in high redshift radio-loud source spectra as a result of 21-cm absorption by intervening clouds of neutral hydrogen (e.g. Carilli et al., 2002; Furlanetto & Loeb, 2002; Furlanetto, 2006; Carilli et al., 2007; Xu et al., 2009; Meiksin, 2011; Xu et al., 2011; Ciardi et al., 2013; Mack & Wyithe, 2012). These observations

naturally side-step many of the challenges facing fluctuation experiments. For example, since the CMB does not act as a background source the IGM is visible even when $T_S = T_{CMB}$, the IGM can be resolved on scales of 10s kpc or smaller since the strongest absorption features result from small structures and otherwise dominating systematics such as the foregrounds are not a problem. Recently, Ciardi et al. (2013) has shown through their reionization simulations that 21-cm forest observations are unlikely to be able to distinguish between different reionization histories, unless those histories are very different from one another.

The main limitation of 21-cm forest experiments is the lack of high redshift radio-loud sources. Currently the highest redshift QSO observed is accepted to be at z=7.085 (Mortlock et al., 2011) and the population density at higher redshift is currently unknown. It has been estimated that there are only $10 - 10^4$ usable radio-loud sources per unit redshift at redshifts higher than 10 (e.g. Carilli et al., 2002; Xu et al., 2009) making comprehensive observations of the 21-cm forest a challenge.

The Global Signal

When discussing the global signal, it is useful to use the COBE measurements as an analogy. COBE measured both the CMB blackbody temperature and the CMB temperature fluctuations - analogous here to the global 21-cm signal and the 21-cm fluctuations measured by experiments such as LOFAR. While the majority of work concentrates on the measurement of fluctuations, there has been consideration put into measurement of a global signal (Sethi, 2005; Madau et al., 1997; Pritchard & Loeb, 2010).

With the motivation of a much simpler and cheaper experiment, it is useful to consider what we could learn from a single dipole measurement of the global 21-cm signal, with facilities such as EDGES[3]. As described in Section 1.2.4, the 21-cm signal has several well described stages of evolution which introduce well defined maxima and minima into the global 21-cm signal. A minimum occurs where collisional coupling becomes ineffective followed by a maxima as Ly-α coupling becomes effective. Then, an absorption minima as heating begins before an emission maxima as the signal saturates and tends to zero as reionization ends. Global experiments hope to detect these stages and, by comparing to theoretical models of how these peaks shift and change with changing parameter values such as UV emissivity, constrain reionization and source models. Pritchard & Loeb (2010) found that global experiments are sensitive to reionization histories where the range of redshifts over which ionization occurs is short. This was seen as unfortunate as Pritchard et al. (2010) has shown that it was the longer reionization histories

[3]http://www.haystack.mit.edu/ast/arrays/Edges/

which appear to be most compatible with the data constraints, however work continues in the hope that the constraint to sharper histories was a result of simple toy models as opposed to an experimental roadblock.

Tomography

The high signal-to-noise ratios expected of the next generation of radio telescopes such as the SKA will allow us to construct several hundred distinct 21-cm maps for the EoR allowing a new dimension of interpretation. Tomography will allow the visualization of the evolution of a region, telling us much about how reionization progressed and allowing the analysis of individual features in the 21-cm data such as the ionized bubble around a quasar (Majumdar et al., 2012). Though this level of tomography is reserved for SKA-like instruments, recent work has shown that, at least in theory, map making will be possible with LOFAR (Zaroubi et al., 2012; Chapman et al., 2013).

1.3 Radio Instrumentation

Radio interferometry was born in the mid-20th century with the basic two-element Michelson interferometer. It was designed to measure the angular diameter of stars after it was found that no single aperture telescope could map the sun at any level of interesting resolution. M.Ryle & D.D.Vonberg (1946); McCready et al. (1947) utilised the Michelson interferometer for the first time at radio wavelengths to measure the angular diameter of sunspots and map the entire sun's radio emission respectively. As the power of radio interferometry was recognised, the Michelson interferometer naturally extended to whole arrays of radio telescopes, forming an aperture-synthesis array. Two radio telescopes form a baseline, with more baselines available the more elements an array has. For an array with N elements, there are $N(N-1)/2$ possible baselines.

A subtype of radio interferometer relevant to this project is the Earth-rotation array. Ryle & Neville (1962) noted that baselines were lengthened and their orientation altered with the rotation of the Earth in such a way as to extend the sky coverage.

Consider Fig. 1.19: a propagation front will arrive at the left antenna with a time delay equal to $\tau_g = D\sin\theta/c$ such that the right and left antenna measure voltages of $V\sin[2\pi\nu t]$ and $V\sin[2\pi\nu(t-\tau_g)]$ respectively. The telescope receiver will combine the squared sum of the voltage measured at each antenna and filter out the higher frequency components leaving an output proportional to a fringe function $\cos(2\pi\nu\tau_g)$ and the received power.

Now consider a source in the sky, where the centre of the source to be mapped is defined as

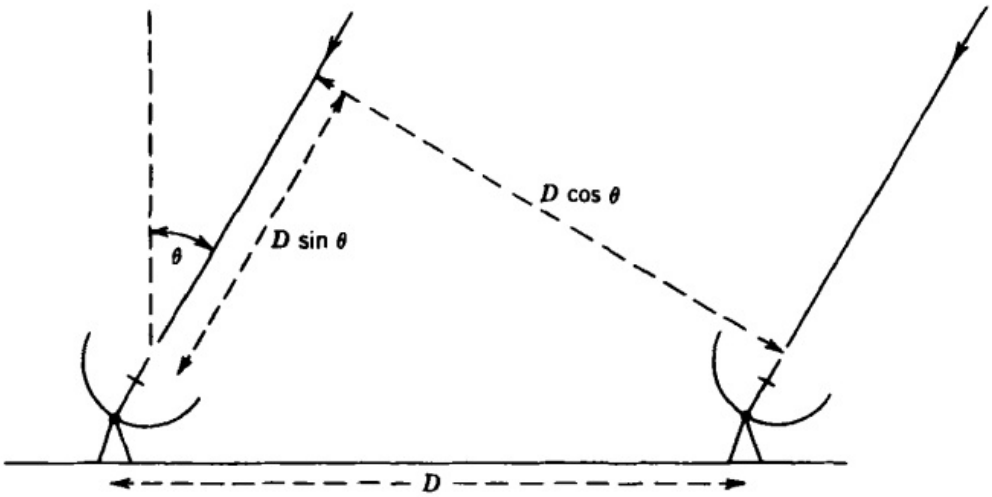

Figure 1.19: The geometry of two antenna in an interferometric array where D is the baseline. Taken from Thompson et al. (2001).

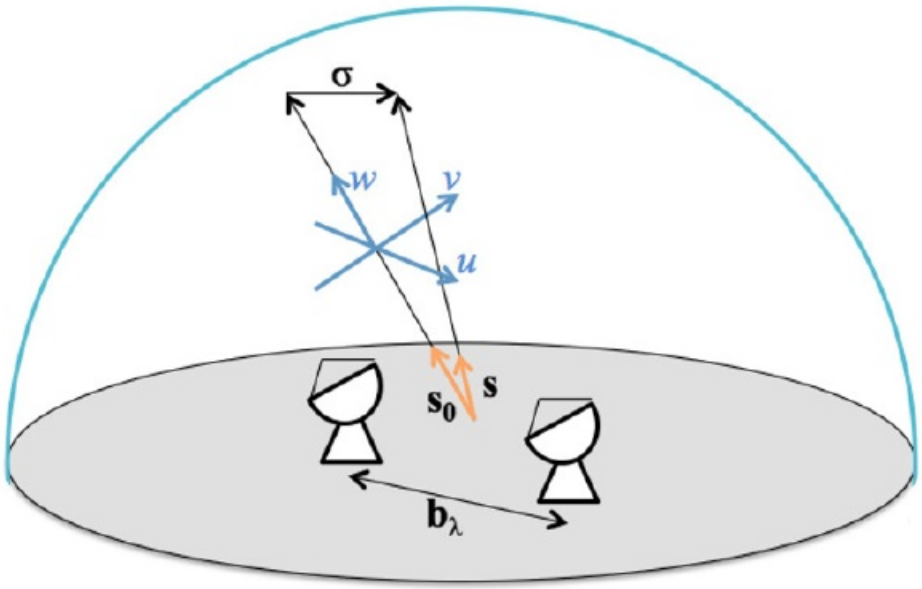

Figure 1.20: The geometry of the uv plane. b_λ is the baseline and is referred to as D in the text. Taken from Avison & George (2013).

being in a direction $\mathbf{s}_0$, Fig. 1.20. A source element of solid angle $d\Omega$ on the sky in direction $\mathbf{s} = \mathbf{s}_0 + \boldsymbol{\sigma}$ will contribute power $\frac{1}{2}A(\boldsymbol{\sigma})I(\boldsymbol{\sigma})\delta\nu d\Omega$ to each of the two antennas in a baseline. Therefore the correlator output is an integral over the source element $d\Omega$ such that:

$$r(\mathbf{D}_\lambda, \mathbf{s}_0) = \Delta\nu \int_{4\pi} A(\boldsymbol{\sigma})I(\boldsymbol{\sigma})cos[2\pi\mathbf{D}_\lambda \cdot \mathbf{s}]d\Omega. \tag{1.9}$$

Each baseline provides a 'visibility' (the measured spatial correlation of the electric field between the two antennas) corresponding to a point on the uv plane. The uv plane of an observation is perpendicular to the unit vector describing the direction to the source being observed, $\mathbf{s}_0$. A right handed recti-linear coordinate is defined where by w is in the direction of $\mathbf{s}_0$ and the baseline between two elements i and j is described using the coordinate system (u, v, w) (Burke & Graham-Smith, 2010).

The visibility contributed by a interferometric pair can therefore be defined as:

$$V_{ij}(\mathbf{s}_0, u, v) = \int \mathcal{A}(l, m)I(l, m)\exp[i2\pi(ul + vm + wn)]d\Omega, \tag{1.10}$$

where $d\Omega = dldm/\sqrt{1 - l^2 - m^2}$.

The more baselines, the more points on the uv plane, and the more fully sampled the sky is. A fully sampled uv plane is equivalent to a perfect measurement of the brightness distribution and a good uv coverage is important for precise sky models (Nijboer et al., 2006; Smirnov & Noordam, 2004), accurate foreground removal and to improve the sampling of the 21-cm power spectrum.

The uv coverage depends on the number, size and organisation of array elements as well as the time over which an observation is carried out (the integration time). The larger a station the worse the uv coverage however a balance must be struck between this and the technological ability to process the visibilities and the noise levels (Zaroubi, 2010). LOFAR has rather large station sizes resulting in a small number of baselines and a large integration time (5-6 hours) necessary to fill the uv plane as the Earth rotates (Zaroubi, 2010). Smaller stations result in more baselines and instantaneous coverage, a strategy MWA[4] has adopted, Fig. 1.21. With more baselines, one can get a more accurate estimation of the power spectrum.

1.3.1 LOFAR and LOFAR-EoR Instrumentation

LOFAR[5] (van Haarlem, M. P. et al., 2013) is based in the Netherlands, with the core stations located in a 2 km wide region near to Exloo. Two types of antenna are used in LOFAR, the low

[4]http://www.haystack.mit.edu/ast/arrays/mwa/
[5]http://www.lofar.org/

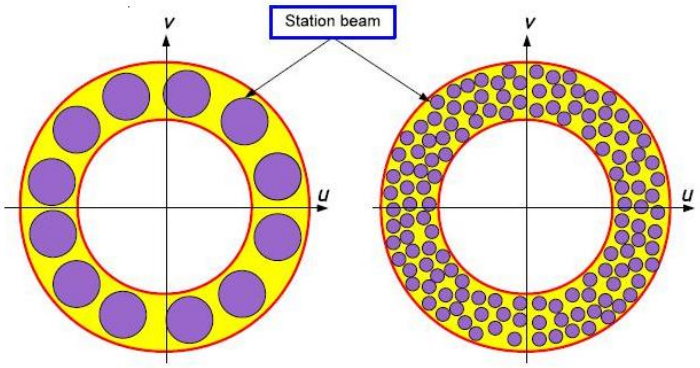

Figure 1.21: Larger stations result in a larger *uv* 'footprint' (purple circle). The two diagrams show the same amount of uv sampling, however the smaller stations sample the annulus more resulting in more accurate statistics. Figure taken from Zaroubi (2010).

band antennas (LBA) which observe at 30-80 MHz and the high band antennas (HBA) which observe at 110-240 MHz. The core consists of 24 stations (Fig. 1.22), each with 96 LBA antennas and two sets of 24 HBA antennas (or 'tiles'). Within the Netherlands at distances smaller than 100 km from the core, there are 16 remote stations, each with 96 LBA antennas and 48 HBA tiles. In addition there are 8 international stations (5 in Germany and one in each of France, Sweden and the UK) with 96 LBA antennas and 96 HBA tiles. The close gathering of stations in the core and the inclusion of the international stations results in a baseline distribution ranging from 100m - 1500 km, though this upper limit could be increased with other countries expressing an interest in hosting their own LOFAR station.

Beamforming and Signal Corruptions

The LOFAR-EoR observation will take place using the HBA dipoles. Each of the tiles consist of 16 dipoles arranged in a 4-by-4 pattern. The dipoles are crossed dipoles enabling measurement of dual polarization. The signals from each dipole are coherently combined using a digital beamformer. In addition, so that the sidelobe contribution of any two stations cancel, each station is randomly orientated resulting in the rotation of the main station beams also. The radio signal is sampled and filtered into narrow sub-bands before being beamformed and encoded for transmission to the correlator.

The signal will have had several sources of noise already introduced into it before the instrument itself contributes. The change in the polarization and direction of the incoming radiation due to the ionosphere can be modelled within the measurement equation of LOFAR and minimized by avoiding active periods such as sunrise and sunset.

Radio frequency interference (RFI) can be introduced by many external agents such as aero-

Figure 1.22: The 'superterp' where six LOFAR stations lie. The black tiles are the casings of the HBA antennas. Taken from van Haarlem, M. P. et al. (2013).

planes, lightning strikes, sparking electric fences and TV stations. Mitigation techniques have been successfully researched (Offringa, 2012) though small amount of RFI related noise could still be present in a calibrated signal.

Sensitivities and Noise

The sensitivity of any radio telescope is highly dependent on the system noise temperature, T_{sys}. T_{sys} is the amount of excess noise introduced into a measurement due to the telescope system and can be broken down as:

$$T_{sys} = T_{sky} + T_{inst}, \tag{1.11}$$

where T_{sky} is the radiation which enters the telescope system from the outside and T_{inst} accounts for the losses in the antennas and amplifier system.

The foregrounds set a limit on a radio telescope's sensitivity:

$$\Delta T_{min} \approx \frac{T_{sys}}{\sqrt{\delta\nu t}}, \tag{1.12}$$

where $\delta\nu$ the bandwidth and t the integration time. Shaver et al. (1999) calculated that for $[T_{sys},\delta\nu,t]$=[150 K,5 MHz,24 h], $\Delta T_{min} \approx 0.0002$ K - small enough for sensitivity to not be an issue in the detection of the 21-cm signal.

'Noise' is a term often used in this context to encompass thermal noise, confusion noise and

Table 1.2: LOFAR and simulation parameters

Parameter	Description	Value
n_d	number of dipoles per tile	16
n_t	number of tiles per station	24
n_s	number of stations	48
η_a	antenna efficiency	1
η_s	system efficiency	0.9
$\Delta\nu$	frequency interval [MHz]	0.5
$t_{\rm int}$	integration time [h]	600
$\Omega_{\rm arcmin}$	area of synthesized beam [arcmin^2]	4
$\Omega_{\rm sr}$	area of synthesized beam [sr]	1.35×10^{-6}

calibration residuals i.e. system noise and a frequency dependent sky noise component.

The thermal noise for a single visibility, (e.g. Zaroubi, 2010), is:

$$\Delta V(u,v) \approx \frac{2k_B T_{sys}}{\eta dA\sqrt{\delta\nu t}}, \tag{1.13}$$

where η is the array efficiency, and dA is the station area.

The confusion noise is related to the maximum number of sources a telescope can separate (Condon, 1974). Above that number, sources can no longer be resolved leading to a diffuse map of emission. For LOFAR this number is 500 sources, whereas for MWA it is 250,000 sources (Lampropoulos, 2010).

For LOFAR, the theoretical rms noise level is calculated as in (Lampropoulos, 2010) in terms of the complex visibilities for any station pair, p and q:

$$\Delta V(Re,Im)_{p,q} = \frac{1}{\nu_s}\sqrt{\frac{SEFD_p \times SEFD_q}{2\delta\nu\tau_{avg}}}, \tag{1.14}$$

where ν_s is the system efficiency, τ_{avg} is the averaging time during which the station accumulates data, system equivalent flux density $= SEFD = \frac{T_{sys}}{K}$, $K = \frac{\nu_A A_{eff}}{2k_B}$ with ν_A the station efficiency and A_{eff} the effective collecting area of the stations. This effective area introduces a frequency dependence.

Our parameters for calculating the noise are listed in Table 1.2. In order to create a noise curve we use the prescription detailed below.

The system noise temperature consists of sky brightness and instrumental components. We calculate this system temperature using:

$$T_{\rm sys} = 140 + 60\left(\frac{\nu}{300\ {\rm MHz}}\right)^{-2.55}. \tag{1.15}$$

The effective area of the array is determined by multiplying the effective area of a single dipole by the number of dipoles in the array where the effective area of a dipole is limited by the size of the tile. We calculate the effective area of the LOFAR array using:

$$A_{\rm eff} = \min\left(\frac{\lambda^2}{3}, 1.5625\right) n_d n_t. \tag{1.16}$$

The System Equivalent Flux Density (SEFD) then depends on both of the quantities calculated above:

$$\text{SEFD} = \frac{2T_{\rm sys}k_b}{\eta_a A_{\rm eff}}. \tag{1.17}$$

Finally we calculate the LOFAR noise sensitivity:

$$\sigma = \frac{1}{\eta_s}\frac{\text{SEFD}}{\sqrt{n_s(n_s-1)\Delta\nu t_{\rm int}\Omega_{\rm sr}}}. \tag{1.18}$$

For example the noise sensitivity at 150 MHz for the parameters listed in Table 1.2 is 64 mK.

1.3.2 Other Interferometers

Aside from LOFAR, there are several other radio interferometric experiments aiming to make a statistical detection of the EoR.

The Murchison Widefield Array[6] (MWA) (Tingay et al., 2013) is an interferometer based in a remote location in Western Australia. The site allows for high elevation observations and there is extremely low RFI. MWA can observe between 80-300 MHz with a field of view of $25^\circ \times 25^\circ$ at 150 MHz. Although MWA has a lower angular resolution than LOFAR, the wide field of view has been optimized to collect as much statistical information about reionization as possible. The telescope consists of 128 tiles made up of 16 dipoles in a 4×4 array, with the vast majority of tiles (112 of the 128) placed within a core of 1.5 km. Observations using a 32 core tile MWA configuration placed an upper limit on the 21-cm power spectrum of $\Delta(k) < 0.3K$ at $z = 9.5$ and at a scale of $k = 0.046$ Mpc^{-1} with 95% confidence (Dillon et al., 2013), where $\Delta(k) = \sqrt{\frac{k^3}{2\pi^2}P(k)}$ and P(k) is defined in Equation 1.6.

The Giant Metrewave Radio Telescope[7] (GMRT) is situated in India, 80 km north of Pune. Unlike the other interferometers mentioned in this section, GMRT consists of 30 fully steerable parabolic dishes, each of 45 m diameter. While 14 of the dishes are sited randomly in a 1 km^2 core, the remaining dishes are placed in a 'Y' shape around the core, up to a distance of 25 km away. GMRT previously reported an upper limit of $\Delta(k) < 70$ mK at k =0.65 h/Mpc and z=8.6

[6] http://www.mwatelescope.org
[7] http://gmrt.ncra.tifr.res.in

Table 1.3: Interferometer Comparison

Telescope	FoV (deg)	Array Configuration	Upper Limits on 21-cm Power Spectrum
LOFAR	30	A 1.5 km core of 24 stations consisting of 48 antenna tiles. 16 remote stations consisting of 48 antenna tiles. 8 international stations consisting of 96 antennas tiles.	n/a
MWA	15-50	112 tiles of 16 dipoles in 1 km core. 16 tiles at 1.5 km.	$\Delta(k) < 0.3K$ at $z = 9.5$ and at a scale of $k = 0.046$ Mpc^{-1}
GMRT	$\approx$ 10-33	14 parabolic dishes in 1 km core. 16 dishes at distances up to 25 km.	$\Delta(k) < 248$ mK at k =0.65 h/Mpc at z=8.6
PAPER	40	128 antenna to be in South Africa. 32 in Green Bank, USA.	$\Delta(k) < 53$ mK for k=0.11 h Mpc^{-1} at z =7.7

(Paciga et al., 2011) but this has recently been revised to $\Delta(k) < 248$ mK at k =0.65 h/Mpc with 95% confidence using a more robust method of foreground subtraction (Paciga et al., 2013).

The Precision Array to Probe the Epoch of Reionization[8] (PAPER) is based in both Karoo, South Africa (eventually to consist of 128 antennas) and Green Bank, USA (32 antennas). The Green Bank array has been used to produce sky maps between 130-178 MHz (Parsons et al., 2010) and is now being used to improve the global sky model and optimize array configurations for a statistical detection. Using a 32 antenna array in South Africa, the team have been able to place an upper limit of $\Delta(k) < 53$ mK for k=0.11 h Mpc^{-}1 at z =7.7 with 95% confidence (Parsons et al., 2013).

The 21 Centimeter Array[9] (21CMA) is based in western China. The 'T' shaped array is made of 81 groups of 127 logarithmically spaced antennas and is supposed to observe the North Celestial Pole (NCP) continuously, with a field of view of approximately 33°$\times$ 33°. Not much is known about the status of observations except that the telescope was completed in 2006 and observations have been somewhat interrupted by funding problems (Clery, 2009). Wang et al. (2013) alluded to current observations being carried out with FoV=5°$\times$ 5°, with a thermal noise of 60 mK at z=8 expected to be reached after one year of observations.

1.4 LOFAR-EoR Foregrounds

The various Galactic and extragalactic foregrounds will form an overwhelming contribution to the total measured signal. These foregrounds can be up to five magnitudes larger than the EoR

[8]http://eor.berkeley.edu
[9]http://21cma.bao.ac.cn

21-cm signal we hope to detect, though since facilities such as LOFAR measure only fluctuations from the mean it is thought that the foreground fluctuations will dominate by roughly three magnitudes.

There have been a couple of foreground observations at frequencies relevant to LOFAR using WSRT (Bernardi et al., 2009, 2010) and the Giant Metrewave Radio Telescope (GMRT) (Ali et al., 2008). However, since an observation has not been carried out with LOFAR itself yet, foreground models directly relevant for this era rely on using constraints from observations at different frequency and resolution ranges. These constraints are used to normalize the necessary extrapolations made from observations to create a model relevant for LOFAR-EoR observations. The three observational studies most utilised for building EoR foreground models are at 150 MHz with 5° resolution (Landecker & Wielebinski, 1970), 408 MHz with 0.85° resolution (Haslam et al., 1982) and 1420 MHz with 0.95° resolution (Reich, 1982; Reich & Reich, 1986).

We now summarise the evolution and currently accepted models for the various foreground components.

1.4.1 Galactic Synchrotron Radiation

Galactic synchrotron radiation contributes $\approx 70\%$ of the total foreground contamination (Jelić et al., 2008) and can be from either diffuse or localized sources.

Diffuse Sources

The emission of galactic diffuse synchrotron emission (GDSE) due to the interaction of free electrons in the interstellar medium (ISM) and the galactic magnetic field is the dominant component of foreground contamination at EoR frequencies. The magnitude of the GDSE at LOFAR frequencies is under some debate with extrapolations from data at different frequencies leading to estimations of several hundred to a few Kelvin at 150 MHz (Wang et al., 2006; Gleser et al., 2008; Bernardi et al., 2010).

The GDSE and other foreground components (see below sections) are generally modelled as power laws, $T_b \propto \nu^{\beta}$ where Reich & Reich (1988) defines $-2.3 \leq \beta \leq -3.0$ and Shaver et al. (1999); Jelić et al. (2008) defines $\beta = -2.55$ at 100 MHz. Different lines of sight have slightly different spectral index, with a standard deviation of σ_{β}=0.1 between 100 MHz and 200 MHz, mainly due to the galactic loops (Shaver et al., 1999) and the coldest areas of the sky. As a result, Wang et al. (2006) and Gleser et al. (2008) model the GDSE brightness temperature as a running power law:

$$T_{syn} = A_{syn} \left(\frac{\nu}{\nu_*} \right)^{-\beta - \Delta\beta \log(\frac{\nu}{\nu_*})}, \tag{1.19}$$

where $A_{syn} = T_{syn}(\nu_*)$ and $\nu_* = 150$ MHz. Wang et al. (2006) assume [β,$\Delta\beta$,A_{syn}]=[-2.8,0.1,335.4] where $\Delta\beta$ is the spectral running. Gleser et al. (2008) set [β,$\Delta\beta$,A_{syn}]=[-2.7,0.1,442.0].

The angular power spectrum of the galactic diffuse synchrotron emission can be modelled as $C_l \propto l^{-\alpha}$. Tegmark et al. (2000) defines $2.4 < \alpha < 3$ while Giardino et al. (2002) define $\alpha = 2.37 \pm 0.21$. Santos et al. (2005) chooses a fiducial value of $\alpha = 2.4$ and Jelić et al. (2008), $\alpha = 2.7$.

The latter paper goes one step further in their account of the spatial and spectral variation of the GDSE. Jelić et al. (2008) simulates the GDSE in 4D (3 spatial and one frequency), integrating over the z coordinate to obtain a map at each frequency. Fig. 1.23 is an example map of the GDSE at 150 MHz for a 5° observing window, taken from Jelić et al. (2008).

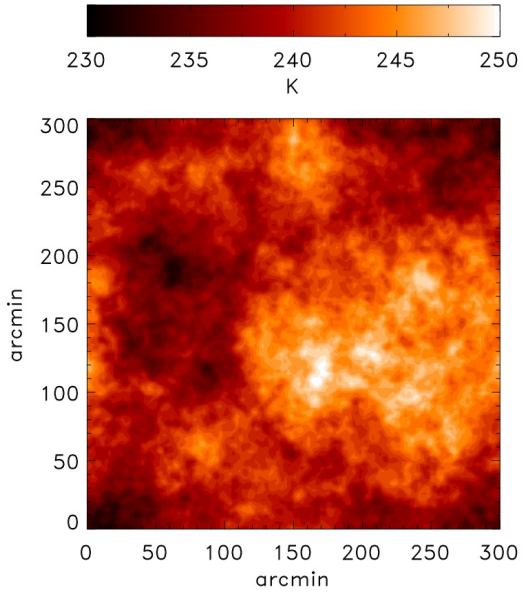

Figure 1.23: A 5° × 5° simulated map of the GDSE taken from Jelić et al. (2008). They defined $\alpha = 2.7$ and $\beta = -2.55$.

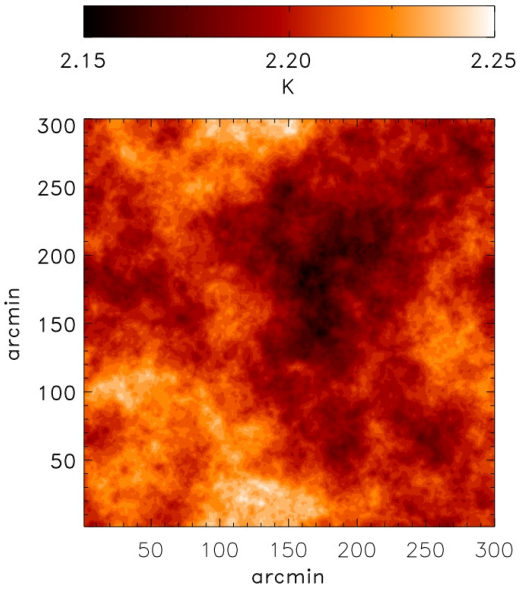

Figure 1.24: A 5° × 5° simulated map of the Gff using simulations detailed in Jelić et al. (2008). They assume $\alpha = 3$ and $\beta = -2.15$

Since β is accepted to be a function of both frequency and position on the sky, the model describing the frequency evolution of GDSE brightness temperature is actually a superposition of many power laws. However, the foreground model is still very smooth as a function of frequency.

Localized Sources

Supernovae remnants (SNRs) are expanding shells consisting of material from the star and interstellar medium caught by the shockwave. The magnetic fields in these environments are

very strong and very high energy cosmic rays are produced which, as these cosmic rays escape the shell, undergo severe synchrotron cooling, emitting synchrotron radiation that we see at radio frequencies.

The treatment of SNRs as a foreground is rather rare in the literature relating to the EoR but there are fairly complete relations between their distribution, radio surface brightness and diameter with height from galactic plane (e.g. Caswell & Lerche, 1979). Jelić et al. (2008) uses such relations to calculate that one should expect 1-2 SNRs in a $5^\circ \times 5^\circ$ observing window and assume a power law spectra for each SNR of the form:

$$S_\nu = S_0 \left(\frac{\nu}{\nu_0}\right)^\alpha . \tag{1.20}$$

They place discs randomly on the map with random values for the spectral index, supernovae flux constant and angular size taken from the Green (2006) catalogue of observed SNRs.

1.4.2 Galactic Free-Free Emission

The galactic free-free foreground makes up roughly 1% of the total contamination (Shaver et al., 1999), however both the spatial and angular fluctuations of the free-free emission are large enough to wipe out the cosmological signal if unaccounted for (Cooray & Furlanetto, 2004). More importantly, the free-free spectral index is quite different to the other foreground components, providing a test of the foreground removal algorithms' flexibility.

The diffuse Galactic ionized medium is populated with many free electrons. When these electrons pass by each other they are deflected and decelerated, resulting in bremsstrahlung radiation - free-free emission. This Galactic gas is optically thin at frequencies above 1 MHz and traced well by Hα (Smoot, 1998) and possibly dust emission (e.g. Kogut et al., 1996). As a result, the free-free emission spectrum is well observed and characterized at the frequencies relevant to EoR experiments. The power law index for Galactic free-free emission is $\beta = -2.1$ at EoR frequencies.

While the spectrum is well established, the amplitude and power spectrum of the free-free emission are less so. This is because of dust, CMB and synchrotron domination at low, medium and high frequencies respectively making the creation of a spatial amplitude template for free-free a challenge. Recently however, the use of Hα as a tracer has resulted in a first order template (Dickinson et al., 2003) at CMB frequencies which can be extrapolated. Both Jelić et al. (2008) and Santos et al. (2005) define a fiducial power spectrum index ($C_l \propto l^{-\alpha}$) $\alpha = 3.0$ whereas Tegmark et al. (2000) set $2.2 \leq \alpha \leq 3.0$ depending on how pessimistic their model is.

Using relations between Hα intensity and free-free brightness temperature, Jelić et al. (2008) obtains a free-free brightness temperature of $T_{b,ff} = 2.20 \pm 0.05K$ at 120 MHz. In contrast, Gleser et al. (2008) uses the 70:1 ratio of synchrotron to free-free emission (Shaver et al., 1999) and, using the well constrained synchrotron brightness temperature values, finds $T_{b,ff} = 6.33 \pm 0.63K$ at 150 MHz. Using models of the clumping of ionized gas, Cooray & Furlanetto (2004) found variations in the free-free background of order a few to tens of percent.

An example galactic free-free simulation taken from (Jelić et al., 2008) is shown in Fig. 1.24.

1.4.3 Galactic Dust Emission

The emission of radiation via the vibration and rotation of dust grains in the interstellar medium has been deemed insignificant at the frequencies relevant to EoR (Gleser et al., 2008). Though dominant at much higher frequencies such as those used by CMB experiments, the dust emission is dominated by synchrotron and even free-free at lower frequencies (Platania et al., 2003).

1.4.4 Galactic Radio Recombination Lines

In low density ISM regions, free electrons can be captured by high quantum number atoms. As the resulting atom transitions to successively lower energy states, a series of radio recombination lines, or RRLs are emitted every 1-2 MHz. In the vast majority of the literature on EoR foregrounds, radio recombination lines are either not mentioned or dismissed as insignificant (e.g. Gleser et al., 2008).

Shaver et al. (1999) recognised that peak line intensities can reach significant values of 1 K, however went on to explain that this would be diluted down to 0.002 K in a 5 MHz observation band.

Peters et al. (2011) argued that, since we do not know the strength of RRLs at the latitudes targeted by EoR experiments, making such a conclusion may be premature. They argue that there have been RRL observations of brightness temperature $\approx$ 100 K in the Galactic plane at 150 MHz and, as such, even residual effects of high latitude RRL regions would be significant in comparison to the mK scale of the cosmological signal. The same paper also points out that the EoR frequency ranges are also where the RRL transitions from absorption to emission and so they would be at a minimum even if high latitude RRL-producing regions existed to the point of experimental significance in our galaxy.

Whatever the probability and amplitude of RRLs occurring in EoR observations, it is generally accepted that, since they occur at known frequencies, they can easily be identified and removed early on in the background cleaning process (Shaver et al., 1999).

1.4.5 Extragalactic Foregrounds

The isotropic radio emissions from outside our galaxy accounts for roughly 10% of the total contamination, however can account for up to 25% at high Galactic latitudes, where the brightness temperature of the Galactic foregrounds drops significantly (Gleser et al., 2008).

The magnitude of the extragalactic contribution has been estimated by extrapolation of brightness temperature measurements at different frequencies and through integrated source counts. The former yields $T_{b,EG} = 17$ K and 30 K (Bridle, 1967; Cane, 1979) using power law indices of $\beta = -2.8$ and -2.75 respectively. Integrated source counts have produced an even wider range of estimates: $T_{b,EG} = 5 - 178$ K (Simon, 1977; Willis et al., 1977; Lawson et al., 1987).

The spectral indices of individual sources can range quite drastically - for example strong synchrotron self-absorption sources can have $\beta = 2$ while pulsars have an index closer to $\beta = -3$ (Shaver et al., 1999). Kellermann et al. (1969) classified the 299 extragalactic sources in the revised Third Cambridge Catalogue of Radio Sources (3C and 3CR) according to whether their temperature spectra could be described by a single power law (42%), a spectra steepening at higher frequencies (convex; 52%), a spectra flattening at higher frequencies (concave; 3%) or a spectra containing multiple components (complex; 3%). Shaver et al. (1999) used these statistics to appropriately weight a sample of 37 galaxies from the 3C spectra (Kellermann, 1966; Kellermann & Pauliny-Toth, 1969; Kellermann et al., 1969; Kellermann, 1974; Kellermann & Owen, 1988) before combining the spectra to give a composite spectrum of the extra galactic foregrounds. Averaging over all of the sources should result in any strong features being smoothed out leaving the extragalactic background as a slowly varying function of frequency. Indeed, Shaver et al. (1999) found the composite spectrum to be close to a power law between frequencies 50-300 MHz, with $\beta = -2.65$. Any deviation from the power law was slow and over the frequency range the index ranged only between $\beta = -2.59$ and $\beta = -2.66$. The authors concluded that the extragalactic foreground should be smooth as a function of frequency - especially with more sources included in the sample.

The extragalactic foregrounds can be split into several contributing entities. In order of significance, there are contributions from point sources related to AGN activity, radio haloes and radio relics and free-free emission from star-forming galaxies, diffuse IGM and ionizing haloes.

Extragalactic Point Sources

At EoR radio experiment frequencies, the dominant extragalactic bright source radiation originates from radio-loud galaxies, quasars and the AGN class of BL LAC objects. Radio emission results from gas accretion onto the black hole at the source centres.

Di Matteo et al. (2004) has shown that the angular clustering of bright sources dominate over any cosmological signal fluctuations on scales of above 1 arcmin. As a result, unlike previous papers, Jelić et al. (2008) utilised a Rayleigh-Lèvy random walk algorithm to cluster bright radio sources chosen randomly from the galaxy distribution tables of Jackson (2005). In a $5° \times 5°$ observing window, they included 20690 point like radio galaxies, Fig. 1.25.

Late type, star forming galaxies are natural environments for synchrotron and free-free emission (detached from that of the AGN activity) as the ISM is heated and ionized by supernovae, stellar winds and cosmic rays, however their contribution to the total foreground component is negligible (Gleser et al., 2008).

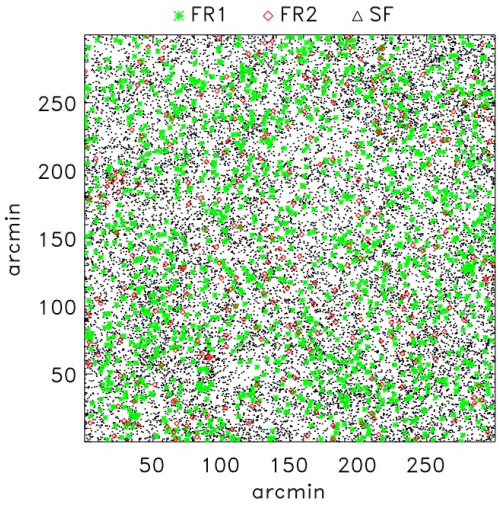

Figure 1.25: A $5° \times 5°$ simulated map of the extragalactic radio radiation from radio galaxies using simulations detailed in Jelić et al. (2008).

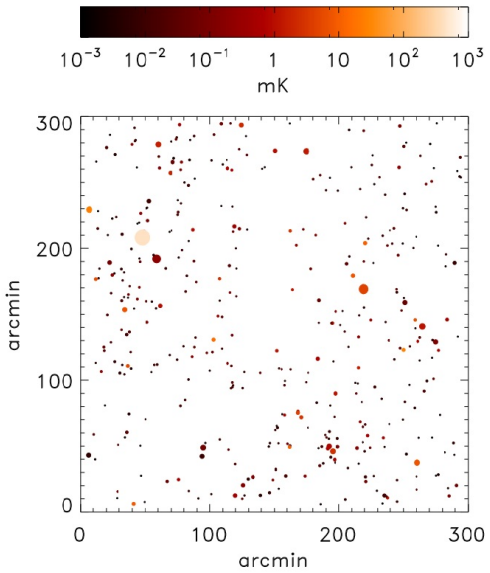

Figure 1.26: A $5° \times 5°$ simulated map of the extragalactic radio radiation from radio haloes and relics using simulations detailed in Jelić et al. (2008).

Radio Haloes and Radio Relics

Cluster radio haloes and cluster radio relics form a diffuse extragalactic background. The former are mostly unpolarized and found in cluster centres whereas the latter are more irregular, mostly polarized and found in the cluster periphery. Radio relics are extended radio sources which do not seem to be associated with a host galaxy. Recent literature has concluded that they are

probably related to cluster merger shockwaves reviving radio ghosts (Enßlin, 2001; Hoeft et al., 2004). Just as in our galaxy, free electrons interact with the cluster magnetic fields resulting in synchrotron radiation.

The radio halo distribution appears to follow the free-free X-ray emission of galaxy clusters (Govoni et al., 2001) however only $30 - 40\%$ of clusters host radio haloes. One can use galaxy catalogues to estimate the number of cluster halos in any observation window. For example Jelić et al. (2008) randomly selected 30% of The Hubble Volume Project ΛCDM deep wedge cluster catalogue's radio clusters (Colberg et al., 2002; Jenkins et al., 2001; Evrard et al., 2002), Fig. 1.26. Gleser et al. (2008) concluded that radio haloes and relics, while insignificant on average compared to point sources, could contribute contamination of the order of 10s of K on individual lines of sight.

Diffuse Extragalactic Free-Free Emission

The favoured extragalactic free-free models are based on large scale structure distribution and assume free electrons reside in dark matter haloes. Gleser et al. (2008) described extragalactic free-free (EGff) emissions as contributing 0.15% of total foreground contamination. Due to the small scale of the cosmological signal however, it is still recognised as a significant foreground (Oh, 1999; Di Matteo et al., 2002; Oh & Mack, 2003; Cooray & Furlanetto, 2004; Santos et al., 2005).

Due to a lack of observational data on brightness temperature magnitude or spatial fluctuations of extragalactic free-free emission, models are highly uncertain - by 2 magnitudes according to some estimates (Cooray & Furlanetto, 2004). Cooray & Furlanetto (2004) used a variety of the current EGff models to conclude that EGff is dominated by sources at $z < 3$. This means that compared to the high redshift production of the 21-cm signal, the free-free frequency spectrum will be easily cleaned. Though there is expected to be an extragalactic free-free signal from the epoch of reionization, it is now expected to be below the noise level of the experiments and therefore insignificant (Cooray & Furlanetto, 2004).

1.5 Foreground Removal Methods

The statistical detection of the 21-cm reionization signal depends on an accurate and robust method for removing the foregrounds from the total signal. Since it is impossible to observe the foregrounds alone this is not a simple task.

The first attempts focused on exploiting the angular fluctuations of the 21-cm signal (e.g. Di Matteo et al., 2002; Oh & Mack, 2003; Di Matteo et al., 2004), but the 21-cm signal was found

to be swamped by various foregrounds. The focus then moved on to the frequency correlation of the foregrounds, with the cross-correlation of pairs of maps used as a cleaning step (Zaldarriaga et al., 2004; Santos et al., 2005). While the foregrounds are expected to be highly correlated on scales of 1 MHz (e.g. Di Matteo et al., 2002; Gnedin & Shaver, 2004), the cosmological signal is expected to be highly uncorrelated on the same frequency scales, allowing frequency correlation to differentiate the signals.

As more methods have emerged, it has become clear that different methods have different advantages and foreground subtraction has become accepted as a three stage process: bright source removal, spectral fitting and residual error subtraction.

1.5.1 Bright Source Removal

Bright source removal is where sources bright enough to contaminate distant areas of the image cube are removed. This naturally occurs as the frequency and spatial response of an array is not a delta function and so there is leakage of source emission into surrounding pixels and frequency channels.

Both man-made and astrophysical bright sources must be considered though it is often assumed that the worst of the radio frequency interference (RFI) from man made structures has been removed prior to the foreground removal stages. Any remaining RFI can be subtracting by using a filter to identify any frequency channels with elevated signal and remove them. For astrophysical sources, the philosophy remains the same, however the sources must be subtracted directly from the visibilities to ensure the sidelobes are accounted for. Unfortunately, even when both types of sources have been removed down to the mK level, there remains unresolved emission which still dominates over the 21-cm signal (Morales et al., 2006).

Di Matteo et al. (2004) utilised a flux cut off to identify and remove both point and extended bright sources, in order to assess the recovery of 21-cm angular fluctuations. They showed that on all angular scales and frequencies the 21-cm fluctuations were dominated by cluster radio haloes and relics. At scales larger than 1 arcminute the subtraction of all bright sources above 0.1 mJy (roughly the expected sensitivity of LOFAR) removed the excess angular fluctuations due to angular clustering of bright sources. At smaller scales, the same flux cut off should reduce the foreground fluctuations down to the 21-cm signal level, ripe for the second stage of the removal process. Fig. 1.27 shows how the domination by radio galaxies and haloes can be drastically reduced using this flux cut off method.

Di Matteo et al. (2002) modelled the contribution of extragalactic unresolved sources, including their clustering tendency and found that, even if resolved point sources above a limiting flux

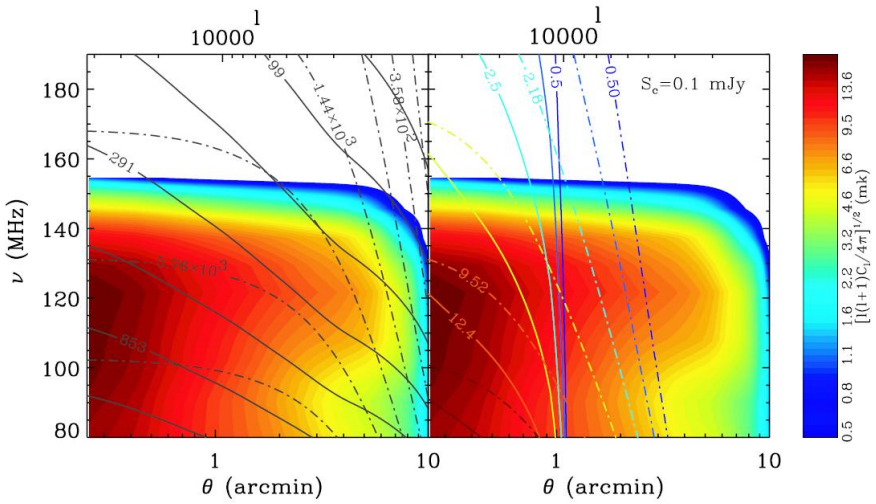

Figure 1.27: The angular power spectrum contours of the 21-cm fluctuations (shaded), radio galaxies (solid) and radio haloes (dot-dash). The original simulations are shown on the left and the result of applying a flux limit of 0.1 mJy is on the right. Taken from Di Matteo et al. (2004).

were removed, the confusion noise of the sources below that flux density would still dominate over the angular fluctuations of the 21-cm signal. This conclusion was supported by a robust analysis by Oh & Mack (2003) of the minimum unresolved source noise bound, necessitating further foreground cleaning methods.

1.5.2 Spectral Fitting

Once the bright sources have been removed, the frequency properties of the foregrounds can be considered (Morales et al., 2006). One of the 'saving graces' of foreground contamination is its smoothness over frequency space. While the foregrounds are expected to be highly correlated on scales of 1MHz, the cosmological signal in comparison is expected to be highly uncorrelated. Cooray & Furlanetto (2004) calculated the cross correlation between the free-free background and the 21-cm signal using current models and found a cross correlations less than a few percent level and concluded that multi-frequency analysis, for free-free emission at least, would be an effective method of cleaning (see also Zaldarriaga et al. (2004)). Di Matteo et al. (2002) found that with a foreground spectral index error of $\Delta\beta = 0.05$ at a 2 MHz resolution, the smoothness of the foreground spectra would allow the detection of a cosmological signal $\approx 6 \times 10^{-4}$ times smaller than the foregrounds.

This foreground fitting over frequency space, or line of sight (LOS) fitting, is by far the most popular in literature and has been numerically shown to be the most optimal method for power spectrum recovery (Liu & Tegmark, 2011). LOS methods can be divided into subcategories of parametric and non-parametric methods. Both aim to find the form of the smooth foreground

function along frequency for each line of sight and subtract this from the total signal leaving residuals of noise, fitting errors and the cosmological signal.

The majority of line of sight methods in literature can be termed parametric as at some point they assume a specific form for the foregrounds (e.g. Santos et al. 2005; Wang et al. 2006; McQuinn et al. 2006; Bowman et al. 2006; Jelić et al. 2008; Gleser et al. 2008; Liu, Tegmark & Zaldarriaga 2009; Liu et al. 2009; Petrovic & Oh 2011; Liu & Tegmark 2011). The usual method is to fit the total observed spectrum along the line of sight with a smooth function such as a nth order polynomial: $\log T_{b,fg}(\nu) = a_0 + \sum_{i=1}^{n} a^i \log \nu^i$. The order of polynomial varies slightly between papers, for example Wang et al. (2006) set $n = 2$ while Jelić et al. (2008) sets $n = 3$. Recently, there has been more consideration into the frequency bandwidth over which a polynomial should be fitted to minimise fitting out the 21-cm signal. While it is fairly standard practice to simply fit the function over the whole frequency range of observation, it has been pointed out that in the late stages of reionization, the ionized bubbles sizes can reach scales of ≈ 1 MHz, introducing a slowly varying component which could erroneously become part of the foreground model (Wang et al., 2013). These authors went on to demonstrate that they could achieve a better 21-cm EoR reconstruction by fitting a polynomial simultaneously in three narrow 2 MHz frequency segments separated in redshift space enough to guarantee no ionized bubbles would be present in both segments.

Despite the successes of the parametric methods, the fact remains that the form of the foregrounds are not definitively known across the frequency range of interest. Too great an assumption of their spectral form risks introducing a large element of uncertainty into the cosmological signal detection. It is with this argument that, more recently, 'blind' methods have been investigated. These allow the data to determine the form of the foregrounds - not assuming any particular shape beforehand. This has obvious advantages for a cosmological era so far not directly observed, but results are often not as promising as parametric results. Arguably, this is common sense since in parametric methods one has modelled the foregrounds based on the simulation knowledge. If these methods were applied to foregrounds of different shape to the accepted form, they would risk suffering a large drop in accuracy.

Harker et al. (2009) considered two non-parametric methods - smoothing splines and Wp smoothing. The former, whereby a piecewise polynomial function with a term to minimize the sum of squared residuals and a term to measure the integrated square curvature, was found to have undesirable limiting behavior. The integrated square curvature term measures the roughness of the data but this can lead to ambiguity, as a nearly straight line with small wiggles imposed could be measured as more smooth than a stronger, smooth curve. As a result, the

idea of penalising changes in curvature was pursued, with roughness measured "apart from inflection points". The algorithm chosen is named for the German word for inflection point, "Wendepunkt", or 'Wp' smoothing (Machler, 1993, 1995). The Wp smoothing method was found to have much more desirable behavior in the limit of light or heavy smoothing and produce statistical results on par with parametric methods (Harker et al., 2009, 2010).

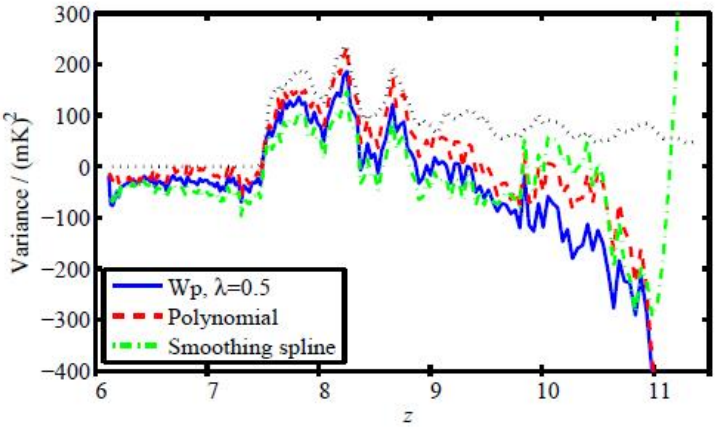

Figure 1.28: The recovered 21-cm variance for two non-parametric methods, Wp smoothing (blue,solid) and a smoothing spline (green,dashdot) and one parametric method, a 3rd order polynomial (red,dash). The simulated 21-cm signal is the black,dotted line. Taken from Harker et al. (2009).

Fig. 1.28 demonstrates the recovery of the 21-cm variance using three different methods: polynomial fitting, smoothing spline (also non-parametric) and Wp smoothing. Non-parametric methods evidently have the potential to recover the 21-cm signal to the same order of accuracy as the parametric polynomial method.

Shaw et al. (2014) looks for a basis set in which the foregrounds are sub-dominant to the 21-cm signal using the Karhunen-Loève transform (e.g. Bond, 1995; Vogeley & Szalay, 1996; Bunn et al., 2003). This transform simultaneously diagonalizes both the signal and the foreground covariance matrices, giving a set of eigenvalues which represent the signal-to-foreground power. Analysis can then be carried out only on modes with eigenvalue over a chosen threshold, or the foreground-dominated modes can be zeroed and the data reverse-transformed for imaging work. This method produced a foreground amplitude reduction of 7 magnitudes leaving a signal-to-noise of 20.

This thesis will introduce two new applications of existing non-parameteric source separation methods - one using statistical independence, FASTICA, and one using discrete wavelets, GMCA, to characterise the foregrounds. These are only two of a field of blind source separation techniques (e.g. SMICA (Delabrouille et al., 2003)) and they were chosen primarily for their ease of

application as a proof-of-principle that the foreground be removed using this type of method. There is most definitely scope for investigation of further blind source separation methods now the proof-of-principle has been clearly set out in this thesis.

1.5.3 Residual Error Subtraction

Once the bright source have been removed and the foregrounds fitted and subtracted along the line of sight, there will remain errors as a result of inaccuracies of both the stages.

Morales & Hewitt (2004) exploited the differences in the foreground and cosmological signal power spectra measured at multiple frequencies to reduce foreground contamination even further. There is no preferred position or direction in space when considering the reionization signal - the expectation of the signal is the same in all directions. Therefore in Fourier space, the 21-cm signal will be spherically symmetric. In comparison, the foregrounds can be shown to have separable-axial symmetry providing a way of identifying the different components of the signal through their power spectra. The angular power spectra methods complement the line of sight methods. The latter is quoted as being better suited for identifying point sources (if not already carried out) and removing areas of high contamination (Wang et al., 2006), whereas the former can then further distinguish the noise and signal and remove very faint contamination.

1.6 Thesis Outline

The Epoch of Reionization is currently an unobserved gap in our cosmological timeline. Though we have managed to constrain parameters such as the start of reionization very roughly using observations from low redshift quasars or observations of the CMB, how reionization progressed, what caused it and when is still in major contention. With the new generation of telescopes such as LOFAR seeing first light and the next generation such as the SKA well into the planning pipeline, the time has come for this gap in our knowledge to be filled.

This thesis sets out two new applications of non-parametric methods for the removal of the foregrounds. In Chapter 2, I introduce Fast Independent Component Analysis (FASTICA), which is a source separation method based on statistical independence, while in Chapter 3, I introduce Generalized Morphological Component Analysis (GMCA) which uses sparsity to separate out the foregrounds. I show that when these methods are applied to a low signal-to-noise simulations consistent with what we expect from LOFAR data, the EoR signal can be extracted to an impressive degree. I discuss the statistics used to make a detection of the EoR and consider wavelets as a de-noising method.

In Chapter 4, I consider the effect of peculiar velocities on the 21-cm observation. I describe a public code which takes real space simulation boxes and produces a light cone adjusted for the peculiar velocities of the hydrogen atoms. Though use of a light cone for analysis is common, the implementation is often incomplete with respect to the peculiar velocities of the hydrogen atoms. I show that when these peculiar velocities are fully considered, the observations maps show significant small scale differences which have the potential to affect any scientific conclusions made from the data.

In Chapter 5 I show that the recent interest in 'foreground avoidance' as an alternative to foreground removal is misguided due to the shape of the Galactic synchrotron radiation in Fourier space. Previous analyses have either used incomplete or unphysical foreground models and concluded that there is an 'EoR window' where the signal dominates over the foregrounds. I show, however, that with a full physical foreground model this window is destroyed completely and can only be recovered after foreground removal. We conclude that, though foreground removal is still essential, foreground avoidance can be used afterwards to find the best area of k-space to measure the power spectrum without bias.

Finally, in Chapter 6, I present the first foreground removal results from the LOFAR-EoR experiment, demonstrating that the techniques developed in this thesis are well applicable to real data. The data contains high levels of systematics and we find that GMCA works well despite this and can in fact be used to identify these systematics. We find that GMCA can separate point source contributions well enough to feed back into the calibration method and improve future point source modelling. Using GMCA, we identify several systematics, such as the action of the primary beam, which will need addressing in future analysis.

Chapter 2

FastICA

This chapter has been published as a scientific paper in Monthly Notices of the Royal Astronomical Society, Volume 423, Issue 3, pp. 2518-2532, 2012.

The method presented here is based on the independent component analysis (ICA) algorithm, FASTICA (Hyvärinen, Karhunen & Oja, 2001). ICA is a method originally designed to separate mixed signals with minimal prior knowledge of the form of the signals. ICA provides us with a foreground removal method which compensates for the fact that we do not know the form of the foregrounds at the exact resolution and frequency range of LOFAR, i.e. a non-parametric method. FASTICA is a versatile tool and has been applied recently in the field of exoplanets (Waldmann, 2012) and CMB foreground removal (e.g. Maino et al. 2002; Maino et al. 2003; Maino et al. 2007; Bottino, Banday & Maino 2008; Bottino, Banday & Maino 2010) with great success motivating its implementation on other cosmological data. The results presented focus on the two main statistical aims of current EoR experiments, namely the recovery of the power spectrum and variance of the cosmological signal.

2.1 The FASTICA method

Introduced in the early 1980s, ICA has established itself as a successful component separation technique with widespread applications. The method relies on the assumption that the multiple elements making up a mixed signal are statistically independent and that the foregrounds are smooth in frequency, since it is this which separates the noise and cosmological signal from the foregrounds statistically.

2.1.1 FASTICA in CMB Data Analysis

FASTICA has been applied to both observed CMB data from a variety of telescopes, and simulated CMB data for the Planck telescope. Early applications to COBE-DMR (Cosmic Background Explorer Differential Microwave Radiometers) data found that foreground separation was not a success with very low signal to noise data (Maino et al., 2003) however was a much more promising technique with enough signal (e.g. by including more frequency channels, such as the Haslam 408 MHz map (Haslam et al., 1982) and DIRBE (Diffuse Infrared Background Experiment) 140 μm map). Their application is of interest due to their investigation of noise. Due to a systematic effect, one of their frequency maps had a different noise distribution to the other frequency channels. This resulted in a spurious component being reconstructed and inaccuracies being introduced into the reconstructed CMB component. The sensitivity of FASTICA to the noise distribution may detract from the suitability of the method for LOFAR-EoR data if the signal-to-noise is too low or the noise distributions are non-uniform across the sky or wildly different for different frequency channels.

Analysis on both 3 and 5 year WMAP (Wilkinson Microwave Anisotropy Probe) data recovered power spectra in agreement with the best estimations of the WMAP team (Maino et al., 2007; Bottino et al., 2010). Similarly, Donzelli et al. (2006) extracted a CMB power spectrum from BEAST (Background Emission Anisotropy Scanning Telescope) data which was in agreement both with other BEAST estimates and the best WMAP estimate.

FASTICA has also been applied to simulated Planck data (Maino et al., 2002). FASTICA performed well and the CMB angular power spectrum was recovered at the per cent level down to small scales, Figure 2.1. As higher signal to noise data has become available, FASTICA has matured into a competitive foreground separation technique - whether stand-alone or used as an estimator for a second stage non-blind method.

2.1.2 The Mixing Model

The general mathematical model for a signal separation problem is called the 'mixing model':

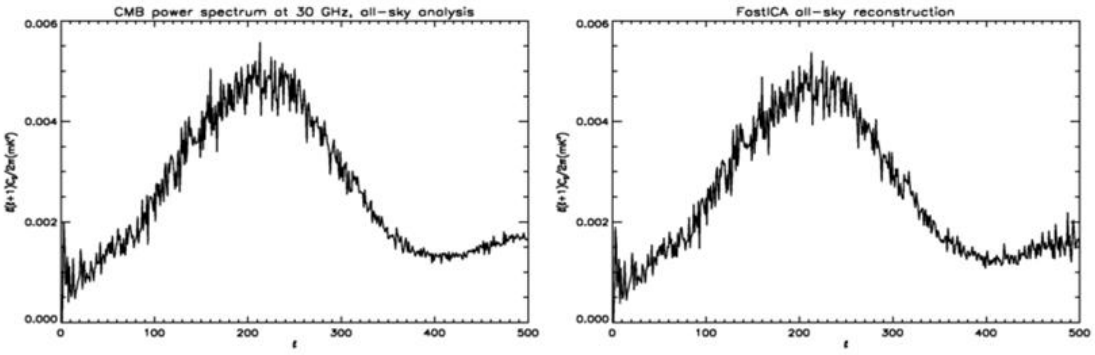

Figure 2.1: Simulated (left) and reconstructed (right) angular power spectrum of the CMB as if observed by Planck at 30 GHz and separated using FASTICA. Taken from Maino et al. (2003).

$$\mathbf{x} = \mathsf{A}\mathbf{s}, \tag{2.1}$$

where $\mathbf{x}$ is a vector representing the observed (mixed) signal, $\mathbf{s}$ is a vector of which the components are assumed mutually independent and A is a mixing matrix to be calculated. For the simulated data used in this work we have maps of 512×512 pixels at 170 different frequencies. Equation 2.1 represents one line of sight where, if m ICs are assumed, the sizes of $\mathbf{x}$, A and $\mathbf{s}$ are [170,1], [170,m] and [m,1] respectively. FASTICA simultaneously considers all lines of sight, so $\mathbf{x}$ and $\mathbf{s}$ are in effect matrices of size [170,512×512] and [m,512×512] respectively. For clarity, we will set out the description as if only one line of sight was being considered but the reader should bear in mind that all lines of sight are simultaneously and independently treated by the algorithm, with A being independent of the line of sight.

It might immediately strike the reader that the model specified here is the noise free ICA model. This is because this implementation makes no effort to model the noise component through the $\mathbf{x} = \mathsf{A}\mathbf{s} + \mathbf{n}$ formulation. Instead one must appreciate that it is the way in which FASTICA is not robust to noisy components that we take advantage of here. Whereas $\mathbf{x}$ will represent the observed signal of foreground, noise and 21-cm signal, $\mathbf{s}$ is considered to be the foregrounds only and we use FASTICA as a way to define the foregrounds. FASTICA ignores the Gaussian or non-smooth spectral components in the observed signal (i.e. the noise and cosmological signal) and we define these by calculating the difference between the original signal and the reconstructed foregrounds. When we specify m ICs, FASTICA reconstructs m ICs relating to the foregrounds only.

To solve Equation 2.1 for $\mathbf{s}$, we seek a linear transform:

$$\mathbf{s} = \mathsf{W}\mathbf{x}, \tag{2.2}$$

where W is a matrix that the ICA method aims to determine assuming the elements of $\mathbf{s}$ are as statistically independent as possible.

FASTICA seeks to estimate W using the concept of mutual information. An outline of the general philosophy behind FASTICA is outlined below, but for a full treatment refer to Hyvärinen (1999) and Hyvärinen et al. (2001).

Let us consider a single component of the signal $\mathbf{s}$:

$$y = \mathbf{w}^T\mathbf{x} = \sum_i w_i x_i, \tag{2.3}$$

where if $\mathbf{w}$ is one of the rows of the inverse of A, y is one of the ICs, s_i. In order to find s_i FASTICA attempts to minimise the Gaussianity of $\mathbf{w}^T\mathbf{x}$. To understand why, we define a vector $\mathbf{z}$:

$$\mathbf{z} = \mathsf{A}^T\mathbf{w}, \tag{2.4}$$

so that we have a weighted sum of the independent signal components:

$$y = \mathbf{z}^T\mathbf{s}. \tag{2.5}$$

The central limit theorem states that the greater the number of independent variables in a distribution, the more Gaussian that distribution will be. $\mathbf{z}^T\mathbf{s}$ is therefore always more Gaussian than any individual s_i. y will be least Gaussian when one, and only one, z_i is non-zero, and in such a case $y = s_i$. Thus by maximising the non-Gaussianity of $\mathbf{w}^T\mathbf{x}$ we find one of the ICs.

In order to estimate and adjust $\mathbf{w}^T\mathbf{x}$ in such a way that its Gaussianity converges to a minimum, the method needs a robust measure of non-Gaussianity. FASTICA favours negentropy as a measure of non-Gaussianity, which is based on the entropy of a variable, $H(y)$:

$$H(y) = -\sum_i P(y = a_i)\log P(y = a_i), \tag{2.6}$$

where a_i are the possible values of y.

Negentropy is then defined as:

$$J(y) = H(y_{\text{gauss}}) - H(y), \tag{2.7}$$

where y_{gauss} is a random Gaussian variable with the same covariance matrix as y. Using the maximum-entropy principle, one can define:

$$J(y) \approx \sum_{i=1}^{n} k_i [E\{G_i(y)\} - E\{G_i(\nu)\}]^2, \tag{2.8}$$

where k_i are positive constants, ν is a Gaussian variable with zero mean and unit variance and G are non-quadratic functions. Though almost any non-quadratic function can be used, the robustness and speed of the FASTICA method can depend on choosing these contrast functions well, with different contrast functions more suited to different scenarios. For this implementation we choose a standard function, $g(u)$ of:

$$g(u) = u \times \exp\left(-\frac{u^2}{2}\right), \tag{2.9}$$

where $g(u) = G'(u) = \frac{dG(u)}{du}$.

Since $\mathbf{s}$ and A are both unknown, FASTICA cannot determine the ICs' magnitudes or order, as we can freely change the order of the components in the mixing model or multiply any of them by a scalar factor which can be balanced out by dividing out elsewhere. As such FASTICA fixes the magnitudes of the ICs by assuming they have unit variance. This is not a problem for our implementation as we are not interested in the magnitudes of the ICs themselves as much as the mixed foreground they define.

2.1.3 Algorithm

Here we summarise the fixed-point FASTICA algorithm for finding one IC (Hyvärinen, 1999; Hyvärinen et al., 2001).

The mixed signal is input along with a parameter representing the number of ICs we assume there to be. A typical choice in this implementation is four ICs.

This data undergoes several preprocessing steps within the FASTICA program. First the data are adjusted to be of zero mean to simplify the algorithm. Then, using a principal component analysis to estimate the eigenvalues and eigenvectors for the data, the data are whitened resulting in the vector $\mathbf{x}$ where the components are uncorrelated, with unit variances.

We wish to choose a unit vector $\mathbf{w}$ such that the non-Gaussianity of $\mathbf{w}^T\mathbf{x}$ is maximized. Under the assumption that the components have unit variance (which for whitened data is equivalent to assuming $||\mathbf{w}||^2$=1) these maxima occur where:

$$E\{\mathbf{x}g(\mathbf{w}^T\mathbf{x})\} - \beta\mathbf{w} = 0 \tag{2.10}$$

is satisfied, where β is a constant. To find the roots of this equation using Newton's method we arrive at the approximate Newton iteration:

$$\mathbf{w}^+ = \mathbf{w} - \frac{[E\{\mathbf{x}g(\mathbf{w}^T\mathbf{x})\} - \beta\mathbf{w}]}{E\{g'(\mathbf{w}^T\mathbf{x})\} - \beta}. \tag{2.11}$$

This iteration is carried out using the algorithm summarised in the following steps (Hyvärinen & Oja, 2000):

1. Choose an initial random weight vector $\mathbf{w}$
2. Let $\mathbf{w}^+ = E\{\mathbf{x}g(\mathbf{w}^T\mathbf{x})\} - E\{g'(\mathbf{w}^T\mathbf{x})\}\mathbf{w}$
3. Let $\mathbf{w} = \frac{\mathbf{w}^+}{\|\mathbf{w}^+\|}$
4. If the old and new values for $\mathbf{w}$ are not converged repeat the process

where g is the derivative and g' is the second derivative of the chosen contrast function G. The use of the contrast function derivatives comes from consideration of where the maxima of the negentropy approximation are obtained. The non-Gaussianity is maximised along the line of sight and across the map simultaneously meaning that the method's constraining power benefits from having more pixels and more frequency maps.

To extend the algorithm to n components requires FASTICA to run simultaneously for n different weight vectors, $\mathbf{w}_1, ...\mathbf{w}_n$ where one $\mathbf{w}_j$ corresponds to $\mathbf{w}$ in the above algorithm. To ensure that the different $\mathbf{w_j x}$ converge to different maxima (i.e. the same IC is not found twice) all the outputs $\mathbf{w_j x}$ must be decorrelated after every iteration.

2.1.4 Why ICA?

One might wonder about the connection between ICA and the well-known statistical method Principal Component Analysis (PCA) (e.g. Jolliffe, 2002). Though the goal of both methods is to find a representation comprising of less redundancy for a given set of data, there are several reasons ICA is a more powerful method. PCA uses the correlations between components to minimize redundancy while ICA uses the 'stronger' concept of independence. While two independent components must, by definition, be uncorrelated, it is not true to say that two uncorrelated components must also be independent. With PCA, there is an emphasis on minimizing the number of components while with ICA minimization is not necessarily the goal but rather is often as a consequence of a data set often being able to be satisfactorily described by few independent components. For a given data set, PCA finds a rotated orthogonal coordinate system in which the components of the data are uncorrelated. By simultaneously maximising the variance and minimizing the covariance of the components, the axes coincide with the principal axes of the

decorrelated data density. The data model for PCA assumes no particular probability distribution and decorrelation is just a linear transform, whereas for ICA, the independent component model is assumed to consist of non-Gaussian and statistically independent components. While PCA is often a powerful method for Gaussian, linear data that can be easily described by second order statistics such as variance, it is not so effective for non-Gaussian, noisy data which cannot be easily described by variance alone. Source separation is an after thought for PCA - its main aim is simply to define an orthogonal basis set whereby the data can be described as projections of maximal variance. In contrast, ICA aims to separate out sources but cannot rank the 'importance' of these components as variance cannot be determined. The data which we are using is noisy and non-Gaussian and we need an extremely accurate foreground model in order to separate out the 21-cm signal. We therefore find ICA a more powerful method, though in actual fact PCA is used within the code to form a starting point for finding independent components since decorrelation is a necessary attribute of independence.

2.1.5 Our Implementation

We make use of the C++ implementation of FASTICA provided by the IT++ library[1]. Our foreground subtraction proceeds in the following steps:

1. Read in the simulation data cube and specify the number of foreground ICs for FASTICA to model.

2. Call FASTICA to calculate the mixing matrix and ICs of the foregrounds.

3. Reconstruct the foregrounds by performing a multiplication of the mixing matrix, which is common to all lines of sight, with the vector of ICs for each line of sight.

4. Find the difference between the reconstructed foreground cube and the input cube. This residual cube should equal the cosmological signal, noise and and any foreground fitting errors.

Statistical tests can then be carried out on the residuals cube to determine if the 21-cm signal is recoverable after the foreground removal process.

It is worth reiterating once more as it such an important point: the ICs referred to in the ICA methodology as applied here are the ICs making up the foregrounds - the cosmological signal and noise are at no point modelled or even taken into account by this FASTICA implementation.

[1] http://itpp.sourceforge.net/devel/fastica_8cpp.html

2.2 Simulated EoR Data

21CMFAST (Mesinger & Furlanetto 2007; Mesinger, Furlanetto & Cen 2011) is used to simulate the cosmological signal. 21CMFAST calculates the density and velocity field initial conditions in Lagrangian space then uses 1st order perturbation theory (Zel'dovich, 1970) to move each matter particle and approximate gravitational collapse. The Zel'dovich approximation is also used to calculate the approximate velocity field as a function of redshift. The ionization fields are calculated using the semi-numerical codes of Zahn et al. (2011) and excursion set formalism (Furlanetto et al., 2004) is used to identify HII regions without explicitly resolving individual halos. Despite treating physical processes with approximate methods, 21CMFAST has shown good agreement with numerical simulations on scales above 1 Mpc. We simulate 170 frequency maps between 115 and 199.5 MHz with spacings of 0.5 MHz. The maps consisted of 512^2 pixels representing a $10^\circ \times 10^\circ$ observation window, or a resolution of 1.17 arcminutes per pixel. Since an interferometer like LOFAR is insensitive to the mean value of the brightness temperature, we use mean-subtracted maps.

2.2.1 Foregrounds

Though there have been foreground observations at frequencies relevant to LOFAR using WSRT (Bernardi et al., 2009, 2010) the foreground contamination at the frequencies and resolution of LOFAR remains poorly constrained. As a result, foreground models directly relevant for this chapter rely on using constraints from observations at different frequency and resolution ranges. These constraints are used to normalize the necessary extrapolations made from observations to create a model relevant for LOFAR-EoR observations.

In general, the foreground components are modelled as power laws in 3+1 dimensions (i.e. three spatial and frequency) such that $T_\mathrm{b} \propto \nu^\beta$ (e.g. Shaver et al., 1999; Ali et al., 2008; Jelić et al., 2008, 2010).

The foreground simulations used in this chapter are obtained using the foreground models described in Jelić et al. (2008, 2010). The foreground contributions considered in these simulations, Fig. 2.2, are:

1. Galactic diffuse synchrotron emission (GDSE) originating from the interaction of free electrons with the Galactic magnetic field. Incorporates both the spatial and frequency variation of β by simulating in 3 spatial and 1 frequency dimension before integrating over the z-coordinate to get a series of frequency maps. Each line of sight has a slightly different power law.

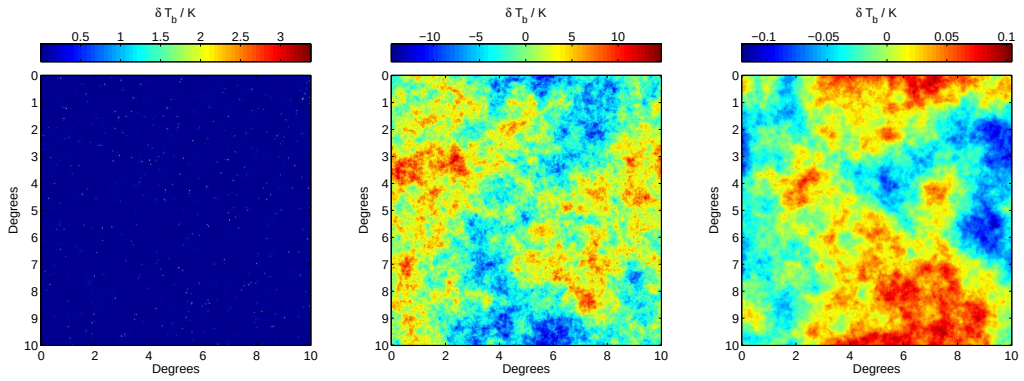

Figure 2.2: The simulated extragalactic, Galactic synchrotron and Galactic free-free foregrounds at 150 MHz (from left to right).

2. Galactic localised synchrotron emission originating from supernovae remnants (SNRs). Together with the GDSE, this emission makes up 70 per cent of the total foreground contamination. Two SNRs were randomly placed as discs per 5° observing window, with properties such as power law index chosen randomly from the Green (2006) catalog[2].

3. Galactic diffuse free-free emission due to bremsstrahlung radiation in diffuse ionised Galactic gas. This emission contributes only 1 per cent of total foreground contamination, however it still dominates the 21-cm signal. The same method as used for the GDSE is used to obtain maps, however the value of β is fixed to -2.15 across the map.

4. Extragalactic foregrounds consisting of contributions from radio galaxies and radio clusters and contributing 27 per cent of the total foreground contamination. The simulated radio galaxies assume a power law and are clustered using a random walk algorithm. The radio clusters have steep power spectra and are based on a cluster catalogue from the Virgo consortium[3] and observed mass-luminosity and X-ray-radio luminosity relations.

Unlike Jelić et al. (2008, 2010), this chapter does not consider the polarisation of the foregrounds. The foregrounds simulated here are up to five orders of magnitude larger than the signal we hope to detect. Since interferometers such as LOFAR measure only fluctuations about the mean, foreground fluctuations dominate by 'only' three orders of magnitude.

2.2.2 Noise

For each frequency, a LOFAR measurement set was filled with Gaussian noise in the *uv* plane. This was then imaged to create a real-space image, the root mean square of which can be normalized to the value as given by the prescription described above in Section 1.3.1. For

[2]http://www.mrao.cam.ac.uk/surveys/snrs/
[3]http://www.virgo.dur.ac.uk/

example the noise sensitivity at 150 MHz for an integration time of 600h and a frequency spacing of 0.5 MHz is 64 mK. The 170 noise maps are uncorrelated over frequency - i.e. a different noise realization was used to fill the measurement set for each frequency.

2.2.3 Dirty Images

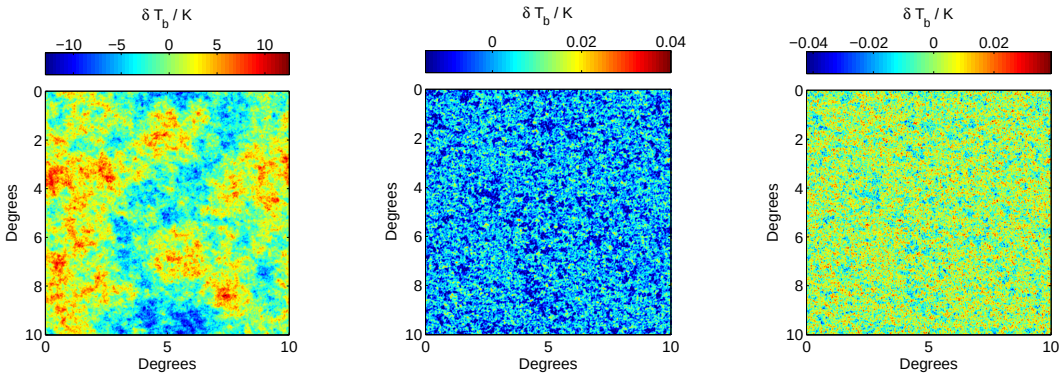

Figure 2.3: Left: The total contribution of the simulated foregrounds. Middle: The simulated cosmological signal. Right: The recovered cosmological signal after FASTICA has been applied to the data and the noise subtracted from the residuals. All data are at 150 MHz have been convolved with the PSF.

The success of an interferometer such as LOFAR is highly dependent on how *uv* space is sampled. The particular pattern of *uv* sampling forms a beam which affects how the components such as the foregrounds are seen by the interferometer. Dirty images were simulated by convolving the clean data cubes with the point spread function (PSF) of the LOFAR set up used to simulate the noise in the previous section, Fig. 2.3.

The PSF used for creating dirty images (and for creating the noise as described in the previous section) was chosen to be the worst in the observation bandwidth - i.e. the PSF at 115 MHz. In observations the synthesized beam decreases in size with increasing frequency, causing point source signals to oscillate with the beam, producing a foreground signal with an oscillatory signal very much like that of the 21-cm signal. However, this mode-mixing contribution has been found not to threaten the 21-cm recovery and have a power well below the 21-cm level (Bowman et al. 2006; Liu, Tegmark & Zaldarriaga 2009).

Once the foregrounds and 21-cm signal have been adjusted for *uv* sampling, the three component cubes are added together. The components of the total $\delta T_{\rm b}$ along a random line of sight are shown in Fig. 2.4.

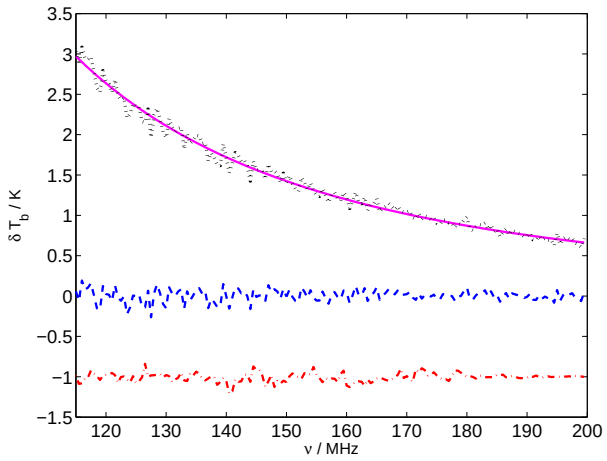

Figure 2.4: The redshift evolution of the simulated cosmological signal (red; dash dot), foregrounds (pink;solid), noise (blue; dash) and total combined signal (black; dot). All components have undergone the PSF convolution. Note the 21-cm signal has been amplified by 10 and displaced by -1K for clarity.

2.2.4 Fourier Transformed Data

The FASTICA method was implemented separately with data both in real and Fourier space. For the latter method, the fiducial image cube was 2D Fourier transformed at each frequency to create a Fourier data cube. The real and imaginary cubes were then processed separately with FASTICA before the output cubes being recombined and reverse Fourier transformed to obtain the ICs in real space. Unless otherwise stated all results refer to real space implementation.

2.3 Results

2.3.1 The Independent Components

The top panel of Fig. 2.5 shows the four ICs found by FASTICA for a clean data cube. These ICs are the columns of the mixing matrix, A. For comparison we show the line of sight $\delta T_{\mathbf{b}}$ of the simulated foreground contributions in the bottom panel of Fig. 2.5.

We can see that no single independent component corresponds to any one single foreground contribution, even when processing a clean data cube. Instead, the independent components are all a mixture of the Galactic free-free, Galactic synchrotron and extragalactic foregrounds. While in ICs 2 and 4 the presence of Galactic synchrotron is obvious, in the other components the combination of the contributions is not so clear. It is also worth noting that while IC4 shows a significant contribution from Galactic synchrotron, it is inverted. FASTICA can only determine the ICs up to a multiplicative constant and so the sign and magnitude of the components are irrelevant.

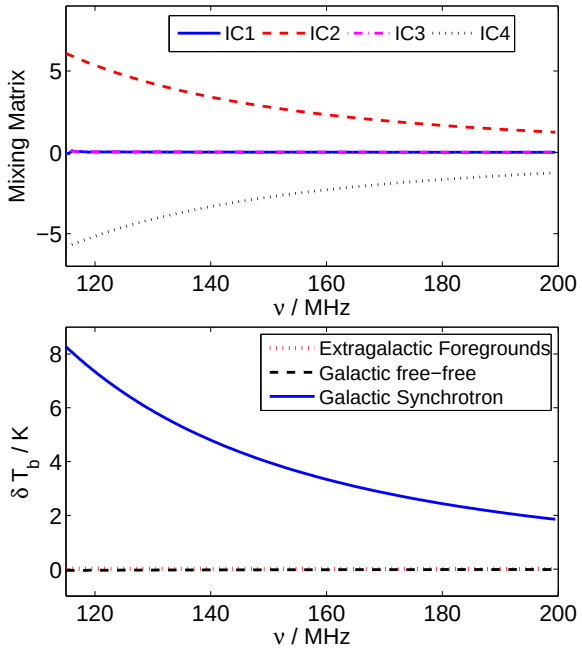

Figure 2.5: In the top panel we show the four columns of the mixing matrix representing the four ICs. The brightness temperatures of the foreground contributions along a random line of sight are shown in the bottom panel. We see that the ICs are each a scaled mixture of the foreground contributions.

The coefficients of the ICs are stored in the matrix `s` and are presented in Fig. 2.6. We can compare these coefficients to the maps of the foreground contributions, Fig. 2.2. We see that all four coefficients are a mixture of the contributions as expected.

In this thesis we are concerned only with the foreground model definition as a whole, in order to separate out the cosmological signal and noise. However, it is worth noting that the way in which FASTICA and, as we will see later, GMCA, defines the independent components of the foregrounds could be of great interest to certain scientific communities. The individual components may produce interesting science for those interested in the independent processes responsible for creating the foregrounds for example. Though I will not pursue this in this thesis, one should bear in mind that one person's noise is another person's signal.

2.3.2 Fitting Errors and Variance

We will first discuss the FASTICA results on the simulation where the data cube has been convolved with the PSF, the data processing is carried out in real space and four ICs are assumed. The word 'simulated' is used to refer to the input maps and 'reconstructed' is used for the estimates resulting from FASTICA. The total input signal is separated into reconstructed foregrounds and residuals. The residuals are the difference between the total input signal and the reconstructed foregrounds.

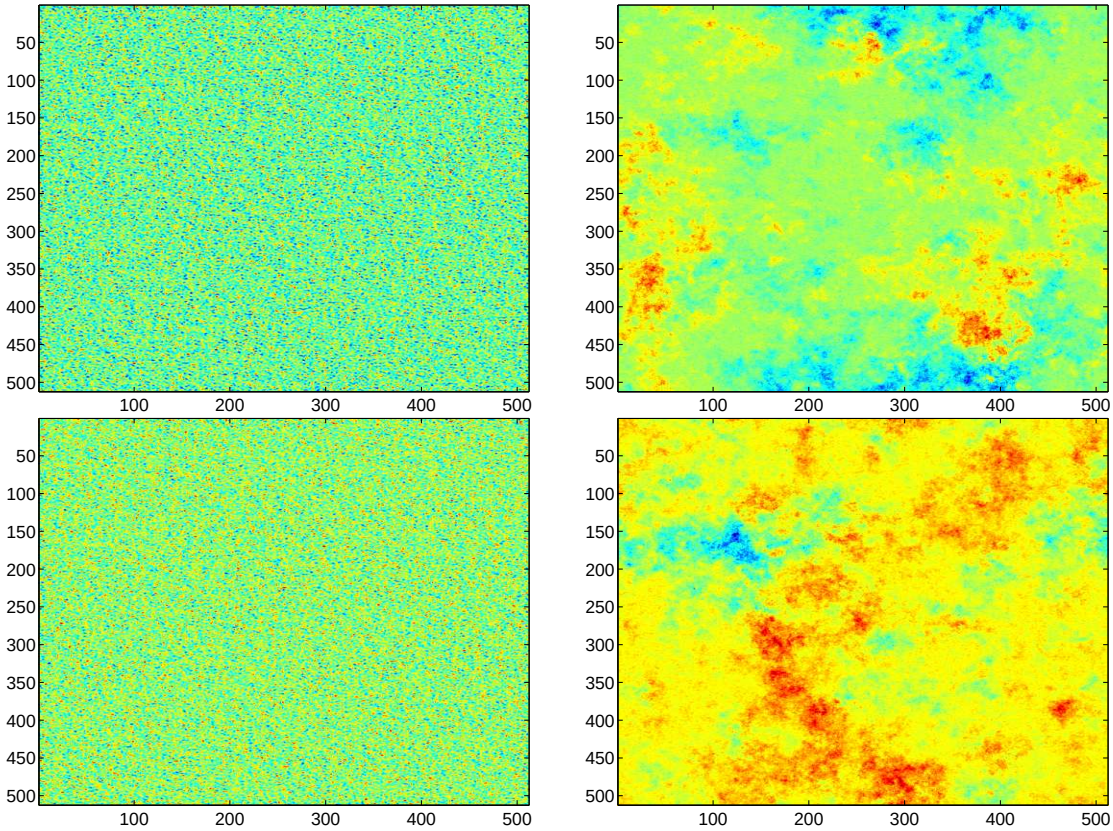

Figure 2.6: The four IC coefficient maps making up $\mathbf{s}$ when FASTICA processes the clean data cube, in reading order.

To evaluate the accuracy of the foreground fitting by FASTICA, we calculated the foreground fitting error for each pixel:

$$\text{fitting error} = \frac{\text{fg}_{\text{reconstructed}} - \text{fg}_{\text{simulated}}}{\text{fg}_{\text{simulated}}} \times 100.0. \tag{2.12}$$

In Fig. 2.7 we plot the Pearson correlation coefficient between the foreground fitting errors and foregrounds (top) and between the foreground fitting errors and the noise (bottom). The Pearson correlation coefficient between two data sets a and b is defined as:

$$r = \frac{\sum_i (a_i - \bar{a})(b_i - \bar{b})}{\left[\sum_i (a_i - \bar{a})^2 \sum_i (b_i - \bar{b})^2\right]^{\frac{1}{2}}}, \tag{2.13}$$

where $\bar{a}$ is the mean of the data set a, $\bar{b}$ is the mean of the data set b and the measure is normalized such that $r = \pm 1$ for perfect correlation/anti-correlation.

We see that there is very little correlation between the foreground maps and the foreground fitting errors, with around six magnitudes more correlation between the noise maps and the foreground fitting errors.

To get a representation of the foreground fitting error over an entire map, the rms error of the fitted foregrounds was calculated, Fig. 2.10. It should be noted that this error takes into account all scales - including those with a disproportionate error as will be seen in the power spectra. The rms difference between the simulated and reconstructed foregrounds was calculated over all 512^2 lines of sight for each frequency. Also, an rms error for each map was calculated using only 68% of the pixels - with the pixels of lowest error selected first. When the outlier pixels are discounted we find that the rms error is below 10 mK for the majority of the frequency range. This is still high enough to be of concern as the 21-cm signal is itself of order tens of mK, however the inclusion of all scales means this is a worst case scenario.

For a statistical detection of the Epoch of Reionization, LOFAR aims to detect a non-zero variance after the noise and foregrounds have been accounted for. We begin by combining the simulated noise and simulated 21-cm signal and taking the variance of this signal. This can then be compared to the variance of the FASTICA residuals - Fig. 2.8. The residual variance is recovered at all but the smallest frequencies. At frequencies below 120 MHz (or $z > 10.8$) the variance is significantly underestimated, probably as a result of foreground overfitting - the leakage of noise power into the estimated foreground power. This failure at very low frequencies is hardly surprising considering that this is where the noise and foregrounds are at their strongest.

We subtract the variance of the simulated noise directly from the variance of these residuals:

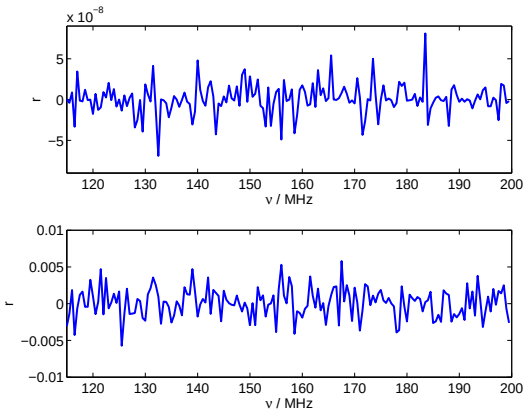

Figure 2.7: a) The Pearson correlation coefficient between the foreground maps and foreground fitting errors. b) The Pearson correlation coefficient between the noise maps and foreground fitting errors.

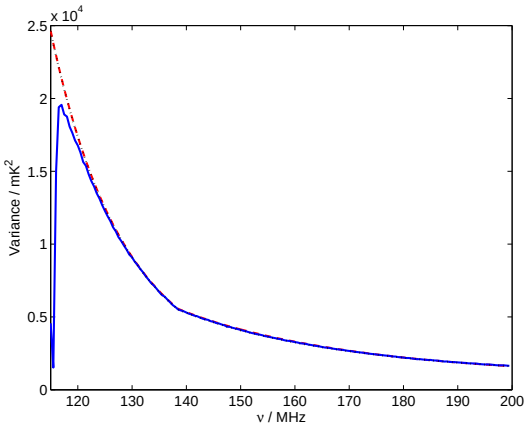

Figure 2.8: The variance across the combined simulated cosmological signal and noise (red, dash), noise alone (black, dot) and residuals (blue, solid).

var(reconstructed 21-cm) = var(residuals) - var(noise). This is a fair assumption as we should be able to look at the data in narrow frequency bins and estimate the statistics (e.g. variance and power spectrum) of the noise to a very high accuracy.

We find that the recovered 21-cm variance, Fig. 2.9 top-left, is not robust to small scale power in the original signal. By removing the noise simulation maps manually from the residual maps in order to get crude maps of the recovered 21-cm signal, excess small scale power is evident, Fig. 2.3. We note that we do this direct noise subtraction for a crude visual inspection only and this would of course not be possible with real data. The excess power is most likely due to FASTICA not being robust to the small scale power (noise) in our data, allowing it to leak into the reconstructed foregrounds. It was found that by Fourier filtering the data to entirely remove k modes above a threshold corresponding to a multiple of the PSF scale, the variance recovery was significantly improved. A very good recovery occurs with filtering out scales below 5 PSF scales (Fig. 2.9 bottom-right).

At the extremes of the frequency range the reconstructed variance increasingly diverges from that of the simulated 21-cm. Both the noise and the foregrounds are at their largest at lower frequencies meaning that both fitting errors and noise leakage is likely to be largest here, leading to less accurate 21-cm reconstruction. Similarly, at the larger frequencies, the 21-cm signal is almost non-existent making an accurate reconstruction difficult when swamped with fitting errors and noise.

This variance calculation was also carried out on a data cube where the residual and noise maps were smoothed from a 512^2 grid to a 256^2 grid before the same variance calculation was carried out above and compared to the variance of a smoothed simulated 21-cm map. The curves

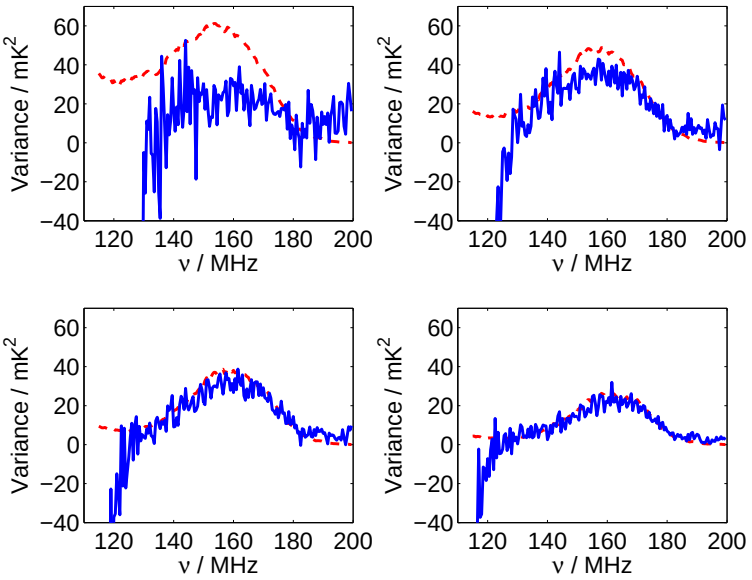

Figure 2.9: The variance across the simulated (red; dash) and reconstructed 21-cm maps (blue; solid) for the fiducial data and data which has had Fourier filtering of modes below 2,3 and 5 PSF scales (in reading order).

are, as expected, slightly smoother however the trend and conclusions remain the same.

Varying the Number of ICs

The FASTICA algorithm requires specification of the number of ICs to be used in the reconstructed foreground model. Though we have modelled the various foreground contributions, it is not a trivial task to determine how these depend on each other and to what degree. To test the sensitivity of our results to the number of ICs chosen we calculate the rms error and variance recovery for IC numbers of 2, 4 and 6 in Fig. 2.10 and Fig. 2.11.

We see that small variations in the number of ICs does not endanger the statistical recovery of the 21-cm signal. For the remainder of this chapter, four ICs are assumed.

2.3.3 Power Spectra

Together with the variance, EoR experiments aim to recover the power spectrum of the cosmological signal over a broad range of frequencies.

Different effects are important for modes parallel and perpendicular to the line of sight. For example, consider the scenario where the foregrounds have been under-fitted by a constant over the frequency range. This offset will not be evident in the 1D power spectrum of the residuals, however will be evident in the angular power spectrum if that constant is dependent on line of sight. Thus it has been argued by Harker et al. (2010) that for LOFAR data, the separate calculation of 1D and 2D power spectra has its advantages. However this does not consider

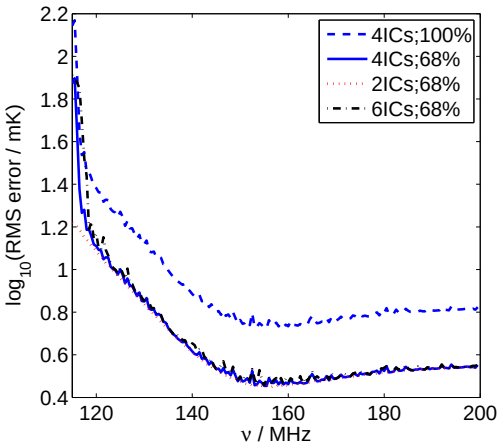

Figure 2.10: The rms error of the 4 IC reconstructed foregrounds for when all pixels are considered (blue;dash) and when only the middle 68 per cent of the error distribution is included (blue;solid). Also, the rms errors of the reconstructed foregrounds for FASTICA applied according to models with 2 (red; dot) and 6 (black; dashdot) ICs, with only the middle 68 per cent of the error distribution included.

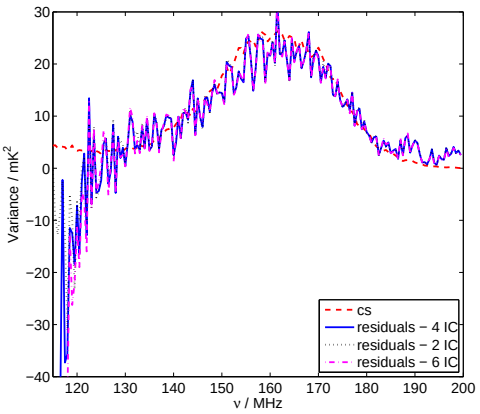

Figure 2.11: The variance across the simulated (red; dash) and reconstructed maps at each frequency, for the FASTICA algorithm run with the assumption of 2 (black; dot), 4 (blue; solid) and 6 (pink; dot dash) ICs. The data has been Fourier filtered at the 5 PSF scale.

modes neither parallel or perpendicular to the line of sight and as such we calculate 2D and 3D power spectra. We note here that we only performed one simulation of the cosmological signal so the power spectrum error bars relate to this specific realisation of the density field.

Angular Power Spectra

The angular power spectrum of a map at a single frequency is calculated by 2D Fourier transforming that map and binning the pixels according to Fourier scale, k. The power at any particular k, $\langle\delta(k)\delta^*(k)\rangle$ is the average power of all the uv cells in the bin centering on k. The error on the point for a particular bin, k_i are calculated as $\alpha_i = \frac{\langle\delta(k_i)\delta^*(k_i)\rangle}{\sqrt{n_{k_i}}}$ where n_{k_i} is the number of uv cells that reside in that k bin. The power spectra were averaged over frequency bandwidths of 2.5 MHz and all frequencies quoted are the middle frequency of the bandwidth. The power spectrum of the reconstructed cosmological signal is calculated by subtraction of the noise power spectrum from the FASTICA residuals power spectrum. The error on the simulated 21-cm power spectrum is added in quadrature with the error on the noise to reflect the error on the reconstructed 21-cm power spectrum. Note that we assume Gaussianity whereas the 21-cm signal is not Gaussian and also we calculate the error bars from the power of a single realization rather than over an ensemble of simulations. We ask the reader to bear in mind that these error bars might be considered incomplete because of this.

The quantity actually plotted is $\Delta^2_{2D}(k) = \frac{Ak^2\langle\delta(k)\delta^*(k)\rangle}{2\pi}$ where A is the area of the simulation map.

Fig. 2.12 shows the extent to which the FASTICA method can recover the 21-cm angular power spectrum. Overall, the 21-cm power spectrum is convincingly recovered across the redshift range. Any points where the power of the residuals are below the power of the noise are omitted, as this leads to an unrealistic negative reconstructed 21-cm power. As such, there is a lack of data at small scales indicative of noise leakage into the foregrounds.

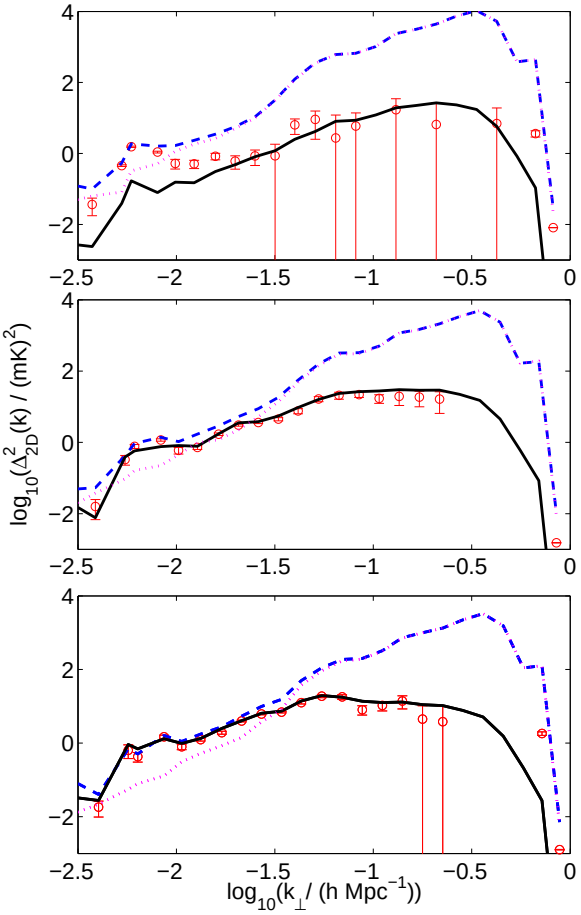

Figure 2.12: 2D power spectrum of the simulated 21-cm signal (black;solid), reconstructed 21-cm signal (red;points), residuals (blue,dash) and noise (pink,dotted) at 131 MHz, or z=9.84, 151 MHz, or z=8.40 and 171 MHz, or z=7.30 from top to bottom. Any error bars extending to below the x axis in linear space are shown extending to negative infinity in log space.

3D Power Spectra

To calculate the 3D power spectra we divide the cube into sub-bands of 8 MHz to avoid signal evolution effects. For each sub band we then carry out a 3D Fourier transform and calculate the 3D power spectrum in spherical annuli in Fourier space. The frequencies attached to the plots correspond to the centre of the sub band plotted. What we actually plot is the quantity

$\Delta^2_{3D}(k) = \frac{Vk^3\langle\delta(k)\delta^*(k)\rangle}{2\pi^2}$ where V is the volume.

We find the same accurate recovery on scales above a few multiples of the PSF but with smaller errors due to the larger amount of data evaluated, Fig. 2.13.

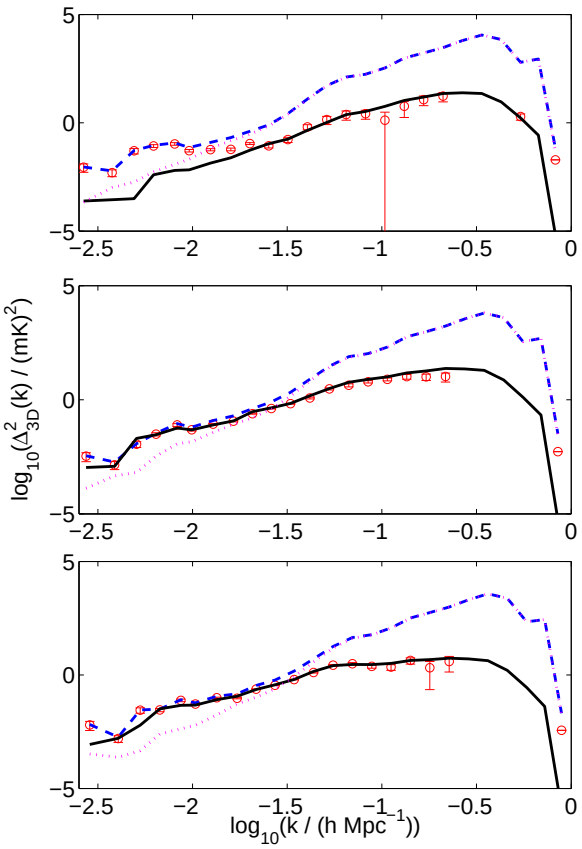

Figure 2.13: 3D power spectrum of the simulated 21-cm signal, reconstructed 21-cm signal, residuals and noise at 135 MHz, or z=9.51, 151 MHz, or z=8.40 and 175 MHz, or z=7.11 over an 8 MHz sub band. Any points where the power of the residuals are below the power of the noise are omitted, as this leads to an unrealistic negative reconstructed 21-cm power. The error bars and linestyles are as described in Fig. 2.12.

Cross Correlation Power Spectra

To try and retrieve a more robust reconstructed 21-cm power spectrum, the cross correlation of two data cube realisations was carried out. Two independent noise realisations were created and combined with identical foregrounds and 21-cm signals to create two data cubes with the only difference being the noise realisation. FASTICA was performed on both of these cubes separately, resulting in two residual files. We carried out cross correlations on the two reconstructed cosmological signals, the two residual files and the two 21-cm fitting error estimates (i.e. reconstructed 21-cm minus the simulated 21-cm). By cross correlating the two residual signals consisting of two different noise realizations, we increase the amount of noise that will drop out in the noise cross terms, hopefully resulting in a more accurate power spectrum recovery when applied to real

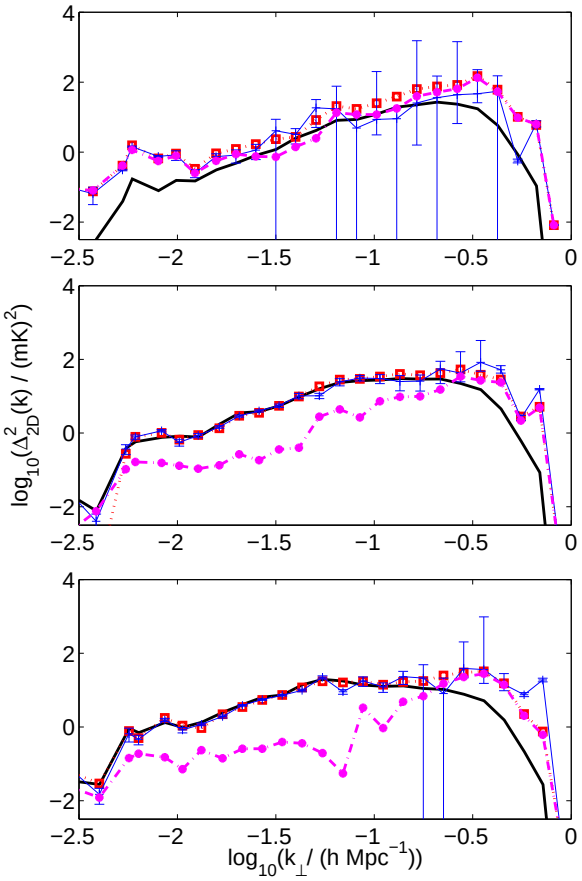

Figure 2.14: Cross correlations of the two residuals (blue,cross), two reconstructed 21-cm signals (red,square), two fitting error estimates (pink,circle) and the auto-correlation of the simulated (black,solid) at 131 MHz, 151 MHz and 171 MHz. Only one set of error bars is shown for clarity.

data. However we do not expect a significant improvement in comparison to our 2D autospectra here as we have already assumed a perfect knowledge of the noise spectrum. Instead we do this as an example of a more robust method of power spectrum recovery for real data. Note that since correlations can be negative, it is the absolute value that is plotted. The errors bars on the cross spectra are calculated in the same way as for the auto spectra, namely: $\alpha_i = \frac{\langle \delta(k_i)\delta^*(k_i)\rangle}{\sqrt{n_{k_i}}}$ where n_{k_i} is the number of pixels that resided in that k bin. The power spectra recovered as a result of this process are shown in Fig. 2.14.

The cross correlations were also carried out on two noise realizations which were adjusted to have roughly 10 times the signal to noise ratio of the LOFAR realizations (similar to what is hoped for SKA), Fig. 2.15. We see that with a higher signal to noise ratio the auto and cross correlation estimates are significantly improved.

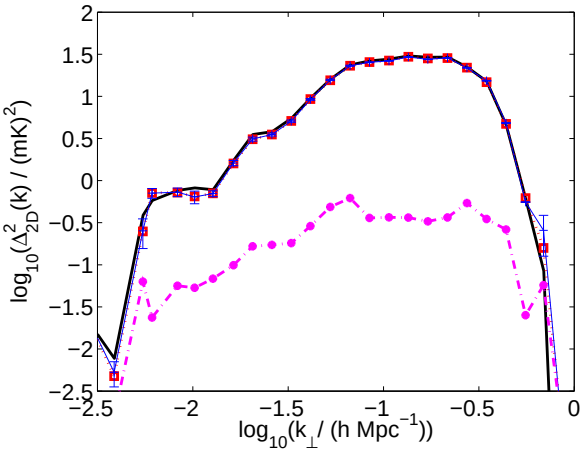

Figure 2.15: Cross correlations of the two residuals (blue,cross), two reconstructed 21-cm signals (red,square), two fitting error estimates (pink,circle) and the auto-correlation of the simulated (black,solid) and reconstructed cosmological signal (for one realization) (red,circles) at 150 MHz. The noise realizations involved have been adjusted to be 10 times smaller than the LOFAR realizations.

2.3.4 Kurtosis and Skewness

Skewness and kurtosis have both been suggested as alternative statistics for the 21-cm detection due to their increased robustness to fitting errors compared to the variance (see Section 1.2.6). We present the skewness and kurtosis of the residuals cubes, Fig. 2.16 and Fig. 2.17.

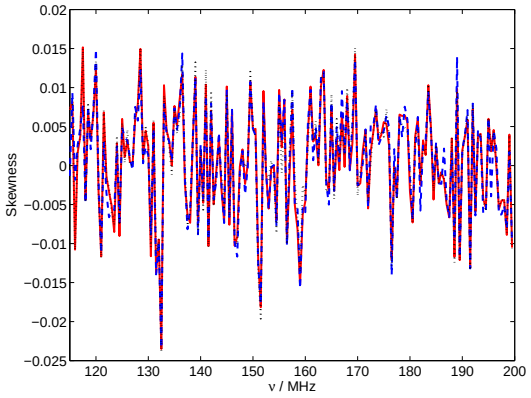

Figure 2.16: The skewness of the simulated 21-cm signal plus noise (red), noise alone (black;dot) and residual maps (blue; dash).

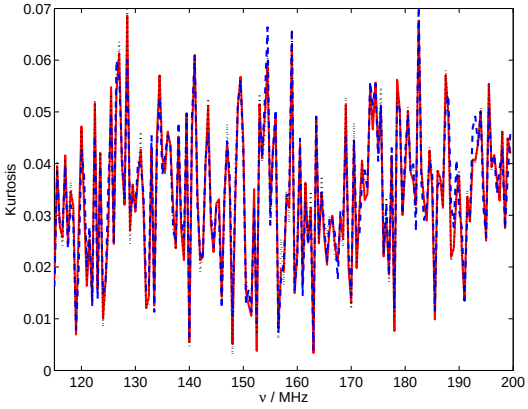

Figure 2.17: The kurtosis of the simulated 21-cm signal plus noise (red), noise alone (black;dot) and residual maps (blue; dash).

The skewness and kurtosis in the residual images is recovered very well, accurately matching the simulated noise plus 21-cm signal skewness and kurtosis across the frequency range.

We now manually subtract the noise cube from the residuals cube and plot the kurtosis/skewness of this reconstructed 21-cm signal, Fig. 2.18 and Fig. 2.19. This amounts to assuming that we know the noise distribution perfectly which, though not viable for real data,

allows us an insight into the recovered signal.

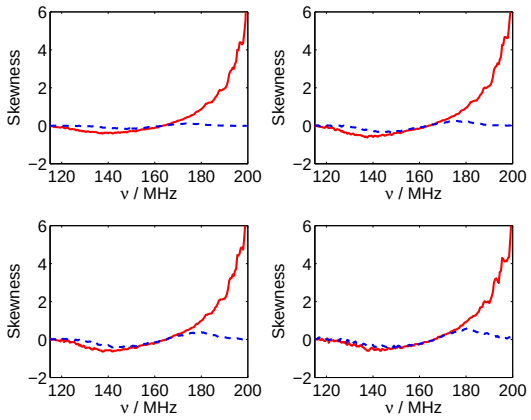

Figure 2.18: The skewness of the simulated 21-cm signal (red; solid) and reconstructed 21-cm maps (blue; dash) for the fiducial signal and for different levels of Fourier filtering: 2,3 and 5 PSF scales (in reading order). We find the same form for the skewness as Fig.1.17.

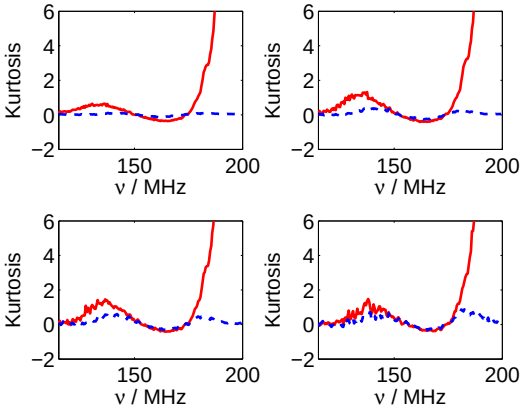

Figure 2.19: The kurtosis of the simulated 21-cm signal (red; solid) and reconstructed 21-cm maps (blue; dash) for the fiducial signal and for different levels of Fourier filtering: 2,3 and 5 PSF scales (in reading order). We find the same form for the kurtosis as Fig.1.18.

We see that the skewness dip at low frequencies is only convincingly recovered with a high level of Fourier filtering. At the high frequencies, where the cosmological signal is very small, the skewness is not recovered. The dip in kurtosis at frequency 165 MHz is somewhat recovered for Fourier filtering below 2 PSF scales while it takes up to 5 PSF scales of k space filtering before the peak centred around 140 MHz is recovered. For both statistics there is a divergence above frequencies of 180 MHz, where the cosmological signal is very small.

All of the results presented in this section are for FASTICA being implemented in real space. While an implementation was carried out in Fourier space, the general conclusions for all results remained the same. Though there were small local variations in, for example, the recovered power spectrum points or kurtosis values, the graphs were for all intents and purposes duplications of the real space versions and are therefore not reproduced here.

2.4 Sensitivity of FASTICA

So far in this chapter we have assumed that the full field of view and frequency bandwidth of the simulation is input to FASTICA but we must also consider whether this method will be as successful under more constrained observations.

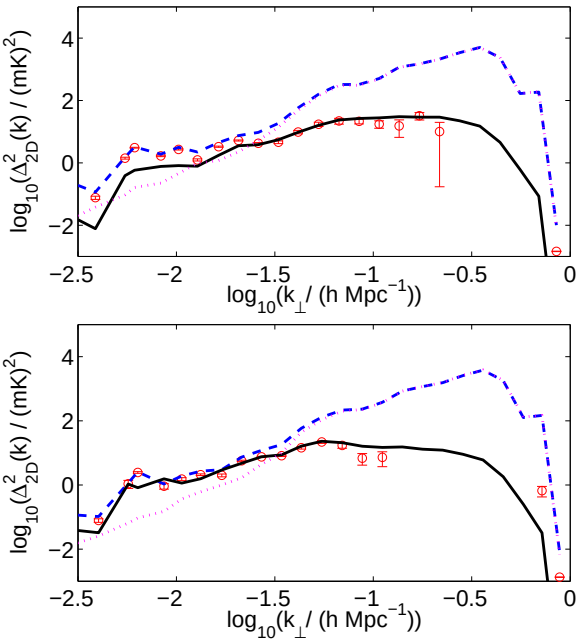

Figure 2.20: 2D power spectrum of the simulated 21-cm signal (black;solid), reconstructed 21-cm signal (red,points), residuals (blue,dash) and noise (pink,dotted) at 151 MHz (top) and 171 MHz (bottom). The graphs are for data cubes of bandwidth 42.5 MHz and ranges 115 MHz - 157 MHz and 157.5 MHz - 199.5 MHz respectively. Any error bars extending to below the x axis in linear space are shown extending to negative infinity in log space.

2.4.1 Bandwidth of Observation

Firstly, we assess the sensitivity to bandwidth and split the dirty data cube into two smaller cubes of bandwidth 42.5 MHz, one from 115 MHz - 157 MHz and one from 157.5 MHz - 199.5 MHz. We perform FASTICA on each of these separately and measure the 2D power spectrum as described previously, Fig. 2.20.

We can see that even for slices at the end of the cube frequency range (i.e. Fig. 2.20, top shows a slice 6 MHz from the end of that cube) the 21-cm reconstruction is successful. The general degradation is not unexpected as the more data a separation technique has to fix the foregrounds, the better the reconstruction will be. We conclude that the method is not sensitive to the point of endangering the signal recovery, but larger bandwidths are preferable.

2.4.2 Noise

Despite the encouraging results so far, the evidence of noise leakage in the recovered maps (Fig. 2.3) and the variance recovery (Fig. 2.9) motivates us to consider the sensitivity of the 21-cm statistical recovery when there is increased noise in the observation.

We have seen that by much reducing the expected LOFAR noise to expected SKA levels, the 21-cm cross correlations power spectrum recovery is extremely accurate, Fig. 2.15. For

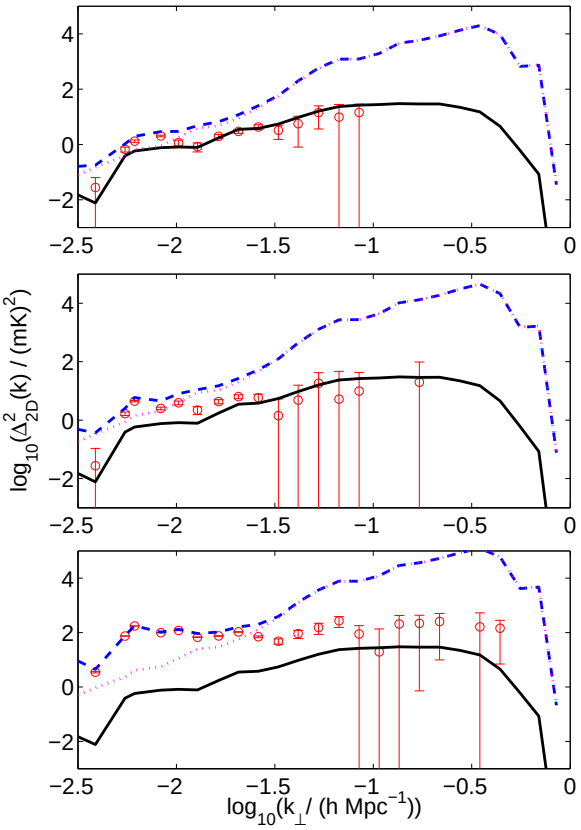

Figure 2.21: 2D power spectrum of the simulated 21-cm signal (black,solid), reconstructed 21-cm signal (red,points), residuals (blue,dash) and noise (pink,dotted) at 151 MHz, or z=8.40. From top to bottom, the noise simulation is set at twice, three times and five times the expected LOFAR noise respectively.

completeness, here we set up some 'worst case' scenarios, whereby we measure the recovered power spectra in the presence of two times, three times and five times the expected LOFAR noise, Fig. 2.21.

As expected, the more noise present, the less accurately the 21-cm power spectrum is recovered. For twice the expected level of noise we see the larger scales beginning to be overestimated, the extent of which worsens for three times the expected noise. For five times the expected amount of noise the power spectrum is significantly overestimated across the scale range. However we must stress that the fact that the 21-cm power spectrum is recovered across a wide scale range, even in the presence of twice the noise levels expected, can only be seen as extremely promising.

2.4.3 Field of View

In this chapter we have assumed a 10°× 10° field of view, which is at the upper limit of what we can expect for LOFAR observations. To explore the sensitivity of the analysis to the field of

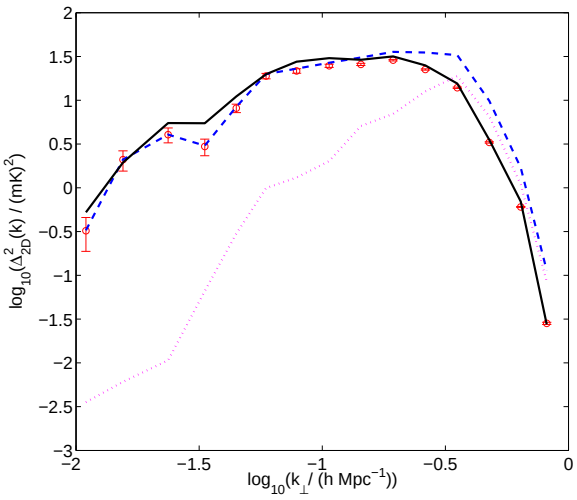

Figure 2.22: 2D power spectrum of the simulated 21-cm signal (black,solid), reconstructed 21-cm signal (red,points), residuals (blue,dash) and noise (pink,dotted) at 151 MHz, or z=8.40, for a 2.5°× 2.5° field of view. Any error bars extending to below the x axis in linear space are shown extending to negative infinity in log space.

view, we now process a 2.5°× 2.5° data cube. If we had kept the noise and the resolution the same, analysing such a data cube would be plagued with noise as we would have reduced the number of pixels that we are analysing. Hence, we can choose to analyse a smaller patch in the sky with a higher resolution and same noise or decrease the noise and have similar resolution in order to have similar constraining power as the fiducial analysis and establish the effect of the sky area coverage. In actual observations a decrease in field of view and an increase in resolution would be related to the size of the stations and distribution of the stations respectively. If we had changed the resolution we would no longer correspond strictly speaking to a LOFAR case scenario. We therefore decide to decrease the field of view by a factor of 4 and enhance the signal to noise by a factor of 16. We see that the residuals are actually lower than the original 21-cm signal at the larger scales, Fig. 2.22, however the 21-cm power spectrum is still well recovered at the smaller scales. We interpret this as evidence that the 21-cm signal has been mixed into the other signals by FASTICA, potentially because FASTICA did not have as many lines of sight to remove the foregrounds, making the reconstruction less accurate though still successful.

2.5 Conclusions

We have presented a new implementation of a non-parametric foreground cleaning method using the FASTICA algorithm. FASTICA is an ICA technique which uses negentropy as a measure of non-Gaussianity. By maximising the non-Gaussianity of a signal mixture the ICs of the foregrounds

can be separated. FASTICA can then reconstruct the foregrounds, with any data not considered to be part of the foregrounds forming the residuals. The residuals consist of the 21-cm signal, system noise and fitting errors.

The success of using the FASTICA method to obtain an EoR signature was tested by attempting extraction of the two main statistical markers of the EoR, the 21-cm power spectrum and variance. The rms foreground fitting error is bounded below 10 mK across almost all of the frequency range when pixels with disproportionate errors due to unusually small foreground values are discarded.

Once the variance of the noise has been subtracted from the variance of the residuals, an excess variance is recovered. To accurately recover the 21-cm variance it was necessary to Fourier filter the data up to about 5 times the PSF scale. In this case the excess variance accurately recovers the order and shape of the simulated 21-cm variance across the majority of the frequency range, failing only where the signal to noise is extremely low.

The 21-cm angular power spectrum and 3D power spectrum are recovered very well across a wide frequency range.

Performing the ICA in Fourier space provides no particular advantages or disadvantages according to the statistical tests carried out in this chapter. This is in contrast to other methods which have shown preference towards processing in Fourier space (Harker et al., 2009).

The FASTICA method has proved not to be robust in the presence of large amounts of noise. Though impressive results are obtained at large scales even for twice the expected levels of noise, levels above this endanger the recovery.

We have shown that FASTICA can be a competitive foreground removal technique for EoR data, though for a full treatment of the LOFAR-EoR data, the polarisation of the simulated data and a more accurate frequency dependent PSF model needs to be considered in future work.

Chapter 3

GMCA

This chapter has been published as a scientific paper in Monthly Notices of the Royal Astronomical Society, Volume 429, Issue 1, pp. 165-176, 2013.

In Chapter 2 we introduced a method to successfully remove the foregrounds while making only minimal assumptions. By introducing another similarly successful method, we acknowledge the possibility that different methods will be well suited for the extraction of different information from the data and that there is an advantage in having several foreground cleaning methods to apply the data independently to confirm a statistical detection. In this chapter we implement another non-parametric method, the sparsity-based blind source separation (BSS) technique Generalized Morphological Component Analysis, or GMCA. GMCA uses an over-complete basis set for foreground removal as opposed to a polynomial fitting method which is not a complete set unless we describe it with a polynomial of the order of the number of frequencies.

3.1 The GMCA method

The non-parametric method of removing the foregrounds is effectively a BSS problem. In 2 I utilised a statistical approach to component separation, namely FASTICA. This assumed that the components of the foregrounds were statistically independent and non-Gaussian in order to reconstruct the smooth spectral form of the foregrounds and leave a residual signal from which we could identify the 21-cm emission statistics. This statistical pursuit of independence is only one form that BSS techniques take, the other utilising morphological diversity and sparsity to separate the components. Zibulevsky & Pearlmutter (2001) proposed a new method of BSS, where one could find a basis set in which the components to be found would be sparsely represented, i.e. a basis set where only a few of the coefficients would be non-zero. With the components being unlikely to have the same few non-zero coefficients one could then use this sparsity to more easily separate the mixture. For example, were the 21-cm signal strong enough to detect directly using this method, we would expect it to be sparse on certain scales given the characteristic size of the ionized bubbles, much in the same way the Sunyaev-Zel'dovich effect can be detected with this method when analysing CMB data (Bobin et al., 2008). These bubble sizes change as a function of redshift so the sparse signal from these would arise as a pattern as a function of wavelength. In comparison, the smooth frequency structure of the foregrounds implies that the few sparse non-zero coefficients describing the foregrounds at the same scales as the 21-cm signal would be unchanging with frequency. Given our noise realisations, the 21-cm signal is far too small for this technique to pick it out as a component in its own right. Instead, it is how the foregrounds can be described as different sparse components which enables us to obtain the 21-cm signal and noise as a residual.

The idea of exploiting the sparseness of components in different bases has evolved into a full and diverse field of applications. The method has evolved to allow components to have different morphologies, exploit multichannel data and consider different bases for different components in order to achieve the most sparse representations.

Consider an observation of m maps each constituting t pixels across m channels of observation. The problem to be solved can be stated in the following manner:

$$\mathsf{X} = \mathsf{AS} + \mathsf{N}, \tag{3.1}$$

where X is the $m \times t$ matrix representing the observed data, n is the number of components to be estimated, S is the signal $n \times t$ matrix to be determined, A is the $m \times n$ mixing matrix and N is the $m \times t$ noise matrix.

As this is a BSS problem, we need to estimate both S and A. We seek to find the 21-cm signal as a residual in the separation process, therefore S represents the foreground signal and, due to the extremely low signal-to-noise of this problem, the 21-cm signal is numerically ignored by the method and can be thought of as an insignificant part of the noise.

We can expand the components, $\mathsf{S} = \sum_{j=0}^{n} \mathbf{s}_j$, in a wavelet basis which can mathematically be thought of as a matrix of T wavelet waveforms, $\Phi = [\phi_1, ..., \phi_T]$, such that $\forall j \in \{1, ..., n\} \quad \mathbf{s}_j = \sum_{k=1}^{T} \alpha_j[k]\phi_k$. $\mathbf{s}_j$ is defined to be sparse if only a few of the $\alpha_j[k]$ are significantly non-zero.

The objective of GMCA is to seek an unmixing scheme, through the estimation of A, which yields the sparsest components S in the wavelet domain. This is expressed by the following optimization problem written in the augmented Lagrangian form :

$$\min \left(\frac{1}{2} ||\mathsf{X} - \mathsf{A}\alpha\Phi||_{\mathrm{F}}^2 + \lambda \sum_{j=1}^{n} ||\alpha_j||_p \right), \tag{3.2}$$

where typically $\|\alpha\|_p = (\sum_k |\alpha[k]|^p)^{1/p}$; sparsity is generally enforced for $p = 0$ which measures the number of non-zero entries of α (or its relaxed convex version with $p = 1$) and $||\mathsf{X}||_{\mathrm{F}} = \left(\mathrm{trace}(\mathsf{X}^T\mathsf{X})\right)^{1/2}$ is the Frobenius norm. In practice, the threshold λ is set to be equal to 3 times the standard deviation of the noise level to exclude noise coefficients. The problem in Equation 3.2 is solved in an iterative two-step algorithm such that at each iteration q :

1. Estimation of S for A fixed to $\mathsf{A}^{(q-1)}$:

   Solving the problem in Equation 3.2 for $p = 0$ assuming A is fixed to $\mathsf{A}^{(q-1)}$, the components are estimated as follows :

   $$\mathsf{S}^{(q)} = \Delta_\lambda \left({\mathsf{A}^{(q-1)}}^{+} \mathsf{X}\Phi^T \right) \Phi$$

   where Δ_λ stands for the hard-thresholding operator which puts to zero all coefficients with amplitudes lower than λ. The term ${\mathsf{A}^{(q-1)}}^{+}$ denotes the Moore pseudo-inverse of the matrix $\mathsf{A}^{(q-1)}$.

2. Estimation of A for S fixed to $\mathsf{S}^{(q)}$:

   Updating the mixing matrix assuming that the components are known and fixed to $\mathsf{S}^{(q)}$ is carried out as follows :

   $$\mathsf{A}^{(q)} = \mathsf{X}{\mathsf{S}^{(q)}}^{+}$$

For more technical details about GMCA, we refer the interested reader to Bobin et al. 2007, Bobin et al. 2008, Bobin, Starck, Moudden & Fadili 2008 and Bobin, J. et al. 2013, where it is shown that sparsity, as used in GMCA, allows for a more precise estimation of the mixing matrix A and more robustness to noise than ICA-based techniques.

GMCA provides an efficient method of separating the foreground signal from the noise and 21-cm signal by locating the most sparse components that the foreground signal could be made of in the wavelet basis Φ. From a Bayesian point of view, using this sparsity method is equivalent to having an in-built prior in the model that the foregrounds are sparse over the basis chosen. While a Bayesian evidence analysis could be possible in order to compare different methods as well as different bases, and quantify the overfitting due to more free parameters, we consider it outside the scope of this project.

3.2 Wavelets

The set of basis functions, Φ, used by GMCA comprises wavelet functions.

The Fourier transform is a well known method of analysing data at different scales with a single set of basis functions - sines and cosines. In reality this confined basis set can obscure information, and so we instead consider an infinite set of basis functions localized in space - the wavelet functions. There are many types of wavelets - with some more localized in space, some smoother and some with fractal structures.

The most common form of wavelet used in astrophysics is the isotropic undecimated wavelet transform (IUWT) which we describe briefly below in reference to the more complete descriptions in literature (e.g. Starck, Murtagh & Bijaoui 1998, Starck & Murtagh 2006). Consider an image with $p \times p$ pixels (where, using the previous section's notation $p \times p = t$ and we will refer to the pixel coordinates as $[k, l]$).

We can decompose an image at a particular frequency, c_0, into a coarse version of itself, c_J, along with a superposition of the original image at different wavelet scales:

$$c_0[k,l] = c_J[k,l] + \sum_{j=1}^{J} w_j[k,l], \tag{3.3}$$

where the wavelet coefficient w_j represents the data at scale 2^{-j}.

The decomposition is typically achieved using low-pass 1D filters, which we call h_{1D}, implemented by the "à trous" algorithm:

$$c_{j+1}[k,l] = \sum_q \sum_p h_{1D}[p] h_{1D}[q] c_j[k + 2^j q, l + 2^j p] \tag{3.4}$$

$$w_{j+1} = c_j[k,l] - c_{j+1}[k,l]. \tag{3.5}$$

When c_0 can be described by only a few significantly non-zero w_j, we say that c_0 is sparse in that basis.

In this chapter we utilise wavelets twice. The first time is within the GMCA algorithm, where we have a choice of different wavelet types that can be used as the basis set. GMCA uses wavelet decomposition to identify the components, S, but then returns a data cube with all scales present. In our analysis in Section 3.4 we wish to look at these results on different scales and so we utilise wavelet decomposition to do this. We will use the IUWT both within GMCA and later to analyse the images at different scales, though we briefly consider other discrete wavelets when we question how much our results depend on this choice of wavelet. The use of continuous wavelets in foreground removal has recently been investigated by Gu et al. (2013).

3.3 Results

The simulated data cubes for the foregrounds, noise and 21-cm cosmological signal are the same as described in Section 2.2. In the following section, the word 'reconstructed' refers to a component which has been estimated from the simulated data using GMCA. The 'residuals' are the difference between the total mixed signal and the reconstructed foregrounds and should therefore consist of the 21-cm signal, noise and any fitting errors.

3.3.1 Component Number

GMCA requires the specification of the number of sparse components that the data can be defined by. We utilise this component separation technique to define the foregrounds in order to subtract them, treating the 21-cm signal as noise. Therefore, the number of components refers to the number of foreground contributions which can be described by unique sparse descriptions (not necessarily the number of different foreground contributions such as Galactic free-free).

As each foreground model might be best described by a different number of components, we seek to choose the number of components by minimizing the leakage of foregrounds into the 21-cm signal. Let us introduce the statistics L_Y and R_Y:

$$\mathsf{L}_Y = \mathsf{A}(\mathsf{A}^T\mathsf{A})^{-1}\mathsf{A}^T\mathsf{Y}, \tag{3.6}$$

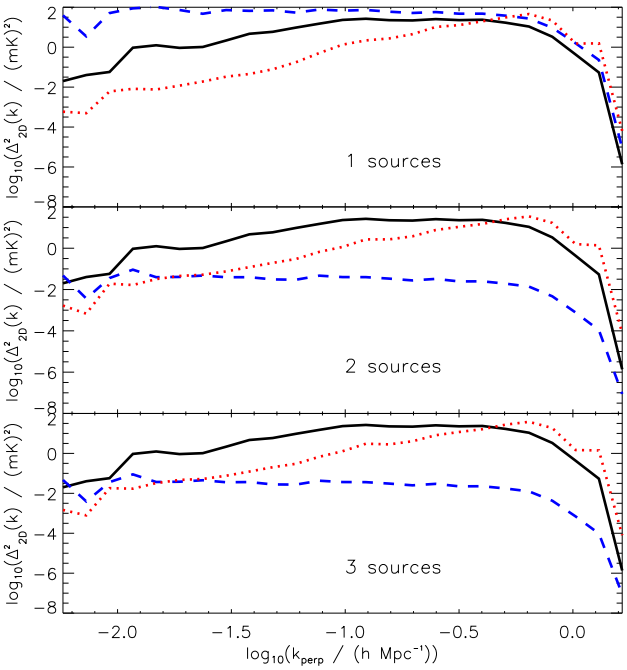

Figure 3.1: The 2D power spectrum of R_{fg} (blue dash) and L_{nocs} (red dot) and the 21-cm power spectrum (black,solid) at a frequency of 160.0 MHz for GMCA with 1, 2 and 3 components (top, middle and bottom respectively).

$$\mathsf{R}_Y = \mathsf{Y} - \mathsf{A}(\mathsf{A}^T\mathsf{A})^{-1}\mathsf{A}^T\mathsf{Y}, \tag{3.7}$$

where A is the mixing matrix calculated by GMCA and Y is a data cube, for example the foregrounds or the 21-cm signal. L_Y is the amount of the data Y that contributes to the GMCA components (in our case the reconstructed foregrounds). Thus we can calculate the amount of leakage of simulated noise and 21-cm signal, L_{nocs} into the reconstructed foregrounds by allowing Y to equal the combined simulated 21-cm and noise data cube. Conversely, R_Y is the amount of data Y which does not contribute to the GMCA component model. For example, letting Y equal the simulated foreground cube, R_{fg}, will tell us how much of the foregrounds leak into the residuals.

We take the power spectra of L_{nocs} and R_{fg} and compare them to the power spectra of the 21-cm signal to see the number of components for which leakage is minimized, Fig. 3.1. Note that, prior to our wavelet type analysis in Section 3.3.2, we adopt the default setting of GMCA for this component number analysis, the IUWT using the à trous algorithm.

To be confident of our reconstructed 21-cm signal, we ideally want both the power spectra of R_{fg} and L_{nocs} to lie below that of the 21-cm signal and to be as small as possible. We see that, while one component does not seem enough to accurately constrain the foregrounds, there is

very little difference between the leakages resulting from a 2 or 3 component foreground model. Indeed, we find this holds true for 4 and 5 components also. As more and more components are added to the model, we might expect the 21-cm signal itself to leak into the foreground model and be picked out as an individual component. However the magnitude of this (seen as part of L_{nocs}) will be small as the signal to noise of the foregrounds is much larger than that of the cosmological signal. When applying to real data we will have to rely on models of the foregrounds as observed by the data to estimate the level of leakage from the signal onto the foregrounds.

We choose to assume two foreground components for the rest of this chapter, though the reader should be aware that different foreground models may require different component numbers in order to optimise the method.

3.3.2 Choice of Wavelet

In Fig. 3.2 we consider how the leakages R_{fg} and L_{nocs} change depending on the choice of wavelet used by GMCA. There are many different types of wavelets, but they can be broadly categorized by whether they are decimated (i.e. provide a redundant signal representation), isotropic and which filter they use for the separation of data at different scales. Here we consider the IUWT, a decimated wavelet transform (referred to as Mallat), a non-dyadic and undecimated wavelet transform (referred to as Feauveau) and an undecimated wavelet transform using the Haar filter (referred to as Haar).

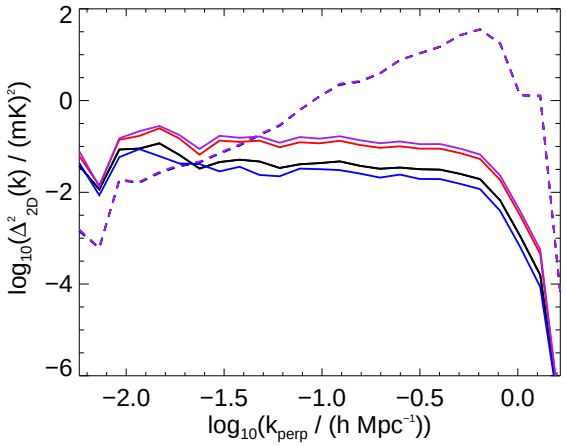

Figure 3.2: The 2D power spectrum of R_{fg} (solid) and L_{nocs} (dashed) at 160 MHz for: IUWT (black), Mallat's wavelet transform (red), Feauveau's wavelet transform without under-sampling (blue), Haar's wavelet transform (purple). Note that the dashed lines all lie on top of each other.

We can see that the choice of wavelet can affect how small the foreground leakages are, and therefore the success of the method. These differences are highly dependent on frequency as well,

with one wavelet type out-performing others at certain frequencies. For our implementation we choose the IUWT as it consistently minimizes the leakages over the frequency range.

3.3.3 Power Spectra

EoR experiments aim to recover the power spectrum of the cosmological signal over a broad range of frequencies.

The power spectrum of a line-of-sight/map/cube at a single frequency is calculated by 1D/2D/3D Fourier transforming that line-of-sight/map/cube and binning the pixels according to Fourier scale, k. The power at any particular k, $\langle\delta(k)\delta^*(k)\rangle$ is the average power of all the uv cells in the bin centering on k. The error on the point for a particular bin, k_i, is calculated as $\sigma_i = \frac{\langle\delta(k_i)\delta^*(k_i)\rangle}{\sqrt{n_{k_i}}}$ where n_{k_i} is the number of uv cells that reside in that k bin. The power spectrum of the reconstructed 21-cm signal is calculated by subtraction of the noise power spectrum from the GMCA residuals power spectrum. The total error on the reconstructed 21-cm power spectrum is calculated using the above error formula applied to the reconstructed 21-cm power spectrum, added in quadrature with the formula applied to the noise power spectrum, in order to take into account both sample variance and the effect of any error in the noise estimate. Note that we assume Gaussianity whereas the 21-cm signal is not Gaussian and also we calculate the error bars from the power of a single realization rather than over an ensemble of simulations. We ask the reader to bear in mind that these error bars might be considered incomplete because of this.

To explain a few graphical conventions: any points where the power of the residuals is below the power of the noise are omitted, as this leads to an unrealistic negative reconstructed 21-cm power; any error bars extending to below the x axis in linear space are shown with a lower error bar of equal length to the upper error bar in log space.

1D Power Spectra

The 1D power spectra are calculated over frequency wedges of 8 MHz to avoid evolution effects. Each line of sight produces a 1D power spectrum, one for each of the 512 $\times$ 512 pixels. These power spectra are then averaged over all the pixels. The frequencies mentioned correspond to the frequency in the middle of each 8 MHz wedge and the quantity plotted in Fig. 3.3 is $\Delta^2_{1D}(k) = \frac{Lk\langle\delta(k)\delta^*(k)\rangle}{\pi}$ where L is the comoving length of the wedge. The 1D power spectra are recovered to high accuracy across the frequency range and across the scales.

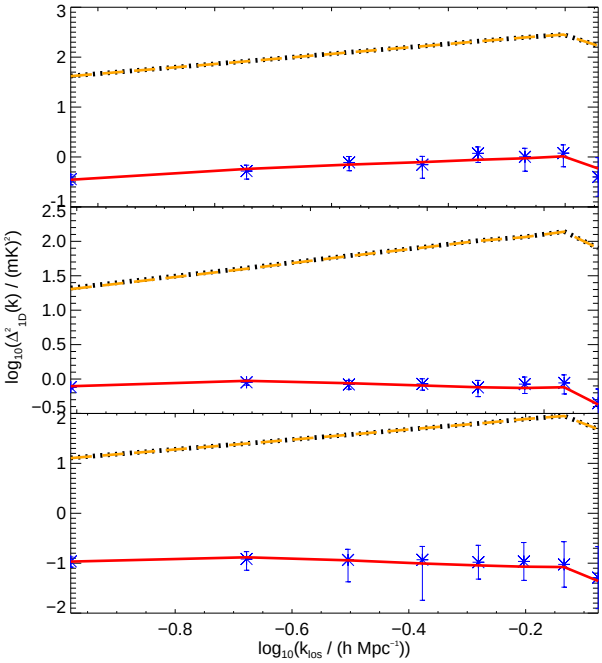

Figure 3.3: The 1D power spectra of the simulated 21-cm (red, solid), the residuals (black, dot), the reconstructed 21-cm (blue, points) and the noise (orange, long dash). Three 8 MHz frequency wedges centred at 127 MHz, 151 MHz and 175 MHz respectively are shown from top to bottom.

2D and 3D Power Spectra

For the 2D power spectra, the quantity plotted is $\Delta^2_{2D}(k) = \frac{Ak^2\langle\delta(k)\delta^*(k)\rangle}{2\pi}$ where A is the area of the simulation map. To calculate the 3D power spectra we divide the cube into sub-bands of 8 MHz to avoid signal evolution effects. The quantity plotted is $\Delta^2_{3D}(k) = \frac{Vk^3\langle\delta(k)\delta^*(k)\rangle}{2\pi^2}$ where V is the volume of the sub-band.

We now consider the recovered 2D and 3D 21-cm power spectra and how best we can minimise the effects of leakage. The noise leakage into the reconstructed foregrounds can be accurately quantified by creating an independent realization of the noise (no2) (for real data it is assumed we will know the statistics of the noise to high precision and can therefore create a second realization from the known noise power spectrum) and applying Equation 3.6 to find L_{no2}. We find that the power spectra of L_{no} and L_{no2} are almost identical meaning that A is not a strong function of the original noise realization. We can use this information to find a better estimate of the 2D and 3D power spectra and compensate for the noise leakage using the following calculation:

$$\tilde{\Delta}^2_{csrec} = \Delta^2_{rest} - \Delta^2_{no} + \Delta^2_{L_{no2}}. \tag{3.8}$$

To calculate a leakage ratio we would generally have to include all the leakages, such that

Leakage Ratio $= \frac{\Delta^2_{cs}}{\Delta^2_{R_{fg}}+\Delta^2_{L_{nocs}}+\Delta^2_{cs}}$. However, since we can correct for L_{no} we can instead calculate:

$$\text{Leakage Ratio} = \frac{\Delta^2_{cs}}{\Delta^2_{R_{fg}} + \Delta^2_{L_{cs}} + \Delta^2_{cs}}, \tag{3.9}$$

which quantifies the amount of 21-cm leakage into the foregrounds and vice versa. We can see the leakage ratio plotted for the 2D and 3D power spectra for multiple frequencies in Fig. 3.4.

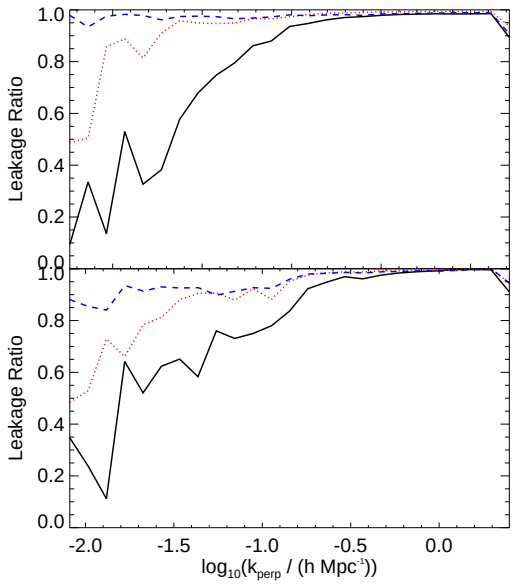

Figure 3.4: Top: The leakage ratio for the 2D power spectra for frequencies of 130 MHz (black,solid), 150 MHz (red,dot) and 170 MHz (blue,dash). Bottom: The leakage ratio for the 3D power spectra for frequencies of 135 MHz (black,solid), 151 MHz (red,dot) and 167 MHz (blue,dash).

We see that we can expect an accurate 21-cm power spectrum recovery at large k once the noise leakage is compensated for. The smaller k recovery is still very dependent on the foreground magnitude and therefore frequency of observation.

We can see the result of applying Equation 3.8 in Figs. 3.5 and 3.6. Wherever R_{fg} and/or L_{nocs} exceeds the power of the simulated 21-cm signal we see a degraded fit in Fig. 3.5. The 2D power spectra are recovered to excellent accuracy and we see that once the noise leakage is taken into account there is much less leakage at large k scales, allowing a more complete power spectrum reconstruction.

For the 3D power spectra, a similarly accurate recovery is made across the frequency range. The recovery in 3D is more precise due to the larger amount of data in a box as opposed to a single slice. We see that the data is recovered even on the larger k scales once we correct for the noise leakage.

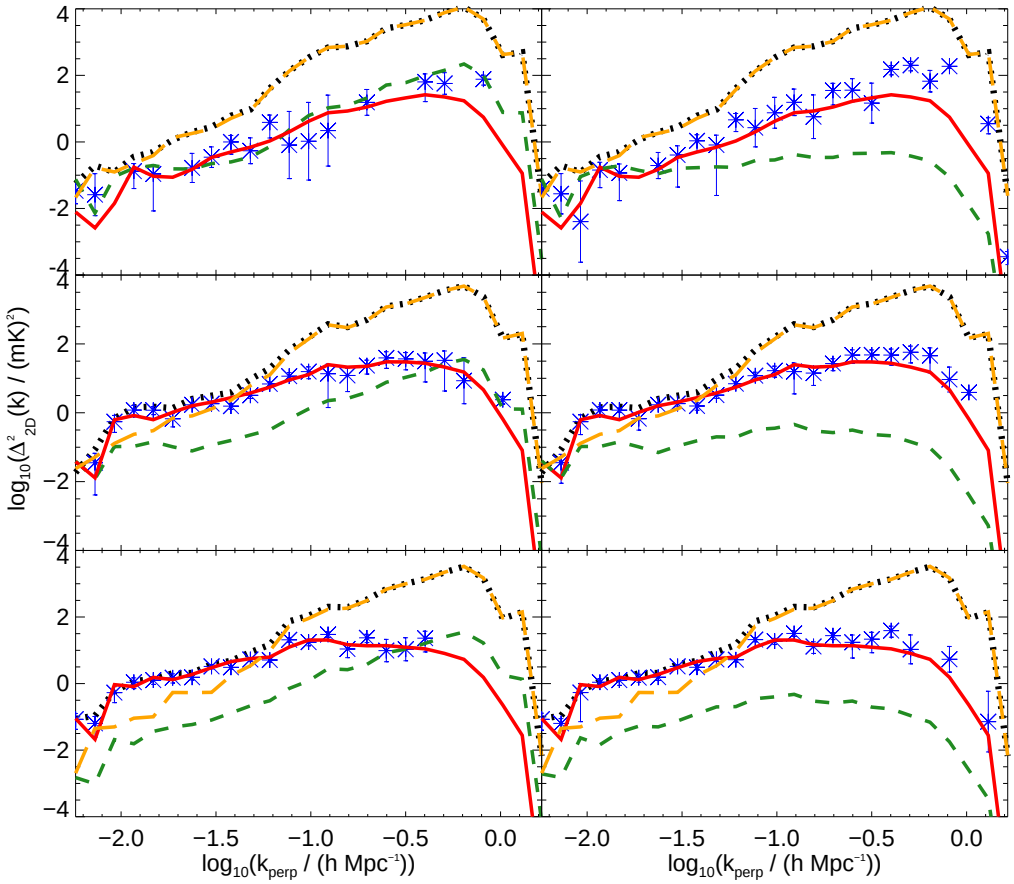

Figure 3.5: 2D power spectrum of the simulated 21-cm signal, reconstructed 21-cm signal, residuals and noise at 130 MHz, or z=9.92, 150 MHz, or z=8.47 and 170 MHz, or z=7.35 from top to bottom. The left column is the fiducial data whereas the right hand column plots the reconstructed 21-cm power spectrum but with the leakage determined from the second noise realization added, as described in Section 3.3.3. Linestyles are as described in Fig. 3.3 with the additional dark green dashed line representing the total leakage power ($\Delta^2_{R_{fg}} + \Delta^2_{L_{nocs}}$) in the left column and the leakage assuming noise leakage has been corrected ($\Delta^2_{R_{fg}} + \Delta^2_{L_{cs}}$) in the right column.

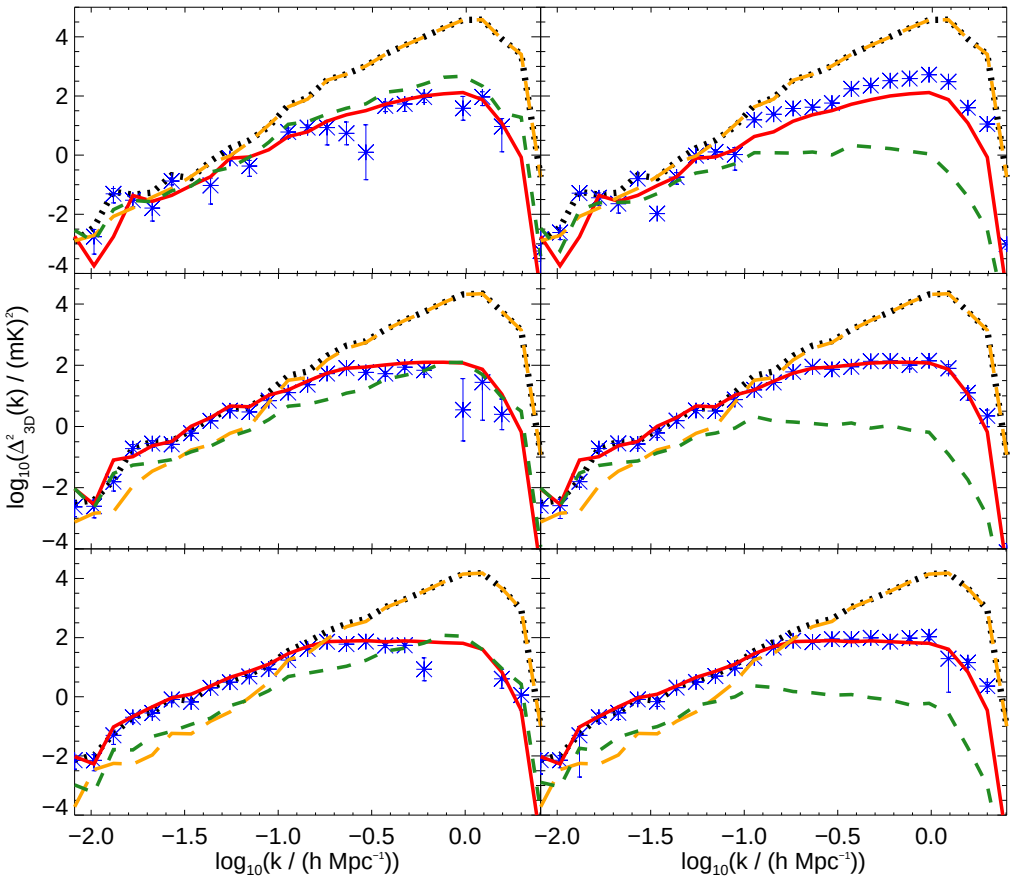

Figure 3.6: 3D power spectrum of the simulated 21-cm signal, reconstructed 21-cm signal, residuals and noise at 135 MHz, or z=9.51, 151 MHz, or z=8.40 and 167 MHz, or z=7.50 over an 8 MHz sub band (top to bottom). The left column is the fiducial data whereas the right hand column plots the reconstructed 21-cm power spectrum but with the second noise realization leakage added. Linestyles are as described in Fig. 3.5.

3.4 Phase Conservation and Imaging

Recently it has been shown that imaging of the neutral hydrogen in the late stages of reionization is possible with the current generation of radio telescopes when angular scales larger than 0.5° are considered, independent of the type of reionization source (Zaroubi et al., 2012). Here, we compare the output residual maps with the simulated 21-cm maps and consider how well the phases of the 21-cm signal are conserved through the foreground removal process. The better the phases are conserved, the more correlation between maps we will observe. We will also consider the maps at different scales and as such we also decompose the output maps into 8 wavelet scales using the IUWT.

For a particular frequency, we calculate the phase of each uv point in a Fourier transformed map, F, as Phase[u,v] = $\tan^{-1}$(Im(F(u,v))/Re(F(u,v))).

In Fig. 3.8 we see the phase density relating to each wavelet scale of the 21-cm and residual cubes. For each frequency we calculate the phase of each pixel in the 21-cm and residual maps and use this as a coordinate on a phase density map where the x axis is the phase of the residuals and the y axis is the phase of the 21-cm map. The more pixels with coordinates corresponding to a particular bin in the phases, the higher the phase density we will observe. If GMCA perfectly preserves the phase of the 21-cm signal we should see a diagonal phase density plot. For clarity, only the phase bins with a pixel count in the largest 67% of the pixel count distribution are plotted. We see that for the three crudest wavelet scales there is excellent phase recovery across the frequency range, while at 160 MHz this excellent recovery can be seen on even smaller wavelet scales. This is in line with expectations since the relative rms values (i.e. ratio of the rms of the 21-cm and noise and ratio of the rms of the 21-cm and foregrounds) for the 21-cm signal both peak at just after 160 MHz.

In Fig. 3.9 we start with the crudest wavelet scale and then add the next crudest scale one at a time to see the effect on phase conservation, finding that this improves the recovery considerably.

In Fig. 3.10 we compare the reconstructed signal maps with the simulated signal maps at the different wavelet scales. It is clear that the foregrounds are reconstructed to a high accuracy at all scales. The residuals show clear correlation with the 21-cm maps - especially at scales 54-434 Mpc. By considering the data on different scales we compensate for the small scale noise leakage and can retrieve convincing reconstructed images in comparison to the map with all scale data included.

We plot the Pearson correlation coefficient between the simulated 21-cm maps and the residual maps at different individual scales in Fig. 3.7. On an individual basis, we can clearly see that

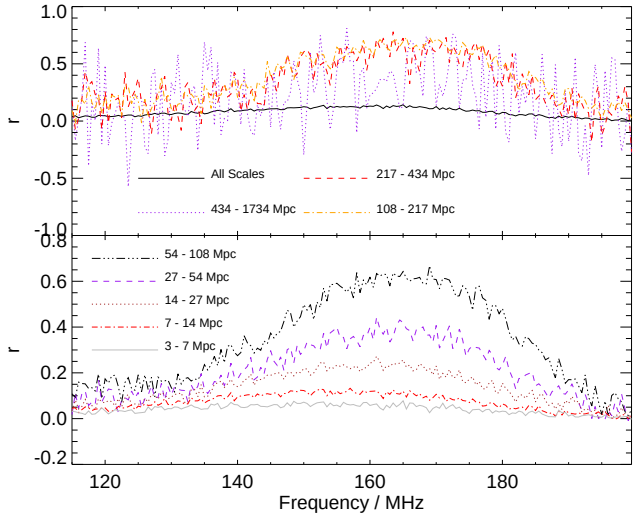

Figure 3.7: The Pearson correlation coefficient between 21-cm and residual maps. There is very little correlation when all scales are present or on the smallest scales, however we reach correlation coefficients of over 0.6 for distance scales 54 - 434 Mpc. The correlations are always much weaker at the lower end of the frequency range because the noise and foregrounds are at their highest and at the higher end of the frequency range because the 21-cm signal is negligible.

the finer the scale of structure we correlate, the less of a correlation there is between the residuals and simulated 21-cm maps. The finer wavelet scale we look at, the more dominant noise leakage will be in the residual maps and so a smaller correlation is observed. By only comparing the crudest wavelet scales however, we risk losing a lot of the small scale 21-cm structure and being increasingly dominated by the foreground signal.

We can add several of the wavelet scales together in order to balance having enough useful information without including too much noise leakage on the smaller wavelet scales. To compare with Zaroubi et al. (2012), we also include images of the full data which have been smoothed with a 20 arcminute Gaussian kernel. Wavelet decomposition has the advantage of providing a selection of scales on which one can analyse the images, as opposed to being restricted by filters such as a Gaussian kernel which simply remove all modes below a certain scale. However, the scales at which one can analyse images with wavelet decomposition are determined by the method itself - one cannot then ask what the data look like at a scale half way between two wavelet scales.

In Fig. 3.11 we recover impressive images of the reionization signal at 165 MHz when the smallest scale information is discarded. Comparing the residual and 21-cm maps on each row we find correlation coefficients of 0.689, 0.687 and 0.588 for the top, middle and bottom rows respectively. We therefore conclude that the wavelet decomposition more optimally removes the noise from the residuals than the smoothing technique (bottom row) employed by Zaroubi et al. (2012). In Fig. 3.10 we can see the wavelet decomposition has the effect of clustering the noise

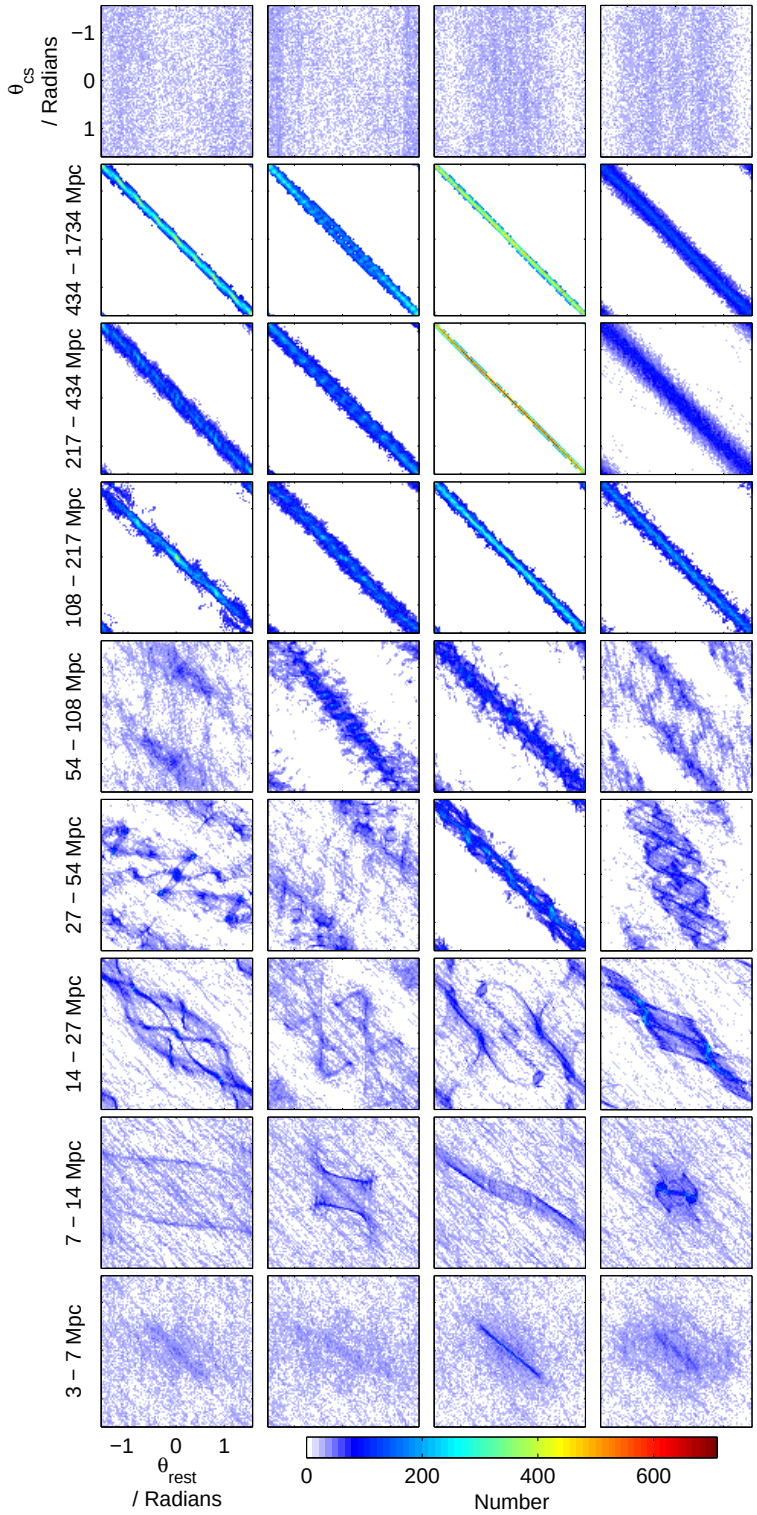

Figure 3.8: Density maps of the phase of maps of the simulated 21-cm and the residuals. From left to right are maps at frequencies 130, 145, 160 and 175 MHz. From top to bottom are maps of the complete cubes and then of increasingly small scale wavelet scales. A clear diagonal signifies excellent phase recovery and therefore clearer images can be recovered. We see that on scales above 108 Mpc, the phases are well preserved; on smaller scales however, the phases are highly uncorrelated. It is clear that considering different wavelet scales can result in much better phase recovery than considering the full cube.

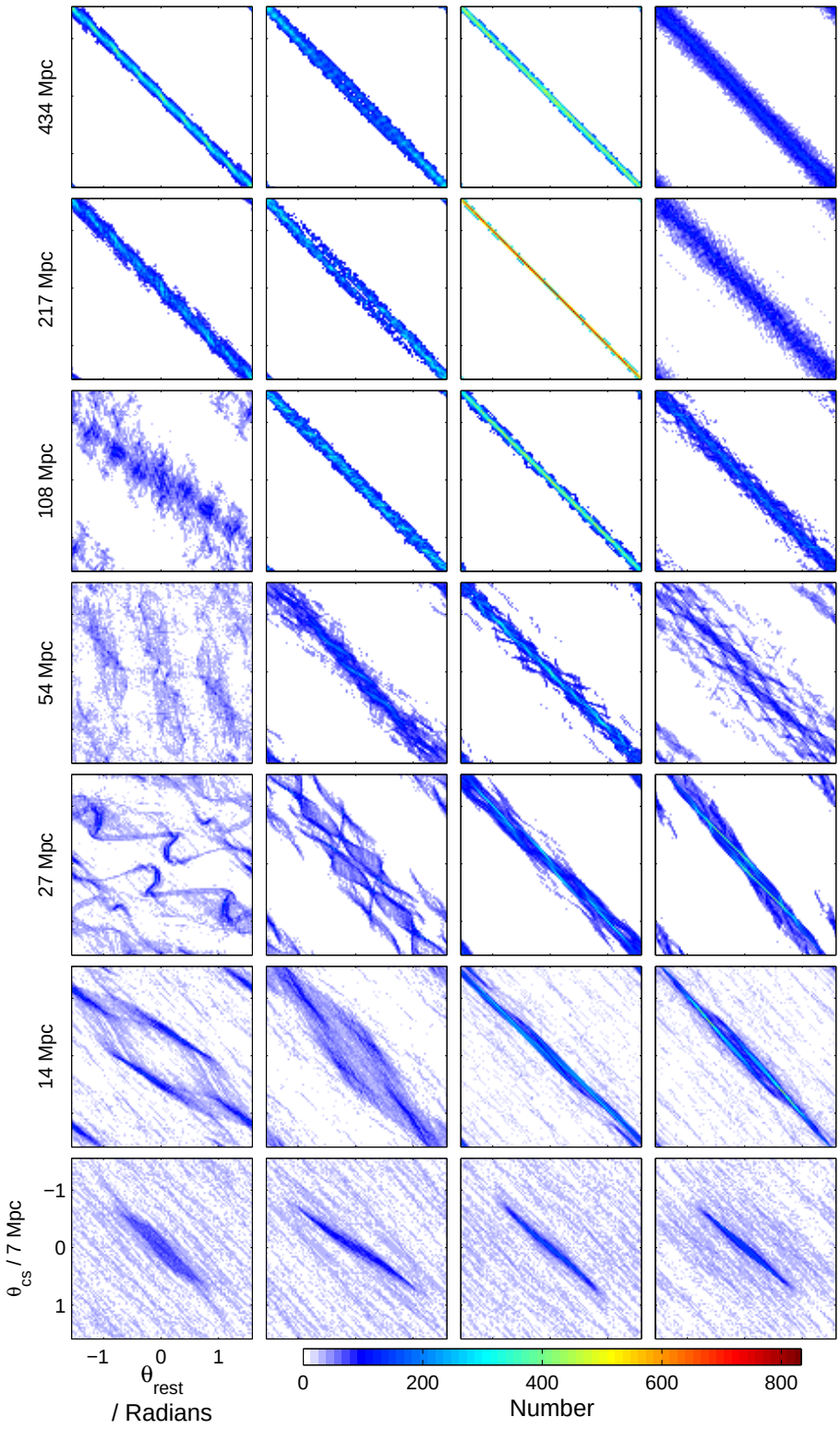

Figure 3.9: Density maps of the phase of maps of the simulated 21-cm and the residuals. From left to right are maps at frequencies 130, 145, 160 and 175 MHz. From top to bottom are maps of cubes with only the crudest scale present and then of only the 2,3,4,5,6 and 7 crudest wavelet scales. The minimum distance scale information included is labelled for each wavelet scale, the maximum is always 1734 Mpc. A clear diagonal signifies excellent phase recovery and therefore clearer images can be recovered. The addition of several scales together results in clearer diagonals than considering scales individually in Fig. 3.8.

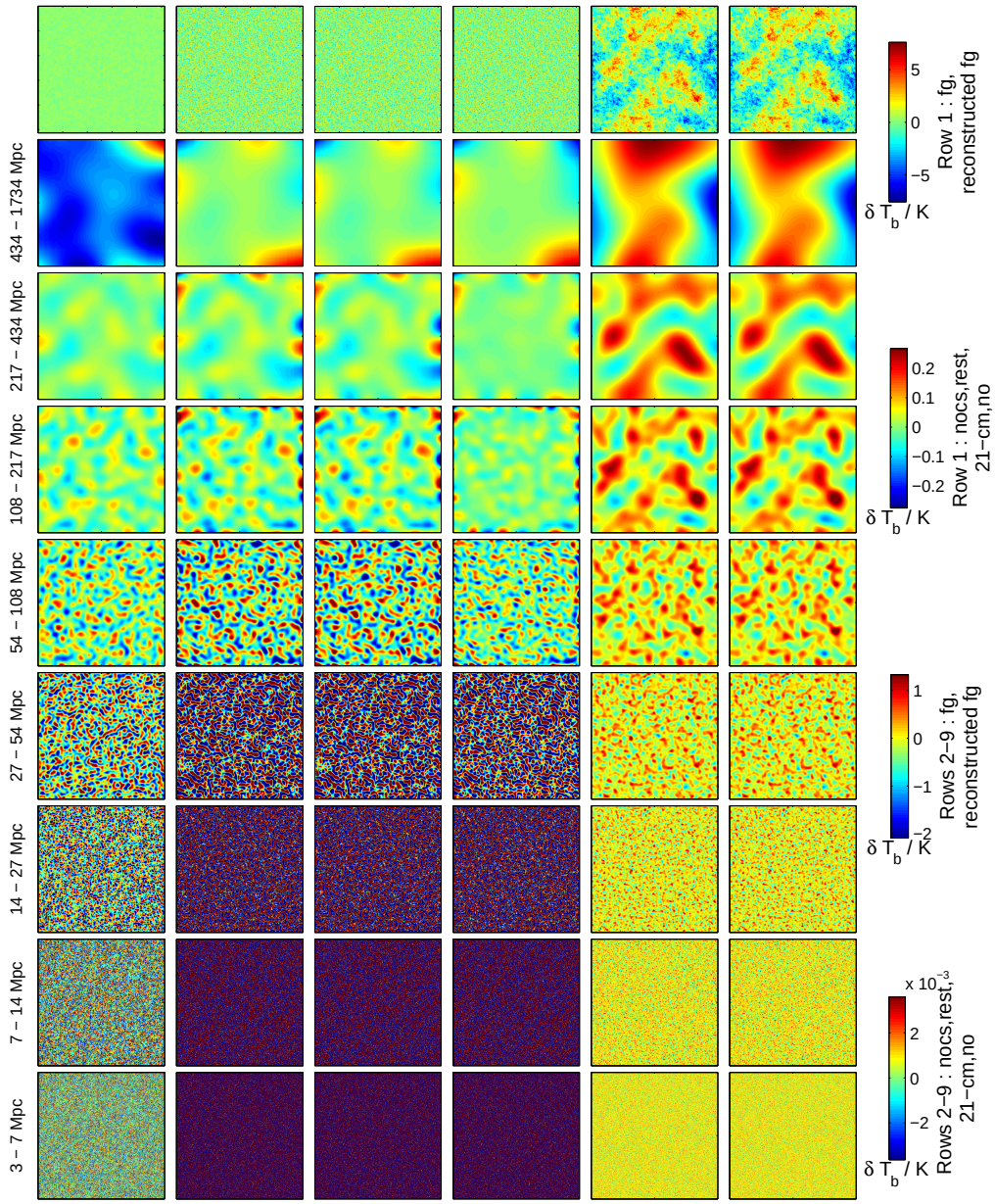

Figure 3.10: The decomposition of the 21-cm signal, residuals, simulated noise + 21-cm signal, noise, foregrounds, reconstructed foregrounds and noise (left to right). From top to bottom, the rows are the original image at 165 MHz, and then the wavelet decomposition of this image at the 8 wavelet scales. We can see that the simulated and reconstructed foregrounds have a high correlation at all scales and even in the full cube. Similarly, the noise + 21-cm and residuals also share this strong correlation. As we cannot remove the noise directly we must look for a correlation between the residuals and simulated 21-cm, which will come as a result of little or no correlation between the noise and residuals at certain scales. The noise dominates too much in the full cube and on the large k scales, however we can clearly see a correlation by eye on distance scales between 108 and 434 Mpc. At the largest scale, the 21-cm signal is so small that the residuals are dominated by noise.

around the edges of the image (this effect is particularly pronounced in rows 3 and 4). To avoid this edge effect we also correlate the maps in Fig. 3.11 again but this time considering only the pixels in a central patch covering 50% of the total map area. We find correlation coefficients of 0.905, 0.788 and 0.605 for the top, middle and bottom rows respectively. With real data, we can assume that this edge effect would not be a problem as the fitting and decomposition can always be carried out over a slightly larger cube with only the central region being used for data analysis.

3.5 Conclusions

In this chapter we have assessed the sparsity-based blind source separation technique GMCA as a possible way of removing the foregrounds on a 21-cm EoR signal. We recover the 1D, 2D and 3D power spectra to high accuracy across the frequency range. Since the mixing matrix calculated by GMCA was shown not to be a strong function of the noise realization, we were able to compensate for leakage of noise power into the reconstructed foregrounds using an independent noise realization, leading to more complete 2D and 3D power spectra.

We also considered if images of reionization could be recovered from the LOFAR-EoR data once foreground removal with GMCA has been carried out. Using wavelet decomposition, we considered the phase correlation between the GMCA residuals and the simulated 21-cm at different scales. We find strong correlations at the cruder wavelet scales and add several scales together to balance the amount of information in an image with the accuracy of the phase recovery. We find that when distance scales of below 54 Mpc are discounted, the GMCA residuals images are highly correlated with the 21-cm images, with correlation coefficients of just less than 0.7. Considering only the pixels in a central patch covering 50% of the total map area, we find a correlation coefficient of 0.905 - a 50% improvement on the Gaussian smoothing method employed by Zaroubi et al. (2012).

GMCA is a highly adaptable method and there remains the possibility that with careful tuning, the 21-cm signal could be picked out as a separate component as opposed to being present as a residual of the process. We intend to explore this further and consider using different mixing matrices for each scale.

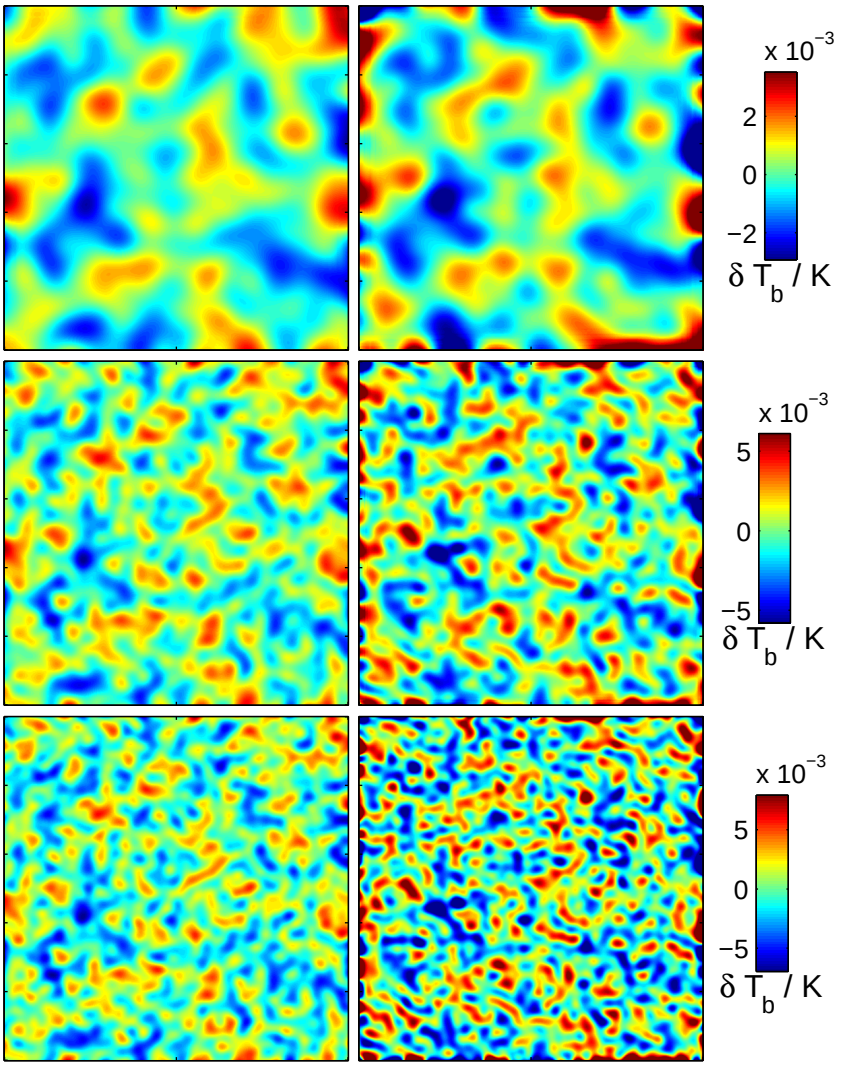

Figure 3.11: In the left column we show the 21-cm signal and in the right column the residuals of GMCA at 165 MHz. In the top row only distance scales between 1734 and 108 Mpc are included, in the middle only distance scales between 1734 and 54 Mpc are included and on the bottom the images with all scales present have been smoothed with a 57 Mpc ($\approx$ 20 arcminutes) Gaussian kernel. Clear correlations can be seen between the columns (coefficients of 0.689, 0.687 and 0.588 for the top, middle and bottom rows respectively). Considering only the pixels in a central patch covering 50% of the total map area we find correlation coefficients of 0.905, 0.788 and 0.605 for the top, middle and bottom rows respectively.

Chapter 4

Peculiar Models

The work in this chapter has been carried out in collaboration with F. Abdalla and M. Santos. This will be submitted for publication as a scientific paper in Monthly Notices of the Royal Astronomical Society, Chapman et al. 2014.

The Epoch of Reionization remains one of the last epochs of the Universe not to be directly observed. Though this is soon about to change, this places great importance on accurate simulations in order to draw constraints and even design future experiments. The majority of reionization codes output brightness temperature boxes in real space. Though building an observation light cone from these boxes is now common, the light cones used can still be considered incomplete. In real observations, the cumulative effect of the peculiar velocities of the hydrogen atoms will distort the signal into so-called redshift space and it is this which we aim to address in this chapter. We build a stand-alone code to take the ionization, density and velocity field real space boxes from a standard reionization code and calculate how an observer would see this simulation in brightness temperature. This involves a full treatment of the peculiar velocities of the hydrogen such that an observation map could have contributions from multiple real space boxes at different redshifts. We show that, even for a conservative peculiar velocity model, the difference in the resulting light cone is significant on the small scales, though the large scale bubble structure remains largely intact.

4.1 Introduction

As a new generation of telescopes begins observing the EoR for the first time (e.g. Low Frequency Array (LOFAR)[1] (van Haarlem, M. P. et al., 2013), Giant Metrewave Radio Telescope (GMRT)[2], Murchison Widefield Array (MWA)[3], Precision Array to Probe the Epoch of Reionization (PAPER)[4], 21 Centimeter Array (21CMA)[5]) there is an urgent need for increasingly accurate simulations of the 21-cm signal. In order to analyse the observations, we will need to compare with multiple simulations containing as much realistic cosmology and astrophysics as possible. The first detections of the EoR will be statistical in nature but redshift space distortions (RSDs) can introduce anisotropies in statistics such as the 3D power spectrum, resulting in serious systematic errors. RSDs are not simply a 'complication' which must be modelled in order to match observation - they have the potential to help separate out astrophysics from cosmology using the statistical anisotropy (e.g. Barkana & Loeb 2005, Mao et al. 2012, Majumdar, Bharadwaj & Choudhury 2012, Shapiro et al. 2013).

RSDs arise as a result of the peculiar velocities of the hydrogen atoms which emit the 21-cm radiation. The resulting Doppler shifting of the 21-cm line complicates the direct frequency-redshift mapping enjoyed by simulations where only the cosmological expansion is considered and results in sources of 21-cm radiation being identified as nearer or farther in redshift-space than their true positions. This can have quite significant effects on the 21-cm signal and its statistics and should therefore be carefully modelled.

In this chapter we implement a code to include the effect of peculiar velocities on the simulated observation box, or 'light cone', using the semi-analytic reionization code, SIMFAST21 (Santos et al., 2010).

4.2 SIMFAST21

In response to the need for large field-of-view EoR simulations to compare with observation, the semi-numeric scheme SIMFAST21 was introduced by Santos et al. (2010). In the original simulation, while peculiar velocities were included in the calculation of the brightness temperature, the effect on the observed light cone was not considered and the simulation output was a real-space simulation box at each redshift of interest. This chapter introduces a modification to this code to output a light cone where the peculiar velocities are fully included. This modification replaces

[1] http://www.lofar.org/
[2] http://gmrt.ncra.tifr.res.in/
[3] http://www.mwatelescope.org/
[4] http://astro.berkeley.edu/ dbacker/eor/
[5] http://21cma.bao.ac.cn/

the original brightness temperature calculation, leaving all other parts of the code intact. In this section we describe the unchanged parts of the code before moving on to the new modification in section 4.4. For a full description of the original SIMFAST21 code, Santos et al. (2010) should be consulted.

To create the linear density field, $\delta(\mathbf{x})$, a random distribution of Gaussian variables, $a_{\mathbf{k}}$ and $b_{\mathbf{k}}$, are used to generate Fourier-space density fluctuations, $\delta(\mathbf{k})$:

$$\delta(\mathbf{k}) = \sqrt{\frac{P_{\delta\delta}(k)L^3}{2}}(a_{\mathbf{k}} + ib_{\mathbf{k}}), \tag{4.1}$$

which can then undergo an inverse Fourier transform:

$$\delta(\mathbf{x}) = \frac{1}{L^3}\sum \delta(\mathbf{k}) \exp i\mathbf{k}\cdot\mathbf{x}, \tag{4.2}$$

where one side of the simulation cube is of comoving length L. $P_{\delta\delta}(k)$ is the dark matter power spectrum which can be evolved linearly from the primordial power spectrum provided by, for example, CAMB[6].

The Press-Schechter formalism (Press & Schechter, 1974; Lacey & Cole, 1993) is used to identify halos in the density field according to the idea that a overdense perturbation acts as a closed Universe. The Friedmann equation can be solved analytically assuming a matter dominated Universe and a spherical collapse, to define the overdensity beyond which a perturbation collapses, $\delta_c(z) \approx 1.68/D(z)$ where $D(z)$ is the linear growth factor.

The extended Press-Schechter (or excursion set) formalism allows for elliptical collapse resulting in the critical overdensity being a function of the mass scale to which the density field is being filtered:

$$\delta_c(M, z) = \sqrt{a}\delta_c(z)\left[1 + b\left(\frac{\sigma^2(M)}{a\delta_c^2(z)}\right)^c\right], \tag{4.3}$$

where a, b and c are fitting parameters (Sheth & Tormen, 2002). In order to identify halos, the density field is subjected to a decreasing size series of top-hat filters. For any cell where the density value is greater than $\delta_c(M, z)$, a halo of mass M is defined, with that cell at the centre. As subsequently smaller filters are applied, halos are only defined if they do not overlap with a previously defined halo. In this way a catalogue of halo locations and masses is created.

Once the linear density field has been simulated and the halo positions established, both are perturbed using the simulated velocity field, $\mathbf{v}$, according to the Zel'dovich approximation

[6] http://camb.info

(Zel'dovich, 1970) as described in Mesinger & Furlanetto (2007):

$$\mathbf{x}_1 = \mathbf{x} + \Psi(\mathbf{x}) \tag{4.4}$$

$$\mathbf{v} \equiv \dot{\mathbf{x}}_1 = \dot{\Psi}(\mathbf{x}) \tag{4.5}$$

$$\delta(\mathbf{x}) \approx -\nabla \cdot \Psi(\mathbf{x}) \tag{4.6}$$

where $\mathbf{x}$ and $\mathbf{x}_1$ are the original and perturbed positions respectively and $\Psi(\mathbf{x})$ is the displacement vector.

The displacement vector and peculiar velocity fields are calculated as:

$$\Psi(\mathbf{x}, z) \approx D(z)\mathbf{v}_x(\mathbf{x}) \tag{4.7}$$

$$\mathbf{v}_x(\mathbf{k}, a) = v_z(a)\mathbf{v}_x(\mathbf{k}) = \frac{ifaH\delta(k, a)}{k}, \tag{4.8}$$

where $D(z)$ is the linear growth factor normalized such that $D(0) = 1$, f is the linear growth rate ($f \approx \Omega_m^{0.6}$) (e.g. Peebles, 1980) and $v_z(a)$ and $\mathbf{v}_x(\mathbf{k})$ are the temporal and spatial velocity factors. One can perturb the density and halo location fields using this displacement vector resulting in quasi-linear density and halo fields.

Once the halo positions have been defined, the excursion set formalism can be used once again to identify the ionization field. The quasi-linear density and halo fields are averaged by spherical top hat filters of decreasing size, whereby an averaged region is defined as completely ionized if $f_{coll} \geq \zeta$, where ζ is the efficiency parameter and f_{coll} is the fraction of mass collapsed in the halos in the filter region. The resulting distribution of ionized bubbles has been shown to be a very good approximation compared with more analytic simulations with radiative feedback and spatially dependent recombination effects.

In the original SIMFAST21 implementation the brightness temperature would then be calculated, however we delay discussing this until we have introduced why this is not sufficient when peculiar velocities are considered.

4.3 Light Cone Effect

The light cone effect is the result on observations of the line-of-sight being in the frequency direction. While simulations will output a 3D realization of the Universe at a chosen redshift, observations will build up a volume where the light from the lower frequency end is from an earlier stage of reionization. The usual method employed to construct a simulated observation

cube from a series of simulation boxes is as follows (also refer to Fig. 4.1):

- Consider a series of simulation cubes representing the Universe between redshifts z_{min} and z_{max}, all of comoving length L and made up of N cells along one side. We label the cells along the line-of-sight as k_i where $0 \leq i < N$ and k_0 is the furthest from the observer. We define the comoving resolution as $\Delta r = L/N$.

- The boxes all occupy the same region of comoving space and we place the furthest edge (i.e. k_0) of all the boxes at a comoving distance x_{max}, the distance to the largest output redshift, z_{max}, where x is defined through: $x(z) = \frac{c}{H_0}\int_0^z \frac{dz'}{\sqrt{\Omega_m(1+z')^3+\Omega_r(1+z')^2+\Omega_\Lambda}}$. In the absence of peculiar velocities, each frequency of observation, ν, corresponds to a simulation box output at a certain redshift through the standard relation $1+z = \frac{\nu_{21}}{\nu}$. If there is no simulation box at that precise redshift, one can be obtained through interpolation.

- From the box z_{max}, we take the furthest slice along the line-of-sight, k_0, of the simulation box, and this becomes the first slice of our light cone at frequency ν_0.

- For observed frequency ν_i, the 21-cm event is emitted at redshift z_i:

$$1 + z_i = \frac{\nu_{21}}{\nu_i}$$

  and at a comoving distance of x_i. We then load box z_i and take the slice at comoving distance x_i. This will have a cell address of: $k_i = \frac{(x_{max}-x_i)}{\Delta r}$. The slice located at line-of-sight address k_i becomes the observed frequency map at frequency ν_i.

- In order to build up a light cone relating to observed frequencies between ν_0 and ν_{max}, a simulation box size L is required such that $L > x(z(\nu_0)) - x(z(\nu_{max}))$, though this can of course be satisfied by using boundary conditions.

We refer to the light cone built up using this prescription from the real space SIMFAST21 brightness temperature boxes as the fiducial light cone. We use this method to build up our cosmological signal simulation box used in chapters 2 and 3 but when peculiar velocities are considered, one can no longer assume that a redshift box maps directly to a frequency map. Instead, photons from more than one slice in more than one redshift box might contribute to a given frequency map. In this chapter we introduce an algorithm which takes the redshift boxes and takes into account the effect of peculiar velocities both in the change in intensities and in the frequency map which that intensity will contribute to.

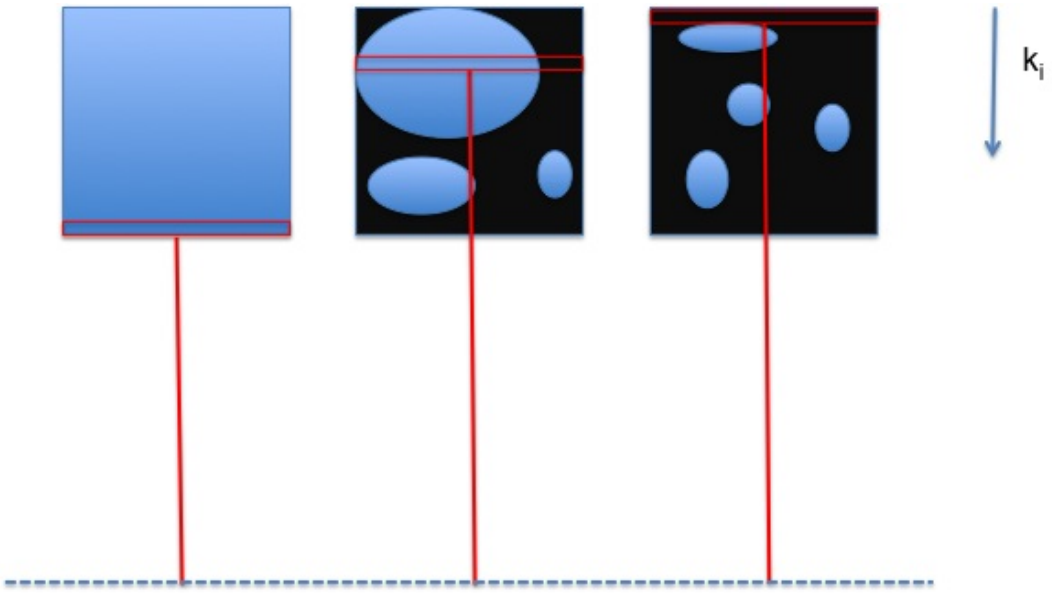

Figure 4.1: A cartoon of a series of redshift simulation boxes with the y axis the comoving line-of-sight. The boxes increase in redshift from left to right, with the right-hand box representing z_{max}. The red boxes represent the slices taken from each box and the vertical solid lines represent the distance x_i described in the text.

4.4 Redshift Space Distortions

In the absence of peculiar velocities, the frequency at which we observe 21-cm radiation would map directly onto the redshift of emission, i.e. $1 + z = \frac{\nu_{21}}{\nu_{obs}}$. However, the underlying density field is inhomogeneous, with high density peaks and low density troughs forming the seeds for structure formation. The neutral hydrogen atoms naturally trace this pattern early in reionization, with hydrogen atoms gravitationally attracted to high density regions. Consider observing a high density region along the line-of-sight. The hydrogen atoms on the near side of the density peak will have a peculiar velocity away from the observer, while the atoms on the far side will have a peculiar velocity towards the observer. The 21-cm radiation emitted by these atoms will therefore appear red-/blue-shifted for the near/far sides respectively, resulting in the high density region appearing contracted along the line-of-sight.

In actual observations, the red-/blue-shifting of 21-cm radiation due to the peculiar velocities destroys the ability to directly map an observed frequency to an emitted redshift, the so-called real-space representation. Instead, all observations are carried out in redshift-space, where an observation at a particular frequency might have contributions from hydrogen atoms at several different redshifts.

The distortions to the power spectrum produced by the peculiar velocities allow the extraction of both cosmological and astrophysical information, making them important to model correctly.

Jensen et al. (2013) modelled the evolution of the power spectrum decomposed according to the angle with the line-of-sight (denoted by subscript los), i.e. $P(k, \mu)$ where $\mu = k_{los}/k$ and $|\mathbf{k}| = |(k_{perp}, k_{los})| = k$, Fig. 4.2.

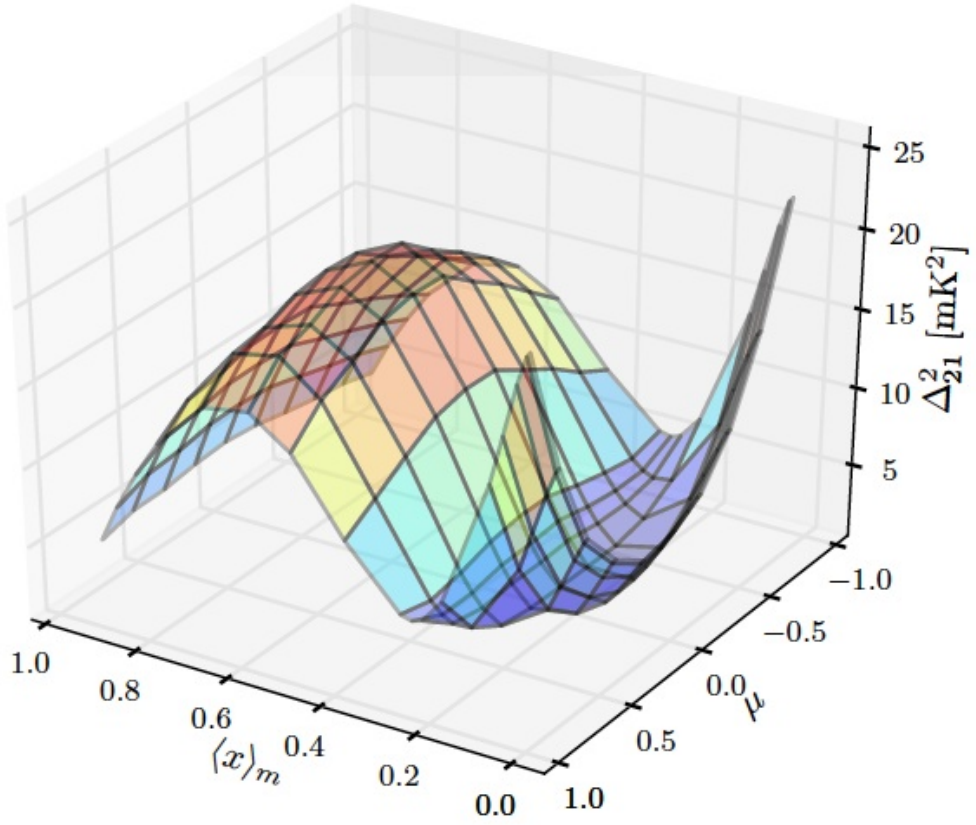

Figure 4.2: The evolution of the μ power spectrum with ionization fraction, x, at $k = 0.21$ Mpc^{-1}. Taken from Jensen et al. (2013).

Careful modelling of the power spectrum in this way could result in a way to separate out the matter field from the ionization field in a high signal-to-noise experiment, since it has been shown that the 21-cm power spectrum can be decomposed as:

$$P_{21}(k, \mu) = \delta T_b^2 (P_{\delta_{\rho_{HI}}, \delta_{\rho_{HI}}}(k) + 2\mu^2 P_{\delta_{\rho_{HI}}, \delta_{\rho_H}}(k) + \mu^4 P_{\delta_{\rho_H}, \delta_{\rho_H}}(k)), \tag{4.9}$$

where ρ_H is the matter density field and ρ_{HI} is the HI field (Barkana & Loeb, 2005; Mao et al., 2012).

Though this separation is not achievable with the current generation of radio telescopes, Jensen et al. (2013) found that LOFAR does have the capability to detect the redshift space distortions on the 21-cm power spectrum (i.e. a curvature in μ) and could possibly differentiate between different models of reionization.

Redshift space distortions are inherent to any observation and that is in itself motivation enough for including them as fully as possible in a simulation. However, it should be remembered that redshift space distortions are not just an observational quirk, they could be the key to understanding the primordial density field.

In order to build up the theory for the 21-cm emission as observed under the effects of peculiar velocities we introduce the different effects separately to avoid confusion.

4.4.1 Non-cosmological Case

In the following section we make extensive use of the standard radiative transfer relations which can be found in many textbooks, for example Mihalas (1978). First we consider a patch of static neutral hydrogen atoms in a non-expanding Universe. In the optically thin limit (when each ray of radiation can be assumed to have one absorption event between us and the point of emission) and the spin temperature, T_s, satisfies $T_s \gg T_{CMB}$ (so spontaneous emission occurs with much greater frequency than stimulated) each hydrogen atom is an individual emitter of luminosity:

$$L_{21} = h\nu_{21}A_{10}, \tag{4.10}$$

where $A_{10} = 2.85 \times 10^{-15}\text{s}^{-1}$ is the Einstein spontaneous emission coefficient for the hyperfine level and $h = 6.626^{-34}$ m^2 kg s^{-1} is the Planck constant. The emissivity follows as

$$j_{21}(\nu) = \frac{L_{21}}{4\pi} n_1 \phi(\nu), \tag{4.11}$$

where n_0/n_1 is the number density of HI atoms in the lower/upper hyperfine level and $\phi(\nu)$ is the 21-cm line profile, assumed to be non-zero for a very small frequency interval, $\phi(\nu) = \frac{1}{d\nu}$ where $d\nu$ is the natural width of the 21-cm line. We now use the definition of spin temperature, $\frac{n_1}{n_0} = \frac{g_1}{g_0} \exp\left(\frac{-T_*}{T_s}\right)$, where $g_1 = 3$ and $g_0 = 1$ are the statistical weights of the hyperfine levels. Assuming $T_s \gg T_*$, we can write:

$$n_1 = 3n_0 \exp\left(-\frac{T_*}{T_s}\right) \approx 3n_0 = \frac{3}{4} n_{HI}, \tag{4.12}$$

since $n_{HI} = n_0 + n_1$ where n_{HI} is the number density of HI atoms in total and so:

$$j_{21}(\nu) \approx 1.6 \times 10^{-40} n_{HI} \phi(\nu). \tag{4.13}$$

Now consider the absorption and emission of 21-cm radiation along a small section of the ray path, ds. First let us introduce the absorption coefficient defined as:

$$k_{21} = \frac{1}{c} h\nu_{21}(n_0 B_{01} - n_1 B_{10})\phi(\nu). \tag{4.14}$$

.

We can use $g_1 B_{10} = g_0 B_{01} = c^3 g_1 A_{10}/(8\pi h\nu_{21}^3)$, where B_{ij} is the Einstein coefficient for the stimulated transition from energy level i to j, to write:

$$\begin{aligned} k_{21} &= \frac{1}{c} h\nu_{21} n_0 B_{01}(1 - e^{\frac{-T_*}{T_s}})\phi(\nu) \\ &\approx \frac{3c^2 A_{10} T_* n_{HI}\phi(\nu)}{32\pi\nu_{21}^2 T_s} \\ &\approx (2.587 \times 10^{-19} \text{ K Hz m}^2) n_{HI}\phi(\nu)/T_S. \end{aligned} \tag{4.15}$$

We can write the change in intensity across the element ds as:

$$dI = -k_{21} I ds + j_{21} ds = d\tau(S_{21} - I), \tag{4.16}$$

where $S_{21} = \frac{j_{21}}{k_{21}}$ is the specific intensity of the 21-cm transition and $d\tau = k_{21} ds$.

The solution to this radiative transfer equation is:

$$I = I_{CMB} e^{-\tau} + \int_0^\tau S_{21} e^{-(\tau - \tau')} d\tau', \tag{4.17}$$

where $\tau(s) = \int_0^s k_{21}(s')ds'$ is the optical depth.

Using the Raleigh-Jeans relation, $\delta T_b = dI \times RJ$, where $RJ = c^2/2k_b\nu_{21}^2$ we have:

$$\delta T_b = d\tau T_s \left(1 - \frac{T_{CMB}}{T_s}\right) = k_{21} ds T_s \left(1 - \frac{T_{CMB}}{T_s}\right). \tag{4.18}$$

4.4.2 Cosmological Case without Peculiar Velocity

In an expanding Universe, a 21-cm photon at redshift z can travel a distance $ds \approx \frac{c}{H(z)} \frac{d\nu_{21}}{\nu_{21}}$ before redshifting out of the 21-cm spectral line. Using this together with $\phi(\nu) \approx 1/d\nu_{21}$, Equation 4.18 becomes:

$$\delta T_b(z) \approx (2.587 \times 10^{-19} \text{ K Hz m}^2) \frac{n_{HI}(z) c}{H(z)\nu_{21}} \left(1 - \frac{T_{CMB}}{T_S}\right). \tag{4.19}$$

Using the definition of the baryon fluctuation $\delta = \frac{n_H - \bar{n}_H}{\bar{n}_H}$, where $\bar{n}_H$ is the average hydrogen number density, we have $n_H = \bar{n}_H(1 + \delta)$. Together with $n_H(z) = n_H(0)(1 + z)^3$ we can write:

$$
\begin{aligned}
n_H(z) &= x_{HI}(z)(1+z)^3 \bar{n}_H(0)(1+\delta(z)) \\
&\approx 0.16 x_{HI}(z)(1+z)^3(1+\delta(z))\mathrm{m}^{-3},
\end{aligned} \tag{4.20}
$$

where we use $n_H(z) = X\rho_b(z)/m_p$ where X is the hydrogen content of the universe ($X \approx 0.73$), ρ_b is the baryon density and m_p is the mass of a proton.

Also,

$$
\begin{aligned}
H(z) &= \sqrt{\Omega_m(1+z)^3 + \Omega_\Lambda} H_0 \\
&\approx 36.9(1+z)^{\frac{3}{2}} \mathrm{km/s/Mpc}.
\end{aligned} \tag{4.21}
$$

Since brightness temperature transforms as $T_b \propto \nu$, then an observation of radiation emitted at a redshift of z will be observed at a frequency of $\nu_{21}/(1+z)$:

$$
\delta T_b(\nu_{21}/(1+z)) \approx 7.3 x_{HI}(z)(1+z)^{1/2}(1+\delta(z)) \left(1 - \frac{T_{CMB}}{T_S}\right) \mathrm{mK}. \tag{4.22}
$$

As an observer, we will only measure a 21-cm brightness temperature for radiation emitted at $\nu_{21} \pm d\nu_{21}$, i.e for observation frequencies $\nu_{21}/(1+z) \pm d\nu_{21}/(1+z)$.

4.4.3 Cosmological Case with Peculiar Velocities

We must now transform Equation 4.18 into an expanding Universe.

The natural width of the 21-cm line, $d\nu_{21}$ translates into a distance:

$$
ds = \frac{d\nu_{21}}{\nu_{21}} \frac{1}{\frac{1}{a}\frac{dV}{dr}\frac{1}{c}}, \tag{4.23}
$$

where V is the total velocity along the line of sight and r is line of sight comoving distance. The total velocity now consists of contributions from the peculiar velocity, v, of the HI cloud and also the cosmological expansion:

$$
\frac{dV}{dr} = aH + \frac{dv}{dr}, \tag{4.24}
$$

giving:

$$
ds = \frac{c}{H} \frac{d\nu_{21}}{\nu_{21}} \frac{1}{1 + 1/(aH)\frac{dv}{dr}}. \tag{4.25}
$$

In the rest frame of the cloud, the radiative transfer equation still applies, i.e.

$$dI(\nu_{21}) = -k_{21} I_i(\nu_{21}) ds + j_{21} ds, \tag{4.26}$$

where I_i is the intensity as a photon enters the patch element ds. A 21-cm event will only occur for frequencies within the line width of $\nu_{21}(1 - v/c)$. The intensity as observed, dI_f, is a Doppler-shifted version of the above equation such that $dI_f = dI(\nu_{21})(1 - v/c)$. Taking into account also that the CMB is seen blueshifted by the hydrogen cloud such that $I_i(\nu_{21}) = I_{CMB}(\nu_{21}(1 + v/c)^{-1})(1 + v/c)$, we have:

$$\begin{aligned} dI_f(\nu_{21}(1 - v/c)) &= -k_{21} I_{CMB}(\nu_{21}(1 + v/c)^{-1})(1 - v/c)(1 + v/c) ds \\ &+ j_{21} ds(1 - v/c) \\ &\approx -k_{21} I_{CMB}(\nu_{21}(1 - v/c)) ds + j_{21} ds(1 - v/c), \end{aligned} \tag{4.27}$$

where we have discarded peculiar velocity square terms and used a Taylor expansion for the blue-shifting term.

Then, following the same adjustments made in section 4.4.2 for redshift and converting to a brightness temperature where the Rayleigh Jeans constant is evaluated at $\nu_{21}(1-v/c)$, we arrive at:

$$\begin{aligned} \delta T_b(\nu_{21}(1 - v/c)/(1 + z)) &\approx 7.3 \frac{(1 + z)^{1/2}}{(1 - v/c)\left(1 + 1/(aH)\frac{dv}{dr}\right)} x_{HI}(z) \\ &\times (1 + \delta(z)) \left(1 - \frac{T_{CMB}(z)}{T_S(z)(1 - v/c)}\right) \text{ mK}. \end{aligned} \tag{4.28}$$

This is the brightness temperature equation fully taking into account peculiar velocities and we see clearly that, given the right peculiar velocities, photons emitted at two different redshifts could be observed at the same frequency.

4.4.4 Approximations

For the vast majority of the observed reionization era we can assume $S_{21} \gg I_{CMB}$. Also, we let:

$$\phi(\nu_{21}) = \begin{cases} \approx 1/d\nu_{21} & \text{if } \nu_{21} - d\nu_{21}/2 < \nu(1 + v/c) < \nu_{21} + d\nu_{21}/2 \\ 0 & \text{otherwise} \end{cases} \tag{4.29}$$

which allows us to write:

$$dI \approx j_{21} ds \approx (1.6 \times 10^{-40} j/s/sr) n_H \frac{ds}{d\nu_{21}}, \tag{4.30}$$

where we use $ds \approx \frac{c}{\nu} \frac{d\nu}{(H + dv/ds)}$ to ensure only the intensity which qualifies as a 21-cm event is added. If the redshifting of the 21-cm line is less than the line width, $d\nu$ is simply the frequency width of the patch being considered (i.e. $\nu(s + \Delta s) - \nu(s)$), or if the line is redshifted out of the 21-cm line width we must instead calculate the intersection of the frequency patch with the line width. This is taken care of in conditions 9a and 9b in section 4.5.

4.4.5 Divergent Velocity Gradients and the Optical Depth Approximation

In the above we have assumed a small optical depth, however in cases of large optical depth we must use the full solution of Equation 4.17 assuming very large optical depth and a constant S_{21} across the whole patch:

$$\delta T_b(\nu_{21}(1 - v/c)/(1 + z)) \approx \frac{1}{1 + z}[T_S(z)(1 - v/c) - T_{CMB}(z)]. \tag{4.31}$$

This is dealt with in condition 9d in section 4.5, however it is a fail-safe as opposed to a well-used condition. Mao et al. (2012) calculated the optical depth as measured by the observer at every point in their N-Body simulations and found that for $T_S/T_{CMB} = 0.1$ only one in 10,000 simulations cells had optical depth approaching 1 and this number fell by a further factor of a thousand if $T_S/T_{CMB} = 100$. As such they found the assumption that the 21-cm line is optically thin for reionization a safe assumption.

We see that Equation 4.28 breaks down when $dv/dr = -aH$. This can occur when either the halo is virialized or at the turn around point of halo collapse just before virialization. The original implementation of SIMFAST defined a velocity gradient limit of $dv/dr > -0.7H$ to avoid singularities. Though this only affects a small number of cells, there has been evidence that this prescription could affect more cells than necessary. Mao et al. (2012) found that significantly more cells had $dv/dr < -0.7H$ than were actually optically thick and so this velocity gradient limiting method affects more cells than necessary. In the new brightness temperature code, we avoid the need for such stark cut-offs completely. Whereas before we were attempting to calculate the 21-cm intensity on each cell individually, we are now integrating the intensity over an observed frequency interval which will also tend to 0 for $dv/dr = -aH$ as the radiation is then not being redshifted with the expansion of the Universe. In Equation 4.30 we see that dI appears

to become singular for $dv/ds = -H$. However, in this case, we also have $d\nu = \nu_i - \nu_f = 0$ and as such we have no singularity.

4.5 Implementation

We use SIMFAST21 as presented in Santos et al. (2010) with a standard LCDM cosmology to create the quasi-linear density, velocity and ionization fields. The initial condition boxes are formed on a 512^3 grid while all other boxes are formed on a 128^3 grid. All boxes are 200Mpc^3 and are output between redshifts 6.1 and 11.3 with interval $\Delta z = 0.018$.

We show histograms of the peculiar velocities and peculiar velocity gradients at a central redshift of 8.22 in Fig. 4.3. Though for our simulation the small values of v mean that there will not be a large contribution from different redshift cubes to the same observed frequency, this will not always necessarily be the case. For certain cosmological models, peculiar velocities are much larger and a careful treatment like that written here is even more important. The skew seen in the peculiar velocity gradients is expected as the peculiar velocity contributions balance the expansion of the Universe.

For an ionization field simulation box produced at a particular redshift, we need to go cell-by-cell and determine which frequency map the 21-cm signal in that cell contributes to. We can do this by, for each line of sight, subjecting each cell to a series of conditions, set out in the following algorithm.

1. Consider a set of simulation boxes from $[z_1, z_2]$ $(z_1 < z_2)$ with box size L, comoving resolution Δr and redshift resolution Δz.

2. We wish to output brightness temperature maps with frequencies in the interval $[\nu_2 = \nu_{21}/(1+z_2), \nu_1 = \nu_{21}/(1+z_1)]$.

3. Choose a field of view $FoV = L/(L + r(z_1))$ with $r(z)$ the comoving distance to redshift z. If implementing boundary conditions, where the original box size is multiplied by n along the line of sight, then $FoV = L/(nL + r(z_1))$.

4. We choose a line of sight proper distance increment of $\Delta s = Min\{\Delta r/(1+z_2), c/H(z_2)\Delta z/(1+z_2)\}/2$ and accordingly set $\Delta\nu = \nu_1 \Delta s\, H(z_1)/c$ the equivalent change in frequency associated with the change in proper distance. Alternatively, this frequency separation can be set equal to any desired frequency separation of the output light cone.

5. The angle between lines-of-sight is set as $\Delta\Omega = FoV/N_{pix}$ where N_{pix} is the number of pixels along one side in the output maps.

6. Load the ionization, quasi-linear density and velocity boxes at z_1. Assume the edge is at distance $r(z_1)$. For small simulation volumes it may be necessary to define $r(z_1)$ artificially so interesting signal can be observed in the resulting light cone. Let us call the redshift where place the boxes, z_{box} and for this work we set $z_{box} = 8.0$.

7. For each frequency map which we wish to fill, with frequency ν_p, the corresponding emission frequency at the edge of the box is $\nu_p(1+z_1)$, this is the first value of $\nu(s)$. The frequencies are updated through:

$$\begin{aligned} d\nu(s) &= \nu(s)\Delta s/c\,(H(z(s)) + dv/ds(s)) \\ \nu(s+\Delta s) &= \nu(s) + d\nu(s). \end{aligned} \tag{4.32}$$

   where the velocities and velocity gradients are calculated in the direction of the line-of-sight.

8. Fix the line-of-sight direction Ω. The proper distance to the edge of the box is $s(z_1) = r(z_1)/(1+z_1)$. We integrate the intensity along the line of sight (r, Ω) and increment using: $r = r + \Delta s(1 + z(r))$ where $z(r)$ is the redshift of the cell being looked at. If at any point along the line of sight $z(s+\Delta s)$ is larger than the next simulation redshift, those boxes are then loaded and the process continued. In this way, no 21-cm events are included which would arrive before or after our time of observation. The redshift of the first cell in the central line of sight is equal to z_{box}, with the first redshift for another line-of-sight needing to be adjusted for the different angle accordingly. As r is incremented, $z(r)$ is updated as: $z(r + dr) = z(r) + \Delta s(1 + z(r))H(z(r))/c$.

9. For the cell defined by (s, Ω) check that $\nu(s + \Delta s)$ frequency falls within the 21-cm line when adjusted for the peculiar velocity in that pixel. The $d\nu$ takes into account the fact the pixel itself is not a point, but an extended feature in frequency:

$$\nu_{21} - \Delta\nu_{21}/2 < \nu(s+\Delta s)(1+v/c) < \nu_{21} + \Delta\nu_{21}/2 + d\nu(s) \qquad \text{if } d\nu(s) \geq 0 \tag{4.33}$$

$$\nu_{21} - \Delta\nu_{21}/2 + d\nu(s) < \nu(s+\Delta s)(1+v/c) < \nu_{21} + \Delta\nu_{21}/2 \qquad \text{if } d\nu(s) < 0 \tag{4.34}$$

   If so, then:

   (a) Take $\nu_i = Min\{\nu(s+\Delta s)(1+v/c), \nu_{21} + \Delta\nu_{21}/2\}$

   (b) Take $\nu_f = Max\{\nu(s)(1+v/c), \nu_{21} - \Delta\nu_{21}/2\}$

(c) where the final intensity increment is

$$\Delta I_{21}(s) \approx (1 - v/c)\frac{(1.60137 \times 10^{-40}\ \mathrm{j/s/sr})}{H + dv/ds} \times$$
$$n_{HI}(s)c/\nu_{21}\left(\nu_i - \nu_f\right)/\Delta\nu_{21}. \tag{4.35}$$

Usually $\nu_i - \nu_f \sim \Delta\nu_{21}$.

(d) Note that the above intensity equation applies in the usual situation where $d\nu(s) > 0$. If there is a pixel where the peculiar velocity is greater and in the opposite direction to the Hubble expansion then we would be able to use:

$$\begin{aligned}\Delta I_{21}(s) \quad &\approx \quad (1 - v/c)(1.60137 \times 10^{-40}\ \mathrm{j/s/sr}) \times \\ &\qquad n_{HI}(s)\Delta s/\Delta\nu_{21}.\end{aligned} \tag{4.36}$$

(e) This incremented intensity is independent of the intensity itself and so the increments can be simply added together. We add the intensity adjusted for redshift, $(\nu_p/\nu(s))^3\Delta I_{21}(s)$, to the corresponding pixel in the observed output map.

10. Ω is then incremented by $\Delta\Omega$ and step 9 is repeated.

11. Once all lines of sight have been considered, we can convert the output map to a brightness temperature map by multiplying by the Rayleigh-Jeans constant evaluated at the frequency of observation.

$$\delta_{T_b} = I_{21}\frac{c^2}{2k_b\nu_p^2} \tag{4.37}$$

12. Steps 7 - 11 can now be repeated in order to fill the next light cone frequency map.

For comparison, we also produce a light cone from the original real space brightness temperature boxes, as described in section 4.3 and call this the 'fiducial light cone' in the following.

We compare maps at a redshift of 8.22 in Figure 4.4 and the difference between several slices in Fig. 4.5. First we show a slice from the redshift box output by the original SIMFAST simulation at a redshift of 8.22. Then we show a slice at a frequency equivalent to z=8.22 from a light cone as created using the traditional method. Any differences between these first two images will be as a result of interpolation. We then show the new code but where we have set all peculiar velocities and peculiar velocity gradients to zero. This is almost a step back from the original light cone code but is however interesting to see compared to the last slice, where we show the result of the new code in its fully operational form. Differences are clear bewteen all four slices, but most of all in the last slice, the new light cone. Here we see several pixels which

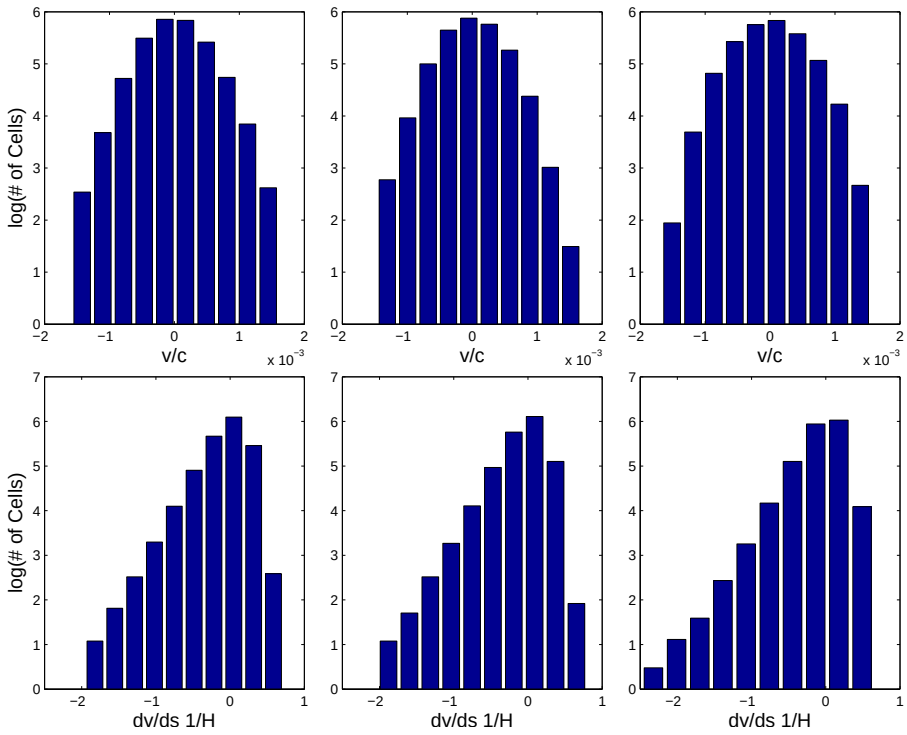

Figure 4.3: Top: A histogram of the peculiar velocities in the three spatial directions x, y and z (from left to right) of the simulation box at z=8.22. Bottom: The same but for the gradient of the peculiar velocities.

have changed drastically in brightness temperature magnitude, indicating the peculiar velocity light cone effect is not a negligible one. This difference would only be greater in cosmological models where the peculiar velocities were large. In order to see the difference more clearly, we plot difference maps in Fig. 4.5. First, we show the difference between a slice of the original simulation box and the new light cone. This difference will include both the light cone effect and the effect of including peculiar velocities on the light cone. We see the difference clearly on the small scales, while the large scale structure remains intact as expected in a small peculiar velocity model. It is important to note that the colour scale on the difference plots is of the same order as the maps themselves, indicating large differences on the pixel level. Secondly, we show the difference within the new code between setting the peculiar velocities to zero and including them. As expected, the differences are still significant, however smaller as the light cone effect is present in both maps.

We plot line-of-sight slices along the light cones in Figure 4.6. The differences between the original light cone and the two new light cones with peculiar velocities ignored and included are small but non-negligible. The difference between the original and new code is more evident in the last plot of this figure, where we plot the difference map, showing that many pixels change non-negligible amounts in temperature.

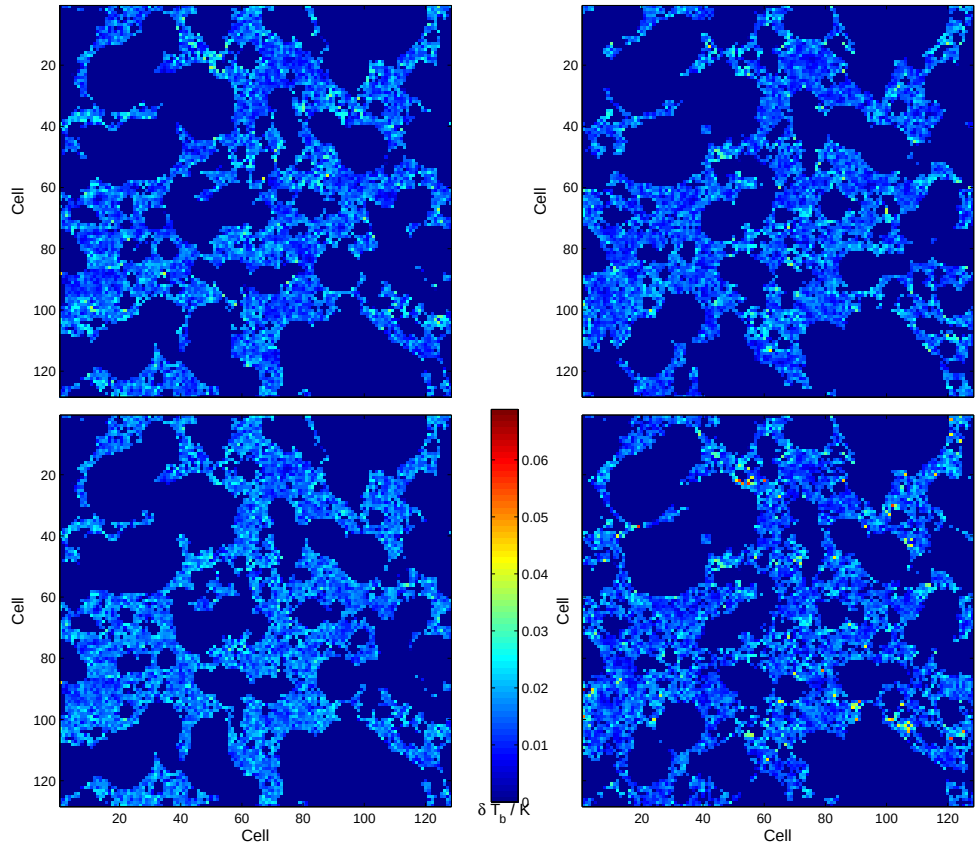

Figure 4.4: In reading order: A slice from the real space simulation box at z=8.22. A slice with an observation frequency equivalent to $z = 8.22$, if the standard redshift-frequency relation is considered, from the fiducial light cone. A slice from the new light cone code, but where all peculiar velocities are set to zero. A slice from the new light cone code.

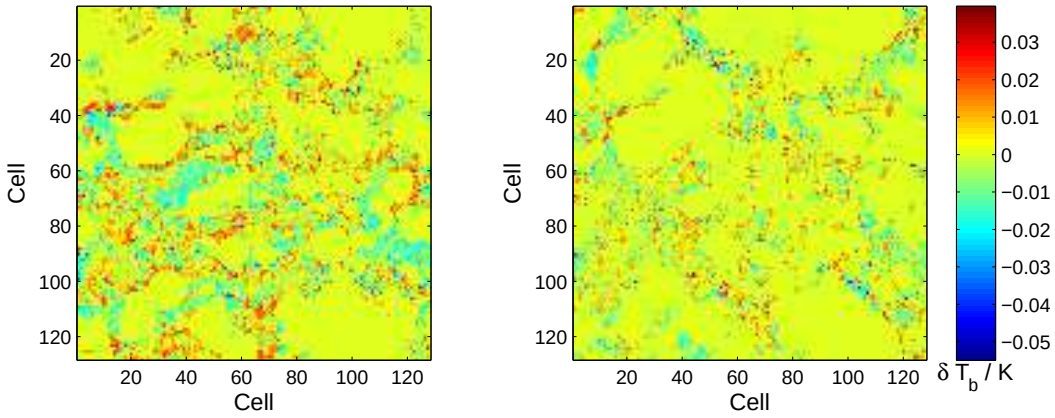

Figure 4.5: Difference slices between the redshift box and new light cone (left) and between the new light cone and the new light cone with peculiar velocities set to zero (right) at z=8.22.

One may be used to seeing the stark compression along the line of sight of high matter density (and therefore high peculiar velocity) patches as a sign of redshift space distortions on 21-cm

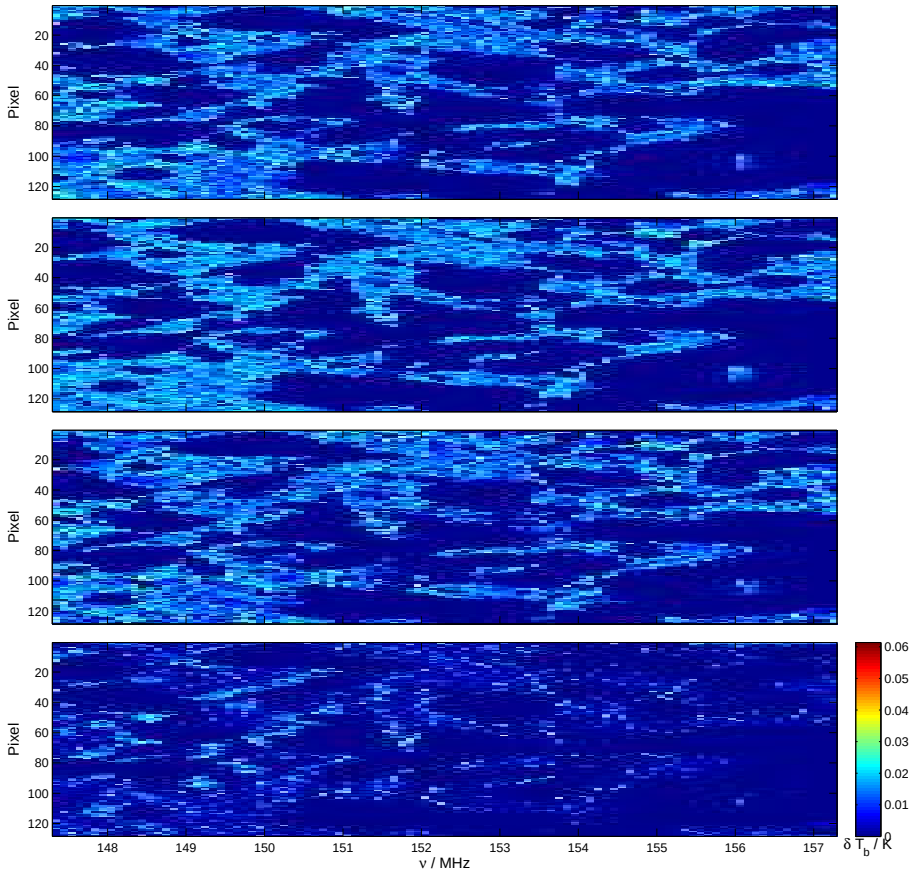

Figure 4.6: From top to bottom: A line-of-sight slice along the fiducial light cone (top), the new light cone where peculiar velocities are set to zero, the new light cone where peculiar velocities are included, the difference between the fiducial and new light cones, where the line of sight is along the x axis.

data (for example see Fig. 1 of Mao et al. (2012)). This effect will never be as immediately obvious when looking at a light cone however we should still be able to quantify the difference with standard statistics. In Fig. 4.7 we plot the cylindrical power spectrum of the real space simulation box, the fiducial light cone and the peculiar velocity light cone without and with peculiar velocities switched on.

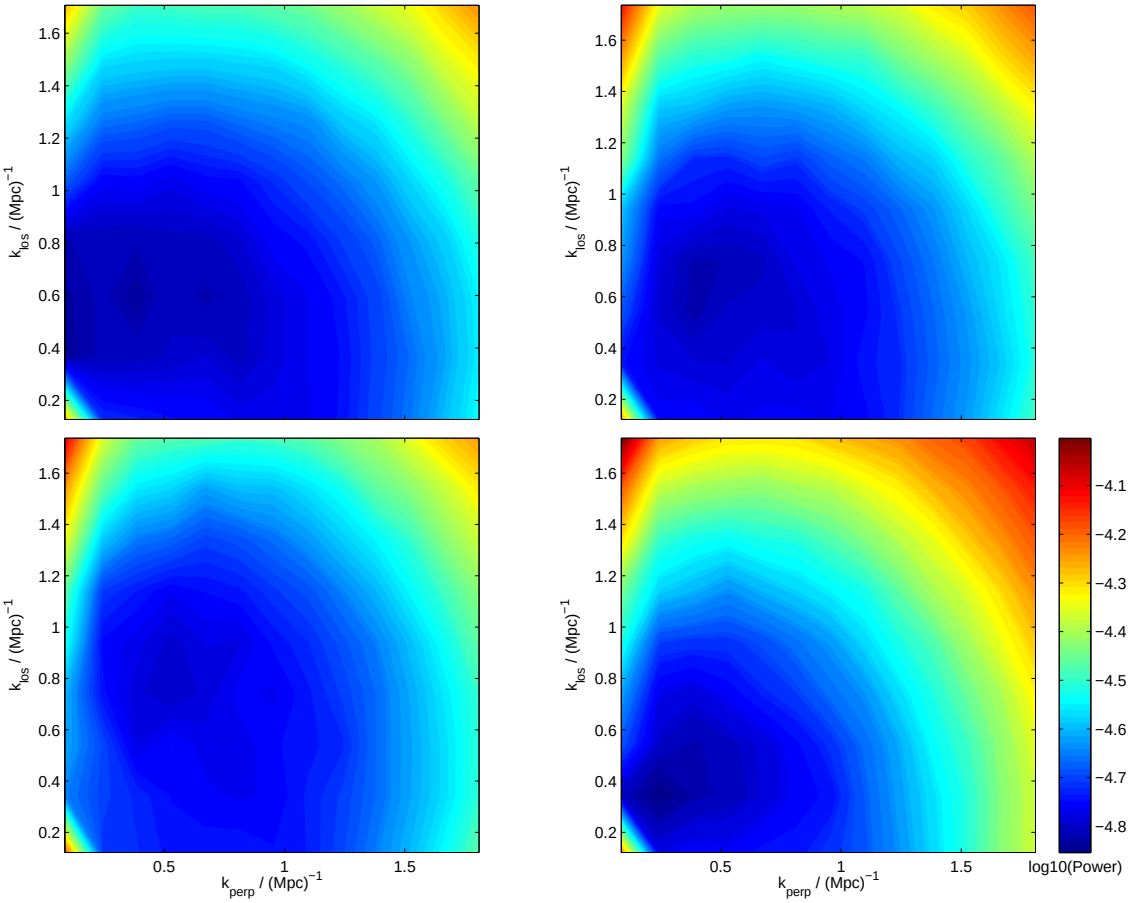

Figure 4.7: In reading order: The cylindrical power spectrum of the redshift box output by Simfast at z=8.22. An 8 MHz slice of the original light cone, centred at frequency 151.4 MHz. A 8 MHz slice of the new light cone centred at 151.4 MHz, with peculiar velocities set to zero. A 8 MHz slice of the new light cone centred at 151.4 MHz, with peculiar velocities included.

We can see that the differences between the new light cone on the bottom right and all the other plots in Fig. 4.4 occur on small spatial scales but with a large difference in temperature, and we see this in Fig. 4.7 as a significant difference in the power spectrum, with increased power at large k scales on the new light cone plot. Note that, because we are evaluating the power spectrum over a chunk of 8 MHz, we do not expect to see the evolution of the signal in the light cone power spectra. We have done this so as to decouple the light cone effect from the peculiar velocity effect somewhat. It is clear from Fig. 4.7 that the inclusion of peculiar velocities as carried out in this chapter has a significant effect on the statistics of the 21-cm power spectrum,

and is therefore an important amendment to the standard simulation output.

4.6 Conclusions

We have presented a new code, which will be published for public use, which calculates the redshift space light cone from the standard real space simulation output of any reionization code. We set out a physically motivated treatment of peculiar velocities, both in the 21-cm intensity equation and in the calculation of the observed frequency for each 21-cm event. This requires the individual assessment of each cell according to whether a 21-cm event would be observed at the frequency of observation and how the intensity must be adjusted as a result of the interaction of cosmological redshift and the peculiar velocity. We have shown that this full treatment produces significant statistical differences when compared to the standard real space simulation boxes or light cone where peculiar velocities are assumed to be zero. These differences are particularly large on the small scales thought the large scale bubble structure remains intact. We conclude that to be confident of any conclusions made from using light cone data, one must be sure to fully incorporate the peculiar velocities as shown here, especially for cosmological models which naturally have larger peculiar velocities.

Chapter 5

The EoR Window

The work in this chapter has been carried out in collaboration with F. Abdalla, S. Zaroubi and the EoR core team. This chapter will be submitted for publication as a scientific paper in Monthly Notices of the Royal Astronomical Society, Chapman et al. 2013b.

In this thesis, foreground removal has been shown to be essential in order to recover the 21-cm EoR signal. The EoR signal and the foregrounds have markedly different representations in k-space and as a result, there has been increased interest in the idea of foreground avoidance as a way of avoiding foreground removal and the biases it may introduce. An 'EoR window' in k-space, where the EoR signal dominates over the foregrounds has been defined in the literature (e.g. Dillon et al. (2013)), however the foreground models used to define this window are often incomplete or unphysical. In this chapter, we show that when a full physical foreground model is considered, the EoR window becomes non-existent due to the variation of the Galactic synchrotron spectral index according to the line of sight. We show that foreground removal recovers the window somewhat, however it is significantly reduced from that seen in the literature. We conclude that foreground avoidance is not a viable alternative to foreground removal, however it could be used after foreground removal as way of minimizing the bias on any estimated statistics.

5.1 Introduction to the EoR Window

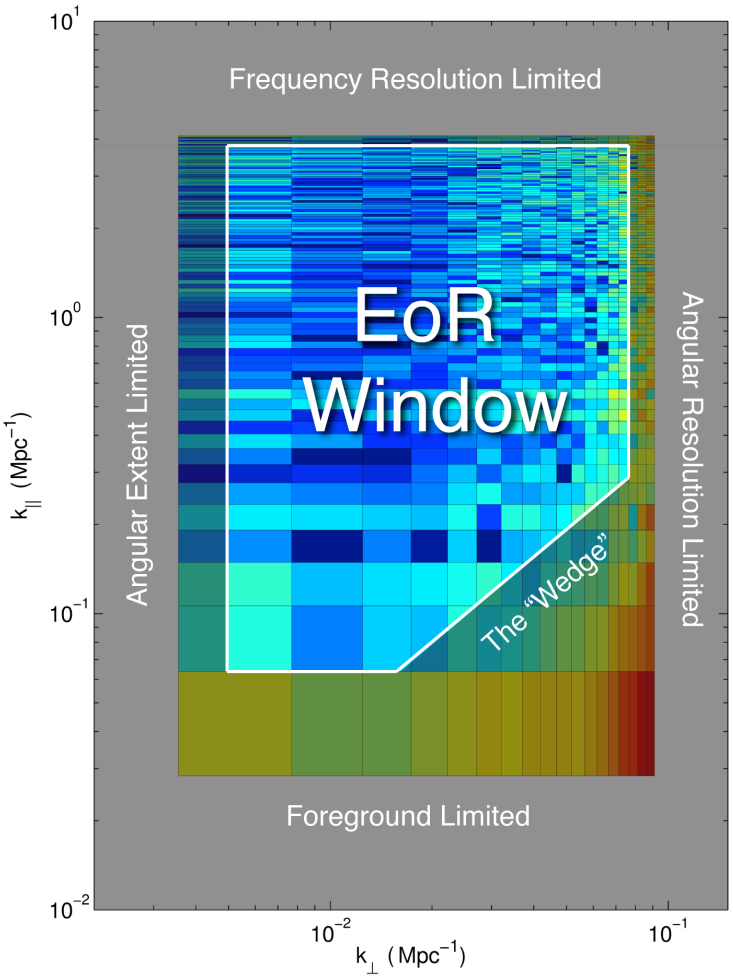

Figure 5.1: An example of the EoR window as shown in Dillon et al. (2013). The foregrounds are clearly seen at low $k_{\parallel}$ and, at high $k_{\perp}$, leaking into higher $k_{\parallel}$ scales.

One of the biggest challenges to overcome in order to detect the EoR signal is the need for extremely precise and accurate foreground removal. Without this removal the signal is buried under a foreground signal greater by order of roughly three magnitudes. In the literature several approaches have been discussed, including polynomial fitting and the non-parameteric methods detailed in this thesis.

Alongside foreground subtraction, there has been discussion of other tactics to extract the signal in a clear way. Foreground avoidance was originally suggested as a way of bypassing the stringent requirements of foreground subtraction by searching for the signal in a region of k-space where foregrounds are sub-dominant compared to the signal. A 2D cylindrical power spectrum in $k_{\perp}, k_{\parallel}$ clearly shows the areas of k-space where different signal components are dominant and can be used to define a region where the cosmological signal can be clearly picked out - an 'EoR

window'.

The EoR window is bounded by five physical properties of the experiment, Fig. 5.1. The $k_\perp$ boundaries are as a direct result of the system noise increasing significantly where there is a lack of baselines. At low $k_\perp$ the window is bounded by the physical extent of the interferometric array, L_{max}. At high $k_\perp$ the boundary is given by the extent of the array in uv space, which is effectively the shortest baseline used in the observation being considered, L_{min}. For $k_\parallel$ it is the frequency characteristics of the array which define the boundaries. At low $k_\parallel$ it is the bandwidth of the instrument, B, whereas at high $k_\parallel$ it is the frequency resolution of the observation, $\Delta\nu$. These boundaries are defined in Equations 5.1-5.4, also described in Vedantham et al. (2012), where $D_M(z)$ is the transverse comoving distance at redshift z and $E(z) = \sqrt{\Omega_m(1+z)^3 + \Omega_\Lambda}$.

$$k_{\perp_{max}} = \frac{2\pi L_{min}\nu_{21}}{c(1+z)D_M(z)} \tag{5.1}$$

$$k_{\perp_{min}} = \frac{2\pi L_{max}\nu_{21}}{c(1+z)D_M(z)} \tag{5.2}$$

$$k_{\parallel_{max}} = \frac{2\pi H_0\nu_{21}E(z)}{c(1+z)^2\Delta\nu} \tag{5.3}$$

$$k_{\parallel_{min}} = \frac{2\pi H_0\nu_{21}E(z)}{c(1+z)^2 B} \tag{5.4}$$

The fifth boundary is a little more complicated. It has been noted in the literature that the foregrounds reside in a specific region in the Fourier domain. For instance, Dillon et al. (2013) defines a bound at low $k_\parallel$ where any EoR detection would be foreground limited. Furthermore, a wedge at high $k_\perp$ is defined due to the mode mixing of the foregrounds as a result of the varying PSF as a function of frequency. This effect is stronger on larger $k_\perp$ scales because of the higher fringe rate for point sources which reside at higher $k_\perp$. The wedge was pointed out originally by Datta et al. (2010) and further mathematically in, for example, Dillon et al. (2013) as reaching no further than the line:

$$k_\parallel = k_\perp \sin(\Theta)\frac{H_0 D_c(z)E(z)}{c(1+z)}, \tag{5.5}$$

where Θ is the field of view and $D_c(z) = \int_0^z = dz'/E(z')$.

All these analyses have been performed on different simulated or real data with different levels of complexity and using different methods of foreground subtraction. Originally, Datta et al. (2010) observed a wedge as a result of considering bright point source extragalactic foregrounds

only and performing a simple polynomial subtraction. In Vedantham et al. (2012), a careful study of the effect of the PSF and uv gridding effects on the wedge was performed, however only bright point sources were considered, without considering the effects of foreground subtraction. Morales et al. (2012) explained that the wedge shape is due to a chromatic instrument response and information loss in each antenna, however it is unclear how physical their model of the diffuse foreground is. Trott et al. (2012) considered imperfect point source subtraction and the effect on the EoR window, suggesting that the contamination from residual point sources would not be a limiting effect in the EoR detection. Parsons et al. (2012) considered diffuse synchrotron emission alongside extragalactic foregrounds however they did so assuming the spectral distribution of the synchrotron is a simple scaling of a $\nu^{-2.5}$ power law derived from the low resolution Haslam map. This neglects small-scale power and any potential variation of the spectral index. The most recent recent study, Dillon et al. (2013), used real MWA data but did not compare to simulation.

5.2 Simulations

We attempt to take a further step in the complexity of the foreground simulations than has been previously considered in the literature. We utilise the full foreground models described in section 1.4. These simulations include contributions from Galactic free-free, extragalactic foregrounds and Galactic synchrotron. The resolution of these simulations is much smaller than those considered in Parsons et al. (2012) and so can be considered to contain much more small-scale power. In addition, we consider the full physics of the Galactic synchrotron which implies a varying spectral index slope as a function of line-of-sight.

These two improvements could modify the EoR window significantly because of the way in which a varying spectral index could introduce a mixing of the power in ($k_\perp$,$k_\parallel$) and hence the EoR window could be compromised due to significant foreground power leaking into the EoR window.

In order to understand this, consider two different lines of sight. If we first consider that both have the same spectral index, $\alpha_0 = \alpha_1$, where $\nu \propto \alpha$, then any anisotropies in the foreground distribution will reside at $k_\parallel = 0$. If we now allow $\alpha_0 \neq \alpha_1$ then these anisotropies can be found at higher $k_\parallel$. This would mean a potential reduction in the foreground sub-dominant region of the EoR window which will depend crucially on how the spectral index varies as a function of sky position as well as how strong the original foregrounds are.

In order to test the more complex model we plot the power spectrum in the $k_\parallel$ vs. $k_\perp$ plane for different model components and frequencies of observation. Note that in the figures, $k_{los} = k_\parallel$

and $k_{perp} = k_{\perp}$.

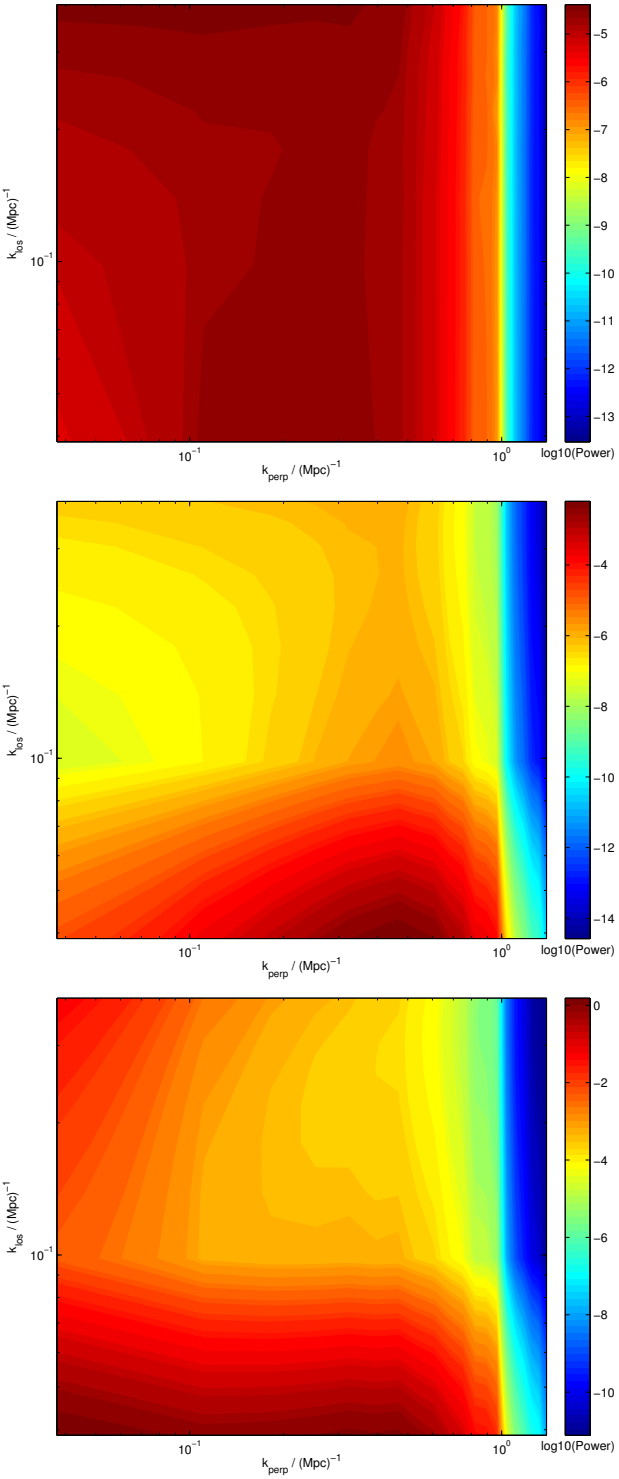

Figure 5.2: The cylindrical power spectra for the simulated cosmological signal (top), the extragalactic foregrounds (middle) and the full foreground model including Galactic synchrotron with a varying spectral index (bottom).

In Fig. 5.2 we can see first the shape of the cosmological signal in the $k_{\parallel}$ vs. $k_{\perp}$ plane. The power is severely decreased at high $k_{\perp}$ due to the action of the PSF which is also seen in the

other panels. In the central panel we clearly see the point sources dominating at low $k_{\parallel}$ but subdominant compared to the 21-cm EoR signal at high $k_{\parallel}$. On the full foreground model we see the extra power at low $k_{\perp}$ and high $k_{\parallel}$ significantly reduces the EoR window. This is due to the fact that, as explained above, there are anisotropies in the synchrotron which, due to varying spectral indices, appear in the low $k_{\perp}$ region. This is because the power spectrum of the Galactic foregrounds is stronger at low $k_{\perp}$, i.e at large sky scales, and the variation of the spectral index mixes power into the larger $k_{\parallel}$ scales.

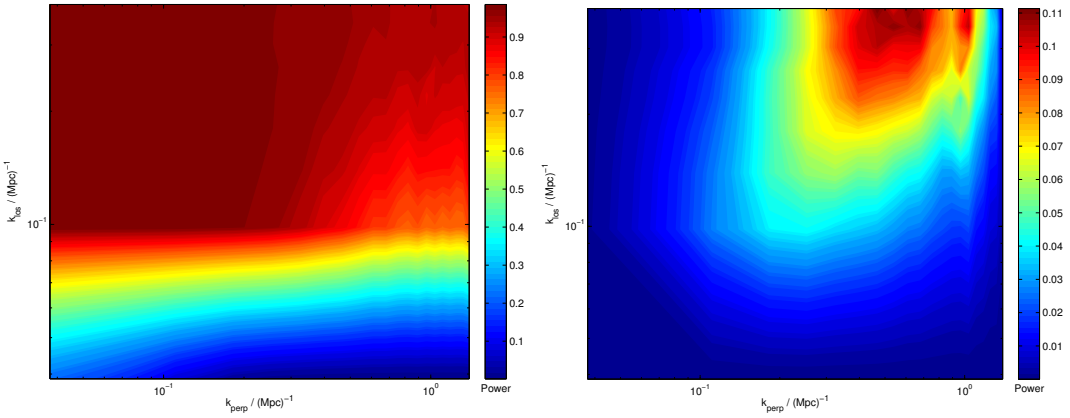

Figure 5.3: On the left we see the ratio of the cosmological signal with the extragalactic foregrounds and can clearly see the EoR window which Datta et al. (2010) found. However once we consider the full foreground model on the right we see this window completely destroyed.

In Fig. 5.3 we show the ratio of the cosmological signal to the extragalactic foreground model and we can clearly see the EoR window appearing in dark red where a dominant fraction of the signal is not due to the extragalactic foregrounds. This happens above $k_{\parallel} = 0.1$ and $k_{\perp} < 0.2$. This is in agreement with previous studies. We note that we have not considered a frequency-dependent PSF and hence the wedge boundary is not present in this plot. However we believe this is not necessary in this study as we are focusing on the effect of a more physical Galactic foreground model on the EoR window. When we do include the full foreground model in the ratio we see the EoR window significantly contaminated due to the anisotropies as discussed previously. This shows that foreground avoidance instead of foreground removal is a difficult concept to use on real data.

5.3 The EoR Window and Foreground Subtraction

We now discuss whether we can recover the EoR window after a foreground subtraction. We use GMCA to remove the foregrounds from the full model, including instrumental noise, and define the foreground fitting errors as the difference between the simulated foreground model

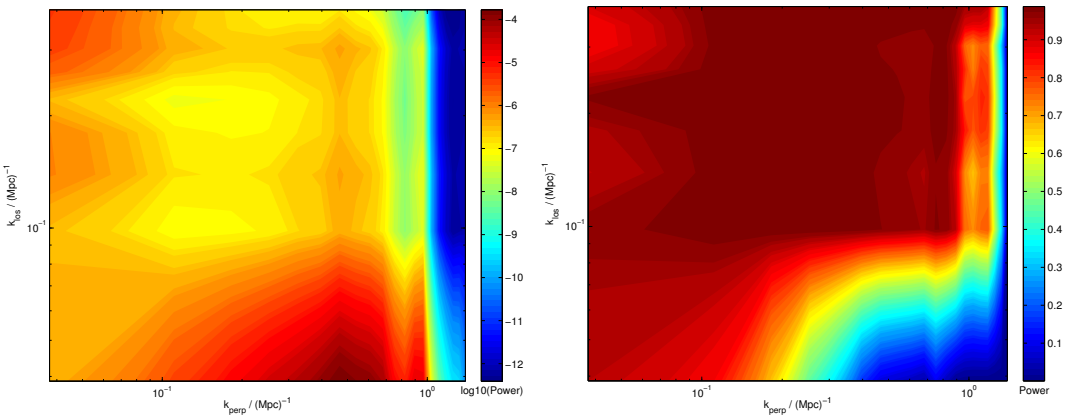

Figure 5.4: We plot the power spectrum of the foreground fitting errors on the left and the ratio of the simulated 21cm signal with the fitting errors on the right. We can see that, after foreground removal, an EoR window is recovered.

and the GMCA foreground model. The data cube is the same as described in section 2.2. In Fig 5.4 we see the cylindrical power spectrum of the fitting errors. We can see clear foreground leakage as a result of GMCA not fitting the foregrounds equally well across k-space. If we take the ratio of the simulated EoR signal and the foreground fitting errors we show that we would be able to recover the EoR window well, once the instrumental noise is taken into account. Without foreground removal there was no part of the power spectrum where the 21-cm signal dominated the foregrounds with the EoR signal being, at best, a magnitude smaller. With foreground removal we see a large area of k-space where the cosmological signal dominates over the foreground fitting errors. It should be noted that his window is significantly reduced from the window theorized in literature - with contamination at small $k_\perp$.

The practice of foreground avoidance is not unique to EoR data and has been considered in other fields such as intensity mapping. For example, Shaw et al. (2014) use an eigenvalue decomposition to select modes with signal-to-foreground power above a certain threshold for their analysis. Although it is not totally obvious from first instance that these methods are the same as foreground avoidance, the spirit of finding a basis where the foregrounds and signal are split in an optimal way is similar in spirit to the EoR window literature. This eigenvalue analysis would be a more effective method than using the EoR window, especially for diffuse sources, as it would ensure the maximum amount of contamination was ignored without compromising the amount of signal left to analyse.

The obscuration of the EoR window is an important thing to consider when measuring statistics such as the redshift-space distortions. Redshift space distortions create a small anisotropy in the cylindrical power spectrum which can only be carefully measured in the absence of contamination. If one was to attempt to measure the redshift space distortions on the whole measurement

window without first considering the foreground residual contamination, the results would be in danger of great inaccuracy.

5.4 Conclusions

Due to the small signal-to-noise of the EoR observations and the relatively unconstrained nature of the foregrounds there has recently been increased speculation about using 'foreground avoidance' as opposed to 'foreground subtraction' as a method to detect the EoR. These speculations have been largely based on low complexity foreground models and simple foreground removal and here we attempted to remedy this by checking that the conclusions are still valid under more complex assumptions for the foregrounds. We showed that the EoR window defined in the literature is significantly contaminated when a full physically motivated foreground model is used. This is as a result of the Galactic synchrotron having different line-of-sight spectra primarily due to spatial fluctuations of the spectral index which appears as an anisotropy along the line of sight, imposing a much stronger $k_{\parallel}$ bound than previously defined. For the full data cube this results in the area of the EoR window being shrunk to zero. We then performed a non-parameteric foreground subtraction using GMCA and showed that the EoR window can be recovered quite well though significant contamination remains at small $k_{\parallel}$ and small $k_{\perp}$. Though we have shown that utilising the EoR window as a method of foreground avoidance is untenable, foreground avoidance on the residuals of a foreground removal process is a possible way of obtaining a potential systematic-free detection. By doing so one would have to restrain measurement to within a shrunken EoR window which will depend on the complexity of the foregrounds. For example the simulated data in Fig. 5.4 suggests that we can recover an accurate EoR signal only in the central and upper part of the entire window available with the experimental setup modelled.

Chapter 6

First Light

The work in this chapter will be part of the analysis to be published in a future paper by the LOFAR-EoR core team.

Real data always presents challenges which were not expected or fully treated in the simulation stage of an experiment. In this chapter we apply GMCA to some of the first LOFAR-EoR data, as a preparatory step in order to identify parts of the pipeline which need optimising. The 54 hours of data was taken over four nights over an 8.5 square degree window centred on the North Celestial Pole, with a resolution of 0.5'. We find that GMCA is a powerful tool for identifying systematics in the data, with the separate components in the reconstructed foreground model seeming to have physical interpretations such as the action of the primary beam or the variation of a point source spectral index. We find that GMCA is so powerful at identifying the point sources than it can be used as a feedback tool to the calibration method in order to improve future point source modeling. In order to mitigate the effect of the high instrumental noise, we take the opportunity to adapt GMCA so that it weights the subbands according to noise values when constructing the mixing matrix. We find that, for certain sources, this noise weighting results in a cleaner residual, however concede that a full statistical analysis will need to be carried out in order to exclude the possibility that too much signal is being down-weighted. We consider how wavelet filtering the data can improve the GMCA analysis and finally we look at the GMCA reconstructed foreground model when it is applied to the Stokes U, Q and V data. We find that estimating the noise from the Stokes V data is an accurate method and conclude that there is much less structure in the polarized foregrounds overall.

6.1 First Light for LOFAR-EoR

After over a decade of development, December 2012 saw first light for the LOFAR EoR project and the first analyzable data has finally arrived. In this Chapter I present a qualitative assessment of the performance of GMCA on 54 hours of Stokes I,Q,U and V data taken over four nights. The data shown here has 0.5' pixel resolution and 195 kHz frequency resolution, with a field of view of 8.5 square degrees centred at the North Celestial Pole (NCP). We show a subband of this data at 151 MHz in Fig. 6.1. 48 core stations and 13 national Dutch stations were used to make the observations between 115 MHz and 189 MHz. Though this data is not quite 'science ready', it is still valuable to apply the foreground removal methods since real data always presents new challenges compared to the simulations we have applied GMCA to before. This preliminary analysis can help identify both systematics and other telescope effects such as the action of the primary beam. It is important to note that this is a preliminary run only, to aid understanding of the systematics for when the modelling is good enough for scientific analysis.

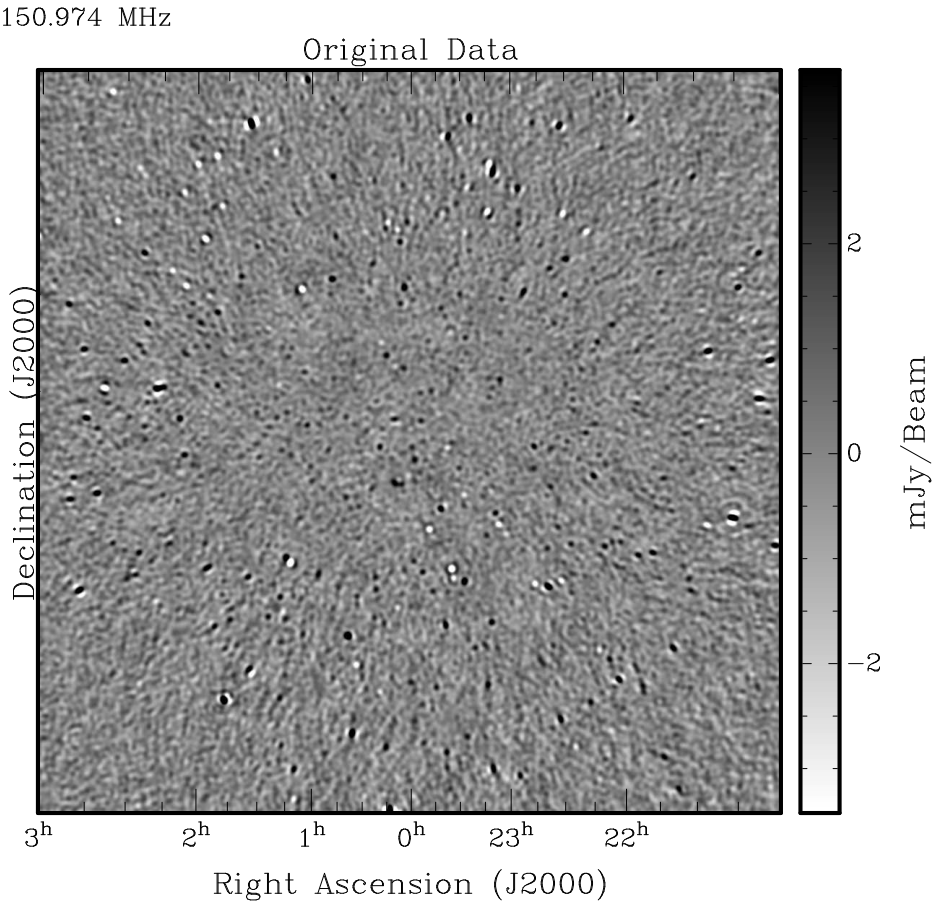

Figure 6.1: The original data centred on the NCP, before foreground removal, at 151 MHz. This map has a resolution of 0.5' over a 8.5 square degree window.

Here we present the results of applying GMCA to the data in several different ways. First,

we apply GMCA to the entire observation frequency range. Then, we experiment with weighting the mixing matrix in GMCA according to the noise values of each subband. We can then go a step further and artificially set the noise covariance matrix values corresponding to very noisy slices to zero. This effectively leaves these slices out of the GMCA foreground model. We also consider how wavelet filtering the data before performing GMCA is beneficial and finally we look at the polarized foreground models constructed by GMCA.

6.2 Foreground Removal on 54hr Stokes I Data

6.2.1 A Preliminary GMCA Application

We first run GMCA on the Stokes I data with all subbands included and no modifications to the code beyond those already defined on the simulation run. We choose a four component foreground model for the results shown in Fig. 6.2.

We can see straight away that GMCA does remove a significant fraction of the foregrounds, including point sources which remained in the data after calibration. We note that most of these point sources were not included and removed in the calibration step. Some will be sources which are poorly subtracted while others will be faint sources not considered.

In order to assess the accuracy of GMCA we can look at the spectra of the residuals to ensure that there are no smooth components remaining along the line of sight. We plot three lines of sight in Fig. 6.3. In the first plot we have chosen a pixel which appears to have no residual foreground contribution in any of the subbands. We can see from the spectrum that the contribution effectively looks likes noise. From the inspection of most of the data, a significant fraction of the pixels look like this, indicating that GMCA has been successful in removing the foreground contribution over the majority of the data.

The systematics in the data which have not yet been addressed in the calibration step result in GMCA being unable to remove certain foreground contributions. In the remaining two plots of Fig. 6.3 we show pixels where this is the case. There is a particularly bright source, close to the centre of the field, which is hard to model because it has spatial structure on the arcsecond scale which is not available to us in the data. Furthermore, it is possible that the spectral modelling also is not sufficient. In the middle plot we show the residual spectrum of this source and can clearly see the effect of incomplete modelling. This information can be fed back into the calibration method which will improve the systematic in further data analysis.

Some residual foreground sources only appear in a few subbands as opposed to across the whole frequency range. This is evidence that, though the source has been modelled, the calibra-

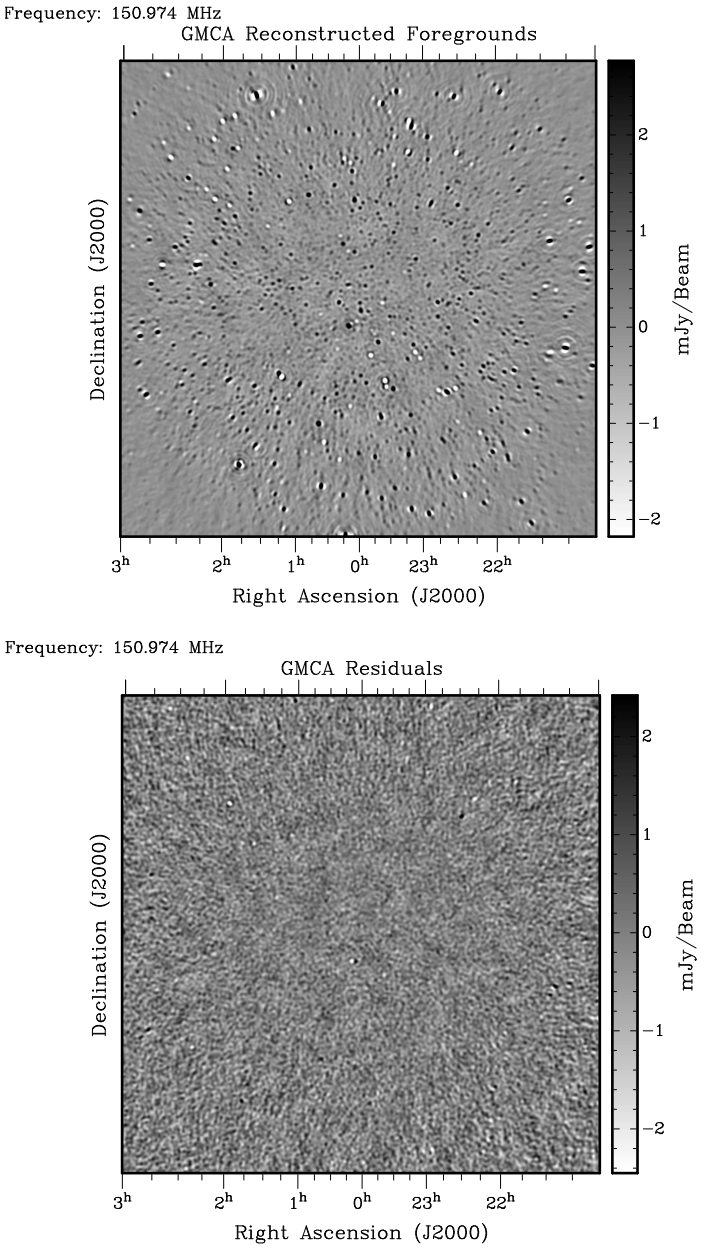

Figure 6.2: Results of applying GMCA on the original data for a four component foreground model. Top: The foreground model calculated by GMCA. Bottom: The residuals of the GMCA foreground removal. This should consist of the cosmological signal, noise and any fitting errors. All images are at 151 MHz. The sum of both of these components is equal to the original data shown in Fig. 6.1.

tion method has not converged to a solution in those subbands. In the bottom plot we show a spectrum of a source like this and we can see the spike corresponding to this behaviour at around 140 MHz and 152 MHz. This is a problem which has been previously identified and improved upon considerably.

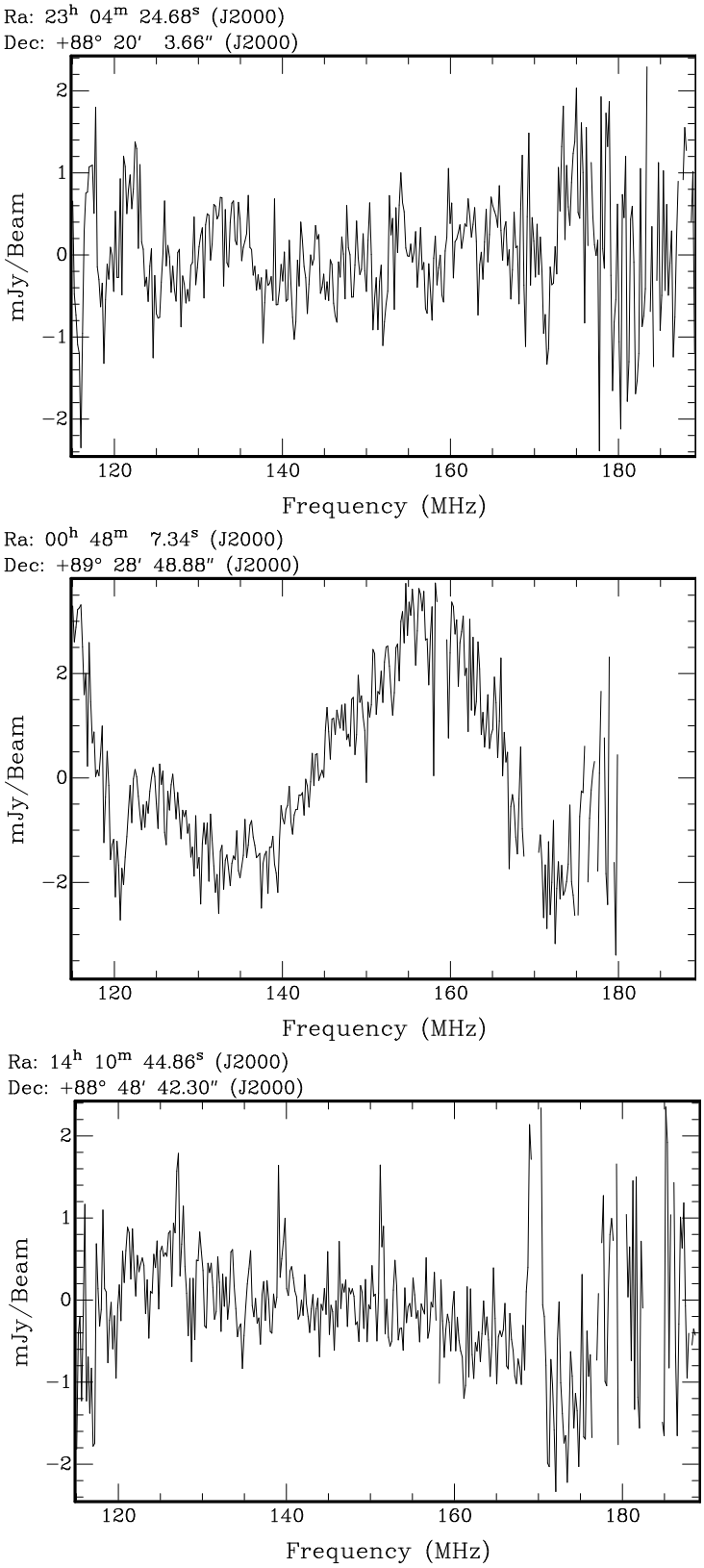

Figure 6.3: Here we look at the residuals along the line of sight. Top: The spectrum of a typical pixel. Middle: The spectrum of a point source which has been poorly subtracted and appears throughout the frequency range. Bottom: The spectrum of a source which has been poorly subtracted in a few subbands only.

6.2.2 Sensitivity to Foreground Component Number

In the previous chapters we ran GMCA on simulations assuming a two component foreground model. This choice of parameter is sensitive to the foregrounds and the systematics in the data, and therefore we reinvestigate the sensitivity of the results to the choice of component number.

It is evident from the left hand panel of Fig. 6.2 that there remain point sources which aren't picked up by either the calibration step or the foreground removal. We now attempt to see whether we can increase the number of these included in the foreground model by adding further components to the GMCA foreground model. In Fig. 6.4 we show difference maps between the residuals with 2 and 4 components and 4 and 6 components. We see clearly that with 4 components more point sources are removed compared to the 2 component model, and even more are picked out when moving from 4 to 6 components. For a full treatment of the data we will need to cross-correlate the residuals with the GMCA foreground model maps in order to quantify the leakage and optimise the number of components chosen so as to maximise the foregrounds fitted while minimizing the amount of 21-cm signal fitted into the foreground model. A similar analysis was carried out on the simulated data in section 3.3.1. We conclude that for studying systematics in the data it is beneficial to use a six component model. We do not consider higher component models as we wish to understand the systematics before we investigate further.

GMCA turns out to be very powerful in defining the different foreground components. In Figs. 6.5 and 6.6 we show the six components which are estimated by GMCA together with their corresponding spectra. Though the components are likely to be a correlated mixture of all the physical foreground elements, and in the case of real data, systematics, the components shown here have quite physical meanings. We note that there is no specific order to the GMCA components and also that the plotted components are not normalized in flux. In the first and third components, the fitted foreground sources appear to be close to the first null of the primary beam and they both have very smooth spectra between 115 MHz and 180 MHz. This data has not been corrected for the primary beam which has the effect of changing the frequency spectrum of a source as the beam changes size with frequency. This results in a modulation in the spectrum along the line of sight depending on the location of the source in relation to the centre of the field. The smooth variation of the spectra over frequency and the concentration of the sources near the null suggest that GMCA is fitting the effects of the primary beam on the source spectra in these components.

The second and sixth components show a multitude of point sources, many of which are correlated spatially between the components. This indicates that the sources in these components

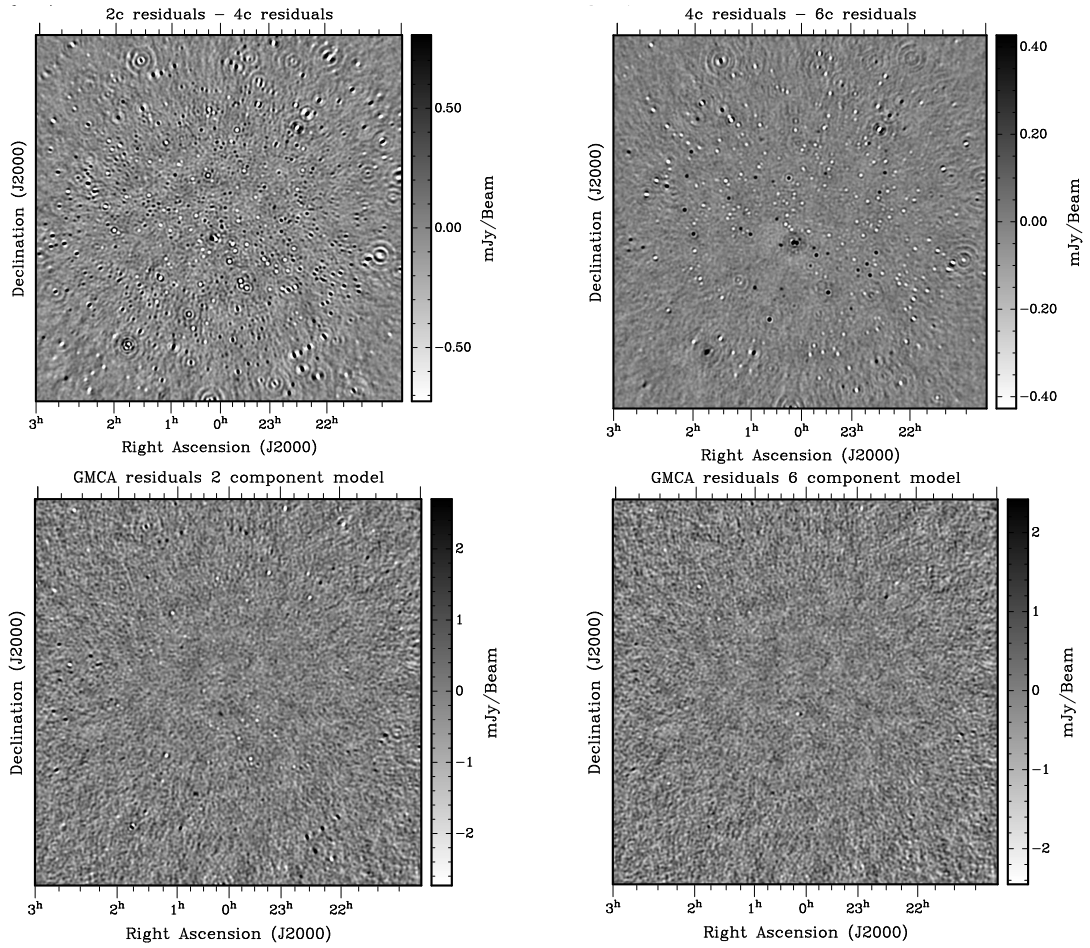

Figure 6.4: On the top left we see a difference map between the residuals with a 2 and 4 component foreground model. On the top right we see a difference map between the residuals with a 4 and 6 component foreground model. On the bottom left are the residuals with a 2 component model and on the right is with a 6 component model. All data is taken at 151 MHz.

have spectra which require more than one sparse representation in order to be fully described. The second component is comprised of sources which are all positive in flux, concentrated within the centre of the field. These are sources which can be fed back into the source calibration methods in order to increase the accuracy of point source calibration in future analysis. The sixth component seems to be the way in which the variation in spectral index of the point sources creates a frequency structure, given that the sources appear in both positive and negative flux.

The fourth component is evidently a single bright source. The fifth component seems to be related the extremely high amount of noise present in one single subband. The component map itself looks extremely noisy and the spectra shows a single peak corresponding to a subband at just below 180 MHz, which we know to have high noise.

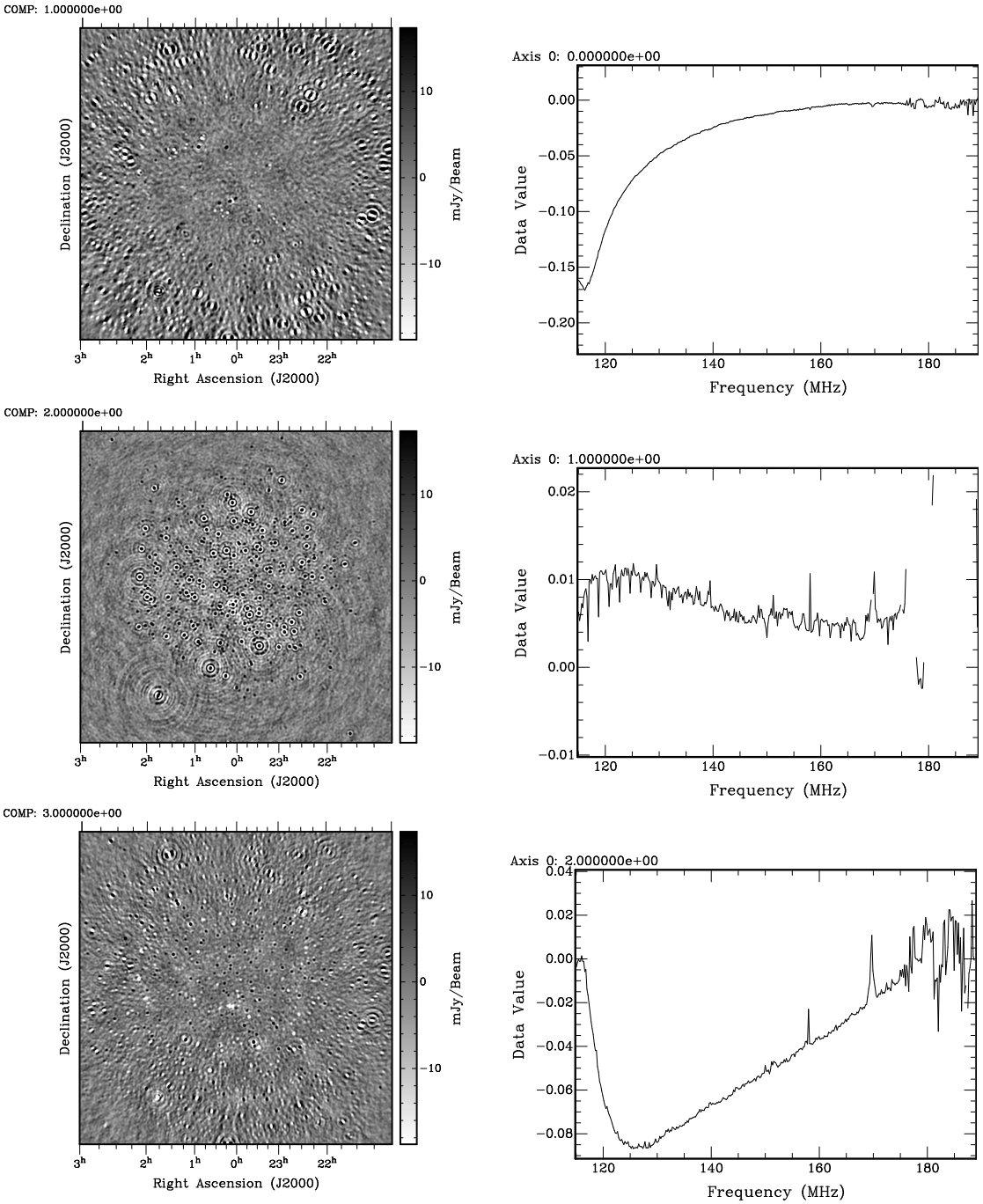

Figure 6.5: The first three GMCA foreground model component maps and their spectra.

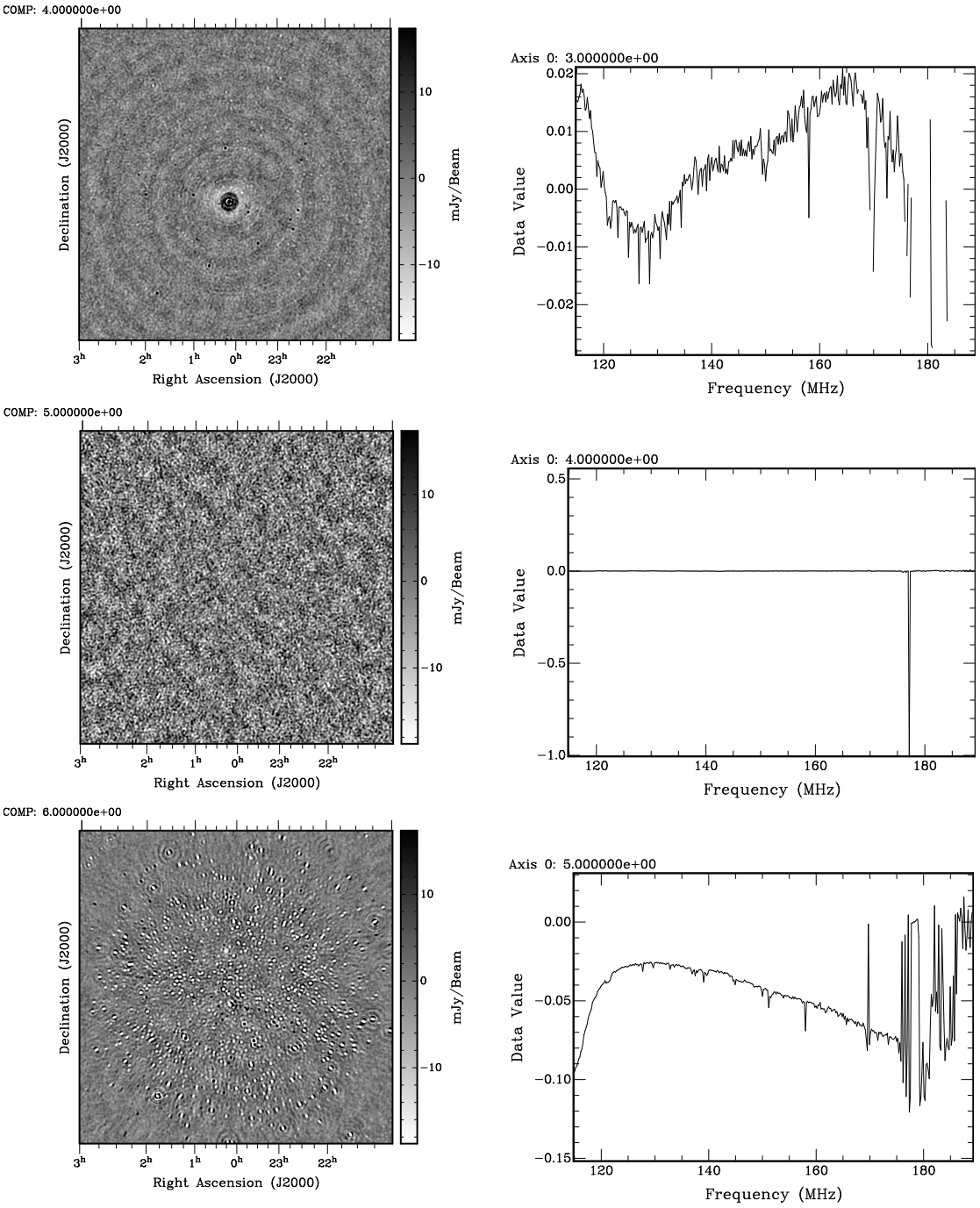

Figure 6.6: The last three GMCA foreground model component maps and their spectra.

By considering the component results it is clear that there are three main contributions to the systematics which need to be addressed before future analysis. First, the effect of the primary beam needs including within the GMCA model. This is beyond the scope of this thesis and will be addressed in a future analysis. Secondly, the effect of the instrumental noise on the performance of GMCA. We make a preliminary attempt at addressing this in the next section. Finally, we have the incomplete modelling of point sources in the calibration steps and this will be dealt with in the LOFAR-EoR pipeline. The ability of GMCA to separate point source contributions in this way show that it can be used as a tool to identify missed point sources and used as a feedback tool to a calibration method such as SAGECAL (Kazemi et al., 2011; Kazemi et al., 2013) which is the method used in the LOFAR-EoR pipeline.

We choose to run GMCA with 6 components for the rest of this chapter, however in future work one should be careful in the component number choice as GMCA is clearly sensitive to systematics with that choice. For different component numbers, one should ultimately cross-correlate the reconstructed foregrounds with the residuals in order to find the component number which minimises the foreground leakage, which we do not attempt in this chapter.

6.3 GMCA with Noise Weighting

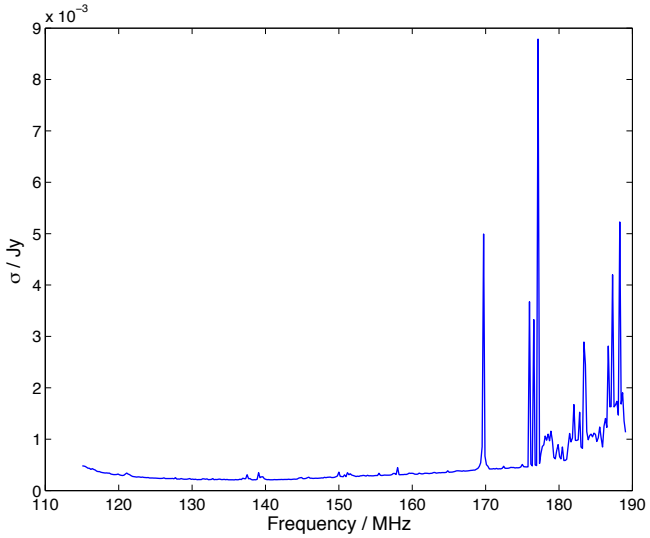

Figure 6.7: The rms of the noise vs. the subband frequency.

There are multiple bands within the data which have noise rms values so high as to endanger the GMCA recovery, Fig. 6.7. This noise spectrum was calculated from the Stokes V data, which is expected to be entirely dominated by instrumental noise. Here we attempt to mitigate the effect of the noisy subbands on the GMCA model by weighting how much importance GMCA

gives the data at a certain frequency when determining the foreground model.

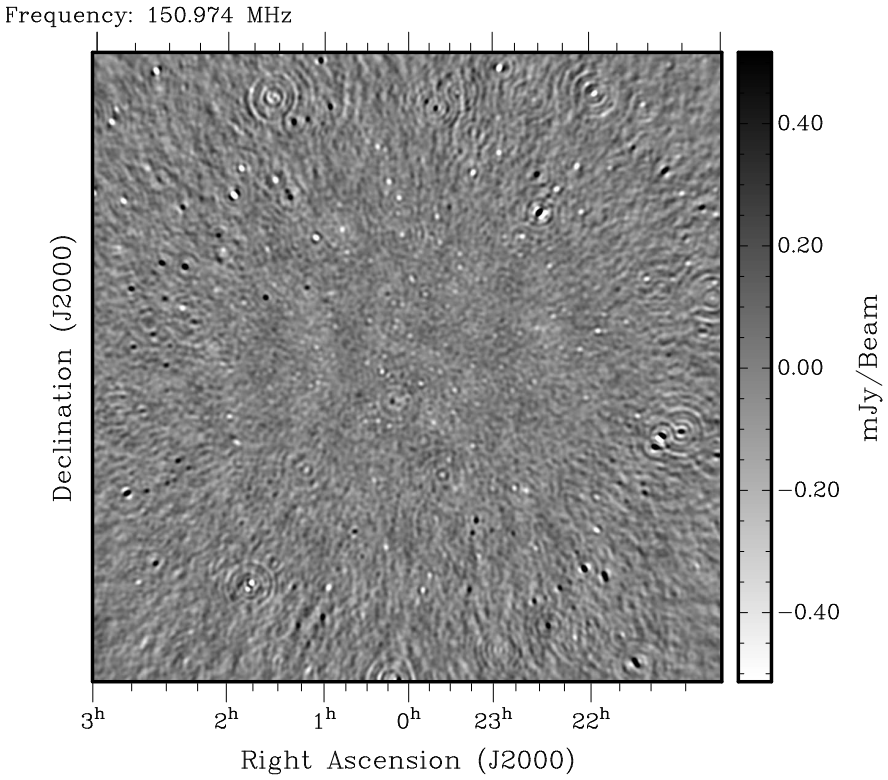

Figure 6.8: The difference map at 151 MHz between the GMCA residuals with and without noise weighting.

The original GMCA equation to calculate the pseudoinverse of the mixing matrix, $\hat{A}$, is as follows:

$$\hat{A}^{-1} = (A^T A)^{-1} A^T. \tag{6.1}$$

In order to weight the columns of the mixing matrix according to the noise covariance matrix, C, we can include it in the GMCA model as follows:

$$\hat{A}^{-1} = (A^T C^{-1} A)^{-1} A^T C^{-1}. \tag{6.2}$$

We construct a diagonal covariance matrix from the data in Fig. 6.7 as there is no noise correlation between any two subbands. We note from Fig. 6.7 that the last 100 subbands are noticeably more noisy than the rest. We look at how GMCA is improved by doing the noise weighting as above and also setting the last 105 subbands to have zero contribution to the noise covariance matrix - effectively telling GMCA to ignore them when estimating the mixing matrix.

We plot the difference maps between the original residuals and the noise weighted residuals

for a six component GMCA model in Fig. 6.8. We see that the weighting of the mixing matrix results in several point sources being fitted differently between the two maps. It is not obvious at this stage whether the fitting is beneficial or not, as by weighting down some subbands there is the risk of weighting down any good data in those subbands also. We therefore show the residuals around a specific source which we know is contaminating the map when weighting is not used, Fig. 6.9. In the top left plot we show the residuals without noise weighting and can clearly see the point source contamination. We then show the residuals with the two noise weighting schemes described above, and the contamination is significantly reduced in both. We conclude that noise weighting can be beneficial to the foreground removal process in the case of some specific sources but we would have to carry out a full statistical analysis to make any secure conclusions. We will carry this out in a future work.

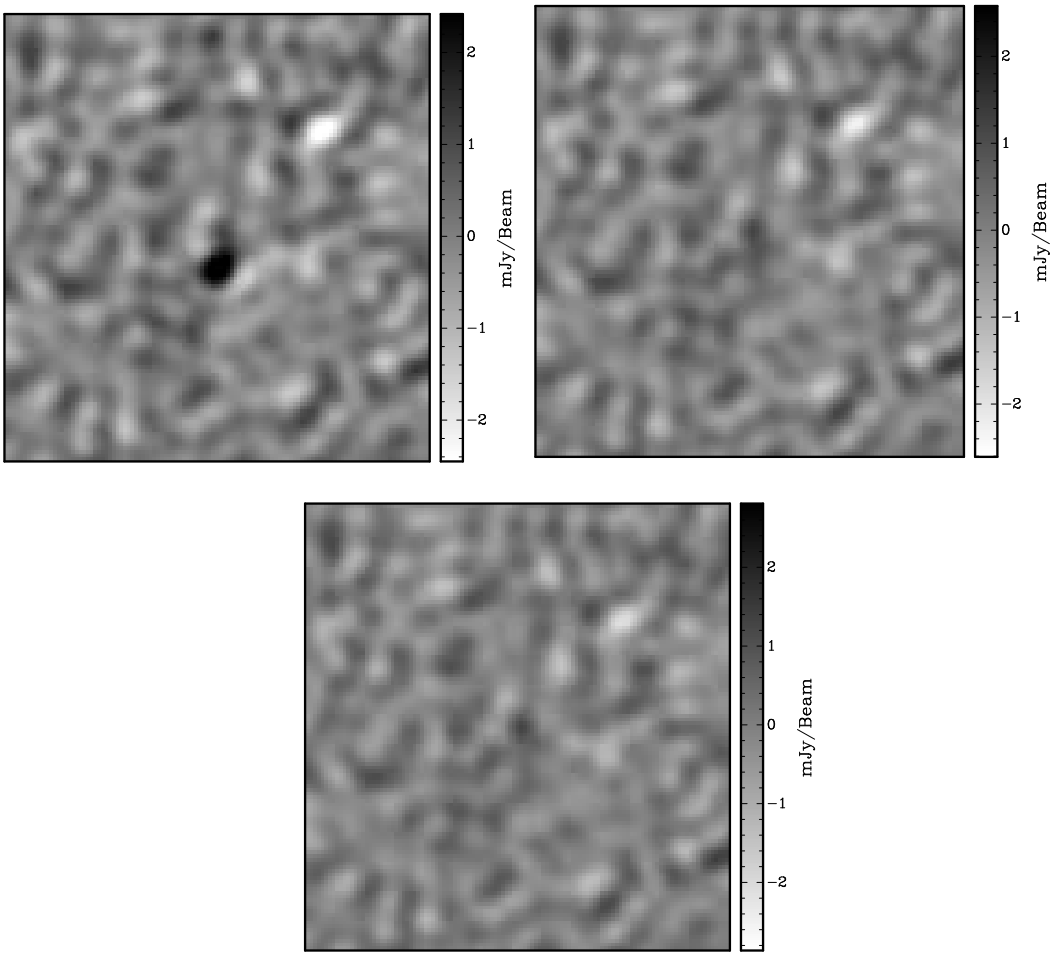

Figure 6.9: On the top left we see a map of the original residuals at 151 MHz. On the top right we see the same map but where GMCA has included noise weighting. On the bottom we see again the same map but where GMCA has included noise weighting and ignored the last 105 subbands when fitting the data.

6.4 Wavelet Filtered Data

We have seen that the point sources are proving to be a challenge in the EoR recovery. Point sources are small scale by definition and so by finding a method to remove the small scale power on the data we can remove a lot of the point source contribution. In previous analysis we have shown that wavelet filtering the data is a more effective way of removing small scale noise than the traditional smoothing methods. We can use a standard wavelet filtering algorithm to decompose any data cube into several cubes, each containing only information on a small range of scales. We can then simply recombine the cubes containing the larger scale data only, in order to get a data cube with the small scale information removed. In Fig. 6.10 we show a subband from the original data and from the data which has been wavelet filtered to remove all spatial scales below 8 arcminutes. As expected, this results in a lot less point source contamination. There is of course a risk that in removing small scale data we will remove some of the 21-cm EoR signal and in the real scientific analysis this will need to be offset against the need for an uncontaminated residual. This is however easily modelled as we know the effect of the filtering on the 21-cm power spectrum.

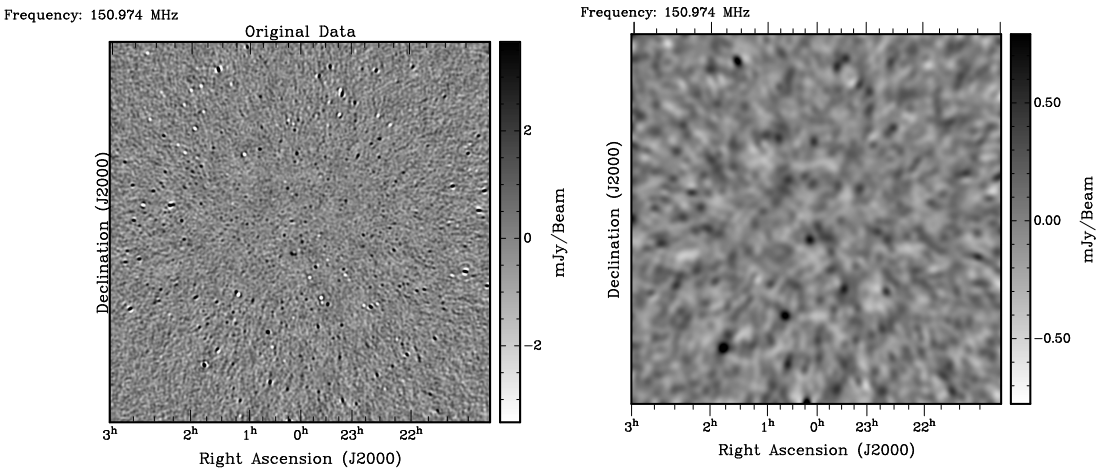

Figure 6.10: On the left we have the observed data at 151 MHz and we can see a large contribution from point sources. On the right we wavelet filter the data to remove angular scales below 8 arcminutes on the sky.

We can then apply GMCA to this filtered data, in order to get an idea of how GMCA would perform without the significant point source contamination we have seen so far. In Fig 6.11 we show the residuals of GMCA when applied to the wavelet filtered cube, with component model numbers of two and six. Whereas before we noted that there were many more point sources in the two source residuals, motivating the choice of a higher model component number, we see that there is little difference between the residuals when applied to the wavelet filtered data.

This indicates that the sensitivity of GMCA to the model component number is indeed led by the point source contamination level and that without this systematic the sensitivity is much lower.

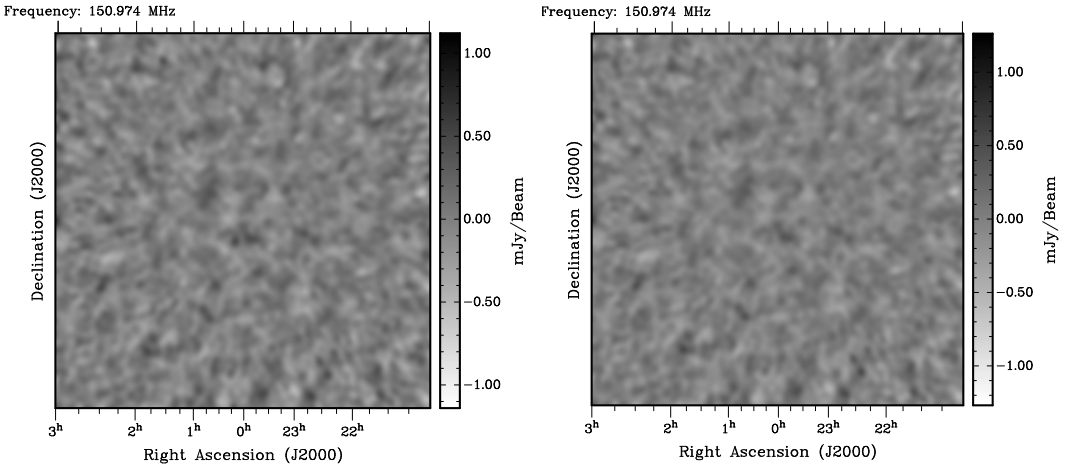

Figure 6.11: On the left we see a map at 151 MHz of the residuals with a two component model performed on wavelet filtered data. On the right we see the GMCA residuals performed on the same wavelet filtered data but with a 6 component model. We see a very small difference between the images, compared to the much greater difference when the data is not wavelet filtered (see. Fig. 6.4).

In the data we have shown so far, we note the presence of an apparent scale being imposed along the frequency direction, for example in the spectrum of components 2 and 4 in Fig. 6.5. The cause of this scale is thought to be as a result of calibration errors resulting from point sources outside the field and in more recent data where improved calibration has been carried out the scale appears to have been improved. The data used in this chapter is preliminary only and changing often on a short timescale, making the systematic tests carried out in this chapter essential.

6.5 Polarized Data

We now apply GMCA to the data in the other polarization modes: Q, U and V, and look at the GMCA reconstructed foreground model for each. As expected, the Stokes V map, which corresponds to circularly polarized light, appears empty apart from instrumental noise. This is as expected because the foregrounds are expected to be polarized only in the Q and U maps (i.e. linearly polarized). We can therefore be confident of our estimation of the noise from the V map as used in the previous sections.

In both the U and Q foreground maps we see a certain amount of point source and extended foreground contamination. The poorly subtracted strong point source appears most strongly in

the Q map but is also present in the U map. By looking at the spectral components of the Q and U foreground model we notice that, out of the six components, only two are significant in the Q map and only one in the U map. We can conclude that there is significantly less structure along the line of sight in the polarized foregrounds.

6.6 Conclusions

We have demonstrated that GMCA is a powerful way of characterising and removing foregrounds on real data and also an excellent tool for identifying systematics. Though the 54hr data used here is not quite 'science ready', we can make useful preparations by optimising the performance of GMCA with such data. We have shown that changing the component number of the GMCA foreground model has a significant effect on the cleanliness of the residuals and conclude that six components is a reasonable model number given the state of systematics in the data. This conclusion might change for future data sets. In order to optimise the component number, one should, for different component numbers, cross-correlate the reconstructed foregrounds with the residuals in order to find the component number which minimises the foreground leakage. We demonstrate that with a simple amendment to the mixing matrix equation in the GMCA model, we can ensure GMCA places more importance on less noisy channels when estimating the mixing matrix. This results in more point sources being modelled in the reconstructed foregrounds. We also show that one can artificially set the noise of very bad channels to infinity within GMCA so as to disregard them completely in the model. This appears to result in significantly fewer point sources leaking into the residuals but a full statistical analysis needs to be carried out to ensure this is not at the expense of a loss of signal information. The sheer number of point sources appears to be an important limit for the detection of the EoR signal. By wavelet filtering the data we show that GMCA is less sensitive to the choice of component number once the effect of the point sources can be disregarded after improved calibration.

Finally we look at the polarized foreground models constructed by GMCA and we confirm that the Stokes V map is a good indicator of the noise.

GMCA has proven to be a powerful tool on the real data, even when that data is extremely noisy and not optimally calibrated. Even before the data is ready for foreground removal in order to detect a signal, GMCA has proven to be a useful way of checking systematics and even feeding back to the calibration method.

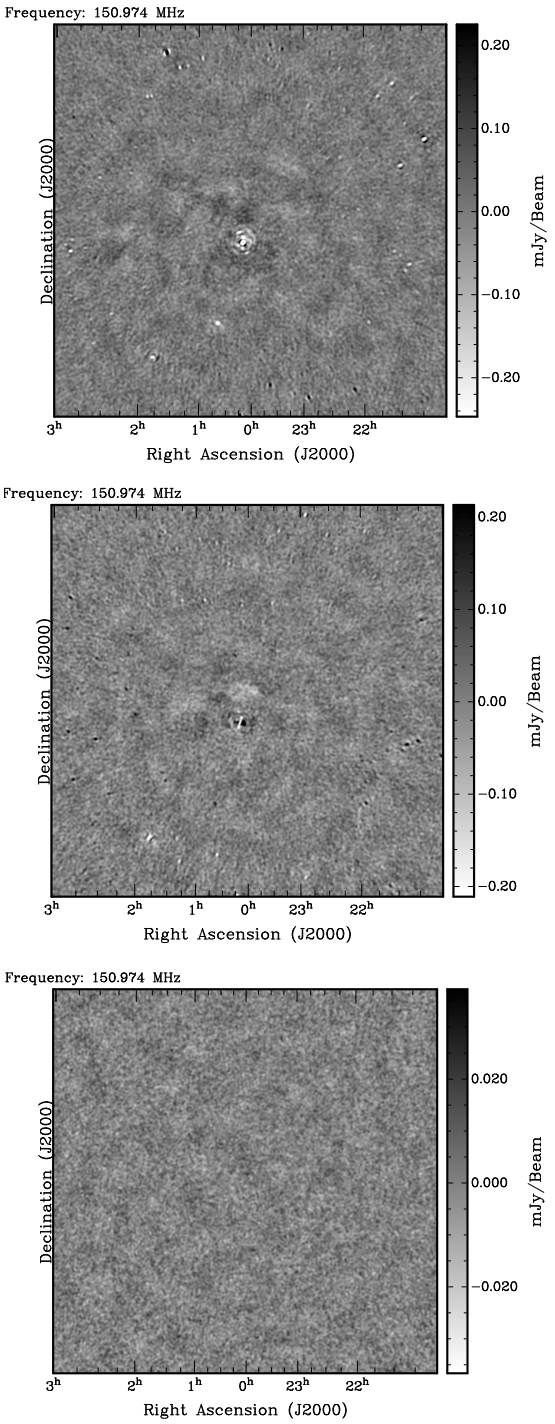

Figure 6.12: The reconstructed foregrounds at 151 Mhz for the Stokes Q, U and V data (from top to bottom.

Chapter 7

Thesis Conclusions

> We are all in the gutter, but some of us are looking at the stars.
>
> **Oscar Wilde**

Approximately 400,000 years after the Big Bang, the Universe had cooled enough so that most free electrons were swept up into stable atoms, ending the first era of ionization. As the Universe expanded and cooled, the overdensities in the density field steadily attracted more and more matter, forming dark matter haloes and ionizing sources. Whether these first ionizing sources were quasars, Population III stars or something more exotic, 400 million years after the Big Bang the hydrogen surrounding the sources was ionized forming bubbles in the neutral hydrogen. Over time, these bubbles grew and overlapped until the Universe was majoratively ionized. Though we know enough from other cosmological data sets to be able to roughly sketch the progression of Epoch of Reionization, the details are largely unknown. When did it start? When did it end? Did it all happen in one go or did the Universe partially reionize at some point? What were the ionizing sources or were there more than one type responsible?

The Epoch of Reionization is one of the last truly unexplored eras of our Universe and the excitement within the field is tangible as we rapidly approach the first 21-cm EoR detection. Though there are several teams working to this same aim, the high level of friendly collaboration and healthy competition within the EoR field is, in my opinion, unique and applaudable. This thesis is just one of the many pieces which fit together to make the detection and study of the EoR possible, but it is a piece which is, in my terribly biased opinion, is important in its own right.

Faced with such an wealth of new data to explore it is all too easy to rush in head first and miss the subtleties of the process. The careful removal of the foregrounds and an understanding

of the effect on the data is absolutely essential if we are to trust any of the conclusions drawn from the EoR observations. With such a small signal-to-noise ratio, every incorrect parameterization, no matter how small, has the potential to destroy or a reshape a signal, the form of which we are not even sure of in the first place.

In this thesis I have demonstrated that so-called 'non-parameteric' methods can accurately and precisely remove the EoR foregrounds with minimal user parameterization. The first method, FASTICA, defines the foregrounds by finding their statistically independent components. These components are a mixture of the different foregrounds and the EoR signal is treated as noise and discarded by the FASTICA model. By calculating the difference between the input mixed signal and the foreground model we have an estimate for the 21-cm signal and instrumental noise. The statistics of the instrumental noise will be known to a high accuracy and as such we can extract the reconstructed power spectrum of the 21-cm signal. We have reconstructed the 21-cm signal to impressive accuracy and precision across a wide range of frequencies and scales. The second method, GMCA, uses sparsity to define the foregrounds in a wavelet basis, again treating the EoR signal as noise. The EoR statistics are spectacularly recovered again and an analysis into how the noise/foregrounds leak into/out of the foreground model is performed. We find that, since the mixing matrix used to define the foregrounds is independent of the noise model, we can use a second noise signal to correct for the noise leakage in the 21-cm power spectrum, producing a more accurate reconstruction. Wavelet decomposition of the resulting noise+EoR signal maps is shown to be an effective method of denoising the maps, producing a 90% correlation with the simulated EoR map and a 50% improvement on the Gaussian smoothing denoising method used in previous EoR literature.

For the second strand of this thesis, I tackled an outstanding problem of how to include peculiar velocities of the hydrogen atoms into a 21-cm simulation. The majority of current reionization simulations output a series of brightness temperature boxes in real space. The peculiar velocities of the hydrogen atoms at a particular redshift mean that we cannot use a simple redshift-frequency relation to construct an simulated observation (i.e. a light cone) from these boxes. Instead, I have written a code which takes multiple real space simulation boxes, works cell-by-cell test whether there is a 21-cm event which is measured at the chosen observed frequency and outputs a light cone. The inclusion of peculiar velocities in this way is essential if we are to trust the cosmological conclusions made on the back of EoR data and this is the first time such a code has been written for the public domain. I showed that, even with the modest peculiar velocities produced by the cosmological model used, there are significant small scale differences to the light cone. Though the large scale bubble structure remains intact, the small

scale differences are large enough to change the cylindrical power spectrum in a very noticeable way. This could affect statistical conclusions made from simulations and I therefore concluded that this full treatment of peculiar velocities is essential for confidence in one's conclusions.

I then considered whether foreground removal can be dispensed with entirely in favour of foreground avoidance, as has been suggested recently in the literature. I show that, when a fully physically-motivated foreground model is used, the area of k-space where the EoR signal dominates over the foregrounds (the EoR window) is reduced to zero. This is in direct opposition to the conclusions so far made in literature and is as a result of the varying spectral index of the Galactic synchrotron with line of sight. Ignoring this obscuration of the window could easily lead to erroneous conclusions for statistics such as redshift space distortions. I find that the EoR window can be somewhat recovered after foreground removal and concluded that foreground avoidance could be used as a way of minimizing bias on statistics after foreground removal has taken place.

Finally, I have the privilege of applying the GMCA code to some of the first data from the LOFAR-EoR experiment. As the data is not quite 'science ready', this is a preparatory step taken to identify and mitigate systematics. I find that GMCA separates out the foregrounds to an impressive degree, despite the data being noisy and with some calibration errors. GMCA turns out to be very powerful in identifying the systematics as separate components in the foreground model - for example the action of the primary beam and the variation of point source spectral index is clear in separate components. I attempt to mitigate the effect on the GMCA foreground model of the large instrumental noise rms in some subbands by weighting the mixing matrix according to this rms. I find that, for some sources at least, the residuals are considerably cleaner with noise weighting though a full statistical analysis is required to be confident of this. By looking at the Stokes V map, we do not observe foregrounds and so can be confident of our noise estimate calculated using Stokes V data. Overall, I find that GMCA gives extremely positive results considering the nature of the data and that, after acting a feedback tool to the calibration method, we can expect great things from GMCA on future, cleaner, data.

Throughout the course of this thesis I have tackled problems statistical, theoretical, practical and instrumental in nature. From simulating the EoR signal in an accurate manner to developing leading foreground removal methods which will allow us to detect that signal, I have been lucky enough to gain a broad understanding of the EoR field. The next few years promise to be extremely exciting for this field and I hope that the work presented here will aid the detection and analysis of the EoR signal when the time finally comes. I have a feeling it is just around the corner ....

Bibliography

Abel T., Bryan G. L., Norman M. L., 2000, ApJ, 540, 39

Abel T., Bryan G. L., Norman M. L., 2002, Science, 295, 93

Ade P., Aghanim N., C.Armitage-Caplan and the Planck Collaboration, 2013a, Planck 2013 results. I. Overview of products and scientific results, arXiv:astro-ph/1303.5062

Ade P., Aghanim N., C.Armitage-Caplan and the Planck Collaboration, 2013b, Planck 2013 results. XVI. Cosmological parameters, arXiv:astro-ph/1303.5076

Ahn K., Iliev I. T., Shapiro P. R., Mellema G., Koda J., Mao Y., 2012, ApJL, 756, L16

Ali S. S., Bharadwaj S., Chengalur J. N., 2008, MNRAS, 385, 2166

Alpher R. A., Bethe H., Gamow G., 1948, Phys. Rev., 73, 803

Avison A., George S. J., 2013, European Journal of Physics, 34, 7

Baade W., 1944, ApJ, 100, 137

Babcock H., 1939, Lick Obs. Bull, 19, 41

Baek, S. Semelin, B. Di Matteo, P. Revaz, Y. Combes, F. 2010, A&A, 523, A4

Barkana R., Loeb A., 2004, ApJ, 601, 64

Barkana R., Loeb A., 2005, ApJL, 624, L65

Bennett C., et al., 1992, ApJ, 396, L7

Bernardi G., de Bruyn A. G., Brentjens M. A., and the LOFAR-EoR Group, 2009, A&A, 500, 965

Bernardi G., de Bruyn A. G., Harker G., and the LOFAR-EoR Group, 2010, A&A, 522, A67

Bertone G., Hooper D., Silk J., 2005, Phys. Rept, 405, 279

Blumenthal G., Faber S., Primack J., Rees M., 1984, Nature, 311, 517

Bobin J., Moudden Y., Starck J.-L., Fadili J., Aghanim N., 2008, Statistical Methodology, 5, 307

Bobin J., Starck J.-L., Fadili J., Moudden Y., 2007, IEEE Transactions on Image Processing, 16, 2662

Bobin J., Starck J.-L., Moudden Y., Fadili M. J., 2008, Elsevier, pp 221 – 302

Bobin, J. Starck, J.-L. Sureau, F. Basak, S. 2013, A&A, 550, A73

Bolton J. S., Becker G. D., Wyithe J. S. B., Haehnelt M. G., Sargent W. L. W., 2010, MNRAS, 406, 612

Bond J. R., 1995, Phys. Rev. Lett., 74, 4369

Bosma A., 1978, PhD thesis, University of Groningen

Bottino M., Banday A. J., Maino D., 2008, MNRAS, 389, 1190

Bottino M., Banday A. J., Maino D., 2010, MNRAS, 402, 207

Bowman J. D., Morales M. F., Hewitt J. N., 2006, ApJ, 638, 20

Bridle A. H., 1967, MNRAS, 136, 219

Bromm V., Kudritzki R. P., Loeb A., 2001, ApJ, 552, 464

Bromm V., Larson R. B., 2004, Annual Review of Astronomy and Astrophysics, 42, 79

Bunker A. J., Wilkins S., Ellis R. S., Stark D. P., Lorenzoni S., Chiu K., Lacy M., Jarvis M. J., Hickey S., 2010, MNRAS, 409, 855

Bunn E. F., Zaldarriaga M., Tegmark M., de Oliveira-Costa A., 2003, Phys. Rev. D, 67, 023501

Burke B. F., Graham-Smith F., 2010, An Introduction to Radio Astronomy. Cambridge University Press

Burles S., Nollett K. M., Turner M. S., 2001, ApJL, 552, L1

Burles S., Tytler D., 1998, ApJ, 499, 699

Cane H., 1979, MNRAS, 189, 465

Carilli C. L., Gnedin N. Y., Owen F., 2002, ApJ, 577, 22

Carilli C. L., Wang R., van Hoven M. B., Dwarakanath K., Chengalur J. N., Wyithe S., 2007, AJ, 133, 2841

Caswell J. L., Lerche I., 1979, MNRAS, 187, 201

Cen R., 2003, ApJ, 591, L5

Chapman E., Abdalla F. B., Bobin J., Starck J.-L., Harker G., Jeli V., Labropoulos P., Zaroubi S., Brentjens M. A., de Bruyn A. G., Koopmans L. V. E., 2013, MNRAS, 429, 165

Choudhury T., Ferrara A., 2006, Physics of Cosmic Reionization, arXiv:astro-ph/0603149

Chuzhoy L., Alvarez M. A., Shapiro P. R., 2006, ApJ, 648, L1

Ciardi B., Labropoulos P., Maselli A., and the LOFAR-EoR Group, 2013, MNRAS, 428, 1755

Ciardi B., Madau P., 2003, ApJ, 596, 1

Clark P. C., Glover S. C. O., Smith R. J., Greif T. H., Klessen R. S., Bromm V., 2011, Science, 331, 1040

Clery D., 2009, Science, 325, 1617

Colberg J. M., White S. D. M., Yoshida N., MacFarland T. J., Jenkins A., Frenk C. S., Pearce F. R., Evrard A. E., Couchman H. M. P., Efstathiou G., Peacock J. A., Thomas P. A., 2002, MNRAS, 319, 209

Condon J. J., 1974, ApJ, 188, 279

Cooray A., Furlanetto S. R., 2004, ApJL, 606, L5

Croft R., 1998 Eighteenth texas symposium on relativistic astrophysics and cosmology:"texas in chicago", chicago, 15-20 december 1996. World Scientific Publishing Company, Incorporated, p. 664

Datta A., Bowman J. D., Carilli C. L., 2010, ApJ, 724, 526

Delabrouille J., Cardoso J.-F., Patanchon G., 2003, MNRAS, 346, 1089

Di Matteo T., Ciardi B., Miniati F., 2004, MNRAS, 355, 1053

Di Matteo T., Perna R., Abel T., Rees M. J., 2002, ApJ, 564, 576

Dickinson C., Davies R. D., Davis R. J., 2003, MNRAS, 341, 369

Dillon J. S., Liu A., Williams C. L., Hewitt J. N., Tegmark M., Morgan E. H., Levine A. M., Morales M. F., Tingay S. J., Bernardi G., Bowman J. D., Briggs F. H., Emrich D., Mitchell D. A., Oberoi D., Prabu T., Wayth R., Webster R. L., 2013, Overcoming real-world obstacles in 21 cm power spectrum estimation: A method demonstration and results from early Murchison Widefield Array data, arXiv:astro-ph/1304.4229

Donzelli S., Maino D., Bersanelli M., Childers J., Figueiredo N., Lubin P. M., Meinhold P. R., O'Dwyer I. J., Seiffert M. D., Villela T., Wandelt B. D., Wuensche C. A., 2006, MNRAS, 369, 441

Efstathiou G., Sutherland W., Maddox S., 1990, Nature, 348, 705

Einasto J., Kaasik A., Saar E., 1974, Nature, 250, 309

Enßlin T., 2001, A&A, 366, 26

Evrard A. E., MacFarland T. J., Couchman H. M. P., Colberg J. M., Yoshida N., White S. D. M., Jenkins A., Frenk C. S., Pearce F. R., Peacock J. A., Thomas P. A., Consortium T. V., 2002, ApJ, 573, 7

Ewen H., Purcell E., 1951, Nature, 168, 356

Faber S., Gallagher J., 1979, ARA&A, 17, 135

Fan X., Strauss M. A., Becker R. H., White R. L., Gunn J. E., Knapp G. R., Richards G. T., Schneider D. P., Brinkmann J., Fukugita M., 2006, AJ, 132, 117

Fan X., Strauss M. A., Richards G. T., Hennawi J. F., Becker R. H., White R. L., Diamond-Stanic A. M., Donley J. L., Jiang L., Kim J. S., Vestergaard M., Young J. E., Gunn J. E., Lupton R. H., Knapp G. R., Schneider D. P., Brandt W. N., Bahcall N. A., et al., 2006, AJ, 131, 1203

Fan X., Strauss M. A., Schneider D. P., et al., 2003, AJ, 125, 1649

Field G., 1958, Proceedings of the IRE, 46, 240

Field G., 1959, ApJ, 129, 536

Freeman K., 1970, ApJ, 160, 811

Furlanetto S., 2006, MNRAS, 370, 1867

Furlanetto S., Loeb A., 2002, ApJ, 579, 1

Furlanetto S., Oh S. P., Briggs F., 2006, Phys. Rep., 433, 181

Furlanetto S., Zaldarriaga M., Hernquist L., 2004, ApJ, 613, 1

Gallerani S., Choudhury T. R., Ferrara A., 2006, MNRAS, 370, 1401

Giardino G., Banday A. J., Bennett K., Jonas J. L., Tauber J., 2002, A&A, 387, 82

Gleser L., Nusser A., Benson A. J., 2008, MNRAS, 391, 383

Glover S., 2005, Space Science Reviews, 117, 445

Gnedin N. Y., Shaver P. A., 2004, ApJ, 608, 611

Govoni F., Enßlin T. A., Feretti L., Giovannini G., 2001, A&A, 369, 441

Green D., 2006, A Catalogue of Galactic Supernova Remnants (2006 April version), http://www.mrao.cam.ac.uk/surveys/snrs/

Greif T. H., Bromm V., Clark P. C., Glover S. C. O., Smith R. J., Klessen R. S., Yoshida N., Springel V., 2012, MNRAS, 424, 399

Greif T. H., Springel V., White S. D. M., Glover S. C. O., Clark P. C., Smith R. J., Klessen R. S., Bromm V., 2011, ApJ, 737, 75

Gu J., Xu H., Wang J., An T., Chen W., 2013, ApJ, 773, 38

Gunn J., Peterson B., 1965, ApJ, 142, 1633

Guth A. H., 1981, Phys. Rev. D, 23, 347

Haiman Z., Abel T., Rees M. J., 2000, ApJ, 534, 11

Haiman Z., Holder G. P., 2003, ApJ, 595, 1

Harker G., Zaroubi S., Bernardi G., Brentjens M. A., de Bruyn A. G., Ciardi B., Jelić V., Koopmans L. V. E., Labropoulos P., Mellema G., Offringa A., Pandey V. N., Pawlik A. H., Schaye J., Thomas R. M., Yatawatta S., 2010, MNRAS, 405, 2492

Harker G., Zaroubi S., Bernardi G., Brentjens M. A., De Bruyn A. G., Ciardi B., Jelić V., Koopmans L. V. E., Labropoulos P., Mellema G., Offringa A., Pandey V. N., Schaye J., Thomas R. M., Yatawatta S., 2009, MNRAS, 397, 1138

Harker G., Zaroubi S., Thomas R. M., Jelić V., Labropoulos P., Mellema G., Iliev I. T., Bernardi G., Brentjens M. A., De Bruyn A. G., Ciardi B., Koopmans L. V. E., Pandey V. N., Pawlik A. H., Schaye J., Yatawatta S., 2009, MNRAS, 393, 1449

Haslam C. G. T., Salter C. J., Stoffel H., Wilson W. E., 1982, A&A, 47

Hoeft M., Bruggen M., Yepes G., 2004, MNRAS, 347, 389

Hubble E., 1929, Proc. Natl. Acad. Sci., 15, 168

Hui L., Haiman Z., 2003, ApJ, 596, 9

Hummel J. A., Pawlik A. H., Milosavljevi M., Bromm V., 2012, ApJ, 755, 72

Hyvärinen A., 1999, Neural Networks, IEEE Transactions on, 10, 626

Hyvärinen A., Karhunen J., Oja E., 2001, Independent Component Analysis. John Wiley and Sons

Hyvärinen A., Oja E., 2000, Neural Networks, 13, 411

Iliev I. T., Mellema G., Pen U.-L., Bond J. R., Shapiro P. R., 2008, MNRAS, 384, 863

Iliev I. T., Mellema G., Shapiro P. R., Pen U.-L., Mao Y., Koda J., Ahn K., 2012, MNRAS, 423, 2222

Jackson C., 2005, PASA, 22, 36

Jelić V., Zaroubi S., Labropoulos P., Bernardi G., de Bruyn A. G., Koopmans L. V. E., 2010, MNRAS, 409, 1647

Jelić V., Zaroubi S., Labropoulos P., Thomas R. M., Bernardi G., Brentjens M. A., De Bruyn A. G., Ciardi B., Harker G., Koopmans L. V. E., Pandey V. N., Schaye J., Yatawatta S., 2008, MNRAS, 389, 1319

Jenkins A., Frenk C. S., White S. D. M., Colberg J. M., Cole S., Evrard A. E., Couchman H. M. P., Yoshida N., 2001, MNRAS, 321, 372

Jensen H., Datta K. K., Mellema G., and the LOFAR-EoR Group, 2013, MNRAS

Johnson J. L., Khochfar S., 2011, The Astrophysical Journal, 743, 126

Jolliffe I., 2002, Principal Component Analysis. Springer Series in Statistics, Springer

Kazemi S., Yatawatta S., Zaroubi S., 2013, MNRAS, 434, 3130

Kazemi S., Yatawatta S., Zaroubi S., Lampropoulos P., de Bruyn A. G., Koopmans L. V. E., Noordam J., 2011, MNRAS, 414, 1656

Kellermann K. I., 1966, ApJ, 146, 621

Kellermann K. I., 1974, Verschuur G.L., Kellermann K.I. (eds.) Galactic and Extragalactic Radio Astronomy. Springer-Verlag, Berlin

Kellermann K. I., Owen F., 1988, Verschuur G.L., Kellermann K.I. (eds.) Galactic and Extragalactic Radio Astronomy. Springer-Verlag, Berlin

Kellermann K. I., Pauliny-Toth I. I. K., 1969, ApJ, 155, L71

Kellermann K. I., Pauliny-Toth I. I. K., Williams P. J. S., 1969, ApJ, 157, 1

Kitayama T., Yoshida N., Susa H., Umemura M., 2004, ApJ, 613, 631

Knox L., Page L., 2000, Phys.Rev.Lett., 85, 1366

Kogut A., Banday A. J., Bennett C. L., Gorski K. M., Hinshaw G., Reach W. T., 1996, ApJ, 460, 1

Kogut A., et al., 1992, ApJ, 401, 1

Kogut A., Spergel D. N., Barnes C., et al., 2003, ApJS, 148, 161

Komatsu E., Smith K. M., Dunkley J., Bennett C. L., Gold B., Hinshaw G., Jarosik N., Larson D., Nolta M. R., Page L., Spergel D. N., Halpern M., Hill R. S., Kogut A., Limon M., Meyer S. S., Odegard N., Tucker G. S., Weiland J. L., Wollack E., Wright E. L., 2011, ApJS, 192, 18

Lacey C., Cole S., 1993, MNRAS, 262, 627

Lampropoulos P., 2010, PhD thesis, University of Groningen

Landecker T., Wielebinski R., 1970, AuJPA, 16, 1

Lawson K. D., Mayer C. J., Osborne J. L., Parkinson M. L., 1987, MNRAS, 225, 307

Linde A., 2008, Lecture Notes in Physics, 738, 1

Liu A., Tegmark M., 2011, Phys. Rev. D, 83, 103006

Liu A., Tegmark M., Bowman J., Hewitt J., Zaldarriaga M., 2009, MNRAS, 398, 401

Liu A., Tegmark M., Zaldarriaga M., 2009, MNRAS, 394, 1575

Lynds R., 1971, ApJ, 164, L73

McCready L. L., Pawsey J. L., Payne-Scott R., 1947, Proc. R. Soc. Lond. A, 190, 357

McGreer I. D., Mesinger A., Fan X., 2011, MNRAS, 415, 3237

Machler M., 1993, in Research Report 71 Seminar fur Statistik, ETH Zurich, Very smooth nonparametric curve estimation by penalizing change of curvature

Machler M., 1995, The Annals of Statistics, 23, 1496

Mack K. J., Wyithe J. S. B., 2012, MNRAS, 425, 2988

McQuinn M., Zahn O., Zaldarriaga M., Hernquist L., Furlanetto S. R., 2006, ApJ, 653, 815

Madau P., Meiksin A., Rees M. J., 1997, ApJ, 475, 429

Madau P., Rees M. J., Volonteri M., Haardt F., Oh S. P., 2004, ApJ, 604, 484

Maino D., Banday A. J., Baccigalupi C., Perrotta F., Grski K. M., 2003, MNRAS, 344, 544

Maino D., Donzelli S., Banday A. J., Stivoli F., Baccigalupi C., 2007, MNRAS, 374, 1207

Maino D., Farusi A., Baccigalupi C., Perrotta F., Banday A. J., Bedini L., Burigana C., De Zotti G., Grski K. M., Salerno E., 2002, MNRAS, 334, 53

Majumdar S., Bharadwaj S., Choudhury T. R., 2012, MNRAS, 426, 3178

Malhotra S., Rhoads J. E., 2004, ApJ, 617, L5

Mao Y., Shapiro P. R., Mellema G., Iliev I. T., Koda J., Ahn K., 2012, MNRAS, 422, 926

Mapelli M., Ferrara A., Pierpaoli E., 2006, MNRAS, 369, 1719

Mather J., et al., 1990, ApJ, 354, L37

Mauskopf P., et al., 2000, ApJ, 536, L59

Meiksin A., 2011, MNRAS, 417, 1480

Mellema G., Iliev I. T., Pen U.-L., Shapiro P. R., 2006, MNRAS, 372, 679

Mellema G., Koopmans L., Abdalla F., et al., 2012, Reionization and the Cosmic Dawn with the Square Kilometre Array, arXiv:astro-ph/1210.0197

Mesinger A., Furlanetto S., 2007, ApJ, 669, 663

Mesinger A., Furlanetto S., Cen R., 2011, MNRAS, 411, 955

Mesinger A., Haiman Z., 2007, ApJ, 660, 923

Mihalas D., 1978, Stellar Atmospheres. A Series of books in astronomy and astrophysics, W. H. Freeman

Miller A., et al., 1999, ApJ, 524, L1

Miralda-Escud J., 1998, ApJ, 501, 15

Morales M. F., Bowman J. D., Hewitt J. N., 2006, ApJ, 648, 767

Morales M. F., Hazelton B., Sullivan I., Beardsley A., 2012, ApJ, 752, 137

Morales M. F., Hewitt J., 2004, ApJ, 615, 7

Mortlock D. J., Warren S. J., Venemans B. P., Patel M., Hewett P. C., McMahon R. G., Simpson C., Theuns T., Gonzles-Solares E. A., Adamson A., Dye S., Hambly N. C., Hirst P., Irwin M. J., Kuiper E., Lawrence A., Rttgering H. J. A., 2011, Nature, 474, 616

M.Ryle D.D.Vonberg 1946, Nature, 158, 339

Muller C., Oort J., 1951, Nature, 168, 357

Nicolson I., 2007, Dark side of the universe: dark matter, dark energy, and the fate of the cosmos. Canopus

Nijboer R., Noordam J., Yatawatta S., 2006, ASPC, 351, 291

Nojiri S., Odintsov S. D., 2007, International Journal of Geometric Methods in Modern Physics, 4, 115

Nusser A., Benson A. J., Sugiyama N., Lacey C., 2002, ApJL, 580, L93

Nusser A., Silk J., 1993, ApJ, 411, L1

Offringa A., 2012, PhD thesis, Kapteyn Astronomical Institute Groningen

Oh S. P., 1999, ApJ, 527, 16

Oh S. P., Mack K. J., 2003, MNRAS, 346, 871

Omukai K., Nishi R., 1999, ApJ, 518, 64

Oort J., 1940, ApJ, 91, 273

Ostriker J., Peebles P., Yahill A., 1974, ApJ, 193, L1

Ouchi M., Shimasaku K., Furusawa H., Saito T., Yoshida M., Akiyama M., Ono Y., Yamada T., Ota K., Kashikawa N., Iye M., Kodama T., Okamura S., Simpson C., Yoshida M., 2010, ApJ, 723, 869

Paciga G., Albert J. G., Bandura K., Chang T.-C., Gupta Y., Hirata C., Odegova J., Pen U.-L., Peterson J. B., Roy J., Shaw R., Sigurdson K., Voytek T., 2013, A simulation calibrated limit on the HI power spectrum from the GMRT Epoch of Reionization experiment, arXiv:astro-ph/1301.5906

Paciga G., Chang T.-C., Gupta Y., Nityanada R., Odegova J., Pen U.-L., Peterson J. B., Roy J., Sigurdson K., 2011, MNRAS, 413, 1174

Page L., Hinshaw G., Komatsu E., et al., 2007, ApJS, 170, 335

Parsons A. R., Backer D. C., Foster G. S., Wright M. C. H., Bradley R. F., Gugliucci N. E., Parashare C. R., Benoit E. E., Aguirre J. E., Jacobs D. C., Carilli C. L., Herne D., Lynch M. J., Manley J. R., Werthimer D. J., 2010, AJ, 139, 1468

Parsons A. R., Liu A., Aguirre J. E., Ali Z. S., Bradley R. F., Carilli C. L., DeBoer D. R., Dexter M. R., Gugliucci N. E., Jacobs D. C., Klima P., MacMahon D. H. E., Manley J. R., Moore D. F., Pober J. C., Stefan I. I., Walbrugh W. P., 2013, New Limits on 21cm EoR From PAPER-32 Consistent with an X-Ray Heated IGM at z=7.7, arXiv:astro-ph/1304.4991

Parsons A. R., Pober J. C., Aguirre J. E., Carilli C. L., Jacobs D. C., Moore D. F., 2012, ApJ, 756, 165

Peacock J., 1999, Cosmological Physics. Cambridge Astrophysics Series, Cambridge University Press

Peebles P., 1980, The Large-scale Structure of the Universe. Princeton series in physics, Princeton University Press

Peebles P., 1982, ApJ, 263, L1

Peebles P., 1984, ApJ, 284, 439

Peebles P., Ratra B., 1988, ApJ, 325, L17

Penzias A., Wilson R., 1965, ApJ, 142, 419

Percival W. J., Baugh C. M., Bland-Hawthorn J., et al., 2001, MNRAS, 327, 1297

Perlmutter S., Aldering G., Goldhaber G., and The Supernova Cosmology Project, 1999, ApJ, 517, 565

Peters W. M., Lazio T. J. W., Clarke T. E., Erickson W. C., Kassim N. E., 2011, A&A, 525, A128

Petrovic N., Oh S. P., 2011, MNRAS, 413, 2103

Platania P., Burigana C., Maino D., Caserini E., Bersanelli M., Cappellini B., Mennella A., 2003, A&A, 410, 847

Press W. H., Schechter P., 1974, ApJ, 187, 425

Pritchard J. R., Loeb A., 2008, Phys. Rev. D, 78, 103511

Pritchard J. R., Loeb A., 2010, Phys.Rev.D, 82, 023006

Pritchard J. R., Loeb A., Wyithe J. S. B., 2010, MNRAS, 408, 57

Ratra B., Peebles P., 1988, Phys. Rev. D, 37, 3406

Rauch G. D. B. M., Sargent W. L. W., 2007, ApJ, 662, 72

Reich P., Reich W., 1988, A&A Supplement Series, 74, 7

Reich W., 1982, A&A Supplement Series, 48, 219

Reich W., Reich P., 1986, A&A Supplement Series, 63, 205

Ricotti M., Ostriker J., 2004a, MNRAS, 350, 539

Ricotti M., Ostriker J., 2004b, MNRAS, 352, 547

Riess A. G., Filippenko A. V., Challis P., Clocchiatti A., Diercks A., Garnavich P. M., Gilliland R. L., Hogan C. J., Jha S., Kirshner R. P., Leibundgut B., Phillips M. M., Reiss D., Schmidt B. P., Schommer R. A., Smith R. C., Spyromilio J., Stubbs C., Suntzeff N. B., Tonry J., 1998, AJ, 116, 1009

Roberts M., Whitehurst R., 1975, ApJ, 201, 327

Rubin V., Ford W., 1970, ApJ, 159, 379

Rybicki G. B., Lightman A. P., 1979, Radiative processes in astrophysics. Wiley-VCH

Ryle M., Neville A. C., 1962, MNRAS, 125, 39

Sakharov A. D., 1967, Soviet Journal of Experimental and Theoretical Physics Letters, 5, 24

Santos M. G., Cooray A., Knox L., 2005, ApJ, 625, 575

Santos M. G., Ferramacho L., Silva M. B., Amblard A., Cooray A., 2010, MNRAS, 406, 2421

Sargent W. L. W., Young P. J., Boksenberg A., Tytler D., 1980, ApJS, 42, 41

Schaerer D., 2002, A&A, 382, 28

Schaye J., Theuns T., Rauch M., Efstathiou G., Sargent W. L., 2000, MNRAS, 318, 817

Sethi S. K., 2005, MNRAS, 363, 818

Shapiro P. R., Giroux M. L., 1987, ApJ, 321, L107

Shapiro P. R., Mao Y., Iliev I. T., Mellema G., Datta K. K., Ahn K., Koda J., 2013, Phys. Rev. Lett., 110, 151301

Shapiro S., 2004, in Ho L. C., ed., Coevolution of Black Holes and Galaxies. Carnegie Observatories Astroph. Ser.Cambridge Univ.Press,Cambridge,p. 103

Shaver P. A., Windhorst R. A., Madau P., de Bruyn A. G., 1999, A&A, 345, 380

Shaw J. R., Sigurdson K., Pen U.-L., Stebbins A., Sitwell M., 2014, ApJ, 781, 57

Sheth R. K., Tormen G., 2002, MNRAS, 329, 61

Simon A., 1977, MNRAS, 180, 429

Slipher V., 1914, Lowell Obs. Bull, 62,11,12

Smirnov O., Noordam J., 2004, ASPC, 314, 18

Smith R. J., Glover S. C. O., Clark P. C., Greif T., Klessen R. S., 2011, MNRAS, 414, 3633

Smith R. J., Iocco F., Glover S. C. O., Schleicher D. R. G., Klessen R. S., Hirano S., Yoshida N., 2012, ApJ, 761, 154

Smoot G., 1998, Galactic free-free and h-alpha emission, arXiv:astro-ph/9801121

Smoot G., et al., 1992, ApJ, 396, L1

Sokasian A., Abel T., Hernquist L., Springel V., 2003, MNRAS, 344, 607

Songaila A., Cowie L. L., 2002, AJ, 123, 2183

Spergel D. N., Bean R., Dore O., et al., 2007, ApJS, 170, 377

Stacy A., Bromm V., 2013, 433, 1094

Stacy A., Greif T. H., Bromm V., 2010, MNRAS, 403, 45

Starck J.-L., Murtagh F., 2006, Astronomical image and data analysis. Springer

Starck J.-L., Murtagh F., Bijaoui A., 1998, Image Processing and Data Analysis:The Multiscale Approach. Cambridge University Press

Stompor R., Abroe M., Ade P., et al., 2001, ApJ, 561, L7

Sunyaev R., Zeldovich Y., 1970, Astrophysics and Space Science, 7, 3

Sunyaev R. A., Zel'dovich Y. B., 1980, Annual Review of Astronomy and Astrophysics, 18, 537

Tegmark M., Eisenstein D. J., Hu W., de Oliveira-Costa A., 2000, ApJ, 530, 133

Tegmark M., Eisenstein D. J., Strauss M. A., et al., 2006, Phys. Rev. D, 74, 123507

Theuns T., Schaye J., Zaroubi S., Kim T.-S., Tzanavaris P., Carswell B., 2002, ApJ, 567, L103

Thomas R., Zaroubi S., 2008, MNRAS, 384, 1080

Thomas R., Zaroubi S., 2011, MNRAS, 410, 1377

Thomas R., Zaroubi S., Ciardi B., Pawlik A. H., Labropoulos P., Jeli V., Bernardi G., Brentjens M. A., de Bruyn A. G., Harker G. J. A., Koopmans L. V. E., Mellema G., Pandey V. N., Schaye J., Yatawatta S., 2008, MNRAS, 393, 32

Thompson A. R., Moran J. M., Swenson Jr. G. W., 2001, Interferometry and Synthesis in Radio Astronomy. John Wiley and Sons

Tingay S., Goeke R., Bowman J., Emrich D., Ord S., Mitchell D., Morales M., Booler T., Crosse B., Wayth R., et al., 2013, Publications of the Astronomical Society of Australia, 30, e007

Totani T., Kawai N., Kosugi G., Aoki K., Yamada T., Iye M., Ohta K., Hattori T., 2006, PASJ, 58, 485

Trott C. M., Wayth R. B., Tingay S. J., 2012, ApJ, 757, 101

Turk M. J., Abel T., O'Shea B., 2009, Science, 325, 601

Uson J., Wilkinson D., 1984, ApJ, 277, L1

van de Hulst H., 1945, Ned.Tijdschr.Natuuurk, 11, 201

van de Hulst H., Raimond E., van Woerden H., 1957, Bull. Astron. Inst. Neth., 14, 1

van Haarlem, M. P. Wise, M. W. Gunst, A. W. and the LOFAR Collaboration, 2013, A&A, 556, A2

Vedantham H., Shankar N. U., Subrahmanyan R., 2012, ApJ, 745, 176

Vogeley M. S., Szalay A. S., 1996, ApJ, 465, 34

Volders L., 1959, Bull. Astron. Inst. Neth., 1, 323

Waldmann I. P., 2012, ApJ, 747, 12

Wang J., Xu H., An T., Gu J., Guo X., Li W., Wang Y., Liu C., Martineau-Huynh O., Wu X.-P., 2013, ApJ, 763, 90

Wang X., Tegmark M., Santos M. G., Knox L., 2006, ApJ, 650, 529

Wetterich C., 1988, Nucl.Phys.B, 302, 668

White R. L., Becker R. H., Fan X., Strauss M. A., 2003, AJ, 126, 1

White S., Davis.M. Frenk C., 1984, MNRAS, 209, 27P

White S., Frenk.C.S. Davis.M. 1983, ApJ, 274, L1

Wild J., 1952, ApJ, 115, 206

Willis A., Oosterbaan C., Le Poole R., de Ruiter H., Strom R., Valentijn E., Katgert P., Katgert-Merkelijn J. J. D., 1977, Radio Astronomy and Cosmology. Reidel, Dordrecht

Wilson M., Silk J., 1981, ApJ, 243, 14

Wilson R., Penzias A., 1965, AJ, 70, 697

Wolf M., 1914, Vierteljahresschr Astron. Ges., 49, 162

Wouthuysen S., 1952, AJ, 57, 31

Wright E., et al., 1992, ApJ, 396, L13

Wyithe J., Loeb A., 2003, ApJ, 588, L69

Wyithe J. S. B., Loeb A., Carilli C., 2005, ApJ, 628, 575

Xu Y., Chen X., Fan Z., Trac H., Cen R., 2009, ApJ, 704, 1396

Xu Y., Ferrara A., Chen X., 2011, MNRAS, 410, 2025

Zahn O., Lidz A., McQuinn M., Dutta S., Hernquist L., Zaldarriaga M., Furlanetto S. R., 2007, ApJ, 654, 12

Zahn O., Mesinger A., McQuinn M., Trac H., Cen R., Hernquist L. E., 2011, MNRAS, 414, 727

Zahn O., Reichardt C. L., Shaw L., et al., 2012, ApJ, 756, 65

Zaldarriaga M., Furlanetto S. R., Hernquist L., 2004, ApJ, 608, 622

Zaroubi S., 2010, in Proceedings of the Widefield Science and Technology for the SKA SKADS Conference 2009 S.A. Torchinsky, A. van Ardenne, T. van den Brink-Havinga, A. van Es, A.J. Faulkner (eds.). Probing the epoch of reionization with low frequency arrays

Zaroubi S., de Bruyn A. G., Harker G., Thomas R. M., Labropolous P., Jeli V., Koopmans L. V. E., Brentjens M. A., Bernardi G., Ciardi B., Daiboo S., Kazemi S., Martinez-Rubi O., Mellema G., Offringa A. R., Pandey V. N., Schaye J., Veligatla V., Vedantham H., Yatawatta S., 2012, MNRAS, 425, 2964

Zaroubi S., Silk J., 2005, MNRAS, 360, L64

Zaroubi S., Thomas R. M., Sugiyama N., Silk J., 2007, MNRAS, 375, 1269

Zel'dovich Y. B., 1970, A&A, 5, 84

Zibulevsky M., Pearlmutter B. A., 2001, Neural Computation, 13, 863

Zwicky F., 1933, Helv. Phys. Acta., 6, 110